Jorge Romero

# Development of the MARA-LEB Facility



UNIVERSITY OF JYVÄSKYLÄ

FACULTY OF MATHEMATICS
AND SCIENCE

Jorge Romero

# Development of the MARA-LEB Facility

JYVÄSKYLÄN YLIOPISTO
UNIVERSITY OF JYVÄSKYLÄ

# ABSTRACT

Romero, Jorge
Development of the MARA-LEB Facility

The Mass Analyzing Recoil Apparatus Low-Energy Branch (MARA-LEB) is a new facility under development at the Accelerator Laboratory of the University of Jyväskylä, Finland, that has been designed to obtain isotopically pure radioactive beams of exotic nuclei and perform high-precision experiments to study their nuclear structure.

The design of MARA-LEB is discussed, delineating the similarities and inspirations from other nuclear research facilities around the world, along with the unique set of components that differentiates it from other devices. The elements that comprise the facility are outlined in terms of their design concepts and their role in the experimental objectives of the MARA-LEB scientific programme.

Simulations and preliminary tests of instruments are presented. Namely, the MARA-LEB gas cell is characterised in depth via window material simulations and gas flow simulations and experiments, including investigation on both transport efficiency and evacuation time. Simulations of the ion-optical transport and acceleration system are also shown, focused on obtaining preliminary working settings and investigating the transmission efficiency through the beamline.

Experiments performed at both the IGISOL and MARA facilities are showcased. At the IGISOL facility, in-gas-cell resonance laser ionisation of natural tin isotopes was performed with the MARA-LEB gas cell. A characterisation of the resonant lineshapes and their response to different buffer gas pressures is reported. Two experiments performed using the MARA separator served as a source of information on production rates for different nuclei in the nuclear regions of interest for MARA-LEB. Yields of actinide elements via multi-nucleon transfer reactions at MARA are shown for the first time. Data on reaction product dispersion at the MARA focal plane was also collected, informing design aspects of the gas cell entrance window, which are also presented.

Keywords: MARA-LEB, New Instrumentation, Nuclear Spectroscopy, Laser Spectroscopy, Mass Measurements, Decay Spectroscopy, Buffer Gas Cell.

# TIIVISTELMÄ (ABSTRACT IN FINNISH)

Romero, Jorge
MARA-LEB laitteiston kehitys

Massa-Analysoivaan Rekyyli Aparaattiin liitettävä matalan energian haara (MARA-LEB) on uusi kehitteillä oleva koelaitteisto Jyväskylän yliopiston fysiikan laitoksen kiihdytinlaboratoriossa (JYFL-ACCLAB). Laitteisto on suunniteltu tuottamaan isotooppisesti puhtaita eksoottisista ytimistä koostuvia radioaktiivisia hiukkassuihkuja. Näitä hiukkasuihkuja toimitetaan eri mittausasemille, missä voidaan suorittaa ydinrakennetutkimusta suurella tarkkuudella.

Tässä väitöskirjassa kuvaillaan MARA-LEB, vertaillaan MARA-LEB:iä muihin vastaaviin laitteistoihin toisissa kiihdytinlaboratorioissa ja selvitetään MARA-LEB:n vahvuudet. Laitevertailua ja suunniteltua kokeellista ohjelmaa käytettiin pohjana, kun laitteistoa suunniteltiin. Väitöskirjassa esitellään alustavien kokeiden ja simulaatioiden avulla saatuja tuloksia. MARA-LEB:n LEB-laitteiston ensimmäinen osa koostuu kaasutäytteisestä pysäytyskammiosta. MARA:lla eroteltujen rekyylien syvyysprofiileja pysäytyskaasussa simuloidaan ottaen huomioon käytetty ikkunamateriaali, käytetty kaasu ja sen massavirtaus. Kaikki nämä vaikuttavat siihen, kuinka tehokkaasti ja nopeasti rekyylit saadaan ulos kammiosta seuraavaa vaihetta varten. Seuraavassa vaiheessa radioaktiiviset ionit kiihdytetään uudelleen ja siirretään eteenpäin käyttäen ionioptisia siirtolinjoja ja tätä simuloitiin myös tässä työssä. Simulointien tarkoituksena on löytää alustavat laitteiston työskentelyasetukset maksimoiden koko systeemin siirtotehokkuudet.

Alustavia kokeita suoritettiin IGISOL ja MARA koeasemilla. IGISOL koeasemalla ionisoitiin pysyviä tina isotooppeja resonanssilaasereilla MARA-LEB pysäytyskammiossa. Resonanssimuodot ja niiden muutoksia eri pysäytyskaasun paineilla on raportoitu tässä työssä. MARA-erottimella tehtiin kaksi koetta. Näiden kokeiden tarkoituksena oli selvittää eksoottisten ytimien tuottoja, jotka ovat relevantteja liittyen suunniteltuun MARA-LEB kokeelliseen ohjelmaan. Ensimmäistä kertaa MARA:lla tutkittiin aktinidiytimien tuottoja käyttäen monen-nukleonin-siirtoreaktioita (MNT). Toisessa kokeessa tuotetiin ytimiä käyttäen fuusiohöyrystysreaktioita ja selviteltiin, miten LEB-osan pysäytyskammio saadaan kytkettyä mahdollisimman tehokkaasti MARA-erottelijaan.

Avainsanat: MARA-LEB, uusi laitteisto, ydispektroskopia, laserspektroskopia, massamittaus, hajoamisspektroskopia, pysäytyskammio.

**Author**

Jorge Romero
Department of Physics
University of Jyväskylä
Jyväskylä, Finland


**Supervisors**

Dr. Philippos Papadakis
Daresbury Laboratory
Science & Technologies Facilities Council (STFC)
Warrington, United Kingdom

Prof. Iain Moore
Department of Physics
University of Jyväskylä
Jyväskylä, Finland

Dr. Juha Uusitalo
Department of Physics
University of Jyväskylä
Jyväskylä, Finland

Prof. David Joss
Department of Physics
University of Liverpool
Liverpool, United Kingdom


**Reviewers**

Dr. Moritz Pascal Reiter
School of Physics and Astronomy
University of Edinburgh
Edinburgh, United Kingdom

Dr. Rafael Ferrer García
Institute for Nuclear and Radiation Physics
KU Leuven
Leuven, Belgium


**Opponent**

Dr. Hervé Savajols
Grand Accélérateur National d'Ions Lourds (GANIL)
Centre National de la Recherche Scientifique (CNRS)
Caen, France

Siempre que los «sapiens» actuamos juntos nos las arreglamos. Aunar nuestros sentimientos e ideas para colaborar juntos ha sido y será la clave de nuestro progreso. Y no valen atajos externos. Porque esa lucha, siempre, siempre, se libra en el interior de cada persona; para bien o para mal.

*When we "sapiens" act together, we find a way. Joining our feelings and ideas to collaborate together has been and will always be the key to our progress. And this can happen with no external help. Because this fight is always held inside of each individual; for better or for worse.*

<div align="right">

Érase una vez la independencia (2021)
P. Rafael Romero

</div>

---

Maybe we can take a whole lot of little steps that, when looked at together, might seem brilliant to somebody who doesn't know us.

*A lo mejor podemos dar un montón de pasos pequeñitos que, vistos todos juntos, a lo mejor parezcan brillantes a quien no nos conozca.*

<div align="right">

Tress of the Emerald Sea (2023)
Brandon Sanderson

</div>

# ACKNOWLEDGEMENTS

quizzes, nights out, office sports, stupid debates at lunch, rakes and crosswords. A special shoutout to Jamie and Adam McCarter for being excellent travel buddies, a good source of memes and Formula 1 enjoyment. Finally, the biggest of thanks to my very good friend Ricardo. Sharing an office, a team and a friendship with you is definitely one of the biggest things that have made Liverpool my home.

The journey towards the completion of this thesis finished here, but started way in the past.

Therefore, I would like to thank the friends I made during my master's degree (*Los Patos*): Aurora, Ari, Alex, Álvaro, Jaime, Inma and Vicente. We only shared one year together but what an amazing year! I cherish the memories we built travelling around Spain and learning some nuclear physics on the side...

To my friends from the University of València: Alberto $\partial \forall$, Ana, Rodri, Víctor, Diana, Natalia, Jose, Jaume, Victoria, Dani, Manu, Mel, Bea... and all others I shared moments with during those fantastic 4 years: thank you for helping me become the person I am today, and the physicist that wrote this thesis.

I would like to thank Dr. Kike Nácher and Dr. Djalil Kadi-Hanifi for having shown me, from a very early age, what a physicist is and driving my enthusiasm for this field that I adore. But most importantly for being the best teachers I could have had at the earliest stages of my career. I feel very privileged that I can call you friends and mentors.

My friends from school, Núria, Rebeca and Nicky also deserve a shoutout. Thanks for having been there for me for a very long time and for your friendship, even in the distance. And to the very best of friends I could ask for: Madero and Nathan, thanks for being the best adventure mates, for all the memories, and for being brothers to me.

Finally, I would not be in a position to write acknowledgements for a thesis without all the nurture and love that my family has shown me.

I would like to thank my newest family: the Browns. Bernie, Mick, Katie, Danny, Gracie and Ella. Thank you for everything you've done for me during this last year, I really feel like I have a home and a family away from home, and I am truly grateful for how you've welcomed me and for all the Sunday roasts, birthday cakes and Ambedo gigs we've shared. I feel proud to have become a Brownie too.

Of course, my favourite Brownie gets her own thank you. Thank you, Hannah, for being there since the beginning of my PhD and for your unwavering support. You are the kindest person I know and I have been spoilt by your help and love during what has been the last year of both of our PhDs. I am really excited to start this new era in our lives and to be your greatest help and your greatest distraction for a long time to come. I would not have been able to make it without you. I love you.

And last but not least, to those who have been there since the very beginning. Mabe, Chóbal, Carol, Rafe, Nana and Cristóbal, thanks for cheering on me from the distance and for being there for me, loving me unconditionally. Paula, thank you for coming into our family and bringing your always upbeat personality and happiness from the very beginning. Alberto, thanks for being my oldest friend, I know you will always have my back and you can count on me having yours. Thank you for growing with me and for having been the best brother I could have asked for. Mum and Dad, thank you for having given me everything. I would not be here today if it were not for all of the efforts you've made throughout these 27 years. This thesis has over 100 pages of physics, but there are not enough words in any language to thank you for everything you have done for me. This thesis is the end of a marathon for me, but one I could only start because you taught me how to run.

A massive thank you to everyone who appears in these acknowledgements for showing me that I will never walk alone.

Liverpool, October 2023

Jorge Romero

# AGRADECIMIENTOS

Mi primer agradecimiento solo podría ir a mi supervisor, Dr. Philippos Papadakis, por apoyarme y aconsejarme durante estos años más allá de la ciencia, con su siempre afable y bromista actitud. Ευχαριστώ Φίλιππε, no podía haber pedido un mejor supervisor y me siento honrado de haber sido tu primer doctorando. Me gustaría agradecer al Prof. Iain Moore por siempre haber sacado tiempo para mí pese a tu apretada agenda y por compartir tus conocimientos y experiencia de una manera siempre amigable. Dr. Juha Uusitalo, kiitos por tu ayuda en los experimetos y análisis en Jyväskylä, compartiendo tu inmensa sabiduría y experiencia con el mejor humor finés. Finalmente, gracias al Prof. Dave Joss por lidiar con toda la burocracia de este proceso y por tu dirección, especialmente en mis primeros meses en Liverpool.

Me gustaría agradecer a todo el grupo de MARA-LEB, puesto que sin ellos esta tesis no habría visto la luz, con una mención especial a Dr. Wouter Gins, por todo el "LEGO de mayores" que hemos construido y a Dr. Sasha Zadvornaya por servirme de mentora en el laboratorio durante los experimentos en IGISOL. Kiitos Dr. Mikael Reponen por enseñarme a usar láseres y ayudarme con el análisis y por tus apariciones especiales en Vakiopaine. Un gran agradecimiento también a Dr. Jan Sarén, que siempre está dispuesto a ayudar y ilusionado por enseñar. Kiitos myös, että yritit aina puhua suomeksi minun kanssa!

He sido afortunado en hacer un doctorado dual, porque he sido capaz de compartir estos 4 años con el doble de gente increíble. Lo siento si me olvido de mencionar a alguien, ya que ha habido muchísimas personas que han enriquecido mi vida durante este tiempo.

De Jyväskylä, quisiera agradecer a todos los amigos que he hecho dentro y fuera del laboratorio. No hubiera esperado hacer tan buenos amigos para toda la vida en un lugar tan remoto y congelado, pero estoy contento de haberme equivocado. Gracias a Joonas, Henri, Ville, Kalle, Olga, Ilkka, Henna, Marjut y tantos más de IGISOL y NucSpec. Pero sin duda, el mayor agradecimiento va para los miembros de la Embajada Europea en Jyväskylä: Alex, Álvaro, Andrés, Cris, Arthur, Marek, Stelio, Jessica, Daniel, Pablo y, por supuesto, los más bobos, Andrea y Adrian. No puedo agradeceros suficiente por los memes, lonkeros, noches de jueguitos, saunas, peleas de nieve, cabañas, risas y amistad. Habéis hecho que los largos y oscuros inviernos se sintieran acogedores y calurosos, por lo que os estaré siempre agradecido.

De Liverpool, me gustaría empezar agradeciendo a Holly y Adam (y Sprout) por mi primer año. Sois las primeras personas que conocí en esta ciudad y vivimos los meses más locos del confinamiento juntos. Gracias por darme la más calurosa bienvenida a Liverpool. A mis amigos del Oliver Lodge, muchas gracias por hacer de mis dos años en esta gran ciudad maravillosos. Gracias a Andy Briscoe, Charlie, Jacob, Clara, Ben, Tom, Kieran, Lorna, Magda, Owain, Shiyam, Tom Ham, Adam Ruby, Glória, Ellis, Ross, Jack... con quienes he compartido tardes en el pub, concursos en Zoom, noches de fiesta, deportes de oficina, debates estúpidos a la hora de comer, rastrillos y crucigramas. Especialmente, gracias a Jamie y Adam McCarter por ser grandes compañeros de viaje, fuente de memes y por compartir tardes de Fórmula 1. Finalmente, un agradecimiento gigante para mi gran amigo Ricardo. Compartir una oficina, un equipo y una amistad contigo es definitivamente uno de los mayores factores que han ayudado a convertir Liverpool en mi hogar.

El viaje para terminar la tesis ha acabado aquí, pero empezó hace mucho tiempo.

Por ello, quiero agradecer a los amigos que hice en el máster (*Los Patos*): Aurora, Ari, Alex, Álvaro, Jaime, Inma y Vicente. Solo compartimos un año juntos pero ¡qué año! Aprecio mucho todos los recuerdos que creamos viajando juntos por España y aprendiendo algo de física nuclear por el camino...

A mis amigos de la Univesidad de València: Alberto $\partial \forall$, Ana, Rodri, Víctor, Diana, Natalia, Jose, Jaume, Victoria, Dani, Manu, Mel, Bea... y todos los demás con los que compartí momentos en esos maravillosos 4 años: gracias por ayudarme a convertirme en la persona que soy hoy y en el físico que ha escrito esta tesis.

Quiero agradecer a Dr. Kike Nácher y Dr. Djalil Kadi-Hanifi por enseñarme, desde una temprana edad, qué es un físico y alentar mi entusiasmo por este campo que adoro. Pero de manera más importante, por ser los mejores profesores que pude haber tenido al principio de mi carrera. Me siento privilegiado de poder llamaros amigos y mentores.

Mis amigos del colegio, Núria, Rebeca y Nicky también merecen una mención. Gracias por estar ahí desde hace mucho y por vuestra amistad, incluso desde la distancia. Y, a los mejores amigos que se pueden pedir: Madero y Nathan, gracias por ser los mejor compañeros de aventuras, por todos los recuerdos y por ser mis hermanos.

Finalmente, no podría estar en la tesitura de escribir agradecimientos para una tesis sin todo el amor que mi familia siempre me ha dado.

Quisiera agradecer a mi nueva familia: los Brown. Bernie, Mick, Katie, Danny, Gracie y Ella. Gracias por todo lo que habéis hecho por mí durante este último año, siento de verdad que tengo una casa y una familia lejos de mi hogar, y estoy realmente agradecido por cómo me habéis acogido y por todas las cenas de

domingo, las tartas de cumpleaños y los conciertos de Ambedo que hemos compartido. Me siento orgulloso de haberme convertido en un Brownie también.

Por supuesto, mi Brownie favorita también tiene su propio agradecimiento. Gracias, Hannah, por estar ahí desde el principio de mi doctorado y por tu apoyo incondicional. Eres la persona más bondadosa que he conocido y me has mimado demasiado con tu ayuda y tu amor durante el que ha sido el último año de nuestros doctorados. Estoy muy emocionado por empezar esta nueva era en nuestras vidas y seguir siendo tu mayor ayuda y distracción durante mucho tiempo. No podría haber hecho esto sin ti. Te quiero.

Y, por último pero no por ello menos importante, a los que han estado ahí desde el principio. Mabe, Chóbal, Carol, Rafe, Nana y Cristóbal, gracias por animarme desde la distacia y por estar ahí para mí, queriéndome de manera incondicional. Paula, gracias por haber llegado a nuestra familia con la naturalidad y el optimismo que te caracterizan. Alberto, gracias por ser mi primer amigo, sé que siempre vas a estar ahí para mí y puedes contar conmigo para ti. Gracias por crecer a mi lado y por haber sido el mejor hermano que pudiera haber pedido. Mamá y papá, gracias por habérmelo dado todo. No estaría donde estoy hoy si no fuera por vuestro esfuerzos durante estos 27 años. Esta tesis tiene más de 100 páginas de física, pero no hay palabras en ningún idioma para agradeceros todo lo que habéis hecho por mí. Esta tesis es el final de una maratón para mí, pero solo pude empezarla porque vosotros me enseñasteis a correr.

Muchísimas gracias a toda la gente que aparece en estos agradecimientos por mostrarme que nunca caminaré solo.

Liverpool, octubre de 2023

Jorge Romero

# AUTHOR CONTRIBUTIONS TO PUBLICATIONS

PI    **J. Romero**, K. Auranen, M. Block, A. D. Briscoe, T. Eronen, W. Gins, T. Grahn, P. T. Greenlees, A. Illana, R. Julin, H. Joukainen, H. Jutila, J. Khuyagbaatar, J. Krier, M. Leino, J. Louko, M. Luoma, I. D. Moore, P. Mosat, J. Ojala, A. Ortiz-Cortes, J. Pakarinen, P. Papadakis, A. M. Plaza, P. Rahkila, A. Raggio, P. Ruotsalainen, J. Saren, M. Sandzelius, A. Tolosa-Delgado, J. Uusitalo, and G. Zimba *Nuclear Reaction Studies and Prospects for the New MARA-LEB Facility.* Acta Physica Polonica B Proceedings Supplement **16** 4-A12 (2023).

PII    A. Zadvornaya, **J. Romero**, T. Eronen, W. Gins, A. Kankainen, I. D. Moore, P. Papadakis, I. Pohjalainen, M. Reponen, S. Rinta-Antila, J. Sarén, D. Simonovski, and J. Uusitalo *Offline commissioning of a new gas cell for the MARA Low-Energy Branch.* Acta Physica Polonica B Proceedings Supplement **539** 33 (2023).

PI: The author lead the analysis, interpretation of data and the writing of the manuscript, as well as served as liaison in the experiments presented in the publication.
PII: The author had significant contributions to the experimental setup, and the collection and analysis of data, as well as participating in the manuscript proof-reading and correction.

## Other contributions

In addition, the author has participated in the upkeep and exploitation of the IGISOL, MARA and RITU facilities in the Accelerator Laboratory of the University of Jyväskylä, and has participated in experiments as a member of their respective research groups. The author contributed to the experimental part and the writing process of 7 additional peer-reviewed published works, which can be found on ORCiD: Jorge Romero - https://orcid.org/0000-0002-7845-5254 .

API    K. Auranen *et al.*, Phys. Rev. Lett. **128** 112501 (2022).

APII    S. Geldhof *et al.*, Phys. Rev. Lett. **128** 152501 (2022).

APIII    Z. Ge *et al.*, Phys. Rev. C **108** 045502 (2023).

APIV    K. Auranen *et al.*, Phys. Rev. C **108** L011303 (2023).
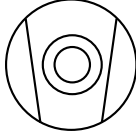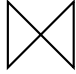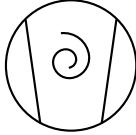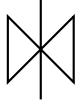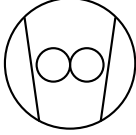
APV    P. Plattner *et al.*, Phys. Rev. Lett. **131** 222502 (2023).

APVI    X. Pereira-López *et al.*, Eur. Phys. J. A, **59** 44 (2023).

APVII    D. A. Nesterenko *et al.*, Phys. Rev. C **108** 054301 (2023).

## LIST OF SYMBOLS

**Vacuum Symbols**

(CG) Capacitive Gauge

(FR) Full Range Gauge

(PG) Pirani Gauge

Turbo Pump

Scroll Pump

Screw Pump

Valve

Gate Valve

Motorised Pendulum Valve

# CONTENTS

## I   Introduction                                                          19

## II   Instrumentation                                                      59

## III   Testing and Experiments         105

## IV   Conclusion         141

# Part I

# Introduction

# 1   INTRODUCTION

Since 1906, when Ernest Rutherford conducted an experiment in which the interaction between $\alpha$ particles and a thin gold foil was studied [1], the atomic nucleus has been at the centre of some of the most advanced and sophisticated scientific endeavours.

In particular, nuclear physics experiments have been at the forefront of technology, spearheading the development of detectors and other devices, such as nuclear research electronics and digital data acquisition systems, and pushing the boundaries of knowledge.

This thesis focuses on the development of a novel nuclear research facility: a low-energy branch (LEB) for the Mass Analysing Recoil Apparatus (MARA) [2], a separator that has been in use in Jyväskylä, Finland, since 2009.

This first chapter will introduce key concepts of the nuclear system that will be referenced throughout the thesis. It will also give an overview of the current state of nuclear research facilities throughout the world, with a special focus on those that have similar working principles and scientific objectives as MARA-LEB. These objectives will also be outlined in this chapter, while the facility's working principles will be explained in subsequent chapters.

## 1.1 The Atomic Nucleus

The atomic nucleus is a collection of $A$ nucleons which are bound together. Of these, $Z$ are protons, which will define the identity of the nucleus in terms of chemical element. The rest of the particles will be $N$ neutrons. Thus, a nucleus of an element with chemical symbol X can be represented with the following notation: $^{A}_{Z}X_{N}$, which can be simplified as $^{A}X$, given that $Z$ is always known given a certain chemical symbol and $N = A - Z$.

If two nuclei have the same $Z$ but different $N$, they are considered *isotopes*. If two nuclei have the same $N$ but different $Z$, they are known as *isotones*. Two nuclei with the same $A$ but not equal $Z$ or $N$ are known as *isobars*. Two isobars that meet the condition $Z_1 = N_2$ and $Z_2 = N_1$ are called *conjugate* nuclei. A nucleus with $N = Z$ can, therefore, be referred as a self-conjugate nucleus.

Nuclei in their lowest energy state, or ground state, can be stable or radioactive. Stable nuclei do not decay. Radioactive or unstable nuclei are those for which their ground state has an energetically viable decay which would reduce their energy. All nuclei can additionally be excited, possessing an energy higher than their ground state. Excited states usually de-excite rapidly ($\sim 10$ ps) by emitting a photon, or gamma ($\gamma$) ray. Longer lived excited states (with half-lives longer than 1 ns) are known as *isomers*.

## 1.2 Nuclear Reactions

Nuclear reactions in experiments usually involve a projectile or beam particle and a target nucleus. These beam and target nuclei can interact in several ways; the most relevant for this thesis are detailed in the following paragraph.

If the beam and target particles combine into an excited nucleus which de-excites solely via the emission of $\gamma$ rays, the reaction is a fusion reaction. If the resulting compound nucleus instead de-excites via the emission of a small number of nucleons or $\alpha$ particles, the reaction is known as a fusion-evaporation reaction, where the emitted particles are said to be evaporated from the compound nucleus. A reaction in which the beam and target particles exchange nucleons is known as a transfer reaction. In particular, a reaction in which the exchange involves several nucleons is called a multi-nucleon transfer (MNT) reaction.

MNT reactions involving heavy nuclei have been recently emerged as a new mechanism to produce heavy and superheavy elements [3]. New exotic isotopes are generally produced via fusion-evaporation, fission or fragmentation reactions. Experiments producing heavy elements via MNT reactions have been

ongoing for over 50 years, but the synthesis of new heavy-element isotopes with this mechanism has only been achieved in more recent times spurred by new theoretical calculations [4].

Nuclei originating from fusion-evaporation reactions are produced mostly in the direction of the primary beam and in a small solid angle around that direction. In contrast, MNT reaction production cross sections generally present maxima at larger laboratory angles ($50° - 60°$) from the beam direction.

In terms of energy, fusion-evaporation reaction products emerge with high excitation energies and subsequently de-excite via the emission of prompt $\gamma$ rays. MNT reactions yield products with relatively low excitation energies, but high spins [5].

The most common notations for nuclear reactions involving a projectile, P, and a target nucleus, T, resulting in a product nucleus, R, and evaporated particles E are as follows:

$$P + T \rightarrow R + E,$$
$$T(P, E)R.$$
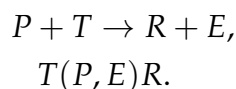
The former is used preferentially when there are no evaporated particles, they are not considered important or there are several steps to the reaction. The latter, more compact notation, is used mainly for fusion-evaporation and fusion-fission reactions. Both of these notations will be used throughout this thesis.

Nuclear reactions in which the projectile and the target material are of similar mass are known as symmetric reactions. An example of one such reaction is $^{40}$Ca($^{40}$Ca, 2n)$^{78}$Zr, in which the beam and target are identical. An asymmetric reaction is one in which the projectile and target have a large mass difference. For these reactions, the beam can be either lighter or heavier than the target nucleus. When the projectile is lighter, the reaction is said to occur in normal kinematics, such as in the reaction $^{58}$Ni($^{24}$Mg, 2n)$^{80}$Zr. The opposite case, a reaction in inverse kinematics, has a heavy beam that impinges on a light target, like in the case of $^{40}$Ca($^{58}$Ni, p3n)$^{94}$Ag.

## 1.3  Cases of Interest

This section will discuss the regions of the nuclear chart that have been of particular interest for the MARA-LEB facility since its inception as a project, in addition to regions that have recently arisen as experimental opportunities.

### 1.3.1 $N \sim Z$ **Nuclei Close to the Proton Drip Line**

Interest in very proton-rich nuclei near the $N = Z$ line has risen in recent times thanks to advances in detection techniques that have given access to these very short-lived nuclei [6]. Focus has increased in particular on the region between Zr and Sn ($Z = 40$ and $50$, respectively), due to their suitability for studies of nuclear phenomena [7, 8], including the proton-neutron interaction and associated pairing effects.
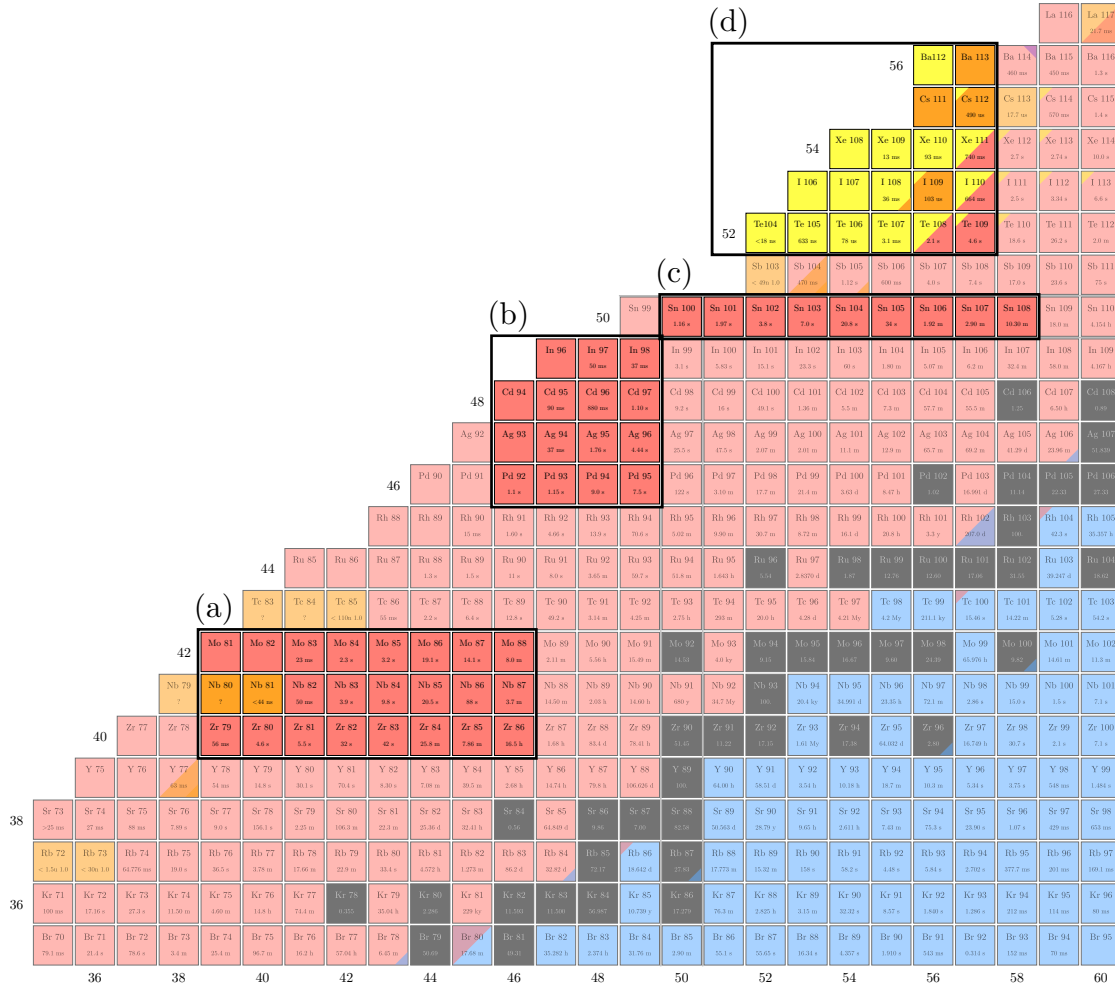


FIGURE 1.1    Regions of interest for MARA-LEB close to the proton drip line: (a) $A \approx 80$, $N \sim Z$ region, (b) long-living isomer region between $^{92}$Pd and $^{100}$Sn, (c) proton-rich Sn isotopes, (d) superallowed α-decay region.

The region of nuclei with $A \approx 80$ is of special relevance due to its rich variety of nuclear shapes [9]. This region of nuclei, highlighted as (a) in Figure 1.1, presents shell effects which make them extremely sensitive to the addition or removal of a single nucleon. In particular, $^{80}$Zr is predicted to be an extreme nucleus in terms of shape coexistence: theoretical calculations indicate a coexistence of five different nuclear shapes [10], which if experimentally verified would constitute a unique case across the nuclear chart. Investigation of deformation and changes

in mean-square charge radii in the nuclei in this region is possible with techniques such as resonant laser ionisation spectroscopy.

Laser ionisation spectroscopy is a technique which exploits the coupling of the electronic and nuclear spin angular momenta to extract nuclear observables by exploring the hyperfine structure in atomic electron orbitals. Electrons are excited via laser light in several steps, typically from the atomic ground state, until the atom is ionised and can be detected. The analysis of the hyperfine structure, which is obtained by scanning the laser frequency of one of the transitions, can give model-independent information on nuclear properties such as the nuclear spin, the magnetic dipole moment and the electric quadrupole moment. The addition or removal of neutrons, in other words, moving along an isotope chain, gives rise to a shift in the transition frequency, the isotope shift. By accounting for atomic factors, the isotope shift provides information on changes in the mean-square charge radius. Properties such as the shape of the nucleus and information on shell closures are among the nuclear structural effects that can be inferred from these observables [11].

Ionisation schemes for elements in the facility's regions of interest are available, in particular for the use of titanium-sapphire lasers. For example, a three-step ionisation scheme of zirconium has been demonstrated [12]. Resonant ionisation schemes that are yet to be confirmed can also be investigated at MARA-LEB and elsewhere. Every scheme will be tested offline prior to online application in order to clarify selectivity, efficiency and sensitivity to the nuclear observables using stable isotopes when possible.

From the theoretical point of view, the region surrounding $^{80}$Zr is also interesting as a test ground for the proton-neutron (p-n) interaction. Even-even N=Z nuclei present an anomalously large double binding energy, which is directly correlated to the p-n interaction strength [13]. Precise mass measurements of isotopes in the region close to $N = Z = 40$ to determine differences in nuclear binding energies would provide a test to the current calculations and provide data to inform new theories exploring the p-n interaction.

Furthermore, $^{80}$Zr is a key isotope in the understanding of the rapid-proton (rp) astrophysical process [14], as it is considered to be a waiting-point nucleus, because its proton capture leads to the proton-unbound isotope $^{81}$Nb [15]. Mass measurements in this region can shed light on the existence of the predicted ZrNb cycle [16], a potential pathway in the rp-process.

Nuclei between $^{92}$Pd ($Z = 46$) and $^{100}$Sn exhibit long-lived isomeric states and a plethora of decay modes. This region is marked (b) in Figure 1.1. A notable instance of the interest in this area is $^{94}$Ag, an $N = Z$ nucleus which possesses a 400 ms-long isomer with an assigned spin of ($21^+$), the highest of any β-decaying isotope. Resonant laser ionisation studies have been performed for silver isotopes

with $A = 96 - 104$ in parallel with precision mass measurements using traps [17]. Additionally, two-proton emission has been reported for this isomer [18], linked to a strongly prolate shape. Other experimental endeavours [19, 20, 21] have failed to reproduce these findings. Unambiguous determination of the energy of the isomer through direct mass measurements and model-independent determination of its shape via resonant laser ionisation studies will be crucial to resolve this puzzling case. Shell-model predictions can be validated especially well with nuclear data from and around the most proton-rich Sn isotopes [22]. High-sensitivity laser spectroscopy of said Sn isotopes, shown in region (c) in Figure 1.1, can be of paramount importance to determine the evolution of nuclear shell gaps away from stability. To date, however, ground-state properties have only been published down to $^{108}$Sn [23]. Laser spectroscopic studies of $^{104-107}$Sn have recently been measured at CRIS (CERN), but a publication is still pending.

Elements in this region of the nuclear chart are characterised by a high chemical reactivity and high melting and boling points. Because of this, their production at facilities using the isotope separation on-line (ISOL) technique is extremely difficult. The ISOL technique relies on the evaporation of reaction products, which becomes challenging with elements in this region. Reaction products forming molecules with impurities in the gas used to extract the produced nuclei is an important source of losses in the ISOL technique. To study these so-called refractory elements, chemical insensitivity during their prodction is paramount [24]. The use of modified ISOL techniques, such as the IGISOL technique, or in-flight production of refractory elements is thus required.

The region around doubly-magic $^{100}$Sn is of special relevance, as it is the heaviest self-conjugate ($N = Z$) nucleus. Its fully occupied shells highly enhance the β-decay channel, leading to the highest Gamow-Teller strength among all β-decaying nuclei [25, 26], known as a "superallowed Gamow-Teller decay". Investigation of this phenomenon has been performed through mass measurements in [27] through two approaches: the Gamow-Teller strength and the shifted two-neutron shell gap. Study of this region through combined laser-ionisation selection techniques and decay spectroscopy can also be used as a test for large-scale shell-model (LSSM) calculations and to provide insight on the hyperfine structure of these nuclei, as well as to track changes in mean square radii along tin isotopes. Furthermore, mass measurements in this region have challenged *ab initio* theory of isotopes in this region [28]. This makes mass measurements of isotopes in this region compelling to test the predictions of these theoretical calculations.

Nuclei just above $^{100}$Sn, labelled (d) in Figure 1.1, are predicted to exhibit strong octupole correlations, which become maximal for $^{112}$Ba ($N = Z = 56$) [29]. These correlations have been experimentally confirmed for less proton-rich species in this nuclear neighbourhood [30], but more exotic nuclei are yet to be explored.

Decay spectroscopy can provide a wealth of nuclear structure information and provides additional capabilities to the MARA-LEB facility (see Section 2.2.3 for details on decay spectroscopy instrumentation at MARA-LEB), such as the investigation of the so called "superallowed" $\alpha$ decay. This decay mode is present in this region, as enhanced proton-neutron interactions might result in large $\alpha$-particle pre-formation factors for self-conjugate nuclei. $^{104}$Te ($N = Z = 52$), the lightest $\alpha$-decaying isotope, is of particular interest, as it is only one of two known nuclei to $\alpha$ decay to a doubly-magic daughter [31]. Further decay spectroscopical studies are required to determine nuclear properties in this relatively unexplored region.

$N \sim Z$ proton-rich isotopes in general are extremely relevant in models of various astrophysical processes, such as the rp- and the neutrino-induced nucleosynthesis ($\nu$p) processes [32], which traverse the region. For an accurate modelling of these astrophysical processes, high-precision measurements of different observables is necessary. One such observable is the nuclear mass, which in turn gives information on $\beta$-decay $Q$ values. In addition to these, information on half-lives and excited levels is required for key nuclei in the regions around $^{80}$Zr, $^{94}$Ag and $^{100}$Sn [33].

### 1.3.2    Proton-rich Lanthanides

The lanthanides, or rare-earth elements, are the chemical elements spanning from lanthanum ($Z = 57$) to lutetium ($Z = 71$), as shown in Figure 1.2. Due to their properties, lanthanides are generally produced with very high levels of contamination. Because of this, in-flight production via fusion-evaporation or fragmentation, for example, proves challenging. Element- and mass-selection procedures are required for contaminant suppression. This is especially important for exotic species with production cross sections that are significantly smaller than other isotopes in their vicinity. Because of their selectivity, ISOL facilities are well suited for the production of lanthanides. Other facilities require the use of additional instrumentation, such as traps, for the purification of the reaction products.

Isotopes of the rare-earth elements lying close to the proton drip line are known for extreme ground-state deformation of different kinds [34, 35, 36]. The most proton-rich of these isotopes decay by proton emission [37, 38]. A relatively well-studied case is $^{151}$Lu, in which both ground- [39] and isomeric-state [35] deformations, and proton decays have been explored.

$^{149}$Lu is a strongly oblate-deformed proton emitter that has been recently discovered in Jyväskylä [40]. Its ground-state proton-decay energy is the highest ever measured, revealing some shortcomings in the proton binding predictions in the region. Further decay studies of this very exotic region are needed to supply data for such theoretical calculations. While production and identification of these

nuclei is possible in the current separators in Jyväskylä, the overwhelming production of contaminants hinders the study of their properties. Contaminant suppression from MARA-LEB is crucial to investigate these nuclei with the required precision.



FIGURE 1.2    The periodic table with lanthanide (top box) and actinide (bottom box) elements highlighted.

### 1.3.3    Actinides

The actinide elements ($89 \leq Z \leq 103$), highlighted in Figure 1.2, include the heaviest naturally occurring (primordial) isotopes, such as $^{232}$Th and $^{238}$U. In recent times, interest to study these nuclei has risen. From the point of view of atomic physics, interest stems from their heavy nature resulting in strong relativistic effects on the electronic structure, which is also affected by electron correlations and quantum electrodynamics [41].

From the nuclear point of view, the actinides' structure is unique due to the competition between Coulomb repulsion and stabilisation by shell effects [42]. The actinides span from the well-established, spherical shell closure at $N = 126$ up to the weak, deformed shell closure at $N = 152$. Most actinides are predicted to possess features such as high-K isomerism [43] or octupole deformation [44]. Systematic studies along actinide isotopic chains can therefore reveal trends on these features between shell closures.

New techniques in laser-based physics have increased the attention that these elements receive from both atomic and nuclear physicists [45], as laser spectroscopy can provide sensitive and model-independent measurements of atomic and nuclear observables.

A recent Jyväskylä experiment has observed the production of light actinides through non-fusion reactions and measured experimental yields at MARA that are compatible with laser spectroscopy [46]. This has sparked the interest to explore these nuclei the MARA-LEB facility, combining the challenging production of actinides with the capabilities of laser spectroscopic studies.

## 1.4   The International Nuclear Facility Landscape

Throughout the world, there are a number of specialised facilities that are able to produce accelerated beams capable of nuclear reactions to access the most exotic of nuclei. Radioactive beam research facilities can be, in general, classified into two groups, depending on the method employed to produce nuclei.

In-flight facilities make use of high-energy ion beams impinging on thin targets, generating reaction products at high charge states that are subsequently separated in mass and charge by the use of electromagnetic fields. This method benefits from very fast delivery times, as the reaction, separation and transport to experimental stations occur at relativistic speeds. Combined with this, the typically high transmission and good particle identification allow in-flight facilities to produce very exotic isotopes.

ISOL facilities, in contrast, make use of thick, hot targets onto which an intense primary beam is impinged. Thick targets allow for a higher beam intensity than in-flight facilites and an increased interaction probability with the primary beam through spallation, fragmentation and fission reactions. The reaction products are volatilised by the high temperature at which the target is kept, leading to a high sensitivity to the chemical properties of the extracted beam. Products are thermalised in the target and then re-ionised and re-accelerated. This results in high-quality secondary beams at the expense of a slower extraction that limits the half-lives of isotopes achievable through this method.

Some facilities utilise techniques that are characteristic of both aforementioned methods. These can be considered hybrid facilities.

In this section, a brief overview of the international landscape of nuclear physics laboratories will be presented, with a focus on seven locations, shown in Figure 1.3, that have the capabilities to produce and explore nuclei in the regions of interest for MARA-LEB. These facilities will be explored regarding their available or planned instrumentation allowing them to undergo the three techniques MARA-LEB is capable of: laser spectroscopy, mass measurements and decay spectroscopy.
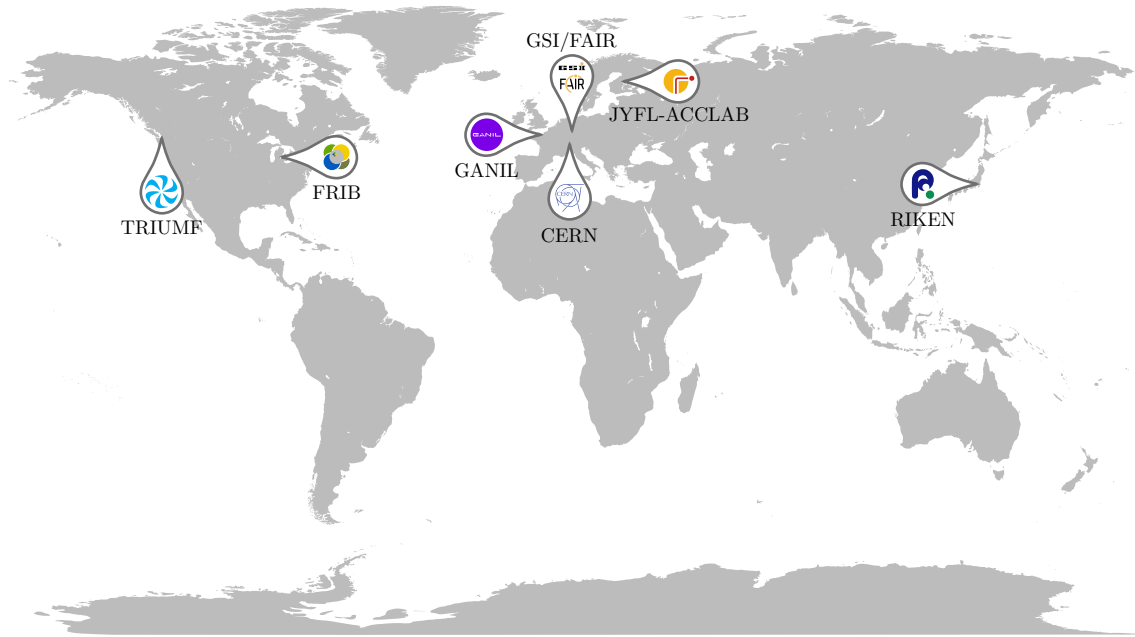
FIGURE 1.3   Map of the world highlighting seven laboratories that are relevant to the work presented in this thesis. Their research is described in the text.

## JYFL-ACCLAB

MARA-LEB is located in the Accelerator Laboratory of the University of Jyväskylä (JYFL-ACCLAB), Finland. This laboratory is home to a K-130 cyclotron, capable of producing heavy-ion beams and proton beams of up to 130 $Q^2/A$ MeV [47]. These primary beams are transported to three separators: MARA, RITU and IGISOL for nuclear physics research, and the facility for Radiation Effects (RADEF) for applied research. Of the nuclear research facilities, MARA and RITU are in-flight separators, while IGISOL can be considered a hybrid facility due to its use of a modified ISOL technique.

The MARA separator [2] will provide reaction products to the MARA-LEB facility. This separator will be discussed in more detail later in this thesis due to its importance to MARA-LEB.

The Recoil Ion Transport Unit (RITU) [48] is a gas-filled separator in a QDQQ configuration, where Q and D stand for magnetic quadrupole and magnetic dipole, respectively. Reaction products, henceforth referred to as "recoils", exchange charge with the helium present in and downstream from the RITU target chamber through collisions. Through charge exchange, an average charge state is produced, resulting in a small image size at the focal plane. This also translates into trajectories of recoils that are, to first order, independent of their kinetic energy. The vertically-focusing magnetic quadrupole before the magnetic dipole increases the mass resolving power and increases the angular acceptance into the separator by about 30% [49]. Gas-filled separators compensate their relatively

small mass resolving power ($\sim$100 in the case of RITU) with a high recoil collection efficiency [50].

This separator was designed for the detection of heavy ($Z \geq 82$), proton-rich recoils. Most of the regions of interest of MARA-LEB are too light for RITU to effectively separate and transport, with the exception of the actinide region, thus MARA was chosen for the low-energy branch expansion.

RITU and MARA have been exploited by the Nuclear Spectroscopy group in Jyväskylä since 1993 and 2009, respectively. To this day, they continue to be at the forefront of nuclear research, being used for experiments performed as part of many international collaborations and pushing the limits of the understanding of nuclear physics.

Both separators have made use of extensive instrumentation for experimental campaigns focusing on the structure of nuclei mainly through $\gamma$-ray, internal conversion electron spectroscopy and decay spectroscopy studies [51]. Some of the nuclear detection instruments used alongside these separators include, but are not limited to: JUROGAM-3 [52], SAGE [53], GREAT [54] and Tuike [55].

In contrast to the other separators at JYFL-ACCLAB, the Ion-Guide Isotope Separation On-Line (IGISOL) facility [56] has used lasers to selectively ionise reaction products to improve beam quality, as a method of optical pumping and to perform spectroscopy to explore properties of nuclei through the probing of the electron-nucleus interactions.

The use of lasers, however, is a more recent addition to IGISOL. The ion guide method has been the main extraction method at the facility since its inception. The use of this technique has allowed for the extraction of ions including refractory elements. IGISOL, in contrast to MARA and RITU, can also access neutron-rich isotopes through fission and MNT reactions.

In addition to its collinear laser spectroscopy line, the IGISOL facility has multiple other experimental stations, such as its own decay station, a double Penning-trap setup (JYFLTRAP) [57] for isobaric purification and mass spectroscopy or RAPTOR [58], a device for purification and high-precision laser spectroscopy.

Combined expertise from all three separators in JYFL-ACCLAB have inspired the development of MARA-LEB, a hybrid facility that will add ISOL-type techniques to the pre-existing MARA in-flight separator.

**GANIL**

The 2nd Generation Linear Radioactive Ion Production System (SPIRAL2) [59] is a linear accelerator at the Great National Heavy Ion Accelerator (GANIL) in Caen, France. This accelerator will deliver beams of radioactive ions, produced using the ISOL method, to the future Super Separator Spectrometer ($S^3$) [60], which is under construction in the laboratory.

$S^3$ is designed to separate products of very high intensity ($>10^{14}$ particles/s). This allows for studies of extremely exotic nuclei, whose production through nuclear reactions is highly unfavourable. The low production cross sections (of the order of a picobarn) of these isotopes is compensated by the high beam intensities, so a detectable number of nuclei is produced. This is coupled with the high mass resolving power of around 300, to be able to efficiently separate and select the recoils of interest from contaminants. This separator can operate in two distinct modes: converging mode and high-resolution mode. In high-resolution mode the separator is able to separate mass-over-charge clusters at its focal plane to select only for the recoil of interest and reduce transmission of contaminants. In converging mode, by contrast, all recoils are focused onto the same point in the focal plane, allowing therefore for high transmission values for both the recoil of interest and its contaminants.

Its Low-Energy Branch ($S^3$-LEB), is under initial testing, with offline results already published for in-gas-jet laser spectroscopy of erbium [61, 62]. $S^3$-LEB will benefit from the converging mode of its separator, as isotopes with low cross sections can be collected in all produced charge states and contaminants can be suppressed by the LEB.

This facility shares many design features with MARA-LEB: their gas cell designs, for instance, are based on the same prototype developed at KU Leuven [63]. $S^3$-LEB will have a mass-measurement system, PILGRIM [64], and a dedicated decay station, SEASON [65], like its Finnish counterpart, and their Titanium:Sapphire (TiSa) laser systems will be very similar. The similarity between the $S^3$-LEB facility and MARA-LEB facility results in overlapping regions of interest. The $N = Z$ line close to $^{80}$Zr and $^{100}$Sn is a common region to both facilities, with a special interest in laser spectroscopy.

The recent inclusion of the lanthanides and actinides into MARA-LEB's interests brings both facilities closer, as these elements have been of interest to $S^3$-LEB since its inception. The synthesis of super-heavy elements (Z>104) at $S^3$ has also been subject of interest for decay spectroscopy and mass measurements [66] at the low-energy branch.

**RIKEN**

The Japanese Institute of Physical and Chemical Research (RIKEN) operates the Radioactive Ion Beam Factory (RIBF), located in the Nishina Center for Accelerator Based Science in Saitama, Japan. This laboratory houses the Superconducting Ring Cyclotron (SRC) which produces exotic nuclei at the highest rate in the world through in-flight fission and fragmentation reactions. Recoils are selected by the Superconducting Radioactive Isotope Beam Separator (BigRIPS) [67].

SRC and BigRIPS have the capability to produce and separate almost every nucleus in the table of isotopes, but have focused their experimental campaigns on neutron-rich isotopes (see for example [68]).

Some decay studies of proton-rich isotopes which lie in the regions of interest to MARA-LEB have been explored with BigRIPS [69, 70], but the lack of laser spectroscopy and mass measurement campaigns in these regions have left experimental prospects open to be explored at MARA-LEB.

**TRIUMF**

The TRIUMF laboratory in Vancouver, Canada, houses a 520 MeV cyclotron which produces proton beams. These beams are directed to the Isotope Separator and Accelerator (ISAC) facility [71], which uses the ISOL technique to produce exotic nuclei and then accelerates them to experimental stations using instrumentation such as GRIFFIN [72] and TIGRESS [73] for $\gamma$-ray spectroscopy, or TITAN [74] for mass measurements.

ISAC also has a collinear laser spectroscopy setup, $C_{FBS}$ [75], which has been in use for optical spectroscopy of very light nuclei (e.g. $_3$Li [76]). The TRIUMF Resonant Ionization Laser Ion Source (TRILIS) [77] has allowed for the in-source resonant laser spectroscopy of heavier (e.g. $_{85}$At [78]) elements.

While the laboratory can produce more massive recoils, scientific efforts at TRIUMF have been focused on lighter, more neutron-rich isotopes than those in the scientific focus of MARA-LEB, with the notable exception of mass measurements of proton-rich isotopes of masses including and above the lanthanides using TITAN [79].

The Advanced Rare Isotope Laboratory (ARIEL) [80] is a planned facility that will run alongside ISAC to deliver multiple rare isotope beams to the existing experimental stations. The ARIEL proton beamline is planned to deliver beams of up to 100 µA to produce rare isotope beams. The addition of ARIEL beams will dramatically increase production rates, thus allowing for the study of more exotic isotopes. ARIEL plans to explore the neutron-rich side of the table of nuclides via

the use of actinide targets, which will be photo-fissioned at a rate of $10^{14}$ fissions per second. This production technique avoids the production of contaminants through spallation, which has limited the access to very neutron-rich isotopes.

## GSI/FAIR

The GSI Helmholtz Centre for Heavy Ion Research, in Darmstadt, Germany, is a heavy-ion accelerator laboratory which employs the Universal Linear Accelerator (UNILAC) to accelerate highly-charged ions to 11.4 MeV/u. Ions from UNILAC are used in in-flight fusion reactions, like the ones used to synthesise elements 108 to 112 for the first time [81, 82, 83, 84, 85], with separation and identification of these super-heavy elements (SHE) performed by the Separator for Heavy Ion reaction Products (SHIP) velocity filter [86].

After separation with SHIP, filtered ions can be stopped in a buffer gas cell and resonant laser ionisation and spectroscopy can be performed [87]. More exotic nuclei have also been reached in experiments following recent efforts to improve the efficiency of the RADRIS setup [88].

Mass spectrometry research is conducted after separation in SHIP aided by ion traps such as SHIPTRAP [89]. These devices have also been used for laser spectroscopy experiments of highly-charged ions with high power lasers [90].

The TransActinide Separator and Chemistry Apparatus (TASCA) gas-filled separator [91] was built at GSI to study the physical and chemical properties of SHE. This separator was used in the confirmation of elements 113 to 117, and the search for elements 119 and 120. TASCA specialises in the most neutron-rich nuclides with $Z \geq 104$, making use of highly efficient spectrometers for these low-production cases, such as the TASCA in Small Image mode Spectroscopy (TASISpec) spectrometer [92].

Decay spectroscopy has been and continues to be the main technique used at GSI with both the SHIP and TASCA separators (see, for example, [93, 94]) for nuclear reasearch. While at GSI decay spectroscopy is focused on heavier nuclei than those in the regions of interest of MARA-LEB, collaborations [95] exist which develop an exchange of knowledge in this technique.

Ions accelerated by UNILAC can also be injected into the Heavy-Ion Synchrotron (SIS18) [96], which can further accelerate ions to 2 GeV/u. The in-flight Fragment Separator (FRS) [97] selects heavy ions magnetically and transports them into the Experimental Storage Ring (ESR) [98], where mass spectrometry can be performed.

Due to its unique capability of producing highly-charged ions up to $U^{92+}$, the main reactions used at FRS have been fission and fragmentation reactions. These

reactions can produce many exotic isotopes accross the nuclear chart, including proton-rich isotopes such as [100]Sn [99]. However, fragmentation reactions generally produce neutron-rich isotopes of medium mass [100, 101], such as [78]Ni, for instance [102].

The Facility for Antiproton and Ion Research (FAIR) [101] is under construction as a major accelerator laboratory adjacent to the current location of GSI. When finished, the experimental scope of the nuclear research group in GSI will be vastly expanded. Higher energies will be available thanks to the SIS100 accelerator, which will be capable of accelerating ions to 99% of the speed of light. It is planned to be able to provide beams of $U^{28+}$ at rates of $1 \times 10^{12}$ ions per second and energies up to $1.5\,\text{GeV/u}$ [103].

The Nuclear Structure, Astrophysics and Reactions (NUSTAR) Collaboration will be one of the pillars of FAIR. Within this collaboration, the Superconducting Fragment Separator (Super-FRS) [104] is being developed, feeding separated recoils into three different experimental branches: the ring branch, the high-energy branch and the low-energy branch.

As part of the Super-FRS low-energy branch, two groups will simultaneously carry out experimental endeavours: the Precision Measurements on very short-lived nuclei using an Advanced Trapping System (MATS) and Laser Spectroscopy of short-lived nuclei at FAIR's low energy branch (LaSpec) [105]. The groups will engage in mass measurements and laser spectroscopy, respectively. The techniques these groups will use, however, have little overlap with those at the MARA-LEB facility.

New experimental setups will also be commissioned at FAIR. The Spectroscopy Trap (SpecTrap) for laser experiments, for example, will be a novel laser-driven project at the new facility [106].

**FRIB**

The Facility for Rare Isotope Beams (FRIB), of Michigan State University, in East Lansing, USA, produces and accelerates rare isotopes using the FRIB linear accelerator (linac), delivering both stable and long-lived radioactive primary beams. Beams available at the FRIB linac range from oxygen ($Z = 8$) to uranium ($Z = 92$), with energies ranging from $177\,\text{MeV/u}$ for the heaviest beams to $290\,\text{MeV/u}$ for the lightest ones. An upgrade is planned to achieve energies of $400\,\text{MeV/u}$ for uranium and higher for lighter beams [107]. Beam intensities of $\sim 1\,\text{pnA}$ are typical for the heavier beam isotopes, while $175\,\text{pnA}$ are achieved for oxygen ions. They are subsequently impinged onto a production target and recoils are filtered by the in-flight A1900 fragment separator [108].

The Low-Energy Branch and Ion-Trap (LEBIT) facility aims to convert the high energy of exotic beams produced with the FRIB linac into low-emittance, low-energy beams [109]. LEBIT stops ions from the A1900 using a helium-filled gas cell. Recoils are then transported by radio-frequency quadrupole (RFQ) guides and then accumulated, cooled and bunched in a linear Paul trap. After the cooler-buncher, several beamlines are available for different experimental purposes: decay spectroscopy is possible with a dedicated decay station and mass measurements are performed in a 9.4 T Penning trap and the Single Ion Penning Trap (SIPT) [110].

Collinear laser spectroscopy in FRIB is performed at the Beam Cooler and Laser Spectroscopy (BECOLA) facility [111], which is a third beamline, after the RFQ guides in LEBIT.

Experimental campaigns in LEBIT have mainly consisted of mass measurements and β-decay investigations. While some of the isotope masses measured at the LEBIT trapping systems fall within the MARA-LEB regions of interest ([112] for example), the bulk of their mass measurements have been of lighter (as in [113, 114]) or much more neutron-rich nuclei (as in [115, 116]).

BECOLA laser spectroscopy campaigns have also focused on lighter nuclei than MARA-LEB's regions of interest, with $^{56}$Ni being the heaviest isotope on which the BECOLA group has performed laser spectroscopy [117].

**CERN**

The European Organization for Nuclear Research (CERN), in Geneva, Switzerland, is home to the Isotope Separator On Line Device (ISOLDE) [118], where thick targets are irradiated with a proton beam from the Proton Synchrotron Booster (PSB) [119], producing exotic nuclei via the ISOL technique. These nuclei are separated after production by one of two separators: the General Purpose Separator (GPS) and the High Resolution Separator (HRS). A post-accelerator to increase the energy and intensity of beams at ISOLDE, the High Energy and Intensity - ISOLDE (HIE-ISOLDE), is under development to upgrade the current achievable energies up to 10 MeV/u [120]. The planned upgrade would make ISOLDE the only facility capable of accelerating medium to heavy radioactive isotopes in this energy range.

Experimental stations at ISOLDE include many different spectroscopy setups, such as the ISOLDE Solenoidal Spectrometer (ISS) [121], the ISOLDE Decay Station (IDS) [122], for decay spectroscopy; the Total Absorption Spectrometer *Lucrecia* [123], for total absorption spectroscopy or the MINIBALL germanium detector array [124] for γ-ray spectroscopy. Laser spectroscopy experiments are carried out at the Collinear Laser Spectroscopy (COLLAPS) line [125], at the Collinear Resonance Ionization Spectroscopy (CRIS) line [126] and at the Multi Ion Reflection Apparatus for Collinear Laser Spectroscopy (MIRACLS) line [127]. Mass measurements are also performed with ISOLTRAP [128].

Due to the long time for which ISOLDE has been operating, and the volume of research carried out with the various experimental setups, there have been many isotopes which have been studied at this facility. Of those relevant to MARA-LEB, examples include mass measurements of neutron-deficient nuclei near but just above the $^{80}$Zr region of interest, namely the most proton-rich indium isotopes [129, 28], and laser spectroscopy of tin has been performed, but only of its more neutron-rich isotopes [130], leaving the neutron-deficient region still unexplored.

# 2 A LOW-ENERGY BRANCH FOR THE MARA SEPARATOR

The Low-Energy Branch (LEB) for the MARA separator is a new facility at the Accelerator Laboratory of the University of Jyväskylä designed to study proton-rich isotopes very far from stability. This chapter will discuss the instrumentation considerations that informed the design of the facility and will introduce the components that comprise MARA-LEB.

## 2.1 The Mass Analysing Recoil Apparatus

MARA is an in-flight, zero-degree vacuum-mode recoil separator [2, 131]. MARA was devised to complement RITU, the gas-filled separator which has been used in JYFL-ACCLAB since 1994. RITU was originally designed for experiments producing heavy ($Z \geq 82$) nuclei via asymmetric reactions, mainly through inverse kinematics.

In general, due to the dynamics of these reactions, the angular dispersion of products in inverse kinematic reactions is much lower, leading to a higher transmission efficiency into the separator. Inverse kinematics also leads to, in general, a higher recoil energy after the target. Stopping of recoils produced via inverse-kinematic reactions is therefore, more challenging than with other production methods.

With increased interest for nuclei at the proton drip line, RITU began being used for lighter isotopes, produced with symmetric reactions, where separation in gas is challenging. This is further exacerbated for inverse-kinematic reactions, where the unreacted primary beam becomes a strong contaminant [131].

Additionally, RITU's mass-resolving power is relatively low, which makes the identification of recoils of interest challenging. This in turn makes the use of tagging methods necessary, such as isomer or particle-emission tagging. Lighter isotopes generally don't emit these particles and primarily decay through beta decay. The aggregate of these limitations and the rise in interest for the study of lighter nuclei in Jyväskylä inspired the construction of the MARA separator.

MARA is composed of a magnetic quadrupole triplet, followed by an electrostatic deflector and a magnetic dipole, as shown in Figure 2.1. MARA is not symmetric, which is in contrast to most other vacuum-mode in-flight separators such as RMS at the Japan Atomic Energy Research Institute, Japan [132], FMA at Argonne National Laboratory, USA [133] and EMMA at TRIUMF, Canada [134]. The quadrupole triplet provides a point-to-parallel focus between the target position and the deflector and a point-to-point focus at the focal plane. Additional details are explained later in this thesis. The deflector and magnetic dipole combination provides an energy focus at a point at the focal plane, making it a double-focusing device. The resulting effect is that ions are spatially separated in clusters corresponding to mass-over-charge ($m/q$) ratios, with a first order mass-resolving power of $\sim 260$. A diagram of this ion-optical setup can be seen in Figure 2.2, where ions with all combinations of three different initial angles, three different masses and three different kinetic energies are simulated.

While the MARA separator was designed with medium-heavy, proton-rich nuclei in mind, it does not possess the mass resolving power needed to isolate very exotic nuclei. These isotopes have cross-sections that are orders of magnitude lower than competing reactions in the region. They are produced in fusion-evaporation reactions at MARA, however, unwanted reaction products will be more abundant.
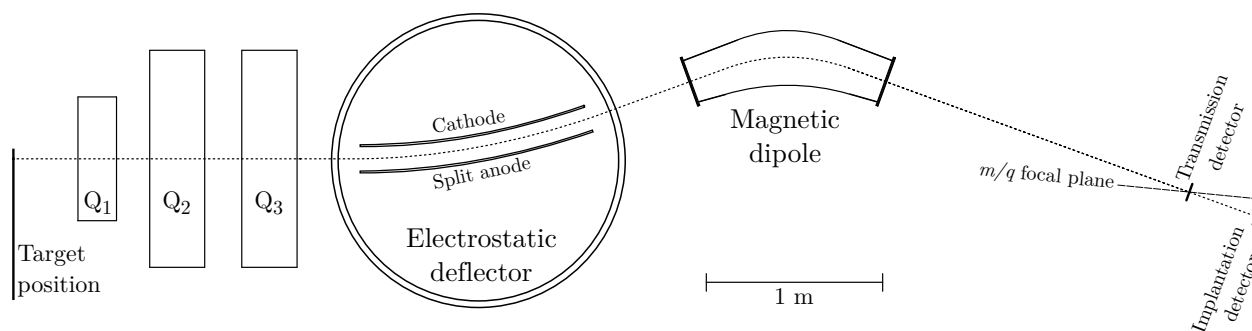


FIGURE 2.1    Diagram of the MARA separator optical elements, with typical detector positions labeled [131]. $Q_i$ represents the $i$-th magnetic quadrupole in the triplet. The dotted line shows the optical axis.

Target
position

Focal
plane

Quadrupole    Electrostatic
triplet           deflector

Magnetic
dipole
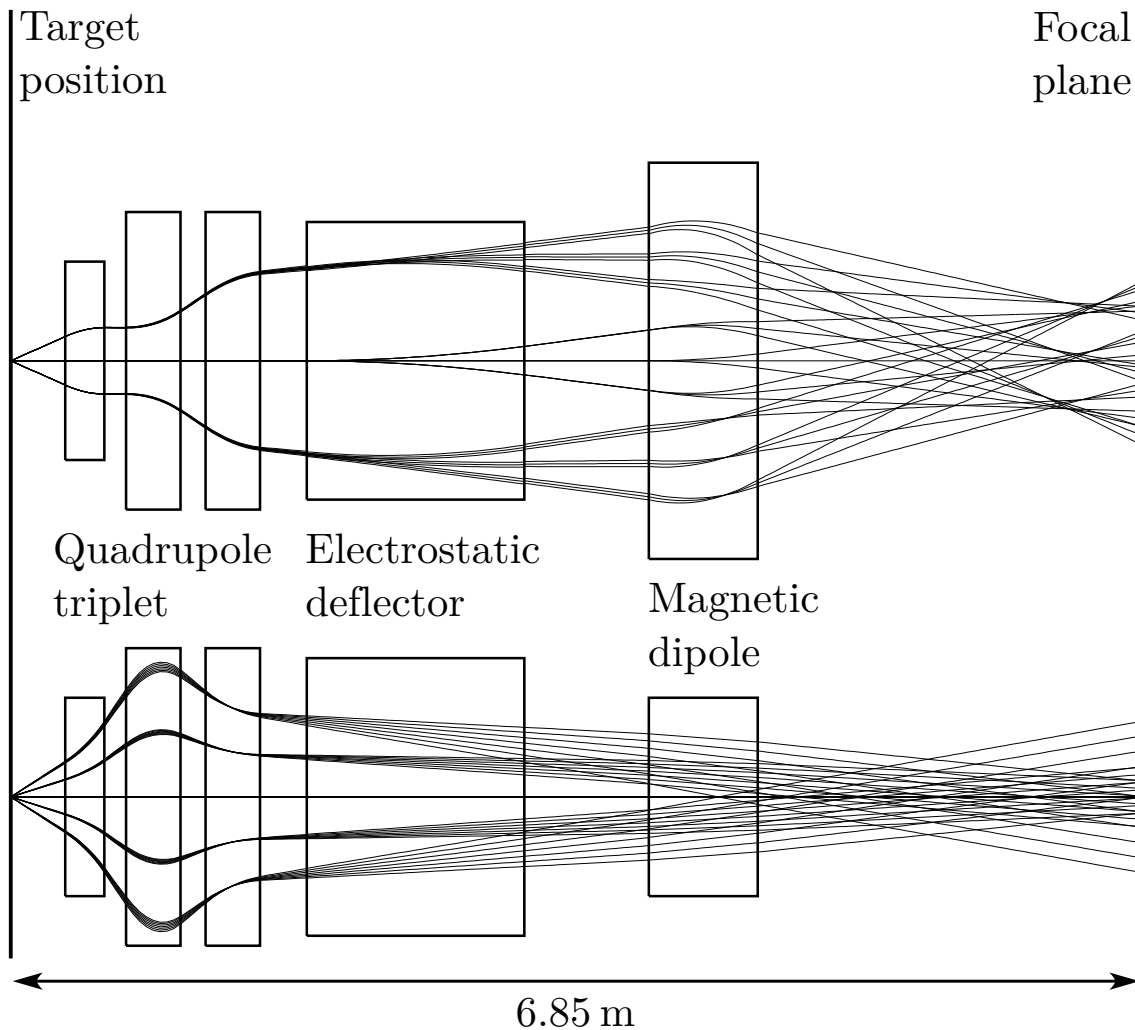
6.85 m

FIGURE 2.2    The ion-optical setup of MARA seen from the top (top) and the side (bot-
tom), relative to the straightened optical axis, which is 6.85 m long. Ion tra-
jectories are shown with different combinations of starting angles, masses
and energies. The dispersion at the focal plane is 8.1 mm/(% in mass-over-
charge ratio) [131].

**Study of Recoil Transport: the $^{24}$Mg($^{58}$Ni,2n)$^{80}$Zr reaction**

As an example of the challenge of beam purification that the MARA-LEB facility
aims to tackle, the $^{24}$Mg($^{58}$Ni,2n)$^{80}$Zr reaction can be explored. $^{80}$Zr, as discussed
in Chapter 1, is a nucleus of particular interest for the MARA-LEB facility. It
is also an example of an exotic nucleus whose production cross section is much
smaller than that of neighbouring nuclei of similar mass. This will translate into
an overwhelming number of contaminating ions at the focal plane of MARA, due
to the impossibility of separating recoils with the same mass number.

TABLE 2.1  Expected focal plane rates for the $^{24}$Mg($^{58}$Ni,2n)$^{80}$Zr reaction, given a 200 pnA primary beam. Yields are estimated with mass slits present in the beamline, which contributes to contaminant suppression.

| Product | Evaporation Channel | Cross Section | Yield at focal plane [ions/s] |
|---------|---------------------|---------------|-------------------------------|
| $^{80}$Zr | 2n | 10 µb | 40 |
| $^{80}$Y | pn | 2 mb | 7 000 |
| $^{80}$Sr | 2p | 44 mb | 150 000 |
| A=79 | 3p,2pn,p2n | 250 mb | 120 000 |
| A=77 | αp, αn and rest | 200 mb | 120 000 |
| Total | | 500 mb | 400 000 |

The production cross section of $^{80}$Zr through this reaction has been measured experimentally to be $\sim$10 µb with a primary beam energy of 190 MeV [135]. In this reaction, the two-nucleon evaporation channels dominate, with a total share of about 10% of the fusion-evaporation cross section. The most intense of these channels is the two-proton emission channel, which produces $^{80}$Sr with a cross section of 44 mb. Evaporation of one proton and one neutron is the second most intense channel, via which $^{80}$Y is produced with a cross section of about 2 mb. These values, along with other intense channels for neighbouring masses, are shown in Table 2.1. In this table, an estimation of yields at the focal plane of MARA for a target thickness of 500 µg/cm$^2$ and a beam intensity of 200 pnA is shown. The use of mass slits is assumed, reducing the neighbouring-mass contaminant yield at the focal plane by $\sim$80%. These are standard experimental conditions in a MARA-LEB experiment, thus producing what will be typically expected yields.

For these experimental conditions, approximately 160 ions of $^{80}$Zr are produced per second at the target position, compared to a total fusion-evaporation yield of this reaction at the target is of the order of $10^7$ ions/s. With the use of ion-optical simulations and taking the use of mass slits into account, it has been estimated that about 25% of the $^{80}$Zr yield can be transported to the focal plane, resulting in 40 ions/s for the nucleus of interest.

At MARA-LEB, a small-volume cell placed at the focal plane of MARA stops and transports recoils for laser ionisation and spectroscopy. A detailed explanation of this is provided later in this work. With an estimated 50% efficiency in the thermalisation, diffusion and transport to the nozzle of the gas cell, a minimal neutralisation efficiency of 50% (which is still unknown and element dependent) and an in-jet laser ionisation efficiency of 10% (from [136]), an estimated 1 ion/s of $^{80}$Zr is available for study at MARA-LEB. This has been shown to be enough for nuclear structure studies, as shown, for instance, in [137].

After this purification process, the beam at MARA-LEB is mostly only composed of nuclei of the element selected by laser ionisation. Subsequently, suppression of isotope contamination is carried out with the use of a dipole magnet and additional mass slits.

## 2.2 The Components of the Low-Energy Branch

The MARA-LEB facility combines various systems to obtain isotopically pure beams from the recoils produced and separated at MARA. The main processes undergone by the facility are: (i) stopping and neutralising recoils from MARA, (ii) selectively re-ionising the recoils of interest, (iii) mass-separating ions and (iv) transporting them to experimental stations. The facility spans two levels in the Accelerator Laboratory. A diagram showcasing the main components is shown in Figure 2.3 and a more realistic depiction of the facility is shown in Figure 2.4.
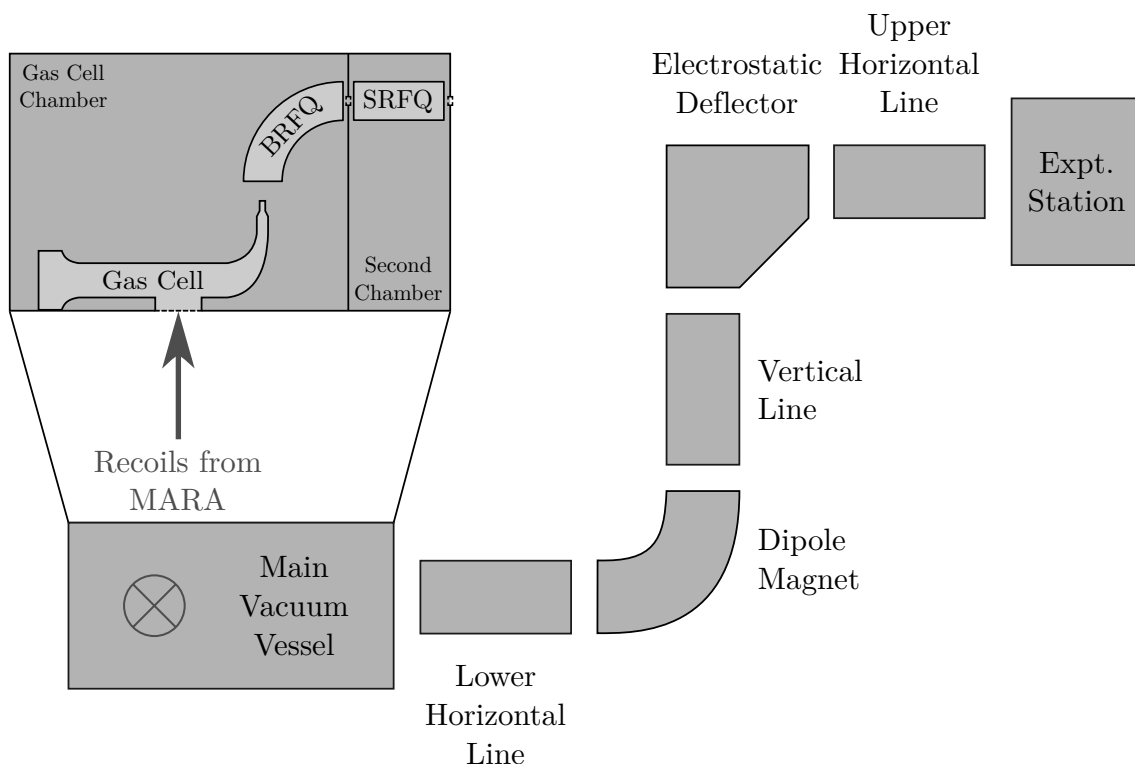


FIGURE 2.3    A basic schematic of the MARA-LEB facility, downstream from the focal plane of MARA, labelled with the main sections of the beamline as seen from MARA. Recoils enter the main vacuum vessel perpendicular to the plane of the page. The inset shows the inside of the main vacuum vessel as seen from above. A description of the parts in the main vacuum vessel is given later in the thesis, in Chapter 4. Parts are not to scale.
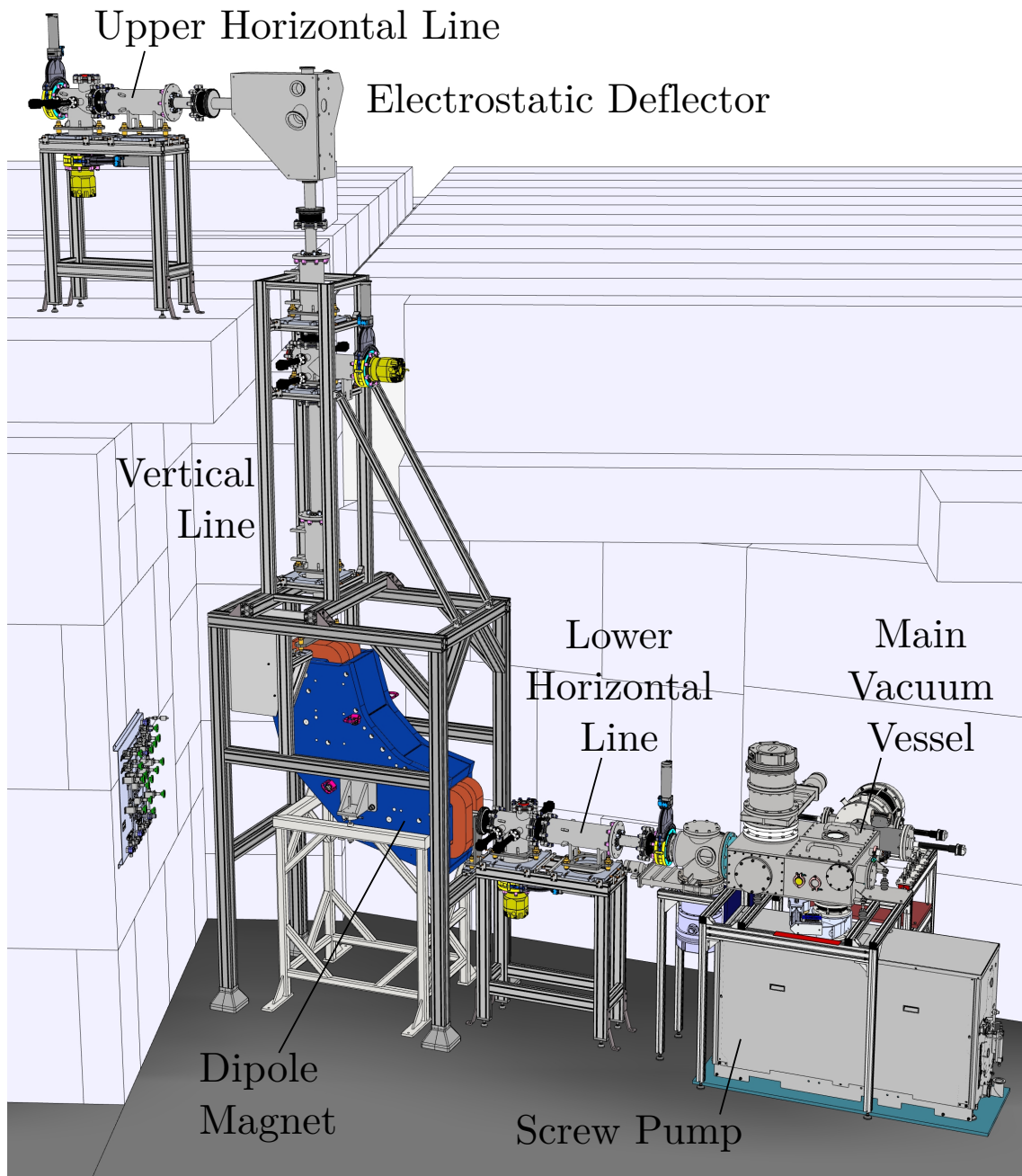
FIGURE 2.4    Realistic depiction of the MARA-LEB facility from the focal plane of MARA to the upper horizontal line, with key parts labelled. The two-floor layout of the facility can be appreciated. The MARA separator is behind the wall and connected to the main vacuum vessel.

Recoils separated at MARA are focused into a thin foil window of the MARA-LEB gas cell, which is housed in the main vacuum vessel. In the gas cell, recoils are stopped and thermalised in a noble buffer gas. For experiments in which recoils need to be neutralised and reionised, argon is used. Helium is used when these effects are not desired, leading to faster extraction out of the gas cell. Recoils are transported out of the gas cell by the flow of gas and can be selectively re-ionised using multistep laser ionisation. This can occur inside the cell (in-gas-cell laser ionisation) or in the collimated gas jet generated by converging-diverging (de Laval) gas cell nozzles (in-gas-jet laser ionisation). The gas cell and laser ionisation of recoils will be explained in detail in Chapter 3.

The buffer gas, alongside the re-ionised recoils of interest and contaminants from MARA, is flushed from the gas cell towards the primary transport system. The primary transport system consists of radio-frequency quadrupole (RFQ) ion guides, which are also housed in the main vacuum vessel. The RFQ guides in this system capture the laser-ionised recoils but not non-charged particles. The buffer gas and any neutral contaminants are pumped away in the main vacuum chamber. This ensures that the species of interest will be transported primarily, with contaminants having been greatly reduced.

Ions are then transported within the ion transfer line, which includes a dipole magnet that will bend ions upwards into the vertical line while also offering mass separation. An electrostatic deflector will redirect the vertically travelling ions into the horizontal line on the second floor and into an experimental station. Quadrupololar electrode multiplets (doublets and triplets) will focus the beam along the ion transfer line. Steering electrodes will be placed at selected points in the vertical and horizontal lines to redirect the beam if necessary.

### 2.2.1   Laser System

Lasers are a fundamental pillar of the MARA-LEB facility. Resonant laser ionisation is performed in experiments for both beam purification and for resonance ionisation spectroscopy (RIS) [138] to study nuclear structure through atomic transitions.

Laser spectroscopy studies require a high spectral resolution to resolve the atomic hyperfine structure and extract nuclear observables from it. The use of in-source laser spectroscopy is well established, having been performed extensively via two main approaches: in a hot cavity (see [139, 140], for example) and in a buffer gas cell (see [141], for instance). The hot cavity technique suffers from loss of resolution due to Doppler broadening because of the high temperatures required to maintain the atoms of interest volatile. The buffer gas cell approach, in addition to the Doppler broadening due to room temperature, has resolution limitations owing to the collision broadening with the buffer gas atoms.

To preclude the effects of these broadening mechanisms, the in-gas-jet technique was developed at KU Leuven for nuclear structure studies [142]. The reduction of pressure and temperature in the supersonic gas jet has proven critical for laser spectroscopy studies of elements such as erbium [62], actinium [136] and tin [143]. All of these elements are in the aforementioned regions of interest for the MARA-LEB facility. Because of this, the use of the in-gas-jet laser ionisation and spectroscopy technique is considered fundamental for the facility. Thus, the formation of gas jets at the exit of the gas cell is considered primordial for laser spectroscopy studies at MARA-LEB. Considerations on jet formation are discussed in Chapter 3.

The lasers used in MARA-LEB are titanium-sapphire (Ti:sa) cavities. Two cavities in a Z configuration have been built based on the design used at the Fast Universal Resonant Laser Ion Source (FURIOS) system [144]. FURIOS provides the laser light used at IGISOL. These Ti:sa lasers are broadband resonators, with fundamental linewidths of approximately 5 GHz. These broadband lasers are adequate for resonant ionisation for purification and for in-gas cell spectroscopy. They benefit from ease of use and higher power when compared to narrowband lasers. To pump these cavities, a diode-pumped neodymium-doped yttrium aluminium garnet (Nd:YAG) laser can be used at a repetition rate of 10 kHz, operating at its second harmonic wavelength of 532 nm. The dual-cavity Mesa 532-60-M [145] can pump two to four cavities simultaneously, thus being able to provide the necessary pumping for both of the broadband cavities at the same time.

A narrowband laser is also required for in-gas-jet RIS. This is provided by a state-of-the art injection-locked Ti:sa laser with a $\sim$20 MHz linewidth [146]. A continuous wave Matisse Ti:sa laser serves as the seed laser for the injection cavity, and a Nd:YAG laser is used as the pump laser. The Ti:sa laser is naturally multimodal, thus generating light with several wavelengths and spatial modes, with a broad output spectrum. However, it is locked to a single emission mode, allowing for a tuning range of $\sim$20 GHz free of mode-hopping. However, at the edges of this range it is possible that the locking is lost and the laser switches to multimode emission momentarily, disturbing the measurement. A schematic of this injection-locked system is shown in Figure 2.5; a more detailed description on this configuration and its electronics can be found in [146]. This design has been proven to be suitable for high-resolution in-gas-jet spectroscopy [136].
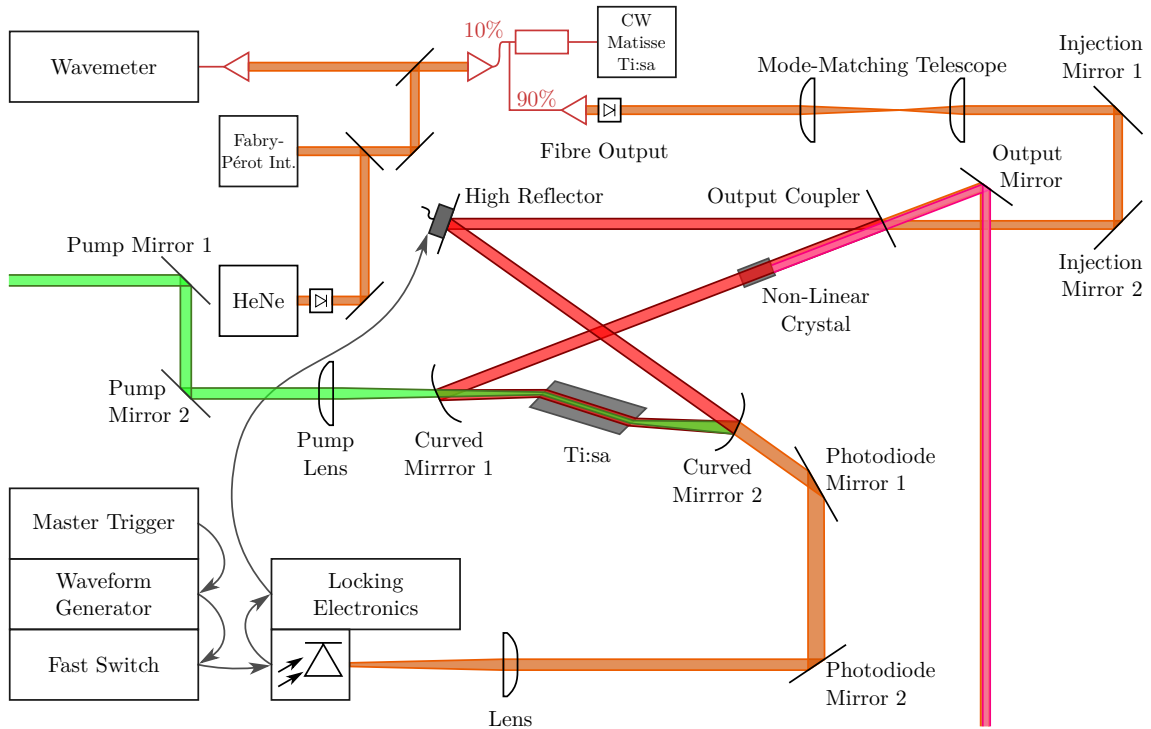
FIGURE 2.5   A schematic view of the injection-locked narrowband Ti:sa laser in bowtie configuration. Green represents the light from the Nd:YAG laser used as a pump. Red represents the laser light from the Ti:sa crystal in bowtie configuration. The output laser light is shown in pink, after frequency doubling via a non-linear crystal. All other laser lights are depicted in orange. Adapted from [146].

### 2.2.2   Mass Measurement System

High-precision measurements of nuclear masses far from stability will be performed using the Multi-Reflection Time-of-Flight Mass-Spectrometer (MR-TOF-MS) [147] at MARA-LEB.

Mass measurements in an MR-TOF-MS rely on measuring the time of flight of ions through a known distance. Ions are reflected multiple times within the device by the use of electrostatic "mirrors". These mirrors consist of strong positive electric fields, which, thanks to electrostatic repulsion, reflect ions back [147]. As the MR-TOF-MS length between mirrors ($l$) is known, the distance travelled by the ions, $d$, in a given number of laps of the spectrometer, $n$, can be calculated as $d = nl$. By measuring the time, $t$, taken for the ions to traverse this distance, it is possible to determine the mass of said ions, $m$, given their kinetic energy, $E_k$. This relies on the kinetic energy of an ion being proportional to its mass and the

square of its velocity, $E_k = \frac{1}{2}mv^2$, as shown in Equation 2.1:

$$t = \frac{d}{v} = nl\sqrt{\frac{m}{2E_k}} = nl\sqrt{\frac{m}{2qV}},$$

$$m = 2qV\left(\frac{t}{nl}\right)^2,$$

(2.1)

where the kinetic energy of the ions in charge state $q$ (in units of the elementary charge) is induced by the electrostatic field with potential $V$ [148]. The mass resolving power, $R$, of a mass spectrometer, is defined as the ratio of the measured mass to the minimum discernable mass difference, $\frac{m}{\Delta m}$. From the above equation, a resolving power can be calculated as in Equation 2.2:

$$R = \frac{m}{\Delta m} = \frac{t}{2\Delta t},$$

(2.2)

where $\Delta t$ is the full width at half maximum (FWHM) of the time of flight spectral peak. Typical mass resolving powers in MR-TOF setups in other facilities are of the order of $R \approx 10^5 - 10^6$, with typical operation times of the order of tens of milliseconds, see for example [149, 150].

A schematic view of the operation of an MR-TOF-MS can be seen in Figure 2.6, where the injection mirror potential is switched off while ions are being introduced into the spectrometer. Both mirrors are on during operation and the extraction mirror is turned off to eject the ions from the MR-TOF-MS.



$l$

Injection mirror      Drift tube      Extraction mirror
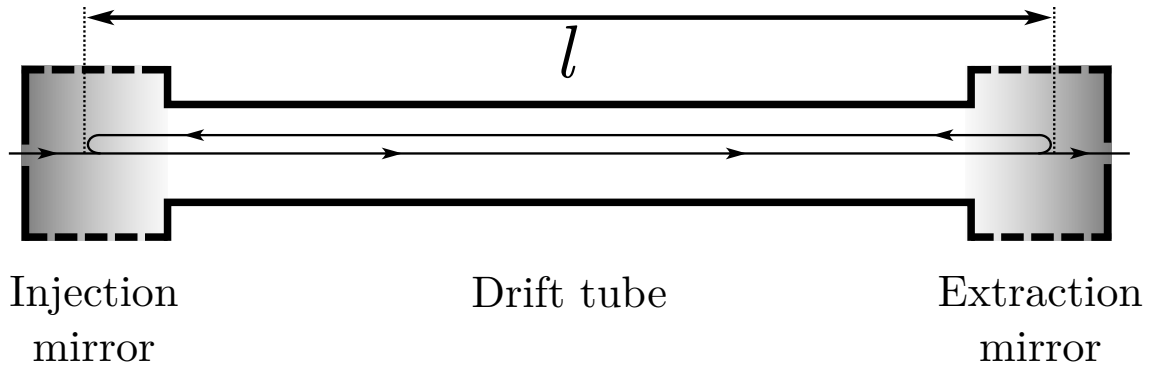
FIGURE 2.6   Operation principle of a Multi-Reflection Time-of-Flight Mass Spectrometer. Ions are kept in the spectrometer by the use of electrostatic mirrors, represented by gradients.

Thanks to its principle of operation, the MR-TOF-MS can be used as a mass measuring device, or as a high-precision mass filter. Its mass separation capabilities allow the MR-TOF-MS to be used to create pure isobaric bunched beams that can be transported to detector stations for decay spectroscopy.

To accurately control the energy of the ions entering the spectrometer to ensure effective trapping in the MR-TOF-MS, a radio-frequency (RF) cooler-buncher is

used. An RF cooler-buncher is a type of ion trap that reduces the energy spread (cools) of a continuous ion beam and releases the ions in discrete bursts (bunches), which are then allowed into the MR-TOF-MS.

The cooling of ions is done in radio-frequency ion guides which are filled with a very low pressure (<1 mbar) noble gas. The working principle of radio-frequency ion guides is explained in more detail in Chapter 4. Ions lose their energy via collisions with the gas particles, but are not diffused thanks to the confining electric fields. This leads to beams with a smaller emittance and energy disperison, thus with a higher luminosity.

An ion buncher utilises electric fields to collect trapped ions and then releases them after a suitable holding time. This is achieved by trapping ions spatially by creating an electric potential well. Ions are then released by removing the potential well and introducing a smooth electric field that carries the ions forward at the same time. For the IGISOL cooler-buncher, energy spreads of <0.6 eV are typical, with bunches of approximately 15 μs in width [151]. A modification of this cooler-buncher, known as the "mini-buncher", was performed, with typical energy spreads in the range of 10-20 eV and temporal bunch widths in the range of 40-150 ns. This very narrow temporal bunch is required for the operation of the MR-TOF-MS.

The MR-TOF-MS design for MARA-LEB will be based upon the recently commissioned IGISOL system [152, 153], while the RF cooler-buncher design will be based on the new RF cooler-buncher currently in development at IGISOL for the MATS-LaSpec collaboration in FAIR. Testing of the IGISOL MR-TOF-MS has yielded mass resolving powers of $R \approx 2.6 \times 10^5$ for $^{87}$Rb in 26 ms [152], comparable to well established systems such as the ISOLTRAP MR-TOF-MS, which achieves a mass resolution of about $2.0 \times 10^5$ for $m = 90$ u in 26 ms [149].

The HIBISCUS cooler-buncher, currently in development for the FAIR laboratory, is based on ISCOOL [154] and the new Radio-Frequency Quadrupole Cooler-Buncher (RFQCB) [155], the cooler-bunchers in use and under design, respectively, at ISOLDE. The active ISCOOL cooler-buncher provides typical energy spreads below 1 eV and temporal bunch widths smaller than 10 μs. The new RFQCB design is aiming to lower these to under 0.3 eV and 3 μs, respectively. It is thus expected that HIBISCUS will provide ion bunches of similar characteristics, with temporal bunches in the order of ~50 ns [156], which will be inherited by the future MARA-LEB cooler-buncher.

A diagram of the facility with the mass measurement system installed is shown in Figure 2.7. The mass measurement system can be used as a mass spectrometer on its own, or followed by further experimental stations.
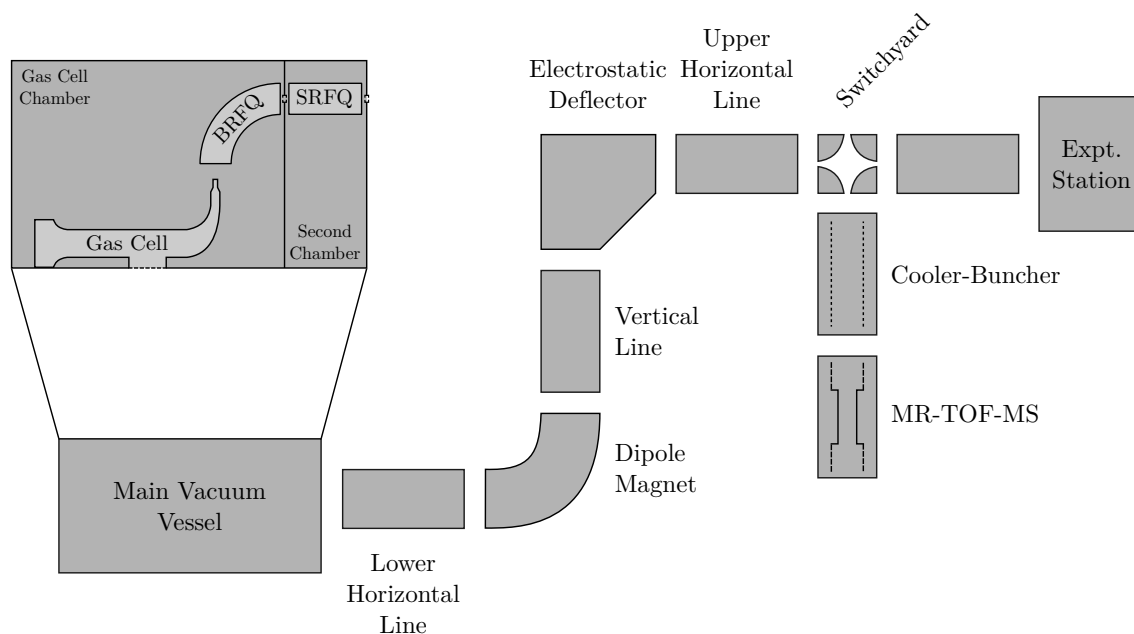
FIGURE 2.7    The entire MARA-LEB facility, labelled with the main sections of the beam-line for mass measurements, including the cooler-buncher and the MR-TOF-MS after an electrostatic switchyard to direct ions towards the desired beamline branch. Parts are not to scale.

### 2.2.3   Decay Station

To carry out nuclear decay studies, one of the three main objectives of the MARA-LEB facility, a bespoke decay station has been proposed and is in the initial phases of design. Three complementary designs for a versatile, compact and highly efficient decay station are under consideration. In all three, the combination of plastic scintillators, and silicon and broad-energy germanium (BEGe) detectors will enable the measurement of $\alpha$ and $\beta$ particles, protons, $\gamma$- and x-rays.

The first of these, intended as a general-purpose station, is depicted in Figure 2.8a. Selected ions from MARA-LEB will be implanted onto a thin carbon foil placed in front of a double-sided silicon strip detector (DSSD). This will allow for the detection of conversion electrons, protons and $\alpha$ particles. A plastic scintillator behind the DSSD allows for the discrimination of $\beta$ particles from other charged particles. One or more silicon box detectors increases the charged-particle detection efficiency by capturing charged-particles which are emitted at angles above 90° with respect to the beam direction.

A second design for the decay station, shown in Figure 2.8b, is a "merry-go-round" design. This arrangement is suited for longer-lived isotopes, which are implanted onto thin carbon foils mounted on a rotating disc. The disc can be rotated according to the half-life of the species of interest. Pairs of detectors on both sides of the disc can detect charged particles in coincidence; this is particularly well suited for $\beta$-p measurements.

In a similar fashion to the "merry-go-round" design, the final design employs a long aluminised mylar tape instead of a rotating disc. The tape station design, illustrated in Figure 2.8c, is most suited for β-γ coincidence measurements.
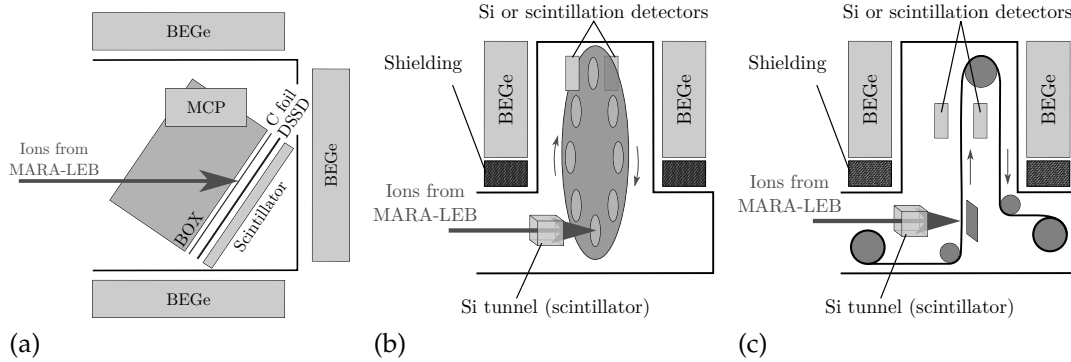


FIGURE 2.8   The three proposed designs of the MARA-LEB versatile decay station. (a) is a general-purpose decay station, (b) is a "merry-go-round" design, and (c) is an implantation tape station. See text for more details.

## 2.2.4   Vacuum System

MARA is a vacuum-mode separator; it is kept at pressures below $10^{-7}$ mbar. Similarly, the ion transfer line of MARA-LEB requires low pressures of the order of $10^{-6} - 10^{-7}$ mbar to operate. An even lower pressure is required for the mass measurement system. The gas cell, however, receives a constant inflow of gas and outputs it into the vacuum chamber housing it through the exit nozzle.

To allow these very different vacuum regimes to exist without physically separating the regions, a two-stage differential pumping section was designed, spanning the main vacuum vessel and the extraction chamber, in the lower horizontal line. This section features a gradual decrease in pressure from the gas cell downstream, with small apertures that limit the gas flow between chambers. The lack of physical separation via windows, for instance, reduces the ion losses.

After the differential pumping section, the facility is divided into three vacuum regions. The first of these regions includes the components between the acceleration electrodes and the magnetic dipole chamber, including the latter but excluding the former. The second region includes the vertical line, the electrostatic deflector and the upper horizontal line. The last region is dedicated to the experimental stations. A vacuum diagram showing all regions can be seen in Figure 2.9, with a detailed list of the pumps used in the facility and their pumping capabilities in Table 2.2. These sections, separated by gate valves, allow for individual pumping down, enabling the possibility to make changes in one of the sections without having to vent the entire facility.

TABLE 2.2   Pumps used in the MARA-LEB facility. Pumping speeds for $N_2$, $v_{N_2}$, are reported. All pumps are manufactured by Edwards Vacuum [157], who report that performance for nitrogen, argon and helium can be taken to be equal within an accuracy of 15%.

| Chamber | Type | Model | $v_{N_2}$ [L/s] |
|---------|------|-------|-----------------|
| Gas Cell Chamber | Screw | GXS750/4200 | 960 |
| Second Chamber | Turbo | STP-iXR2206 | 2200 |
| | Scroll | XDS35i | 10 |
| Extraction Chamber | Turbo | STP-iXR1606 | 1000 |
| | Scroll | XDS35i | 10 |
| Diagnostics Box 1 | Turbo | nEXT400D | 400 |
| | Scroll | nXDS6i | 1.7 |
| | Scroll | nXDS15i | 5 |
| Diagnostics Box 2 | Turbo | nEXT400D | 400 |
| | Scroll | nXDS6i | 1.7 |
| Detector Station | Turbo | nEXT400D | 400 |
| | Scroll | nXDS6i | 1.7 |
| | Scroll | nXDS15i | 5 |
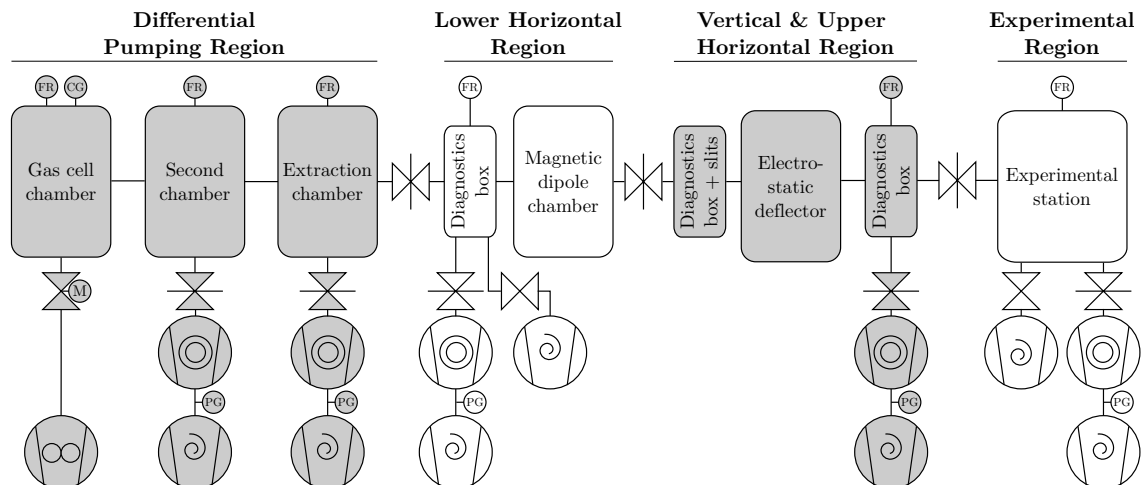


FIGURE 2.9   Vacuum diagram for MARA-LEB. The different vacuum regions are labelled and alternatingly coloured for ease of distinction. See page 16 for the list of vacuum symbols.

### 2.2.4.1 Differential Pumping System

The differential pumping system of MARA-LEB is the first vacuum region of the facility. It is composed of 3 distinct but connected chambers which house the gas cell and the first components of the transport system. These are shown in Figure 2.10.

The main vacuum vessel is divided into two chambers. The first of these is the gas cell chamber, which houses the gas cell and the first RFQ ion guide. The second chamber houses the second RFQ ion guide. The final chamber of the differential pumping section is the extraction chamber, which hosts the first components of the ion transfer line. These three volumes are connected via small apertures, labelled $A_i$ in Figure 2.10, of diameter 5 mm. The small apertures greatly limit the gas exchange between chambers, making it possible to keep the volumes physically connected while gradually reducing the pressure along the system.
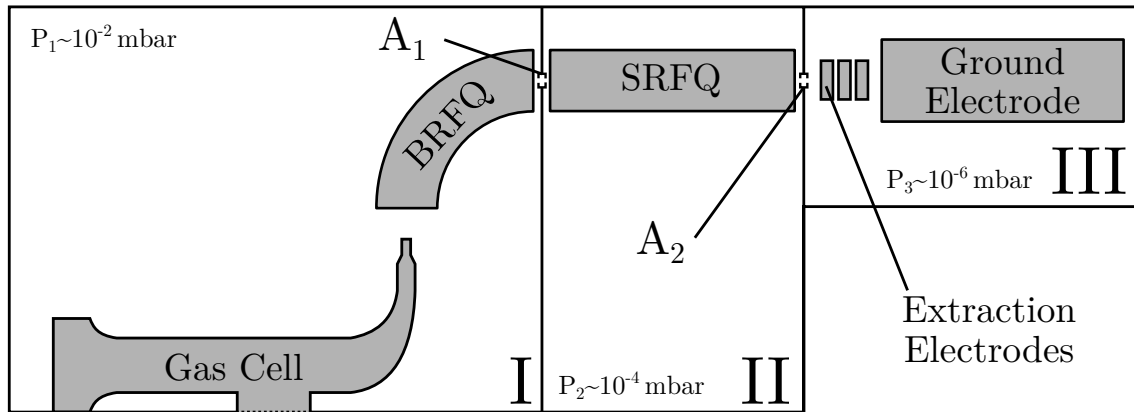


FIGURE 2.10  The differential pumping section of MARA-LEB. The different sections are shown: I) Gas cell chamber, II) Second chamber, and III) Extraction chamber. Typical pressures are shown, as calculated in this chapter (see text). The 5 mm-diameter apertures between these chambers are labelled $A_i$. Electrode operating voltages are discussed separately in a later chapter. The gas cell, RFQ guides and electrodes shown in the figure will be explained in detail later in this thesis.

For a monoatomic gas of molar mass $A$ [g/mol] the throughput or load, $Q$ [mbar L/s], introduced to a vessel through an aperture of diameter $d$ [mm] from a gas at pressure $P_0$ [mbar] and temperature $T$ [K] is [158]:

$$Q = 0.052\, d^2 P_0 \sqrt{\frac{T}{A}}. \tag{2.3}$$

This equation is valid for the MARA-LEB gas cell, as only monoatomic gases, helium and argon, are used as buffer gases. The gas cell operates at room temperature, $T$=293 K.

The load $Q$ [mbar L/s] removed from a chamber at pressure $P_1$ [mbar] at an effective pumping speed $v_c$ [L/s] is:

$$Q = P_1 v_c. \tag{2.4}$$

By combining Equations 2.3 and 2.4, the required pumping speed for a pump to remove all of the gas introduced by the gas cell into the chamber can be found, in terms of the aperture diameter and the pressure of the gas cell and the chamber:

$$v_c = 0.052 \, d^2 \frac{P_0}{P_1} \sqrt{\frac{T}{A}}. \tag{2.5}$$

To achieve a parallel gas jet when using a de Laval nozzle, it is necessary for the ambient pressure in the chamber, $P_1$, to match the pressure of the jet. More details on gas flow and the formation of a collimated gas jet will be given in Chapter 3. $P_1$ is only dependant on the gas cell pressure, $P_0$, the gas jet's Mach number, $M$, and the ratio between specific heat capacities, $\gamma = C_p/C_v$, which is equal to 5/3 for monoatomic gases. The expression for the pressure in the gas jet is shown in Equation 2.6 [142]:

$$P_{\text{jet}} = P_0 \left[ 1 + M^2 \left( \frac{\gamma - 1}{2} \right) \right]^{-\frac{\gamma}{\gamma - 1}} = P_0 \left( 1 + \frac{M^2}{3} \right)^{-5/2}. \tag{2.6}$$

With Equations 2.5 and 2.6, the pumping speed required for the gas cell chamber to produce a gas jet of Mach number $M$ can be calculated in terms of nozzle diameter, gas mass number and Mach number:

$$v_c = 0.89 \, d^2 \left( \frac{3 + M^2}{3A^{1/5}} \right)^{5/2}. \tag{2.7}$$

The pumping speed required for certain Mach numbers is shown for both buffer gases in Figure 2.12 for different nozzle diameters.

For the formation of the gas jet, it is necessary to be able to control the pressure in the gas cell chamber with precision. This is achieved at MARA-LEB with the use of a motorised pendulum valve between the screw pump and the gas cell chamber, which regulates the aperture size. This in turn changes the effective pumping speed at the chamber because the conductance is proportional to the area of the aperture. This is shown in Equation 2.8, where $C$ [L/s] is the conductance of the connection between the pump and chamber, $v_c$ and $v_p$ are the effective pumping speeds in L/s at the chamber and the pump, respectively:

$$v_c = \frac{C \, v_p}{v_p + C}, \tag{2.8}$$

the pressure of the gas cell chamber can hence be controlled to match the pressure of the desired gas jet.
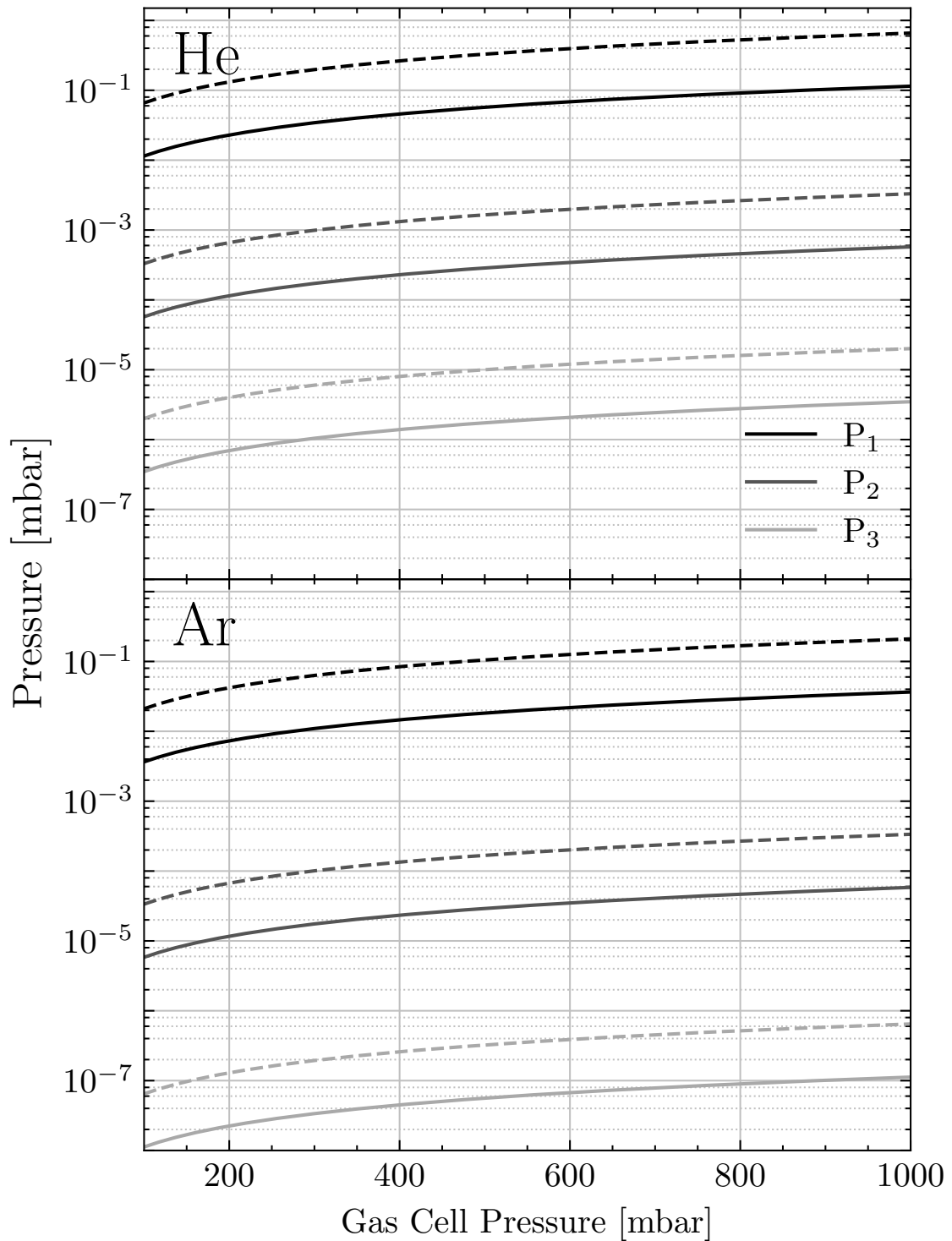
FIGURE 2.11 Pressures in the gas cell chamber ($P_1$, in black), second chamber ($P_2$, in dark grey), and the extraction chamber ($P_3$, in light grey), as a function of the pressure in the gas cell. Calculations for nozzles of 0.5 mm and 1.2 mm in diameter are shown by the solid and dotted lines, respectively. The buffer gases are helium (top) and argon (bottom).

TABLE 2.3   Maximum Mach number for a gas jet generated by a de Laval nozzle with the GXS750/4200 screw pump as the gas cell chamber pump for different nozzle diameters and buffer gases.

| Nozzle | Maximum Mach number | |
|---|---|---|
| diameter [mm] | Helium | Argon |
| 0.5 | 10.7 | 13.5 |
| 1.2 | 7.4 | 9.4 |

The loads introduced by the gas cell operating at pressures 500-1000 mbar range from 20 to 200 mbar L/s for argon and from 55 to 650 mbar L/s for helium. Taking the maximum loads for each gas, the required pumping speed to maintain a pressure of 0.01 mbar in the gas cell chamber is 20 000 L/s for argon and 65 000 L/s for helium. The gas cell chamber screw pump has a pumping speed of 960 L/s (see Table 2.2), making the minimum pressure in the first chamber 0.28 mbar and 0.79 mbar for argon and helium, respecively, if the maximum load from the gas cell is considered. With this pump, the maximum Mach numbers achievable are shown in Table 2.3 for each of the buffer gases and different nozzle diameters.

To calculate the pressures in the subsequent chambers, the following equations, taken from [158], can be used for the conductance in L/s of an aperture of cross-sectional area $S$, in cm$^2$:

$$C_v = S \times 10^{-3} \left( \frac{2}{\gamma + 1} \right)^{1/(\gamma-1)} \sqrt{\frac{2\gamma RT}{A(\gamma + 1)}} \approx \frac{113.3\,S}{\sqrt{A}}, \tag{2.9}$$

and

$$C_m = S \sqrt{\frac{5RT}{\pi A}} \approx \frac{62.3\,S}{\sqrt{A}}, \tag{2.10}$$

for a gas in the viscous and the molecular flow regime, respectively, where $R$ is the universal gas constant, $R = 8.314\,\mathrm{J\,K^{-1}mol^{-1}} = 8.314 \times 10^7\,\mathrm{erg\,K^{-1}mol^{-1}}$. For the approximation, which is only valid for monoatomic gases, $T$ has been taken to be 293 K. For a circular aperture with a diameter of the order of a centimeter, gas is in the molecular regime if its pressure is $\lesssim 10^{-2}$ mbar. If the gas pressure is $\gtrsim 1$ mbar, the viscous regime can be assumed.

For the conductance of the first aperture, $A_1$ in Figure 2.10, Equation 2.9 must be used as the pressures on either side of the aperture are high enough that the gas regime is viscous. The gas passing through aperture $A_2$ can be considered molecular due to the pressure ranges at either side, thus Equation 2.10 will be used to calculate its conductance. With the aperture diameter $d = 5$ mm, the conductances can be calculated to be $C_1(\mathrm{He}) = 11.1\,\mathrm{L/s}$, $C_1(\mathrm{Ar}) = 3.52\,\mathrm{L/s}$, $C_2(\mathrm{He}) = 6.11\,\mathrm{L/s}$ and $C_2(\mathrm{Ar}) = 1.93\,\mathrm{L/s}$.

With these, and with the pumping speeds available from the turbo pumps mounted on the second and extraction chambers $v_2 = 2200\,\mathrm{L/s}$ and $v_3 = 1000\,\mathrm{L/s}$, pressures at all three differential pumping section chambers can be calculated for different buffer gases, gas cell pressures and nozzle diameters. These are shown in Figure 2.11.

The pressure of the extraction chamber ($10^{-6} - 10^{-7}\,\mathrm{mbar}$) is in the same range as the high vacuum in the rest of the facility, with this chamber being the last in the differential pumping section.
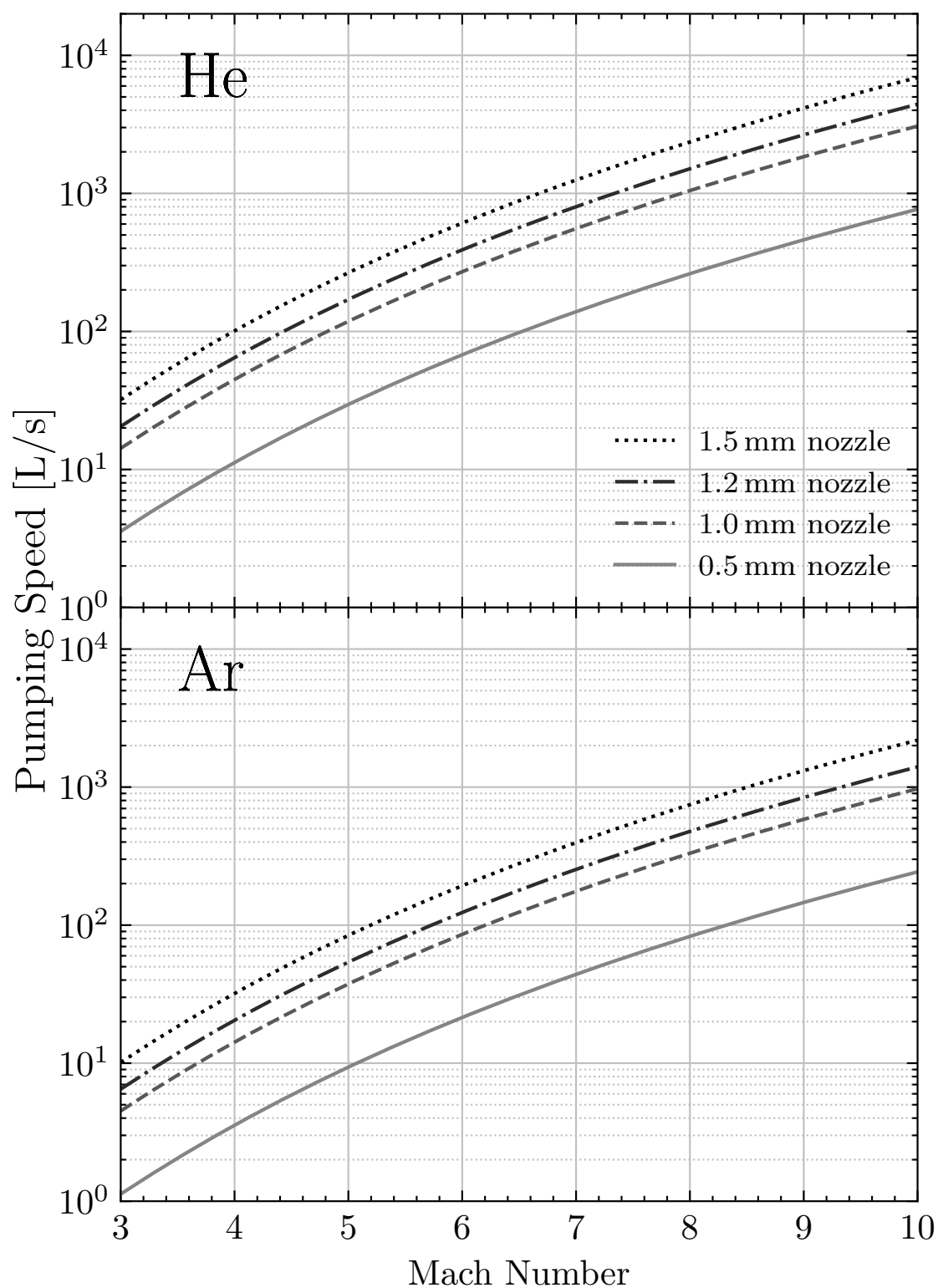
FIGURE 2.12   Pumping speed required in terms of the target Mach number of a gas jet produced by a de Laval nozzle of different diameters. Helium (top) and argon (bottom) used as buffer gases.

# Part II

# Instrumentation

# 3    DESIGN ASPECTS OF THE MARA-LEB GAS CELL

The MARA-LEB gas cell is a small-volume (0.5 L) gas cell that is placed at the focal plane of MARA to stop, thermalise and neutralise recoils. Its design is based upon a prototype developed at the In-Gas Laser Ionization and Spectroscopy (IGLIS) laboratory of KU Leuven (Belgium) for future use at the on-line Rare Element in Gas Laser Ion source and Spectroscopy at $S^3$ (REGLIS$^3$) at GANIL [63]. This chapter will explain the design of the gas cell and the simulation work that informed it.
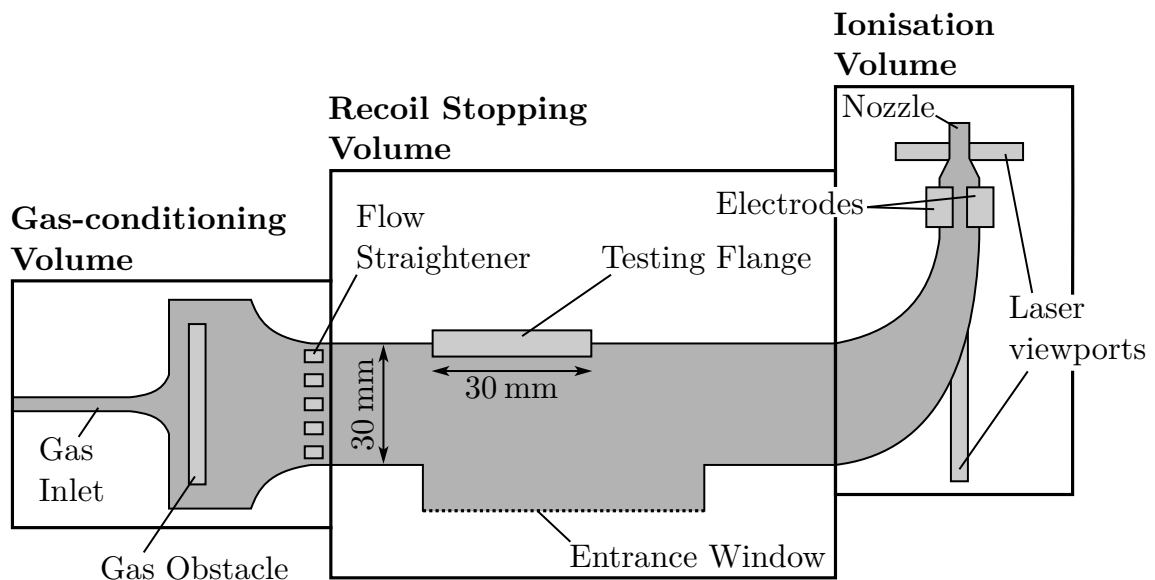


FIGURE 3.1    The MARA-LEB gas cell, with its volumes and components labelled. Parts are not to scale.

The gas cell consists of a horn-shaped cavity and can be described as having three distinct volumes, which are divided by their purpose: a gas-conditioning volume, a recoil stopping volume and an ionisation volume. These volumes are not physically divided. The gas cell can be seen in Figure 3.1, where the volumes are labelled.

The gas-conditioning volume contains structures that modify the flow of the incoming buffer gas to make it more favourable to stop and transport ions. The recoil stopping volume is an oval-faced cylindrical region that contains a laminar flow of gas to stop incoming MARA recoils. This volume has a flange that serves as a connection to MARA via a thin foil window, the material and thickness of which has been studied for different reactions and is presented later in this chapter. The ionisation volume is a tapered, curved volume that smoothly transitions from the recoil stopping volume to a changeable exit nozzle. This volume is designed to be optimal for laser-ionisation of neutralised recoils. It is fitted with laser viewports and ion-collecting electrodes. The former allow laser ionisation to be performed inside the gas cell, either in collinear, transverse or crossed-beam configurations. The ion-collecting electrodes serve as a way of eliminating unwanted species that have not been fully neutralised before they exit the gas cell. By applying a voltage to these electrodes, the trajectories of charged particles will be diverted from the gas cell exit, thus reducing the amount of contamination injected into the transport system.

The design of these volumes was informed by the use of COMSOL Multiphysics software package [159] simulations to optimise the gas flow within the cell for the stopping of recoils, their evacuation and subsequent ionisation and extraction. The results of these simulations are presented in a publication on the commissioning of the MARA-LEB gas cell, along with experimental findings from offline tests at the IGISOL facility [160].

## 3.1 Gas Flow

The gas cell constantly receives a flow of a buffer gas, helium or argon, depending on the experimental requirements. Noble gases are used for their extremely low chemical sensitivity and fast extraction times [161].

The helium and argon used as buffer gases in MARA-LEB experiments must meet high purity requirements. Impurities in the gas can affect the final charge state of the recoils while thermalising. Chemically active recoils, in addition, can react with impurities, reducing the atomic extraction due to the formation of molecules. This is an especially important effect with slow evacuation times [161, 162]. As an example, zirconium, an element of interest for MARA-LEB, is highly reactive and will rapidly form molecules with water and oxygen impurities in

the buffer gas. To avoid such effects, sub-part-per-billion impurity levels are required [163].

MARA-LEB buffer gases are purified in a gas-handling system based on the design presented in [163], which was designed for the IGISOL facility. Helium of grade 4.6 (99.996% purity) and above is purified via liquid nitrogen-cooled cold traps, filled with zeolite 13-X, a porous material which collects impurities. The trap in use is kept at a pressure of about 3.5 bar and a temperature of 77 K, ensuring that only hydrogen, helium and neon remain in a gaseous phase. Grade 5.0 argon (99.999% purity) is purified by a SAES MonoTorr PS4-MT3-R-2 rare gas getter purifier, which uses a heated zirconium alloy to remove impurities by chemical binding [163, 164]. This getter can also additionally purify helium after the cold traps.

Argon has a recombination rate coefficient which is approximately 10 times that of helium [165, 166]. This leads to a higher probability of recoil neutralisation, thus making argon preferable as a buffer gas in resonant laser ionisation experiments [167]. For these experiments, additional methods to enhance neutralisation are being explored. This covers the possibility that the recoils entering the gas cell do not produce enough free-charge carriers to fully neutralise them. This is not an issue in other facilities, such as IGISOL, where the primary beam enters the gas cell and creates many free-charge carriers. The use of an electron gun, $\beta$-decaying source, or other sources of electrons is under investigation for both MARA-LEB and $S^3$-LEB.

For experiments which do not require laser ionisation, helium gas is preferable. Helium has the highest ionisation potential of any element and, if the gas is pure, the recoils survive in an ionic charge state. The gas cell evacuation time with helium is approximately three times shorter due to the different conductance of the exit nozzle. Thus, exotic isotopes with shorter half-lives can be accessed for downstream experiments.

The pressure of gas fed into the gas cell is of the order of $\sim 100$ to $\sim 1000$ mbar, depending on the requirements for recoil stopping. The gas inlet is immediately followed by an obstacle, which slows down the incoming gas. The gas then passes through a honeycomb structure (flow straightener) before the main volume of the gas cell. This ensures a laminar flow of the buffer gas within the gas cell, which reduces ion losses due to, for instance, diffusion to the walls. A turbulent flow would also increase evacuation times, further introducing losses due to decay for exotic isotopes with short half-lives. The behaviour of the gas provided by these structures is shown in the first inset of Figure 3.2.

To separate the relatively high pressure environment of the gas cell from the high vacuum of MARA, a thin foil is used as an entrance window into the recoil-stopping volume. This foil reduces the energy of the recoils as they come into
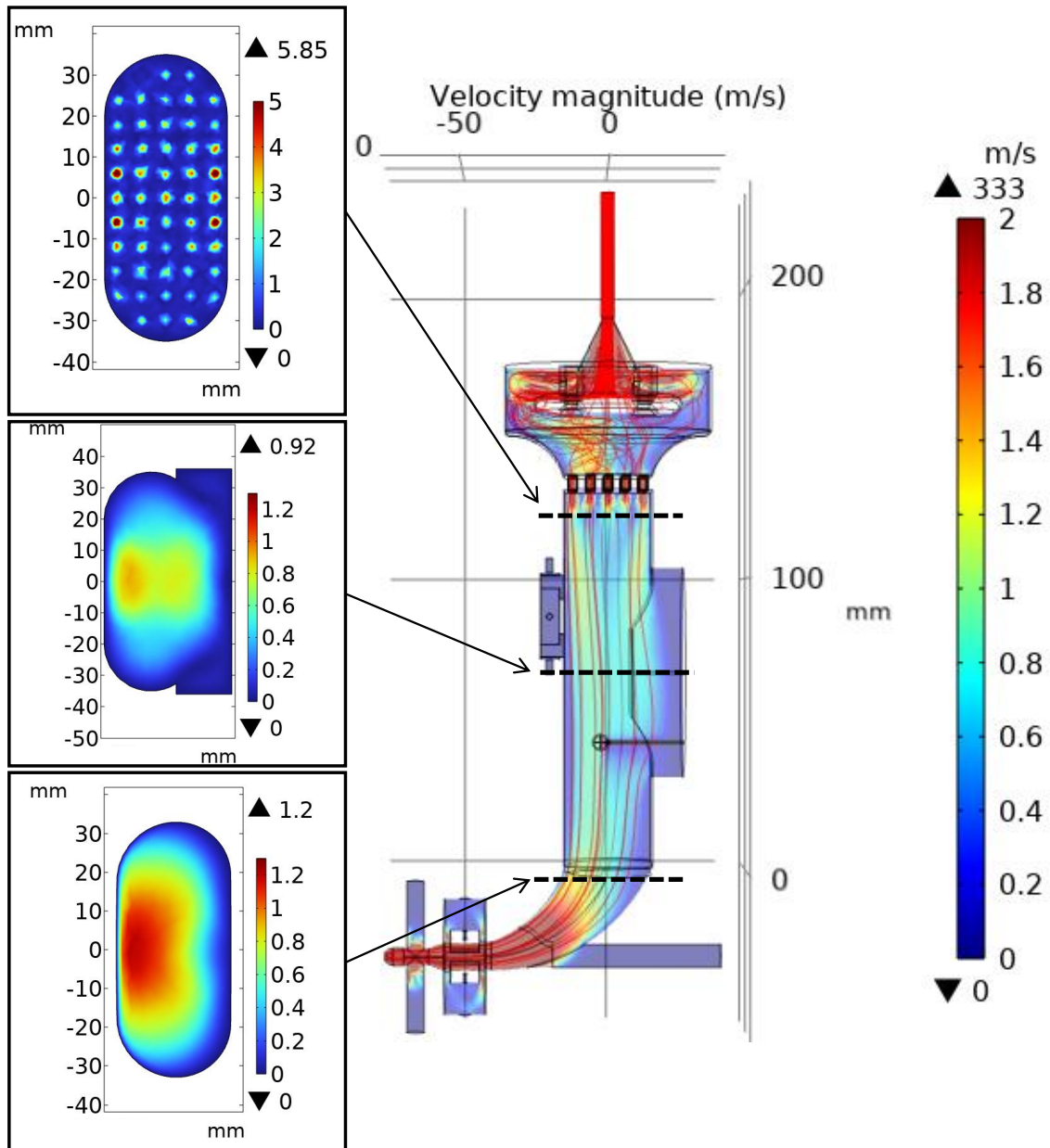
FIGURE 3.2    Results of Comsol numerical calculations of gas flow in the gas cell [160]. Three insets show, from top to bottom, transverse cross-sections at: the flow straightener, the middle of the stopping volume and the beginning of the ionisation volume. The colour scale has been capped at 2 m/s to allow for a better visualisation of the data.

the gas cell, improving their thermalisation and stopping in the buffer gas. The design aspects of the gas cell window and its foils are discussed in Section 3.2. Incoming recoils are thermalised and stopped as close to the centre of the volume as possible, to avoid losses from collisions with the gas cell walls and to minimise extraction times, given that gas velocity at the centre is higher than closer to the walls. When using argon, recoils will be neutralised in this volume.

Thermalised recoils are transported by the gas into the ionisation volume of the gas cell. This horn-shaped volume is designed to increase the speed at which the gas flows, as can be seen by comparing the middle and bottom insets of Figure 3.2. An increased gas velocity in the gas cell, up to Mach number 1, is required to effectively generate a supersonic gas jet after the nozzle. Although the environment within the gas cell is suitable for in-gas laser ionisation, high-resolution spectroscopy is prohibited due to the environmental conditions, with Doppler and collisional broadening mechanisms affecting the spectral linewidth of an atomic transition. However, with an expanding supersonic gas jet, the temperature and pressure drop rapidly as the Mach number increases [142], reducing these broadening mechanisms and allowing for in-gas jet resonance ionisation spectroscopy.

Finally, the isotopes are flushed from the gas cell through a nozzle. The shape and properties of this nozzle can be adjusted on an experiment by experiment basis. Typically, MARA-LEB experiments will use either free-jet or de Laval nozzles. De Laval nozzles are used to generate uniform, supersonic and axis-symmetric jets with high Mach numbers, producing optimal conditions for in-gas-jet laser ionisation and spectroscopy [168]. Free-jet nozzles are used in experiments in which the high resolution of this technique is not required [169].

The formation of the gas jet using de Laval nozzles on a gas cell design that is identical to the MARA-LEB gas cell has been characterised exhaustively at the IGLIS laboratory at KU Leuven; results from these studies are published in [168]. This characterisation of the gas cell was performed with the $S^3$ facility in mind, achieving an overall performance through the facility of 4-24%. Similar experiments are required at the MARA-LEB facility with the realistic experimental setup to assess the efficiency and performance of all systems working collectively.

### 3.1.1 Gas Flow Simulations and Tests

Gas flow simulations, such as the ones presented in Figure 3.2, were compared to experimental tests in the IGISOL facility using helium as a buffer gas and the results of both of these are presented in [160]. These tests used a free-jet nozzle for the gas cell, with diameter 1.65(7) mm. In these tests, a $^{223}$Ra, $\alpha$-emitting source with an activity of 4.0(4) kBq was positioned on the gas cell test flange, and the activity of the daughter nucleus, $^{219}$Rn, was used to determine transport efficiencies.

A maximum recoil extraction efficiency of 12.7(1.3)%, including the transport from the end of the cell to the detector downstream in the IGISOL facility, was achieved experimentally for a pressure of 300 mbar. Because the transport from the gas cell to the detector is taken into consideration, it is expected that the true gas cell extraction efficiency, measured immediately after the exit nozzle, will be slightly larger than the aforementioned figure. Further tests will take place at the MARA-LEB facility, in which the extraction setup will be the same as in on-line experiments, leading to more realistic values for extraction efficiency of the gas cell. Despite differences between the absolute efficiencies experimentally measured and determined by simulations, the trends were in good agreement: both growing with helium pressure. COMSOL simulations estimated extraction efficiencies up to 30%, however, they did not include potential losses due to impurities or due to the transport from the gas cell nozzle to the detectors.

Evacuation times of $^{219}$Rn$^+$ ions were measured in helium at 200 mbar and argon at 100 mbar. $^{20}$Ne$^+$ ions, coming from impurities in the helium gas, and $^{40}$Ar$^+$ ions were also measured to determine their evacuation times in the helium and argon buffer gases, respectively. The buffer gas ions and impurities were ionised by the passage of the $^{219}$Rn$^+$ ions from the $\alpha$-recoil source. The evacuation time of the ions was defined as the time difference between the switching of a negative voltage applied to the $^{223}$Ra source and their detection. The time profiles measured for these ions in their respective buffer gases are shown in Figure 3.3, fitted with an Extreme Peak function (Equation 3.1):

$$f_{EP}(t) = A + B \exp\left[1 + \left(\frac{t_0 - t}{\Delta t}\right) - \exp\left(\frac{t_0 - t}{\Delta t}\right)\right], \qquad (3.1)$$

where $A$ and $B$ are constants, $t_0$ and $\Delta t$ are the centroid and width of the peak, respectively. Evacuation times of $^{20}$Ne$^+$ and $^{219}$Rn$^+$ in helium at 200 mbar were measured at 100 ms, with a time spread of 50 ms. $^{40}$Ar$^+$ and $^{219}$Rn$^+$ in argon at 100 mbar were evacuated from the gas cell in 285 ms and 294 ms, with peak widths of 160 ms and 120 ms, respectively.

The measured evacuation times and their peak widths were compared with simulations performed with the COMSOL Computational Fluid Dynamics (CFD) module. While the measured distribution centroids are in good agreement with simulations, their widths for the cases in helium are much wider in simulations than in the experiment. This is suspected to be because of an erroneous assignment of diffusion coefficients for lighter gases.

The ratio of evacuation times of the $^{219}$Rn$^+$ ions in helium to that of the ions in argon is 2.94(2), reasonably close to the estimate based on the speeds of sound in the buffer gases. The speed of sound, $a$, in a gas is inversely proportional to the gas' atomic mass $a_{\text{gas}} \sim \sqrt{1/A_{\text{gas}}}$. The ratio of speeds of sound, therefore, is $a_{\text{He}}/a_{\text{Ar}} \sim \sqrt{A_{\text{Ar}}/A_{\text{He}}} = 3.16$. This estimate does not take into account the many flow effects that occur in realistic gas flow conditions, such as differences in the dynamic viscosity of the gases or differences in flow structure within the gas cell, among others.

## 3.2 Thin Foil Window

The thin foil window at the focal plane of MARA is the barrier that separates the pressurised environment of the gas cell from the vacuum of MARA. Because of this, the foils must be able to withstand pressure differences of up to 1000 mbar. The foil composition and thickness must also be chosen so that the recoils of interest are stopped close to the centre of the gas cell stopping volume ($\sim$ 15 mm from the window).

Simulations were carried out to determine what foil material and thickness could be used in different reactions of interest. Recoil energies were taken from MARA experimental data.

The Transport of Ions in Matter (TRIM) simulation program was used to calculate the 3-dimensional distribution of recoils after interacting with the window material and the buffer gas in the gas cell at different pressures. TRIM is one of the programs included in the Stopping and Range of Ions in Matter (SRIM) bundle. This software bundle uses a quantum-mechanical treatment of ion-atom interactions to calculate the penetration ranges of ions in materials [170].

The materials considered for the simulations were: titanium, nickel, Mylar and Havar. Mylar, or biaxially oriented polyethylene terephthalate (boPET), is a polyester film made from stretched polyethylene terephthalate (PET) [171]. Havar, or UNS R30004, is a cobalt-based alloy, its composition can be found in [172].
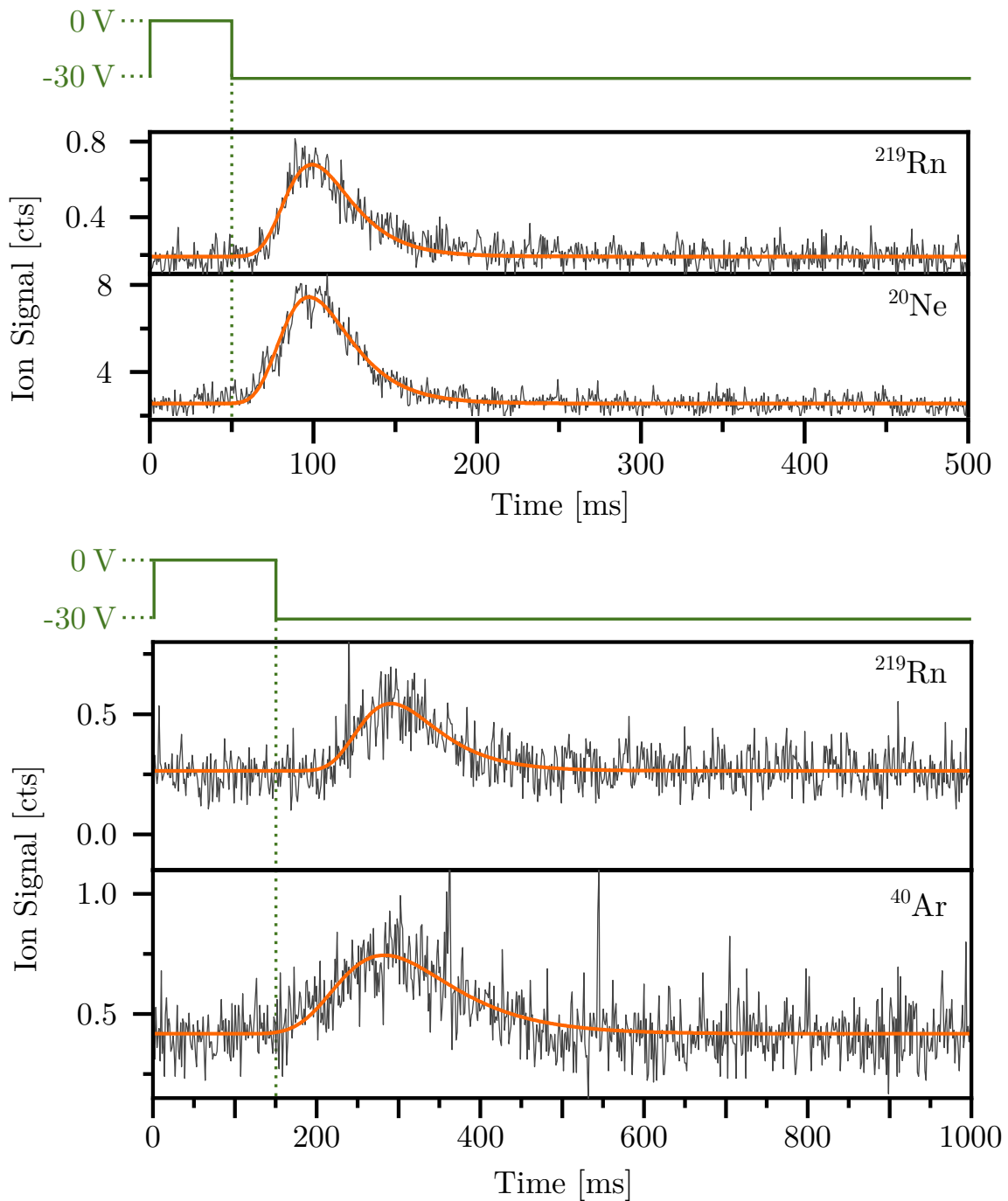
FIGURE 3.3  Evacuation time profiles for $^{219}$Rn$^+$ and $^{20}$Ne$^+$ ions in helium at 200 mbar, with a voltage release time of 50 ms (top) and $^{219}$Rn$^+$ and $^{40}$Ar$^+$ ions in argon at 100 mbar, with a voltage release time of 150 ms (bottom). For both, the voltage applied to the needle as a function of time is plotted in green. Time profiles are fitted to with an Extreme Peak function (in orange). Adapted from [160].

These were chosen as they are readily available commercially in foil form in different thicknesses and are commonly used for similar purposes in other facilities, in addition to their favourable physical properties.

The reactions used for the simulations were the following:

$$
\begin{aligned}
&\text{i)} \ ^{40}\text{Ca} + {}^{58}\text{Ni} \rightarrow {}^{94}\text{Ag} \ @ \ 58\,\text{MeV}, \\
&\text{ii)} \ ^{58}\text{Ni} + {}^{24}\text{Mg} \rightarrow {}^{80}\text{Zr} \ @ \ 120\,\text{MeV}, \\
&\text{iii)} \ ^{65}\text{Cu} + {}^{209}\text{Bi} \rightarrow {}^{213}\text{Rn} @ \ 131\,\text{MeV}, \\
&\text{iv)} \ ^{65}\text{Cu} + {}^{238}\text{U} \rightarrow {}^{226}\text{Th} @ \ 180\,\text{MeV}.
\end{aligned}
\tag{3.2}
$$

The specified energies are the recoil selected energy, the energy with which the recoil is emitted from the target position at MARA. A systematic study was performed for the above recoil composition and energy combinations, where different foil materials and thicknesses were simulated for both helium and argon at 500, 750 and 1000 mbar to ascertain the optimal window configuration for each case. The ions are generated with a Gaussian distribution of energies, centred on the energies stated above, with a FWHM of 10% of the centre value.

In every case, 2000 ions of the recoil of interest were simulated. The ions were generated at the origin of coordinates of a three-dimensional space with the specified kinetic energy in the positive $y$ direction. The thin foil window material of thickness $\tau$ spans the space from $y = 0$ to $y = \tau$. From $y = \tau$ to $y = \tau + 30$ mm, there is the buffer gas. 30 mm is the depth of the gas cell, measured from the inside surfaces of the walls. The only property that can be input into TRIM for a given gas is density. Given that both helium and argon are noble gases, it is possible to utilise the ideal gas law (Equation 3.3) to calculate their density, $\rho$ in terms of their pressure:

$$
\begin{aligned}
P &= \frac{nRT}{V} = \frac{mRT}{VA} = \rho \frac{RT}{A}, \\
\rho &= \frac{PA}{RT},
\end{aligned}
\tag{3.3}
$$

where $A$, $P$, $m$, $V$, and $T$ are the mass number in g/mol, pressure in mbar, mass in g, volume in cm$^3$ and temperature in K, respectively and the ideal gas constant is denoted by $R = 83\,144.6\,\text{mbar cm}^3\,\text{mol}^{-1}\,\text{K}^{-1}$. These simulations are all carried out at room temperature $T = 298.15$ K. The mass numbers of helium and argon are 4 g/mol and 40 g/mol, respectively.

Simulations for every foil material and thickness combinations were repeated for 500, 750 and 1000 mbar of gas pressure, for both helium and argon. The densities of each of the buffer gases at these pressures are shown in Table 3.1.

TABLE 3.1   Buffer gas densities for the pressures used in TRIM simulations.

| Pressure [mbar] | He density [$\times 10^{-5}$ g/cm$^3$] | Ar density [$\times 10^{-5}$ g/cm$^3$] |
| --- | --- | --- |
| 500 | 8.07 | 80.68 |
| 750 | 12.10 | 121.02 |
| 1000 | 16.14 | 161.36 |

Stopping of recoils in argon is much more effective than in helium thanks to the factor $\sim$10 increase in density. For this reason, thinner foils are generally needed for argon given the same material composition. The best window material and composition for each reaction shown in (3.2) and each of the buffer gases is shown in Table 3.2. The stopping positions of the 2000 simulated recoils for these windows are shown in Figure 3.4 for all 3 buffer gas pressures tested.

For the cases in argon, several foil composition and thickness combinations would result in all recoils being stopped within the gas cell. For these, the case where the recoil distributions were more centred within the gas cell volume were selected. The closer to the centre the recoils are stopped, the better gas flow conditions they will encounter. This can lead to a reduction in evacuation time and a minimisation of the diffusion into gas cell walls and is therefore preferred, especially for recoils with short lifetimes.

With helium as a buffer gas, finding a suitable thin foil window proved much more challenging. Because of this, typically only one material and thickness combination would lead to the majority of recoils stopping within the gas cell volume but with a non-trivial amount of them being stopped within the window foil. In the case of reaction i) with helium at 500 mbar pressure, none of the explored materials were able to stop recoils consistently, with most of them being lost to the gas cell wall. The best result for this, shown in the first subfigure in Figure 3.4, was found using a 5.5 μm-thick titanium foil. This was the only material and thickness combination which was able to fully stop silver ions with a helium at 1000 mbar and stop more than half of the simulated ions (56.9%) for 750 mbar of pressure.
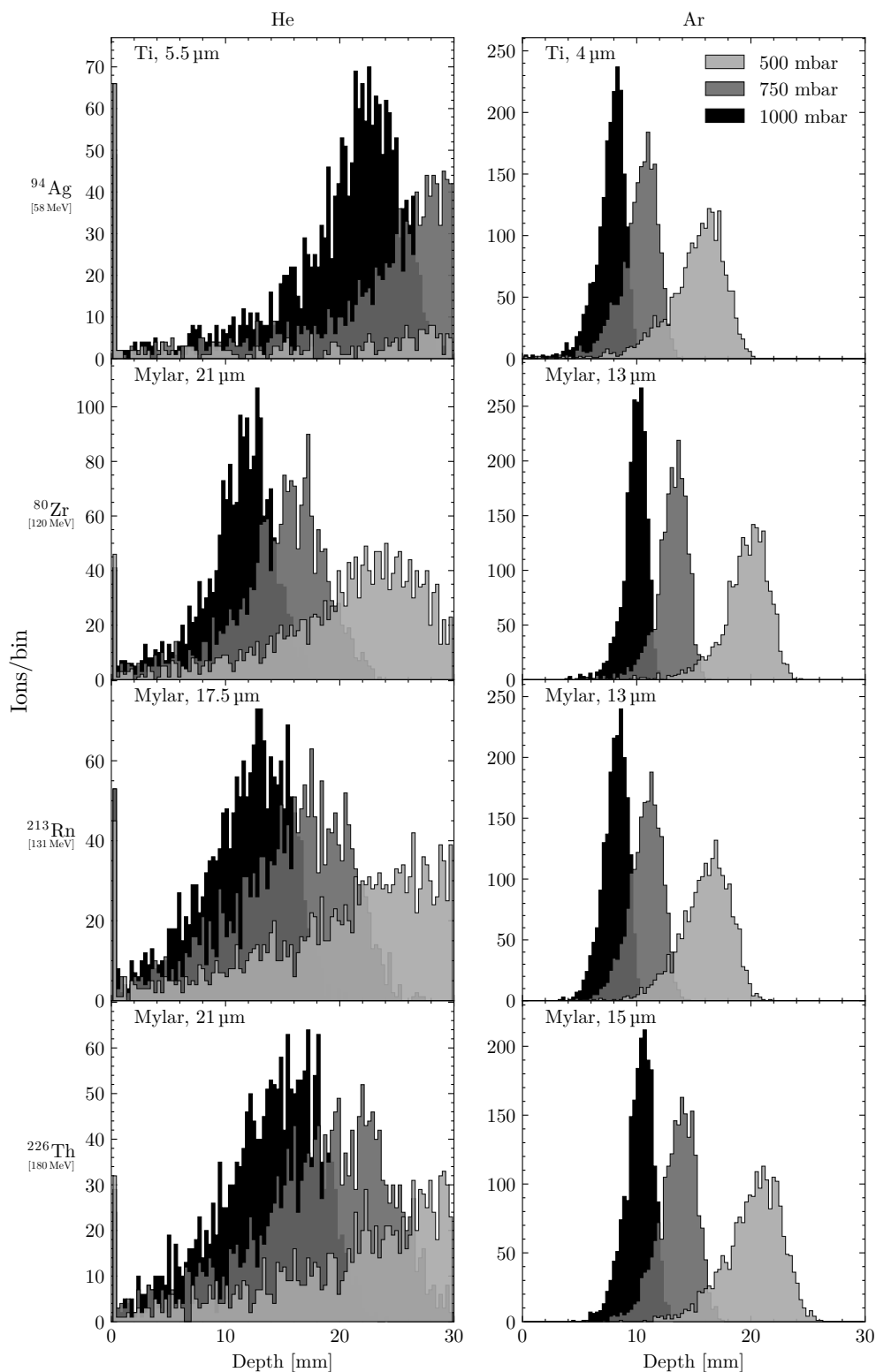
FIGURE 3.4 Stopped recoil distribution for the best window compsition and thickness (indicated in each subfigure) for $^{94}$Ag, $^{80}$Zr, $^{213}$Rn and $^{226}$Th (from top to bottom, respectively) for helium and argon (left and right, respectively) at 500 mbar (light grey), 750 mbar (grey) and 1000 mbar (black). The first bin contains the ions that are stopped within the window material. All histograms are divided into 100 equal bins. Ions not stopped in the gas are not shown.

TABLE 3.2  Optimal window material and thickness for each of the recoils produced in the reactions shown in Equation 3.2 for both helium and argon as buffer gases.

| Recoil | Helium Buffer Gas | | Argon Buffer Gas | |
|---|---|---|---|---|
| | Material | Thickness [µm] | Material | Thickness [µm] |
| $^{94}$Ag @ 58 MeV | Titanium | 5.5 | Titanium | 4 |
| $^{80}$Zr @ 120 MeV | Mylar | 21 | Mylar | 13 |
| $^{213}$Rn @ 131 MeV | Mylar | 17.5 | Mylar | 13 |
| $^{226}$Th @ 180 MeV | Mylar | 21 | Mylar | 15 |

For the rest of the reactions, recoils could be fully stopped within the gas cell with helium at 750 and 1000 mbar, but losses with pressures of 500 mbar were still considerable. The percentage of ions stopped in the cell is $> 97\%$ for all cases with 750 and 1000 mbar, except for the aforementioned case for 750 mbar with reaction i), at 56.9%. For helium at 500 mbar the percentage of ions stopped within the gas cell volume are 12.5%, 92.6%, 79.2% and 55.8%, respectively for reactions i) to iv).

These simulations show that usual window foil materials are adequate for the range of reactions that are of interest for MARA-LEB experiments using argon as a buffer gas. For experiments using helium, further investigations can be carried out to further reduce losses, but working combinations have been determined. In a next step, it will be important to carry out experimental tests in order to verify these simulations.

# 4   SIMULATIONS THROUGH THE ION TRANSPORT SYSTEM

The MARA-LEB ion transport system consists of two radio-frequency quadrupole (RFQ) ion guides, ion-optical acceleration electrodes, a dipole magnet, several radio-frequency quadrupole multiplets and an electrostatic deflector [173]. The working principle of RFQ ion guides is detailed in Section 4.2. The ion transport system components can be seen in Figure 4.1. These will serve to accelerate and transport ions from the exit nozzle of the MARA-LEB gas cell towards the experimental stations at the end of the line.

Simulations on the RFQ ion guides were performed using the SIMION Ion and Electron Optics Simulator [174] to inform the design of the ion transport system by testing different electrode geometries. This design process is described in detail in [175].

The design was further assessed via simulations by investigating the ion transmission efficiency through the guides in terms of the applied DC voltages and RF voltage amplitudes. The simulations were performed for different voltage combinations to gauge how changes affected ion transmission through the transport system, beam emittance, and the position of ion-optical focal points along the system. These parameters can inform decisions for day-one experiments and commissioning tests. These were repeated for the different buffer gases available for MARA-LEB.

The aperture between the first two differential pumping sections, which also serves as an electrode in the primary transport system, was flagged as a potential source of beam disruption. A new geometry for this aperture was designed and new simulations were performed to validate it.

The outputs of the RFQ guide SIMION simulations are used as the input for further simulations using the Python-driven Ion Optics Library (PIOL) [176] to perform a full, concise simulation of the entire MARA-LEB beamline. These simulations informed the design for the ion-optical elements in the ion transfer line, and assessed their working voltages in terms of system ion transmission and beam profile.

## 4.1 Primary Transport System

There are two distinct RFQ ion guides that comprise the MARA-LEB primary ion transport system: (i) a 90°-bent ion guide, installed after the exit nozzle of the gas cell, to capture ions transported out of the cell within the supersonic gas jet; (ii) a straight ion guide after the 90°-bent ion guide to transport ions into acceleration electrodes and ion optics further down the beamline.

The use of a 90°-bent ion guide immediately after the gas cell exit nozzle is required to avoid injecting the gas jet into the aperture separating the two first differential pumping regions. The pressure suppression factor between the gas jet and the second chamber is thus greatly increased solely by including this bend. In the ion guide design used at S$^3$-LEB, originally devised at KU Leuven, an S-shaped RFQ is used [177]. MARA-LEB required a full 90° bend due to space restrictions and to avoid passing laser light through pumping apertures, simplifying the vacuum system design [173].

The 90°-bent ion guide (BRFQ) consists of 36 short cylindrical and 36 10°-angled electrodes arranged quartet-wise as shown in Figure 4.3. Pairs of electrodes, which are electrically connected, are composed of an inner and an outer electrode, as highlighted in Figure 4.2; the latter is slightly wider than the former. This different geometry is needed for the ion guide to be able to curve. The distance between a pair of electrodes at the same voltage in the BRFQ is 6 mm, therefore $r_0(BRFQ) = 3$ mm. Figure 4.4 shows half of the BRFQ mounted on its support plate.

The straight RFQ (SRFQ), also depicted in Figure 4.2, is constructed of 28 longer cylindrical electrodes, arranged pairwise, in the same way as the BRFQ. In the case of the SRFQ, the minimum distance between electrode pairs is 12 mm, which means $r_0(SRFQ) = 6$ mm.
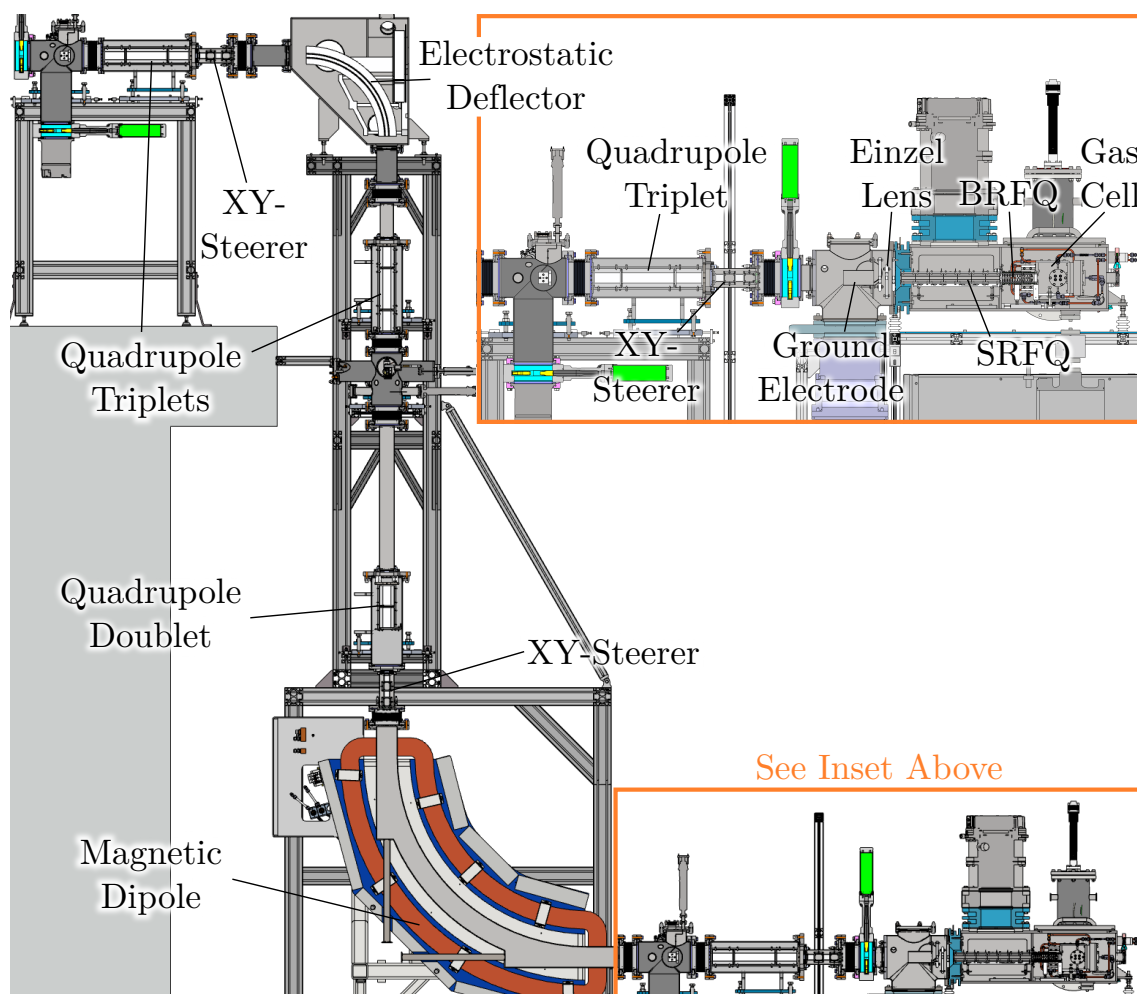
FIGURE 4.1   Overview of the MARA-LEB facility showing the ion transport system components. The lower horizontal line is shown in an inset (orange box) for clarity. Details on the components are given later in this chapter.
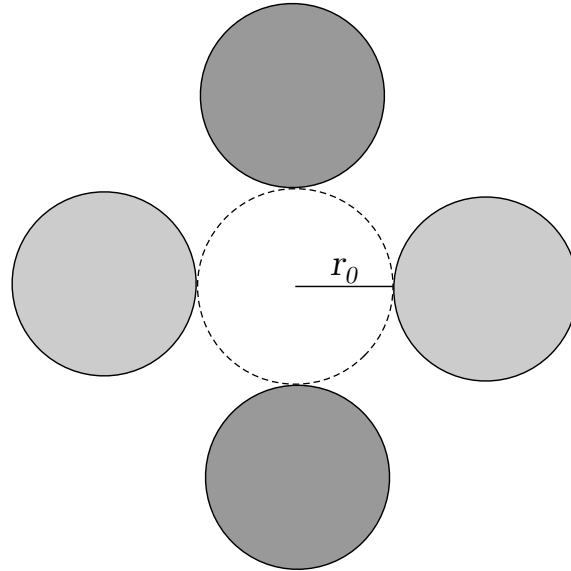
FIGURE 4.3    Axial view of an RFQ with cylindrical-section electrodes. Electrodes at the same potential are shaded in the same colour. $r_0$ is the inner radius of the RFQ ion guide.

The apertures between differential pumping sections ($A_i$ in Figure 2.10) serve as DC electrodes in the transport system, in addition to connecting vacuum regions. They were designed to be suitable for both ion transport as part of the RF ion guide and as a vacuum aperture between differential pumping chambers. The aperture electrode, $A_1$, connects the BRFQ to the SRFQ. The extraction electrode, $A_2$, is the final electrode in the primary ion transport system and guides the ions into the ion transfer system.
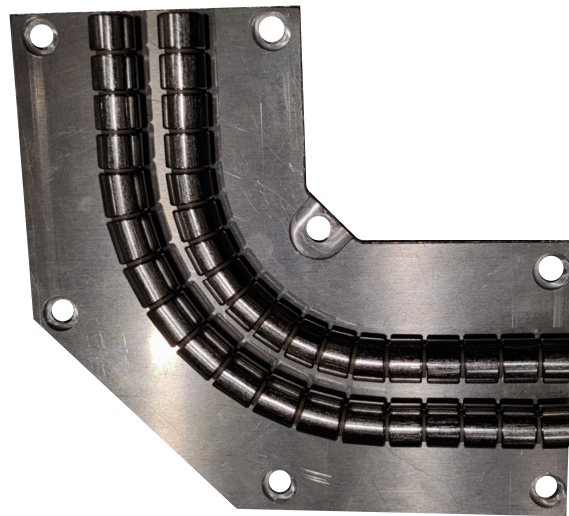


FIGURE 4.4    Picture of the 90°-bent RFQ mounted on its support plate, showing half of the electrodes. The complete BRFQ is composed of two mirrored ensembles.
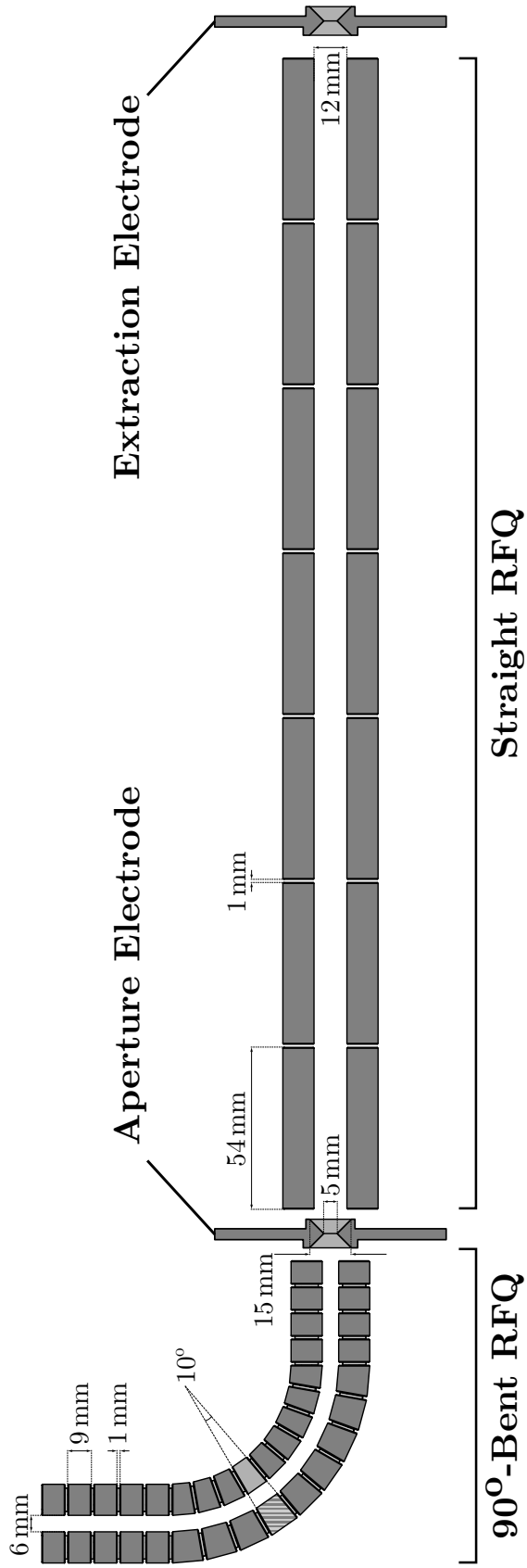
FIGURE 4.2   Longitudinal cross-section of the primary transport system, showing measurements of components and their spacing. The figure includes the aperture between differential pumping sections, which also serves as an electrode in the ion guide. A pair of 10°-curved electrodes is highlighted, with the inner electrode in a lighter grey and the outer electrode in a hatched pattern.

## 4.2 Radio-Frequency Quadrupole

Radio-frequency quadrupoles (RFQ) are two-dimensional Paul traps, whose operation is based on the principle of charged-particle trapping by the use of dynamic electric fields.

In general, Paul traps use quadrupole electric fields to confine charged particles at their centre. The electric potential generated in the trap generates a restoring force to the particles when they stray away from the trap centre. Paul traps use a potential, $\Phi$, that ensures that the resulting force on the particles is proportional to the distance from the central position:

$$\Phi \propto \xi x^2 + v y^2 + \zeta z^2, \tag{4.1}$$

where $\xi$, $v$ and $\zeta$ are dimensionless proportionality constants [178].

Since the region of space where this potential acts is free of electric charges, Laplace's equation must be satisfied:

$$\nabla^2 \Phi = 0. \tag{4.2}$$

This ensures that the proportionality constants must all add to 0:

$$\xi + v + \zeta = 0. \tag{4.3}$$

A solution to this set of equations is $\xi = 1$, $v = -1$, $\zeta = 0$. This eliminates the $z$ term from Equation 4.1, eliminating also the confinement of charged particles on this axis. A trap using this particular solution is known as a linear Paul trap [178]. Taking $z$ as the axial direction and defining $r_0$ as the internal radius of the trap area, as shown in Figure 4.3, the potential of an infinitely long linear Paul trap can be written as:

$$\Phi = \frac{\Phi_0(t)}{r_0^2}(x^2 - y^2), \tag{4.4}$$

where $\Phi_0(t)$ is the time-dependent potential applied to the electrodes.

The working principle behind RFQ ion guides is the use of groups of four hyperbolic electrodes placed in a square arrangement. The electrodes directly opposite each other form a distinct pair. The distance between two electrodes of the same pair is defined as two times the internal radius, $r_0$. Two electrodes in a pair will be connected to the same electric potential, with the other pair being connected to a potential of the same magnitude but opposite sign, ensuring the aforementioned condition $\xi = -v = 1$. Most RFQ ion guide setups use cylindrical electrodes, rather than hyperbolic, to reduce manufacturing complexity and cost. A realistic geometry using cylindrical electrodes, is shown in Figure 4.3.

RFQ ion guides consist of several segments along the axial direction. In addition to the RF voltage applied, a quadrupolar direct current (DC) component, $U$, is also applied to the electrodes. The potential applied to each segment, therefore, will include the fixed quadrupolar DC voltage, $U$, and the time-dependent RF voltage, with amplitude $V_0$ and frequency $\nu$, with $\Omega = 2\pi\nu$. Thus, introducing these conditions into $\Phi_0(t)$ from Equation 4.4, the potential felt by particles in each segment is:

$$\Phi = [U + V_0 \cos{(\Omega t)}] \frac{x^2 - y^2}{r_0^2}. \tag{4.5}$$

Furthermore, by setting an additional DC voltage of each successive RFQ segment to progressively decreasing (increasing) values, a potential slope can be created to drive the trapped positively-charged (negatively-charged) particles along the ion guide axis.

Applying Newton's second law, it is possible to solve the equations of motion of a particle of mass $m$ and charge $q$ within the electric potential $\Phi$. The net force on these particles will be only due to the electrostatic force, $\mathbf{F}_{net} = \mathbf{F}_e = -q\nabla\Phi$. Since $\Phi$ is separable in Cartesian coordinates, an equation of motion can be derived for each coordinate where $\ddot{u}$ represents the second derivative with respect to time of coordinate $u$:

$$m\ddot{x} = -q\frac{\partial\Phi}{\partial x} = -2q[U + V_0 \cos{(\Omega t)}]\frac{x}{r_0^2}, \tag{4.6a}$$

$$m\ddot{y} = -q\frac{\partial\Phi}{\partial y} = +2q[U + V_0 \cos{(\Omega t)}]\frac{y}{r_0^2}, \tag{4.6b}$$

$$m\ddot{z} = -q\frac{\partial\Phi}{\partial z} = 0, \tag{4.6c}$$

It is customary [178] to introduce a dimensionless variable, $\eta := \frac{\Omega t}{2}$, to re-write Equations 4.6a and 4.6b as:

$$\frac{d^2x}{d\eta^2} + \left[\frac{8qU}{mr_0^2\Omega^2} - 2\frac{4qV_0}{mr_0^2\Omega^2}\cos{(2\eta)}\right] x = 0, \tag{4.7a}$$

$$\frac{d^2y}{d\eta^2} - \left[\frac{8qU}{mr_0^2\Omega^2} - 2\frac{4qV_0}{mr_0^2\Omega^2}\cos{(2\eta)}\right] y = 0. \tag{4.7b}$$

which allows these to be identified as Mathieu's equations for the vibration of a circular membrane [179].

By introducing the following parameters for each coordinate:

$$a_x = -a_y = \frac{8qU}{mr_0^2\Omega^2},$$ (4.8)

$$q_x = -q_y = \frac{4qV_0}{mr_0^2\Omega^2},$$ (4.9)

it is possible to combine Equations 4.7a and 4.7b into a single equation, known as Mathieu's differential equation:

$$\frac{\mathrm{d}^2 u_i}{\mathrm{d}\eta^2} + [a_i - 2q_i \cos(2\eta)]\, u_i = 0.$$ (4.10)

The confining condition of the RFQ guide is achieved by optimising the parameters in Equations 4.8 and 4.9. There are two possible solutions to the Mathieu equations: unstable (type I) and stable (type II), both of them periodical [178]. Type II solutions are the ideal working conditions for linear ion traps, whereas type I solutions are the boundary conditions, where particles in the trap become unbound. Figure 4.5 shows the values of $q_u$ and $a_u$ for which type I and II solutions exist. The solution regions are symmetric due to the Mathieu parameters (Equations 4.8 and 4.9) being of opposite signs but equal magnitude for each of the coordinates.
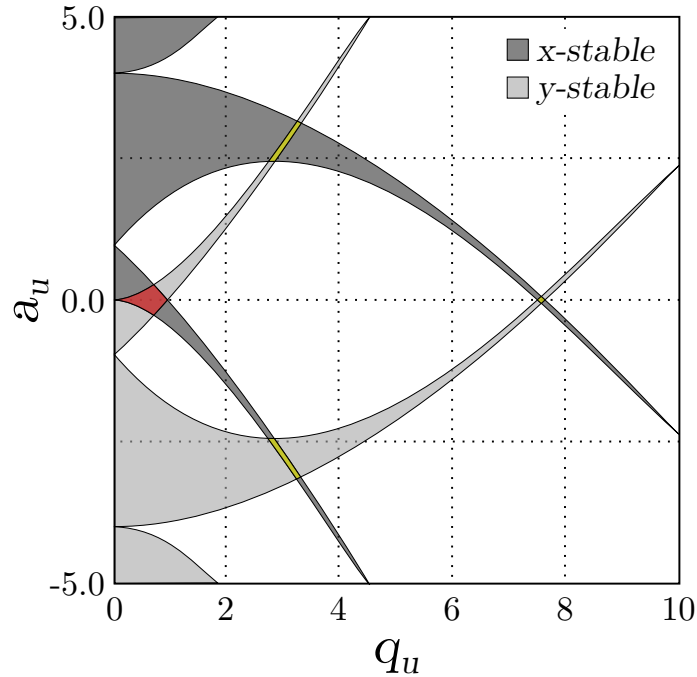


FIGURE 4.5    Stability regions for a linear Paul trap in $(q_u, a_u)$, the shaded regions correspond to type II solutions to the Mathieu equations, while the borders of these regions correspond to type I solutions. Overlap between stability regions for the $x$- and $y$-axes are highlighted: the first stability region in red and all others in yellow.

In experimental setups, the first stability region is used. This is the region of the $(q_u, a_u)$ space where stable solutions for both $x$ and $y$ overlap closest to the origin, shown in red in Figure 4.5. In this region, particles with the desired mass over charge ratios will be confined in the $x$ and $y$ directions without hitting the electrodes. All other particles will not be trapped and thus will be randomly directed into the electrodes or ejected from the ion guide. This also indicates that the RFQ can be used as a mass filter.
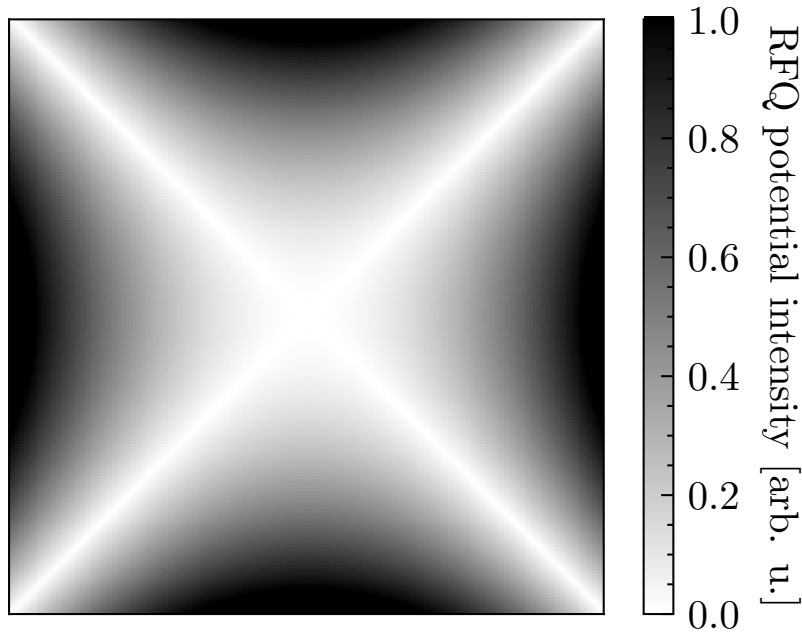


FIGURE 4.6    Plot of Equation 4.5 showing the absolute intensity of the electrical potential inside the RFQ.

## 4.3  Simion

The SIMION software was used to model the MARA-LEB ion optics. SIMION is chosen for this purpose due to it being able to calculate the electric fields in a region of space by solving the Laplace equation. SIMION allows for variable electrode voltages, which are necessary for the simulation of the conditions of radio-frequency ion guides.

The solution of the Laplace equation for variable electrodes allows SIMION to calculate the generated electric fields, an example of which is shown in Figure 4.6. It is then able to simulate ion trajectories within the RFQ, given that the forces acting on the ions are determined by the electric fields.

By default, the ion trajectories are calculated for vacuum conditions, but ad-

ditional models can be implemented to take additional ion interactions with a buffer gas into consideration. These interactions are mainly comprised of ion collisions with the gas atoms when exiting the gas cell as a jet. With the use of a Lua program, adapted from [175], these interactions were simulated using a hard sphere (HS) model coupled with a statistical diffusion simulation (SDS) model. HS is used for lower pressure (<8 mbar) regions of the system, whereas SDS is used for higher pressures, due to its lower computational cost.

### 4.3.1 Hard Sphere Model

The Hard Sphere (HS) model, described in [180], treats both the gas particles and the ions as hard spheres. It then calculates the expected distance between ion collisions, also known as the mean-free path, $\lambda$.

An ion with velocity $v_{rel}$ relative to the gas particles will traverse a length $l$ in a time step $\Delta t$ given by:

$$l = v_{rel}\Delta t. \tag{4.11}$$

In that same time step, the ion will collide elastically with every gas particle in its path. The interaction radius, considering both particles as hard spheres, will be defined as the sum of the radii of these particles:

$$r_{int} = r_{ion} + r_{gas}, \tag{4.12}$$

thus, a cylinder can be imagined, with radius $r_{int}$ and length $l$, which contains all of the gas particles a given ion will collide with in a time step $\Delta t$.

This cylinder has a volume $V_{cyl}$:

$$V_{cyl} = \pi r_{int}^2 l = \pi r_{int}^2 v_{rel}\Delta t. \tag{4.13}$$

The number of collisions for every time step can be derived by multiplying this volume with the particle density of the gas, $n_{gas}$, and dividing by the time step $\Delta t$ to obtain the collision frequency, $f_{coll}$:

$$f_{coll} = n_{gas}\frac{V_{cyl}}{\Delta t} = \pi r_{int}^2 v_{rel} n_{gas}. \tag{4.14}$$

Assuming that an ideal gas is used, the ideal gas law, $P = n_{gas}k_BT$ [181], can be applied, to obtain this collision frequency in terms of the buffer gas temperature, $T$, and pressure, $P$:

$$f_{coll} = \frac{\pi r_{int}^2 P}{k_B T}v_{rel}, \tag{4.15}$$

where $k_B = 1.380649 \times 10^{23}$ J K$^{-1}$ is Boltzmann's constant [182].

The atoms of an ideal gas follow a Maxwell-Boltzmann distribution of velocities, which in three dimensions has the form [183]:

$$h_{MB}(\mathbf{v}) = \left( \frac{m_{gas}}{2\pi k_B T} \right)^{3/2} \exp \left( \frac{-m_{gas}}{2 k_B T} \mathbf{v}^2 \right). \tag{4.16}$$

The ideal gas approximation is valid for the purposes of these simulations because the MARA-LEB gas cell will use the noble gases helium and argon as buffer gases.

The average relative velocity can be computed from Equation 4.16 for a certain ion velocity, $\mathbf{v_{ion}}$, as:

$$\bar{v}_{rel} = \iiint_V \mathbf{v_{ion}} - \mathbf{v_{gas}} h_{MB}(\mathbf{v_{gas}}) \mathrm{d}^3 \mathbf{v_{gas}}. \tag{4.17}$$

The result of this computation [180, 184] is dependant only on the speed of the ion, the gas temperature and the mass of the gas molecules:

$$\bar{v}_{rel} = \sqrt{\frac{2 k_B T}{\pi m_{gas}}} \left[ e^{-s^2} + \left( 2s + s^{-1} \right) \int_0^s e^{-\kappa^2} \mathrm{d}\kappa \right], \tag{4.18}$$

where $s$ is the ratio of the ion speed and median gas speed:

$$s = \frac{v_{ion}}{\tilde{v}_{gas}} = \frac{v_{ion}}{\sqrt{\frac{2 k_B T}{m_{gas}}}} = v_{ion} \sqrt{\frac{m_{gas}}{2 k_B T}}. \tag{4.19}$$

The average relative velocity shown in Equation 4.18 can be now combined with Equation 4.15. The probability of collision between an ion and a gas particle in a time step $\Delta t$ can be deduced to be:

$$P_{coll} = 1 - e^{-f_{coll}(\bar{v}_{rel})\Delta t} = 1 - \exp \left( \frac{-\pi r_{int}^2 P \Delta t}{k_B T} \bar{v}_{rel} \right). \tag{4.20}$$

In SIMION, the HS model is implemented by generating a random number based on Equation 4.20 and determining whether a collision happens in every time step. If a collision happens, SIMION will calculate the new ion trajectory and velocity assuming an elastic collision.

From Equation 4.20, it can be seen that the collision probability is proportional to gas pressure. For high pressures, thus, collisions will occur even for very small time steps. This makes the computational costs of this method impossibly expensive at high pressures.

### 4.3.2 Statistical Diffusion Simulation Model

The use of statistical diffusion simulation models in SIMION was studied in [185] to lighten the demand on computational power that the simulation of millions of collisions per time step would require. This model simplifies the movement of ions in all directions except the direction of motion by modelling the random diffusion and viscous mobility of the ions statistically. An average thermal speed and a mean-free path are calculated for the ions based on their mass and diameter for a certain background gas. The temperature and pressure of the gas at the location of the ion is defined in the program, allowing the model to calculate a maximum radius for thermal movement and generate a random number in that range. The results obtained with this method were comparable to those obtained from Monte Carlo collision models [185, 186].

In the direction of motion, the SDS model used for these simulations calculates the displacement of ions based on their drift velocity, $\mathbf{v}_d$ [185]. Drift velocity (in m/s) is calculated as the product of the ion mobility, $K$, in m$^2$/(V s), and the electric field, $\mathbf{E}$, in V/m:

$$\mathbf{v}_d = K\mathbf{E}. \tag{4.21}$$

A condition-dependant ion mobility can be calculated from $K_o$, the reduced ion mobility, taking into account the pressure and temperature of the buffer gas. $K_o$ represents the mobility at standard conditions of temperature and pressure and can be input into the model by the user or estimated by the model itself from the diameters of the ions and the gas atoms. Thus, given a known $K_o$, the drift velocity of the ions is calculated by the model as:

$$\mathbf{v}_d = \frac{760}{p} \frac{T}{273.16} K_o \mathbf{E}, \tag{4.22}$$

where $p$ is the gas pressure in torrs and $T$ is the gas temperature in kelvins.

## 4.4 Ion-Optical Simulations

SIMION was used to determine the optimal settings for the RF ion guides to maximise transmission while minimising beam emittance. Transmission is defined as the ratio of ions that reach the end of the transport system to those which are introduced into the ion guides. The variables affecting transmission through a given ion guide design are: the DC voltages applied to each individual electrode, the AC voltage amplitude applied to pairs of electrodes in the BRFQ and in the SRFQ, and the buffer gas composition and pressure used in the gas cell. The conditions of gas in the collimated gas jet are used by the program to calculate pressure and temperature throughout the primary transport system.

The primary ion guide system was modelled using CAD software and imported into SIMION; a 3D render of this geometry in SIMION is shown in Figure 4.7. Results from simulations informed changes in design, resulting in re-modelling and further simulations. The only difference between the realistic ion guide electrode setup and the simulation geometry is the addition of the nozzle electrode into the latter, as shown in Figure 4.7. This electrode is a fictitious plate that is positioned where the gas cell nozzle would be relative to the RFQs in the real setup. This plate is set at 30 kV and serves as the reference point for all other electrode voltages. The support plates of the electrodes (as seen in Figure 4.4) is not simulated either.
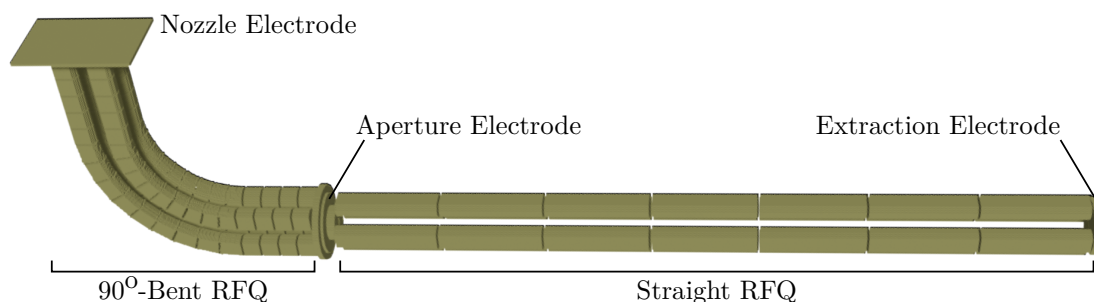


FIGURE 4.7   The primary ion transport system of MARA-LEB. The individual RFQ ion guides and connecting electrodes are labelled.

### 4.4.1   Buffer Gas

The two buffer gases that will typically be used in the gas cell are helium and argon. Simulations were performed for these gases, as well as in vacuum conditions for comparison. When implementing gas models in the simulations, a constant pressure of 500 mbar was used. From this, pressures of 0.79 mbar and $3.6 \times 10^{-4}$ mbar are calculated for the gas cell chamber and the second chamber, respectively, as described in Section 2.2.4. The pressure at every point of the region immediately downstream of the gas cell nozzle can be calculated as a function of distance and Mach number as described in [142]. These pressures are well within the range expected for MARA-LEB experiments, where the gas cell pressure will be set between 100 and 1000 mbar. With these pressures, the results yielded by the simulations will be typical for all MARA-LEB experiments.

TABLE 4.1    Van der Waals radii for the elements used in the simulations [187].

| Element | Van der Waals radius [Å] |
|---------|--------------------------|
| He | 1.40 |
| Ar | 1.88 |
| Ag | 1.72 |

The gases were modelled by the aforementioned models, with their van der Waals radii, shown in Table 4.1, implemented for use in Equation 4.12 and its derivations. Van der Waals radii are used as they are the distance for closest approach of other atoms. Atoms can therefore be imagined to be hard spheres of this radius for the purposes of these simulations.

### 4.4.2    Ion generation

All simulations used $^{94}$Ag$^+$ as the testing ion. This is an ion of particular interest for MARA-LEB [188], and has a mass which is approximately in the centre of the range of masses in the initial region of interest for the facility. Using the same ion for all runs eliminates it as a factor affecting the results of the simulations. Ions of different masses will have different stability regions, but the results of these simulations will serve as a guide for future investigations.

A uniform distribution of silver ions at 0.96 eV was generated in a 0.5 mm-radius circle, concentric to the aperture of the gas cell exit nozzle, as described in previous work [175]. The ions were generated with a random velocity vector direction within a 60°-aperture cone, simulating the possible trajectories that real ions may travel in when exiting the gas cell in the gas jet. A 60° aperture was chosen because it approximates the expansion of a free jet, which will diverge from the central beam axis by 30.5° [142]. This is illustrated in Figure 4.8.

The ions were generated uniformly between 0 and 1 μs from the beginning of the simulation. As 1 μs is the reciprocal of 1 MHz, which is the frequency used by the ion guides, ions generated uniformly throughout that time period will be subjected to all phases in the RF oscillation. This eliminates possible phase effects in the simulated ion trajectories.
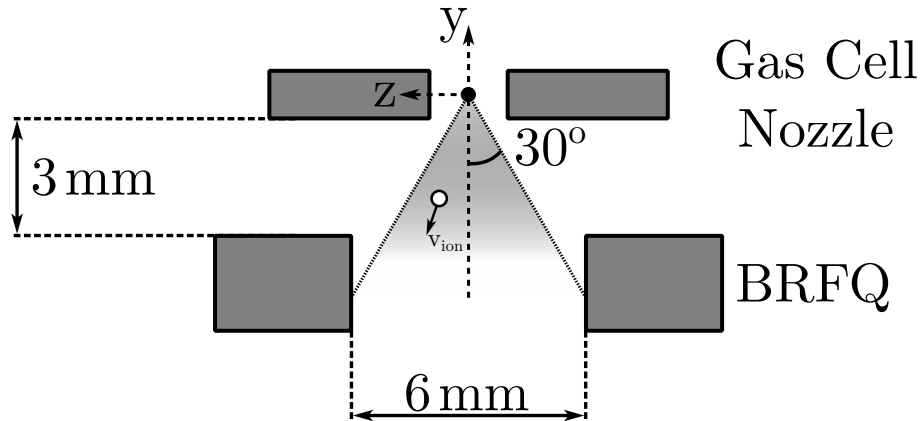
FIGURE 4.8    Illustration of the ion generation cone in SIMION. The solid black dot represents the origin of the coordinate system of the simulation space, coinciding with the centre of the gas cell nozzle. Two electrodes, corresponding to the first quartet of the BRFQ, are shown. The shaded cone represents the space of possible orientations for a particle's velocity vector. An example of an ion (in white) and its velocity vector ($\mathbf{v}_{ion}$) is included.

### 4.4.3    Voltage Optimisation

Firstly, the optimal DC voltages for the ion transport system were determined while maintaining constant AC voltage amplitudes in the bent and straight RFQs. These initial AC voltage amplitudes were estimated from the values that give stable solutions to the Mathieu equations (Equations 4.7). The initial chosen amplitude values were $V_{AC}(BRFQ) = 225\,\text{V}$ and $V_{AC}(SRFQ) = 65\,\text{V}$. With these, the DC voltage in each electrode was adjusted to maximise transmission through the transport system.

The DC voltages were set to be decreasing along the optical axis, to create what is known as a potential ramp. This accelerates ions as they move along the ion guide. Because the main vacuum vessel, which houses the gas cell and the RFQ system, is kept at 30 kV, the nozzle electrode was set at 30 kV, and all subsequent electrode voltages were defined as subtractions from this maximum potential. Within the ion guides, each electrode voltage was 1 V lower than the previous electrode, resulting in a smooth, uniform ramp of 17 V for the BRFQ and 6 V for the SRFQ. In the transitions between ion guides, higher voltage steps were taken to accelerate ions in the axial direction and prevent losses in the areas without RF voltage, such as the aperture electrode between the bent and straight RFQ ($A_1$ in Figure 2.10).

The DC voltages were changed until transmission with helium as a buffer gas was maximised. The same analysis was repeated with argon. The final voltages are shown in Table 4.2 and Figure 4.9. With these, a transmission of 100% was achieved.

Once optimal DC voltages were found, a systematic analysis of the AC voltage effect on transmission can be carried out. A range of possible voltage amplitudes for each of the RFQs was tested: from 60 to 250 V in steps of 10 V for the BRFQ and from 0 to 70 V in steps of 3.5 V for the SRFQ. The results of this systematic simulation can be seen in Figure 4.10.

Transmission values up to 100% were found, but the sensitivity to a change of a single step was found to be more pronounced than expected. Because of this, the final position of ions was investigated to determine where the ions were being lost and thus determine what caused the sensitivity in transmission.
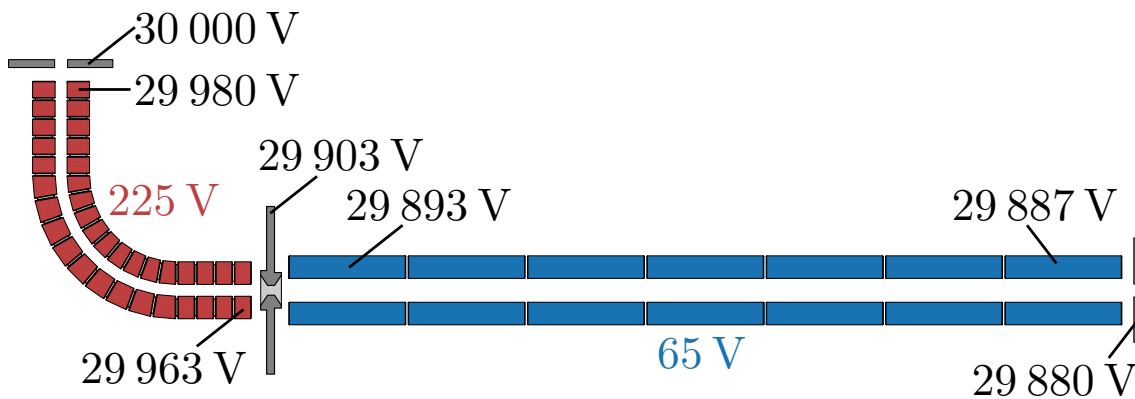


FIGURE 4.9   Schematic view of the optimal DC voltages (black) shown in Table 4.2. The bent and straight RFQ electrodes, along with their initial RF amplitudes, are shown in red and blue, respectively.

TABLE 4.2   Voltages relative to 30 kV that maximised transmission with each of the buffer gases and AC voltage amplitudes $V_{AC}(BRFQ) = 225$ V and $V_{AC}(SRFQ) = 65$ V.

| Buffer | BRFQ | | Aperture | SRFQ | | Extraction |
| Gas | First [V] | Last [V] | $A_1$ [V] | First [V] | Last [V] | Electrode [V] |
| --- | --- | --- | --- | --- | --- | --- |
| He | -20 | -37 | -97 | -107 | -113 | -120 |
| Ar | -20 | -37 | -167 | -207 | -213 | -225 |
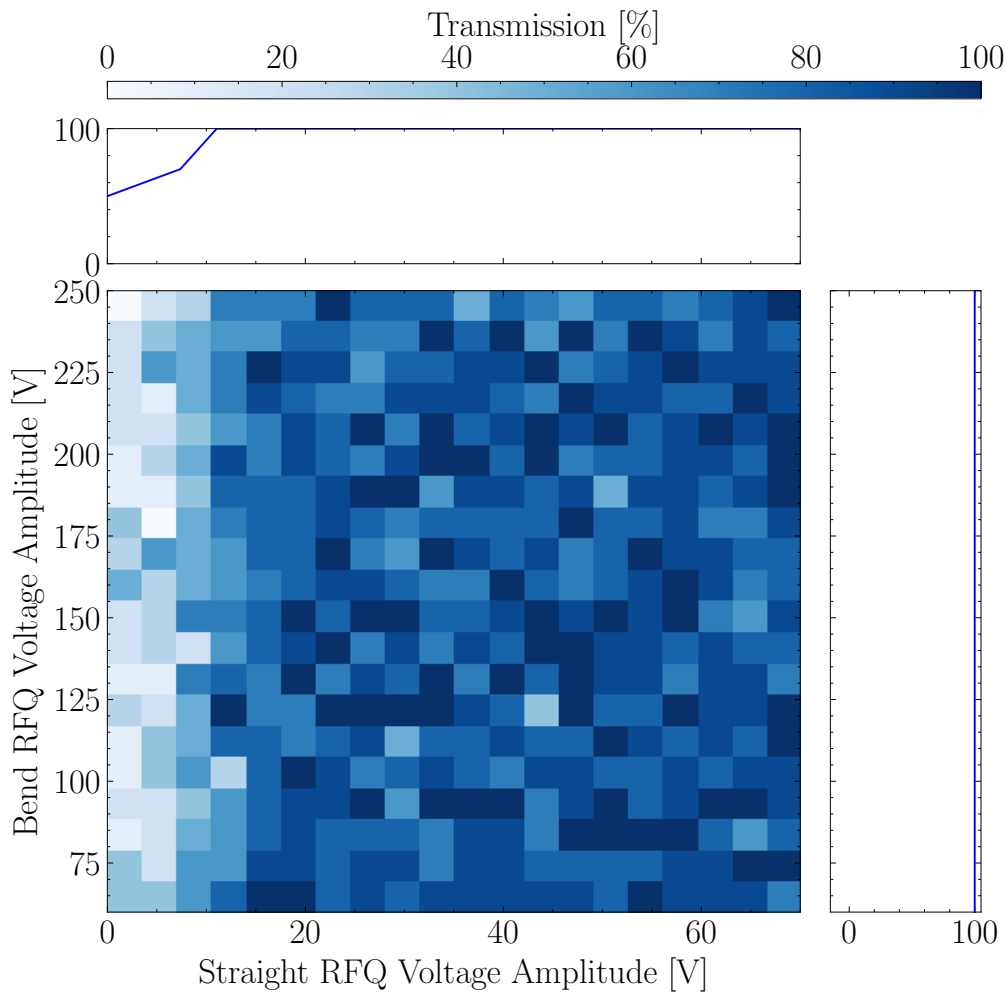
FIGURE 4.10    Results for the SIMION simulations with the optimal DC voltages shown in Table 4.2, using helium as a buffer gas. A projection for each of the axes is shown.

### 4.4.4    Study of Ion Losses and Aperture Geometry

Simulations were repeated with voltage amplitude combinations that yielded transmissions well below 100%, while recording final positions for the ions. In these simulations, the ions that did not traverse the entire RFQ system were predominantly being lost at the aperture electrode between the BRFQ and SRFQ.

To illustrate this, an RF amplitude combination that yielded a transmission of 84% was selected and a simulation of 100 ions was performed, recording the final position of ions. This number was chosen for computational cost limitations. All 16 ions that did not arrive at the end of the RFQ system collided with the aperture electrode between the bent and the straight RFQs. This is displayed in Figure 4.11 where the final position of non-transmitted ions is shown.

Because there was only one source of losses in this simulation, it was not considered necessary to increase the number of simulated ions.

Due to all losses being concentrated in the aperture electrode and specifically in the cylindrical hollow section, a redesign of the aperture electrode was made, reducing the cylindrical section so that the chamfered edges of the electrode met at a circular plane. All other dimensions are kept the same. Both the new and old geometries are shown in Figure 4.12.

A new simulation was performed, keeping the same settings as the one shown in Figure 4.10, but with the new aperture electrode geometry implemented. 100 ions were simulated per voltage combination for this large range of voltage amplitudes, to minimise the computational cost of the simulation. This is necessary due to the calculations required to model the ion-gas interaction at every time step. The result, shown in Figure 4.13 confirms the improved behaviour thanks to the redesigned geometry, displaying much less sensitivity to single-step changes in the voltage amplitudes applied to the RF ion guides.

With the new aperture electrode geometry implemented, simulations were performed using argon as a buffer gas and in vacuum, to compare the performance of the RF ion guides with both possible buffer gases and to understand the importance of the gas in the ion transport efficiency. The simulation results of the RF ion guide transmission efficiency in argon and vacuum are shown in Figure 4.14, with 100 ions per voltage combination, and Figure 4.15, with 1000 ions per voltage combination, respectively. The latter case, due to having no buffer gas, could be performed with more ions in a reasonable time.

The lack of buffer gas generates sinusoidal ion trajectories. The coincidence between these trajectories and the aperture between RFQs is dependant on the phase of the sine wave that describes the trajectory. This, in turn, depends on the BRFQ voltage amplitude, and thus generates the peaks and troughs seen vertically in the histogram and its horizontal projection.

After this initial analysis of a broad range of voltage amplitudes for both RFQ guides, simulations of a smaller range but of more ions were performed, to confirm the findings of the previous simulations in a more statistically significant way. 2000 ions were simulated for both helium and argon with the optimal DC voltages shown in Table 4.2, and are shown in Figure 4.16 and Figure 4.17, respectively. The fluctuations seen in the vertical-axis projection for argon in Figure 4.14 are determined to be statistical, as they disappear when a larger number of ions is used.

From these simulations, optimal working voltage amplitudes for each of the buffer gases were determined. The transmission values for 100-ion simulations are considered only approximations due to the small number of simulated ions. Only the simulations with 2000 ions are considered statistically significant. In the case of helium, transmissions consistently above 99% can be reached at SRFQ voltage amplitudes above 40 V and BRFQ voltage amplitudes over 160 V. A maximum is reached at 99.2% for $V_{\text{BRFQ}} = 240$ V and $V_{\text{SRFQ}} = 60$ V.

With argon as a buffer gas, the broad-range simulation results presented in Figure 4.14 show maxima at SRFQ voltages above 100 V. However, due to aiming at having similar operating conditions and for the aforementioned computational cost, the simulations for a higher number of ions were performed for the same range as for helium. This served to verify the 100 ion simulations, from which a maximum transmission of 93% was obtained for $V_{\text{BRFQ}} = 200$ V and $V_{\text{SRFQ}} = 120$ V. Transmissions over 80% are achieved consistently for SRFQ voltage amplitudes above 80 V and BRFQ voltage amplitudes over 100 V and below 360 V.
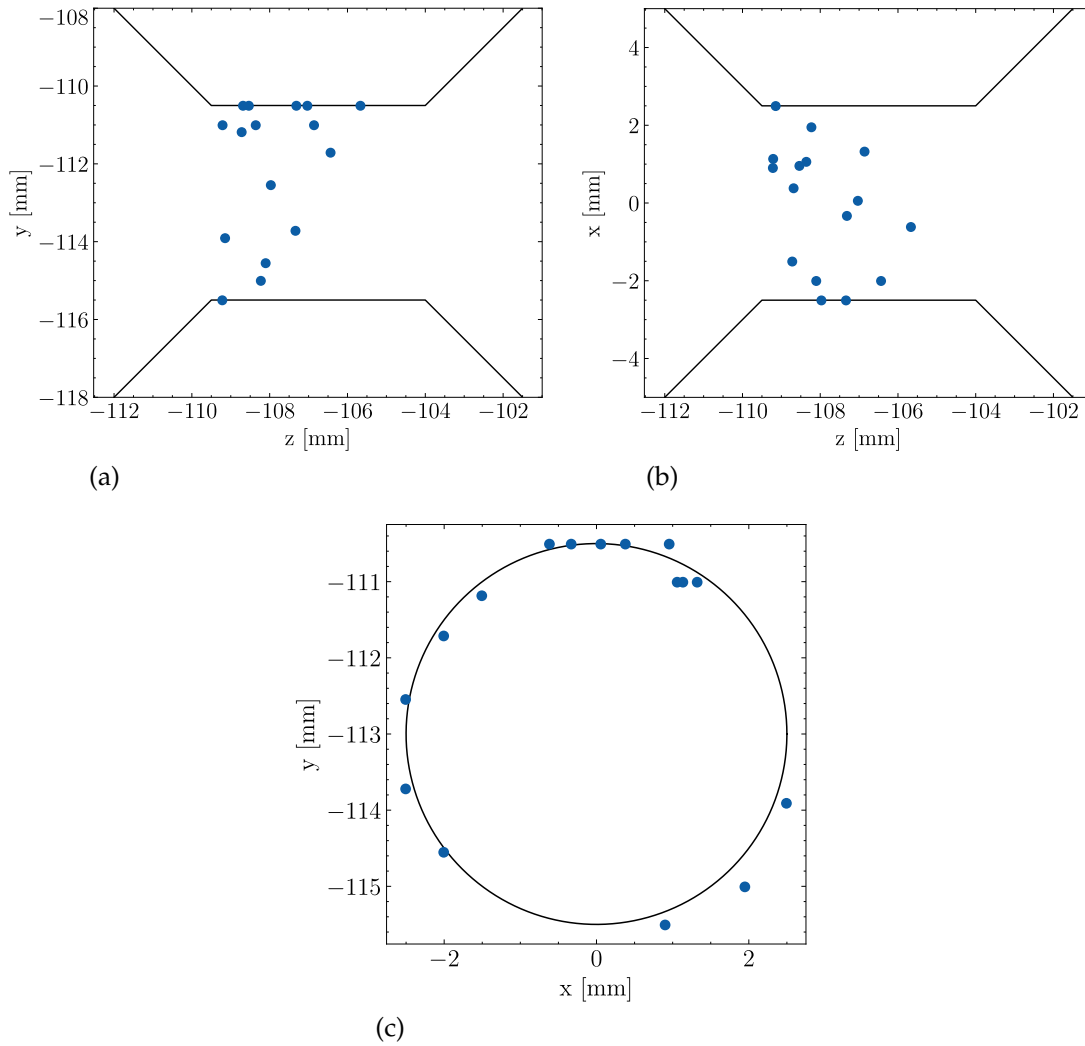
FIGURE 4.11    Final positions of ions that were lost in the aperture electrode between the BRFQ and SRFQ. Cross sections relative to: (a) the *x*-axis, (b) the *y*-axis, and (c) the *z*-axis. The beam travels in the negative *z* direction. The overlaid shapes represent the realistic geometry, but SIMION approximates curves as polygons, hence some of the ions appear to be outside the aperture's edges.
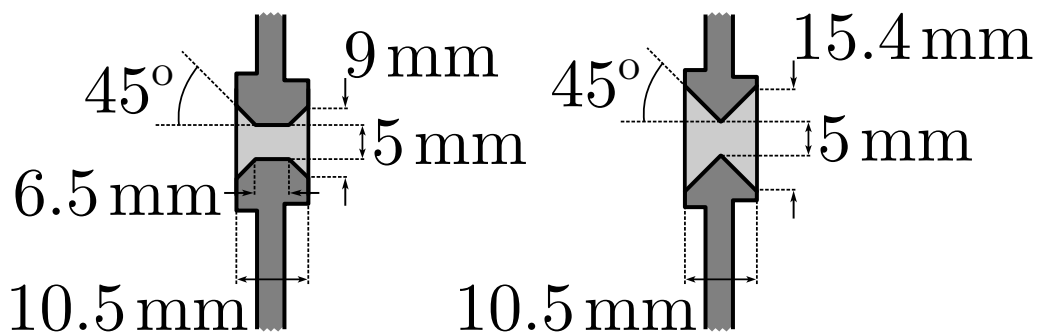


FIGURE 4.12    Redesigned aperture electrode (right) compared to the original design (left).
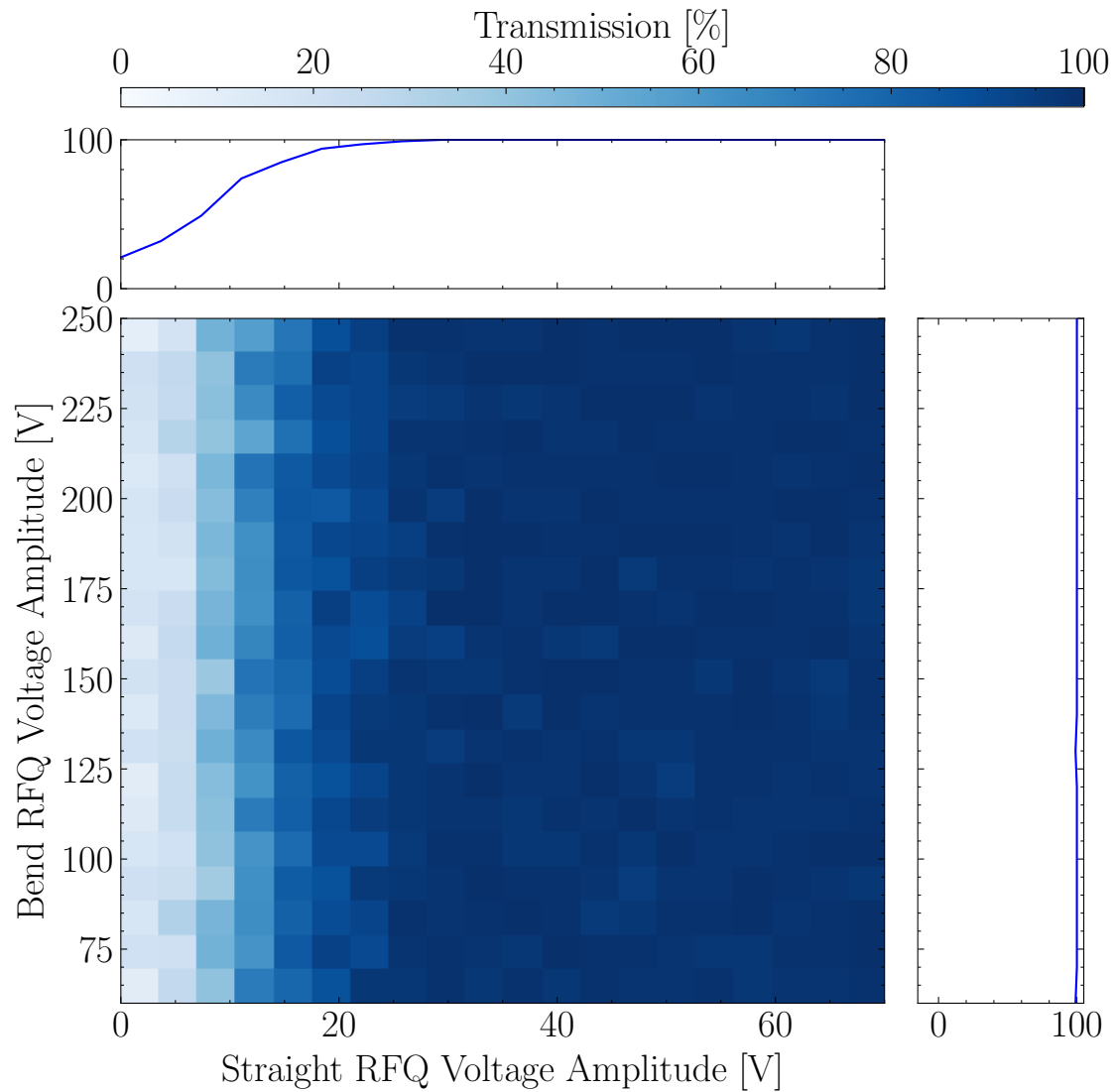
FIGURE 4.13    Results for the SIMION simulations with the new aperture electrode geometry implemented and the optimal DC voltages shown in Table 4.2, using helium as a buffer gas. 100 ions are simulated per voltage combination. A projection for each of the axes is shown.
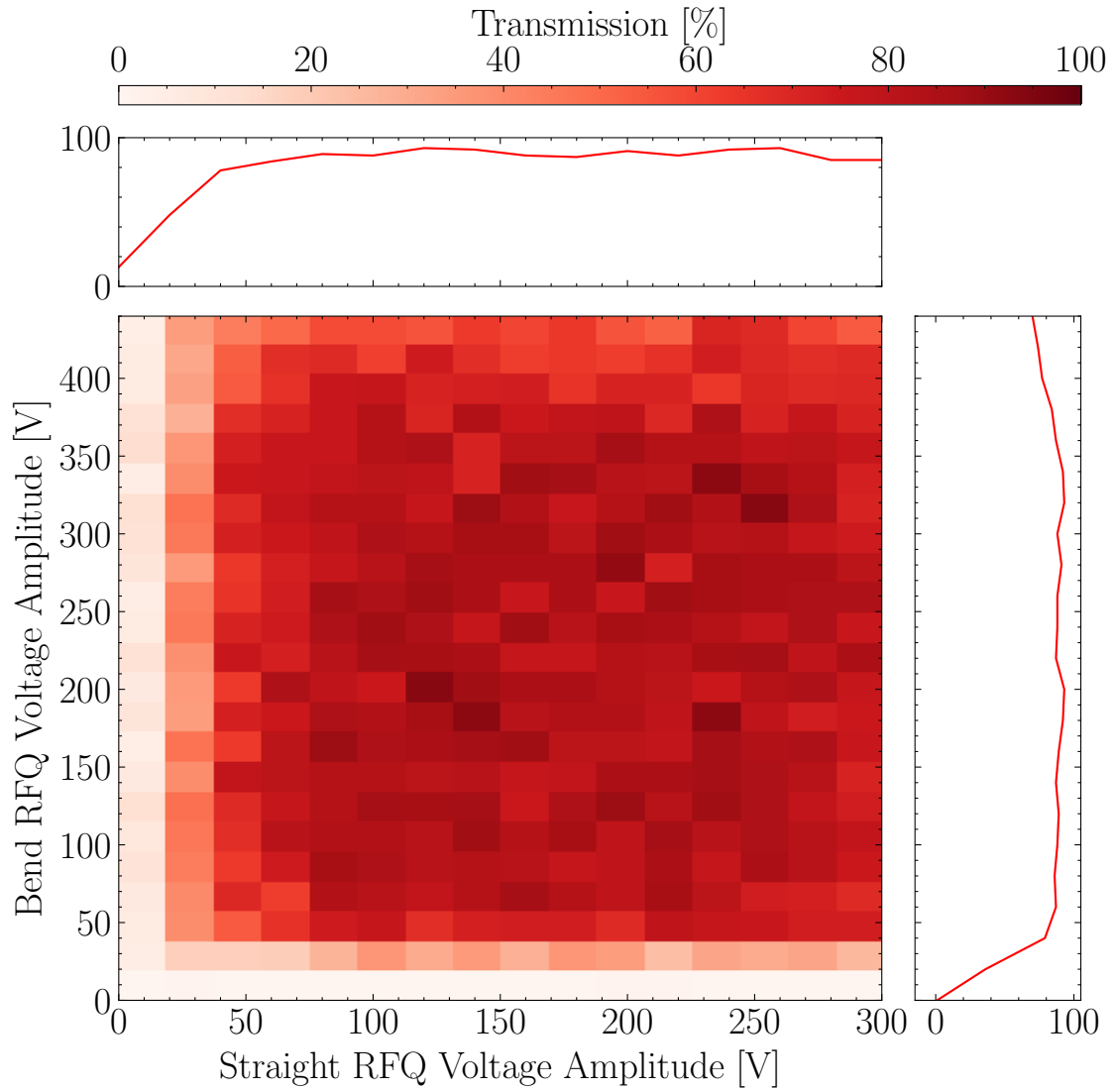
FIGURE 4.14    Results for the SIMION simulations with the new aperture electrode geom-
etry implemented and the optimal DC voltages shown in Table 4.2, using
argon as a buffer gas. 100 ions are simulated per voltage combination. A
projection for each of the axes is shown.
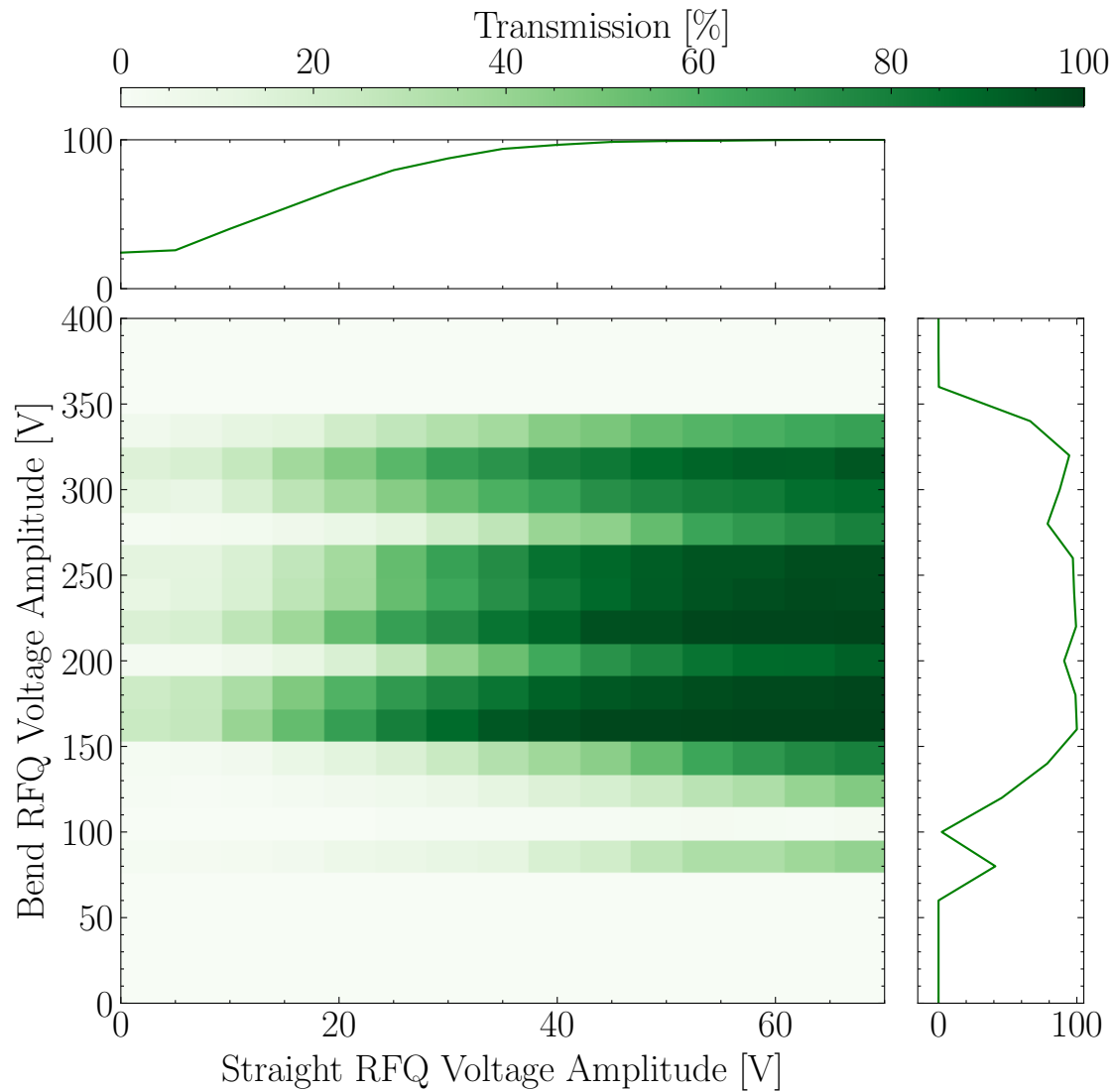
FIGURE 4.15   Results for the SIMION simulations with the new aperture electrode geometry implemented and the optimal DC voltages shown in Table 4.2, using no buffer gas. 1000 ions are simulated per voltage combination. A projection for each of the axes is shown.
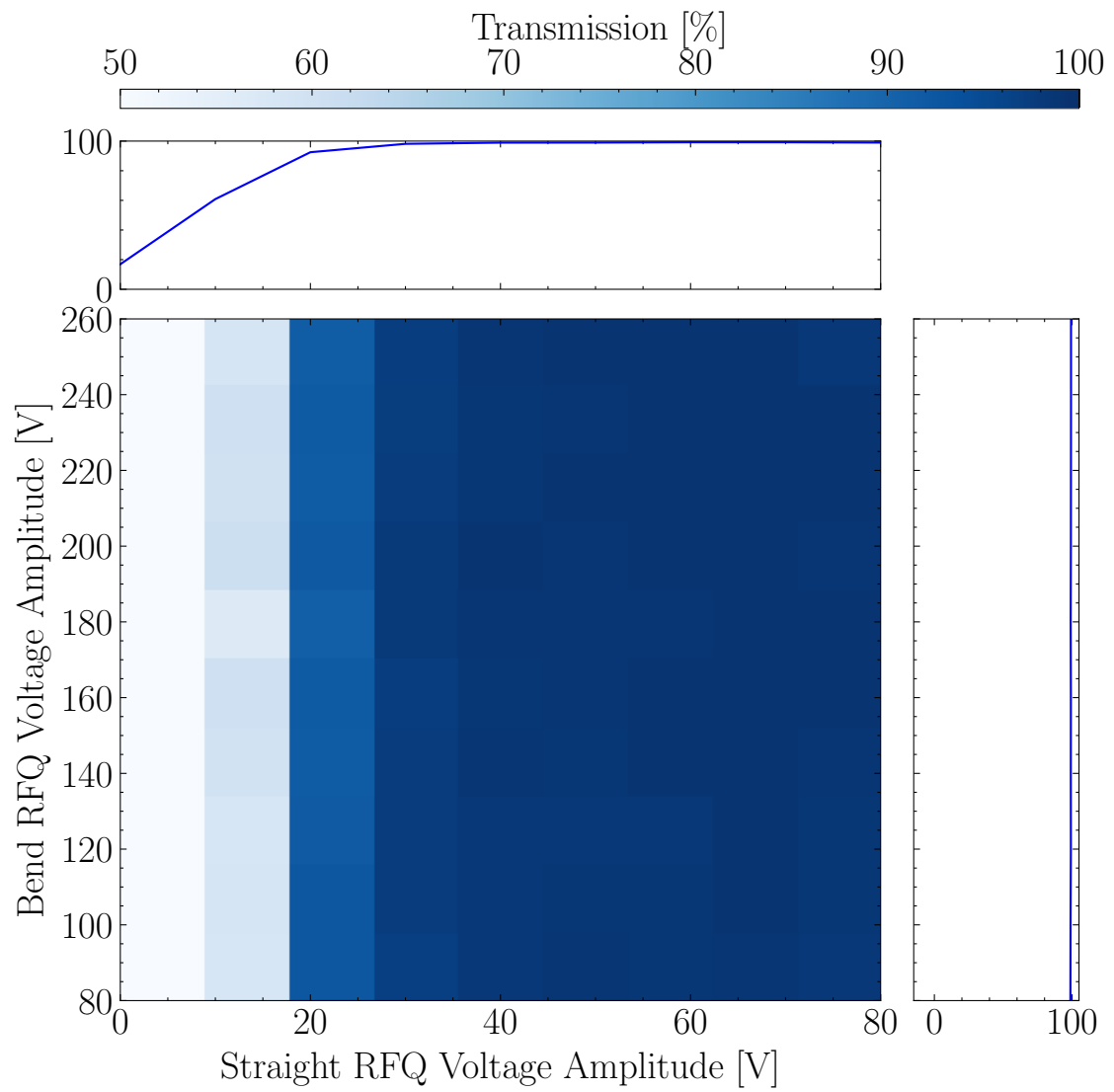
FIGURE 4.16    Results for the SIMION simulations shown in Figure 4.13, with helium as a buffer gas, but for 2000 ions per combination of voltage amplitudes.
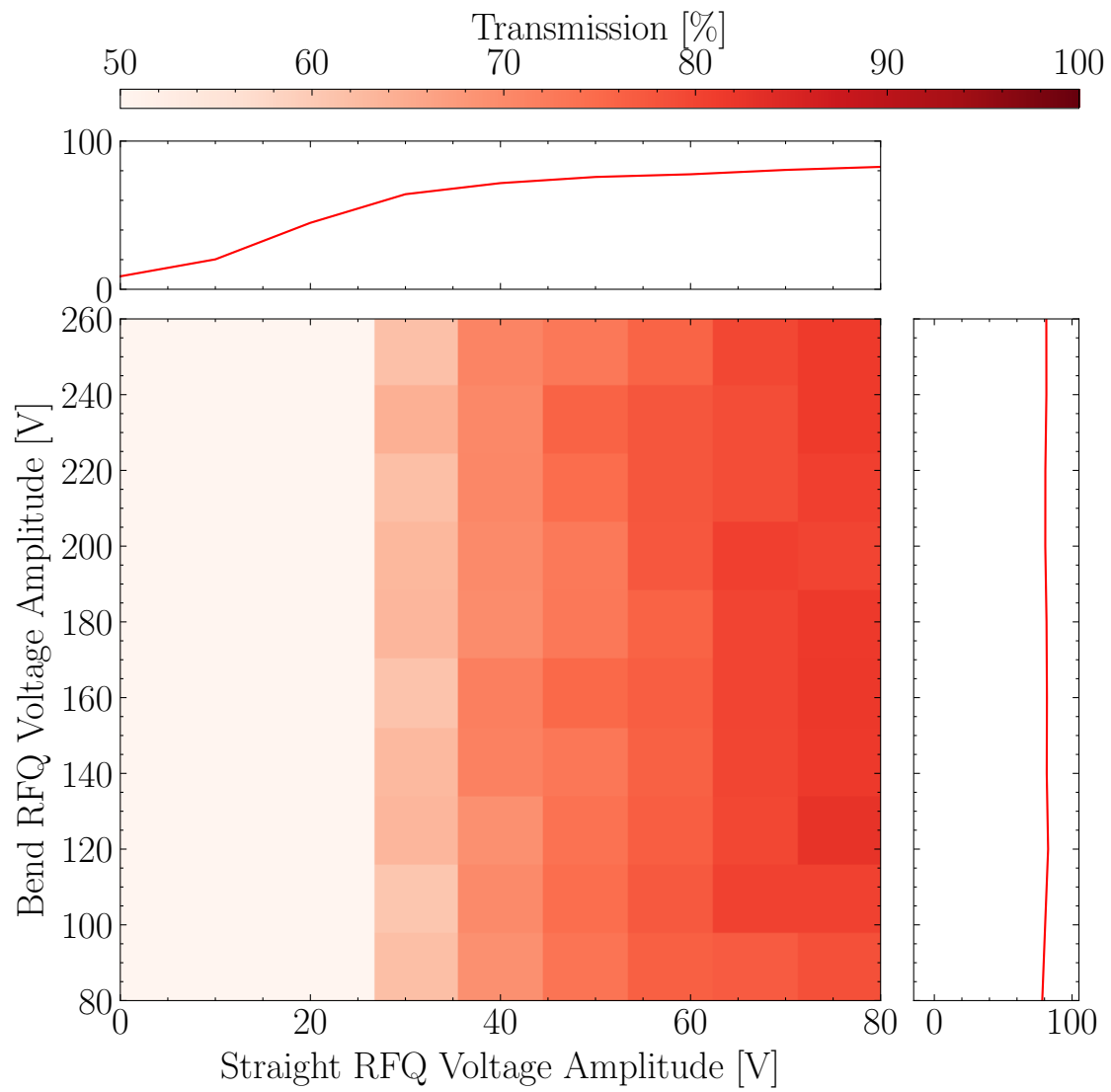
FIGURE 4.17    Results for the SIMION simulations shown in Figure 4.14, with argon as a buffer gas, but for 2000 ions per combination of voltage amplitudes.

## 4.5 Acceleration Optics and Ion Transfer Line

An additional simulation was performed in SIMION with $V_{\text{BRFQ}} = 200\,\text{V}$ and $V_{\text{SRFQ}} = 150\,\text{V}$ in which $50\,000$ $^{94}$Ag ions were generated at $0.96\,\text{eV}$ kinetic energy and their position, velocity and energy recorded after passing through the RFQ guide system. A 99% transmission efficiency through the primary transport system was obtained for this simulation.

The positions, energies and directions of the surviving $49\,440$ ions was inputted into PIOL [176], a collection of tools for beamline modelling. PIOL was chosen as a tool for this section of the transport system for its simplicity and lower computational cost when compared with SIMION. This choice is possible due to the lack of alternating fields in the ion transfer line.

With PIOL, a beamline can be described in a $(x, y, s)$ curvilinear coordinate system, upon which the different ion-optical elements can be defined. In this coordinate system $s$ represents the propagating axis, following the same path as the ions through the beamline. The $(x, y)$ plane is perpendicular to $s$, with $x$ referring to the horizontal transverse direction and $y$ to the vertical one.

Ion-optical transfer matrices are imported from GICOSY [189], where they are calculated individually for every optical element in the beamline. PIOL then uses these matrices to calculate the final coordinates of ions given their initial conditions. Beam transport optimisation can be performed via the minimisation of a user-input function with the SciPy package [190] by tuning beamline element voltages.

An optimisation of voltages was performed using a PIOL simulation for the acceleration optics: an Einzel lens and a ground electrode that are positioned directly downstream of the extraction electrode. The ground electrode is kept at $0\,\text{V}$, in contrast to the high voltage ($30\,\text{kV}$) environment in which the primary transport system is kept. This accelerates the ions to $30\,\text{keV}$. The Einzel lens, consisting of three electrodes, is used to shape the beam before acceleration, to minimise beam dispersion without changing the beam energy. A parallel beam was produced by the Einzel lens by keeping the first and last electrodes at $0\,\text{V}$, and setting the middle electrode to $18\,\text{kV}$. The beam shape with these voltages can be seen in Figure 4.18.

The characteristics of the accelerated parallel beam that emerges from the acceleration optics are recorded and serve as the initial point in a subsequent simulation of the ion transfer line.

SRFQ                                      Einzel Lens                 Ground Electrode
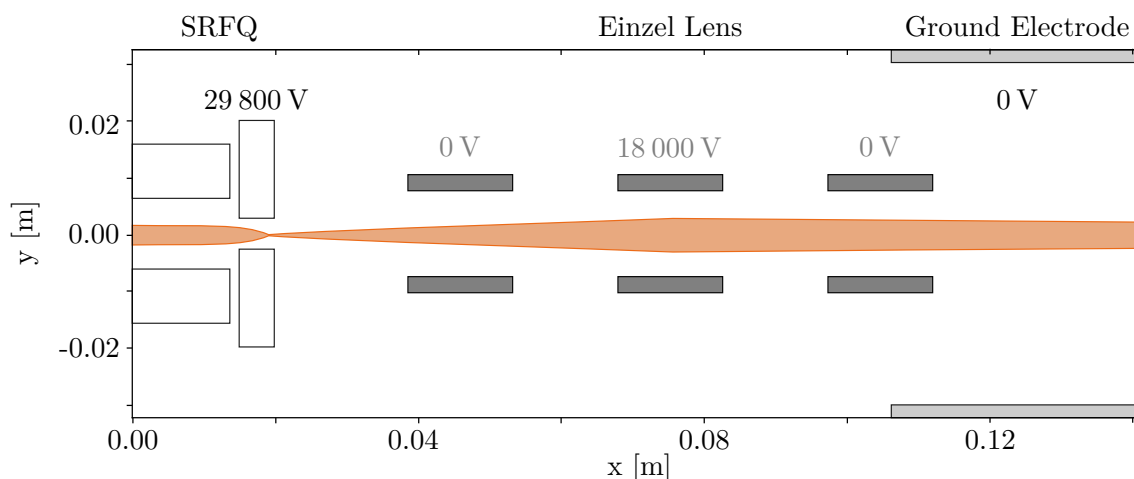
**FIGURE 4.18**     Beam profile (orange) through the Einzel lens (dark grey) and ground electrode (light grey), after exiting the SRFQ (white). Voltages calculated with a PIOL optimisation are shown in grey; predetermined voltages are shown in black.

For the MARA-LEB ion transfer line, the following components were defined: a set of mass slits, the three quadrupole triplets (one of which is pictured in Figure 4.19), the quadrupole doublet, the dipole magnet and the electrostatic deflector.

The ion transfer line also includes 3 XY-steerers, one of which is shown in Figure 4.20. These serve for beam correction accounting for imperfections in the alignment of the beamline. Because of this, the XY-steerers were not included in simulations, as the beamline misalignment they would have to correct for cannot be predicted. Their working voltages will be determined *ad hoc* during comissioning, testing and experiments.

The position of the simulated components in the PIOL coordinate system is shown in Figure 4.21.

The electrostatic deflector voltage and dipole magnet field were set to 1250 V and 0.2 T, respectively, as these are the values for which $^{94}$Ag ions at 30 kV are deflected by 90°. The optimal voltages for the quadrupole multiplets given these simulated conditions were calculated and shown in Figure 4.22. This optimisation takes into account the maximisation of ion transmission, but also considers the beam shape at different positions, such as requiring a focal point at the end, or at the mass slit position. From past simulation work, presented in [173], the mass resolving power at the focal point where the mass slits are positioned is estimated at 350. The voltages for each of the multiplet electrodes are shown in Table 4.3.

The positions of the 49 440 ions that were transmitted into the system from the RFQ guides are shown in Figs. 4.23 and 4.24. The former is a plot of the beam envelope containing 95% of the ions, showcasing the shape of the beam in both transverse planes. The latter shows a histogram of the beam, displaying the number of ions at regular intervals in the ion transfer line with all electrodes at their optimal voltage. The absolute transmission as a function of $s$ is shown in Figure 4.25. This is the percentage of particles arriving at each $s$ position out of the 50 000 simulated ions, taking the losses in the primary transport system into account. An overall transmission of 94.5% is achieved for the ion transport system as a whole.

The obtained ion survival rate through the ion transport system is expected to be higher than in real experimental conditions due to factors such as oscillations in the electronic equipment, variable conditions in experiments and effects from contaminants, among others. The high transmission in simulations, nevertheless, is a positive result, as even with lowered figures due to the aforementioned potential effects, the ion transport system will not be a major source of losses in the MARA-LEB beamline.
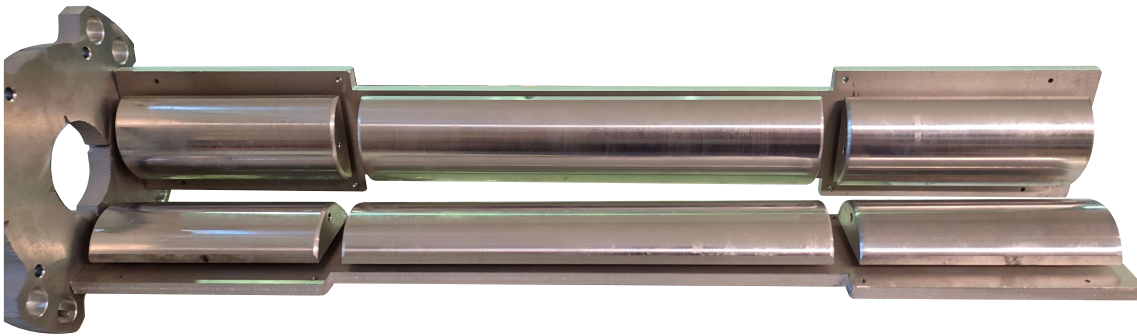


FIGURE 4.19   Picture of the quadrupole triplet and one of its end plates, showing half of the electrodes. The complete triplet is composed of two mirrored ensembles. The quadrupole doublet is similar to this, but with the middle set of electrodes missing.
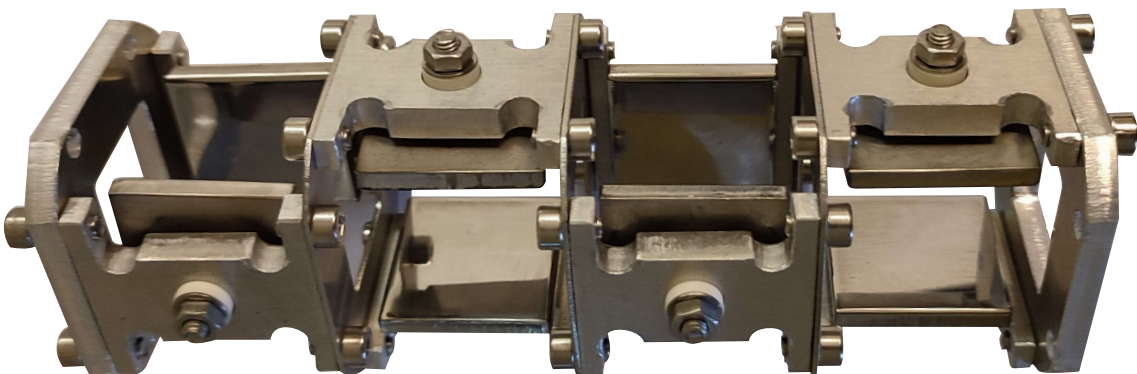


FIGURE 4.20   Picture of one of the XY-steerers. Two pairs of electrodes steer the beam in each axis, arranged in a staggered configuration.
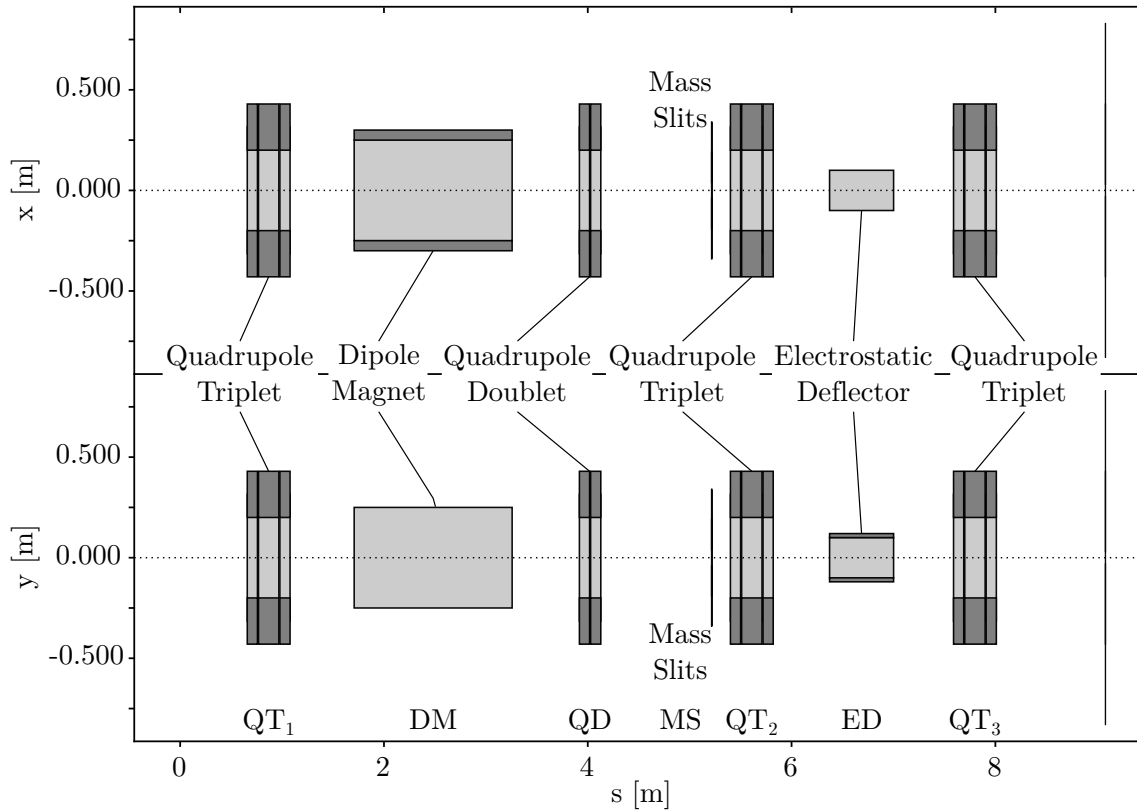
FIGURE 4.21  Labelled components of the MARA-LEB ion transfer line that were defined for PIOL simulations. Abbreviations for the components are also introduced, and will be used in subsequent figures. A slice along the $(s, x)$ plane is shown on the top, and a slice along the $(s, y)$ plane is shown on the bottom. The darker shade of grey indicates the electric or magnetic poles of the components. The dotted lines represent the $s$ axis.

TABLE 4.3    Optimal voltages for the quadrupole multiplets, with $QT_i$ representing the $i$-th triplet and QD representing the quadrupole doublet. $V_i$ is the voltage for the $i$-th electrode in the multiplet.

|  | $QT_1$ | QD | $QT_2$ | $QT_3$ |
|---|---|---|---|---|
| $V_1$ [V] | 477 | 433 | 581 | -389 |
| $V_2$ [V] | -253 | -403 | -510 | 414 |
| $V_3$ [V] | 134 |  | 395 | -495 |
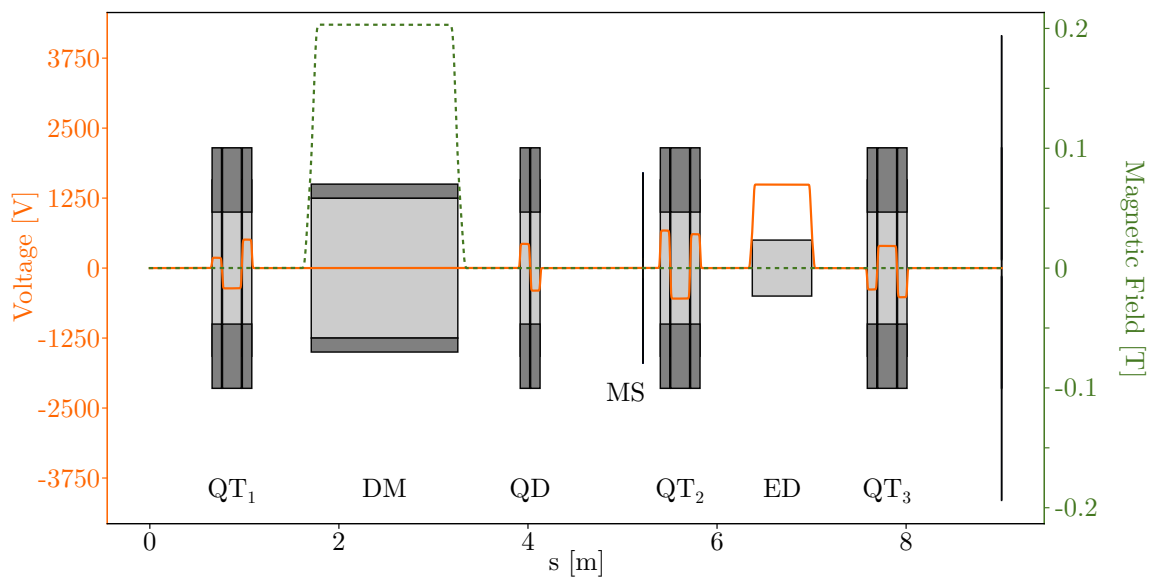


FIGURE 4.22    Optimal voltages (solid orange line) and magnetic fields (dashed green line) for the ion transport system. Values for the quadrupole multiplets are outlined in Table 4.3. See Figure 4.21 for clarification on component labels.
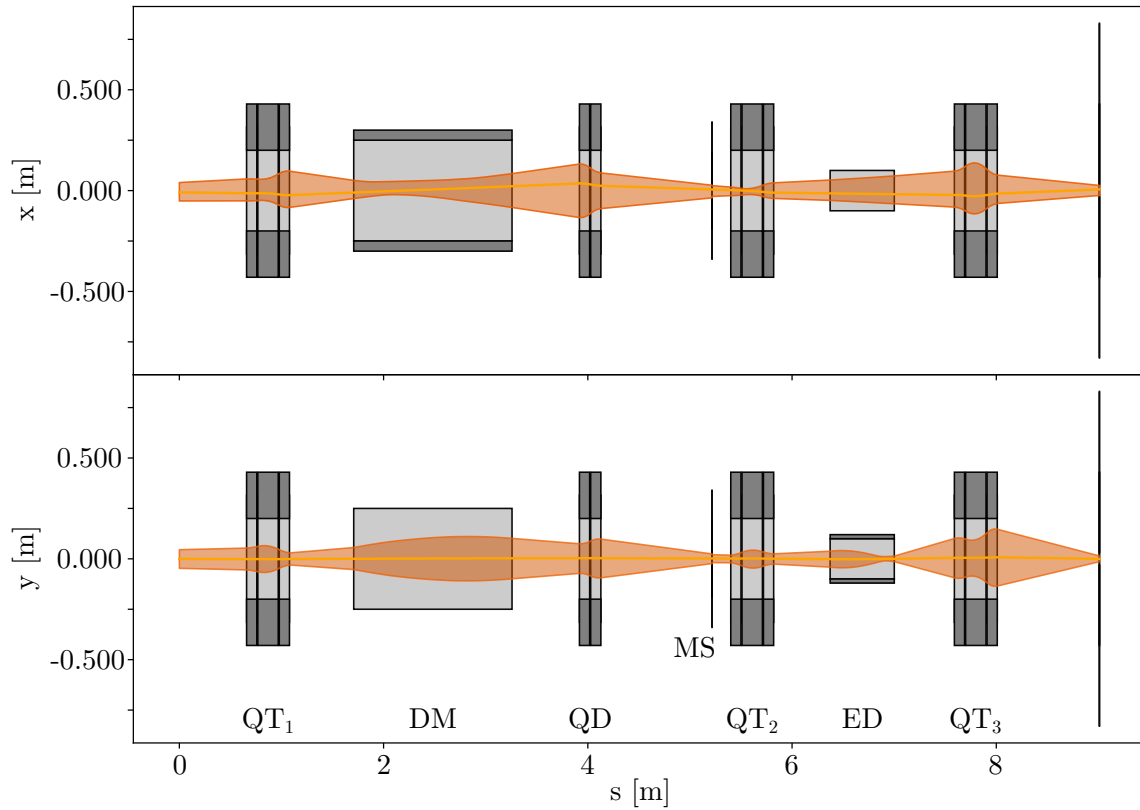
FIGURE 4.23   Beam envelope containing 95% of the ions in the beam in the PIOL coordinate system. See Figure 4.21 for clarification on component labels.
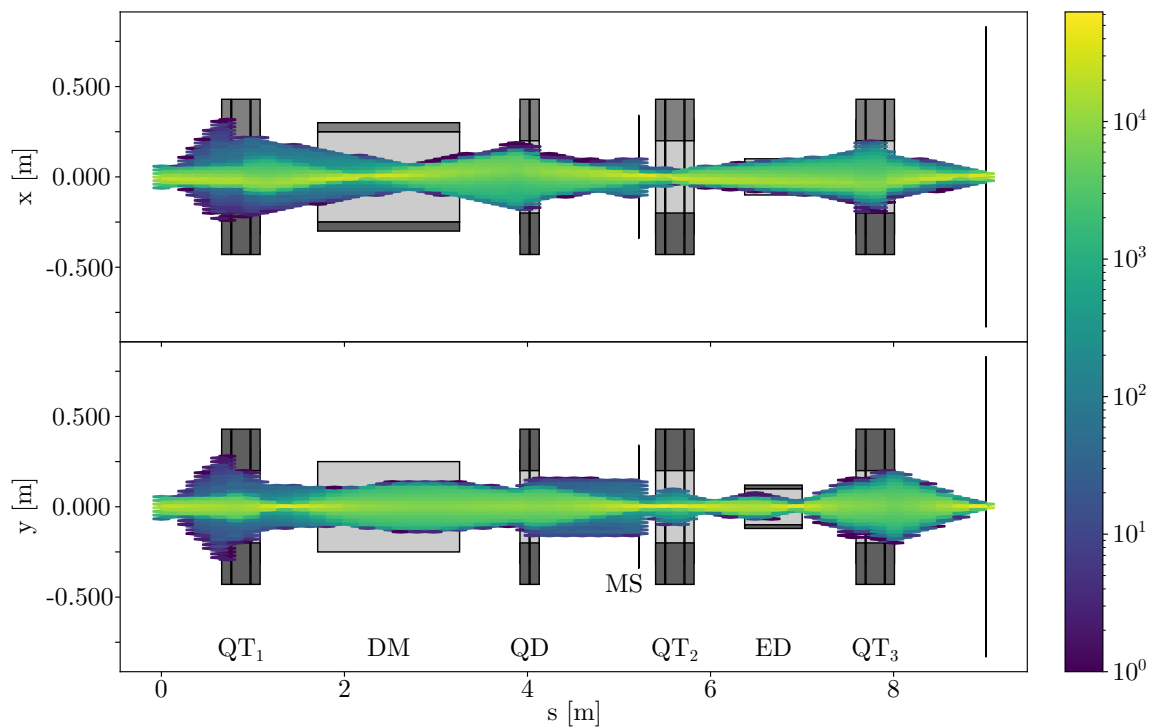


FIGURE 4.24   Histogram showing the number of particles in the beam at different positions in the PIOL coordintate system. See Figure 4.21 for clarification on component labels.
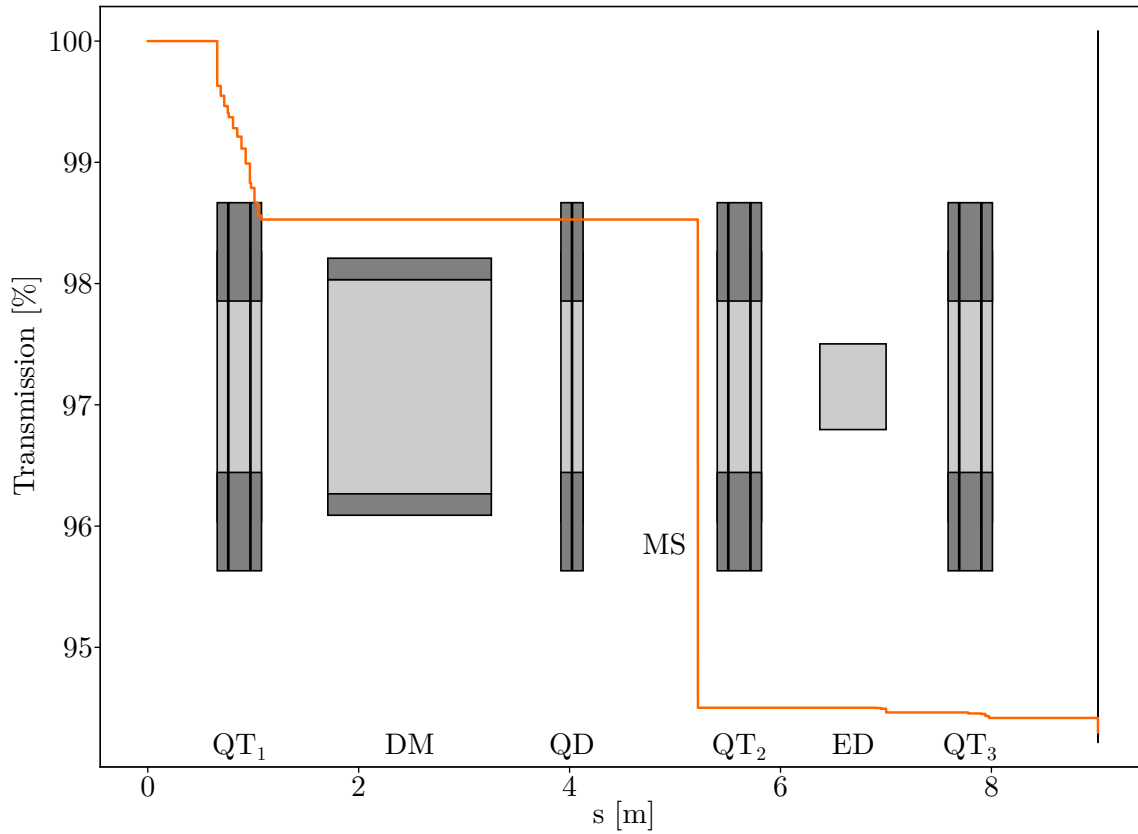
FIGURE 4.25   Absolute transmission in the $s$ coordinate of the 50 000 ions in the combined SIMION-PIOL simulation of the entire ion transport system. The pronounced drop that occurs at $s \approx 5\,\mathrm{m}$ is due to the presence of mass slits. See Figure 4.21 for clarification on component labels.

# Part III

# Testing and Experiments

# 5 IN-GAS-CELL LASER IONISATION OF STABLE TIN

As part of the commissioning of the gas cell for the MARA-LEB facility, two off-line experiments were performed at the IGISOL facility, using the FURIOS laser ion source. The objective of the experiments was to perform in-gas-cell laser ionisation of tin, as a proof of concept for one of the main scientific objectives of MARA-LEB: laser spectroscopy of proton-rich tin isotopes. The experimental setup and associated results are presented in this chapter. An article on the commissioning of the MARA-LEB gas cell was published, which features a portion of the findings presented in this chapter [160].

The experiments performed using the MARA-LEB gas cell and their results are also compared to similar tests of the $S^3$-LEB gas cell at the Leuven Isotope Separator On-Line (LISOL) [191] facility in Belgium, and the GANIL Ion Source using Electron Laser Excitation (GISELE) [192] laboratory at GANIL.

## 5.1 Experimental Setup

The MARA-LEB gas cell was mounted in the IGISOL target chamber, with a variable supply of high-purity argon gas, provided by use of the getter purifier, as explained in Section 3.1. Lasers from FURIOS are directed into the target chamber through bespoke laser ports which transmit the wavelengths of light used in these experiments. The lasers enter the gas cell through the viewport opposite the gas cell nozzle in a collinear configuration with the atom extraction, spanning the length of the ionisation volume.

Within the gas cell, a bronze (91% copper and 9% tin by mass) filament was installed on the testing flange and resistively heated. This generates an atomic vapour of tin, which is transported by the argon buffer gas into the ionisation volume, where it can be resonantly ionised by the lasers.

The ions were extracted from the gas cell via gas flow and entered a Sextupole Ion Guide (SPIG) [193], a sextupolar analogue to the RFQ guides used in MARA-LEB. The ions are guided towards extraction electrodes and are accelerated to 30 keV. Ions were transported through the first portion of the IGISOL beamline, where two detector stations were placed. A diagram of this setup utilising the IGISOL beamline can be seen in Figure 5.1. Detector station 1 consisted of a planar silicon detector and was placed before the IGISOL dipole magnet. The mass resolving power of the IGISOL 55°-bent dipole magnet has been estimated to be between 300 and 500. Detector station 2 was installed after the dipole magnet, to detect mass-separated ions. It consisted of both a planar silicon detector and a microchannel plate (MCP) detector. The two-point setup can be used to determine the losses due to mass separation, and also the contaminant species at different mass-to-charge ratios in the beam.
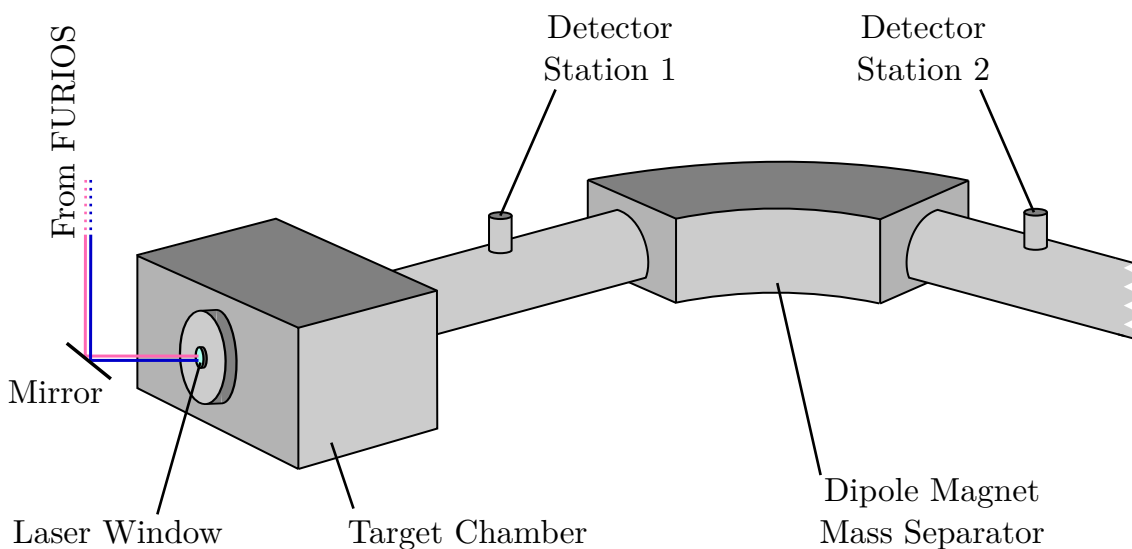


FIGURE 5.1    Part of the IGISOL beamline used for the MARA-LEB gas cell laser tests. The gas cell was housed within the target chamber. The dipole magnet for mass separation and detector stations are marked, alongside a depiction of FURIOS lasers being directed into the target chamber via a mirror. Parts are not to scale.

### 5.1.1 Laser Setup

Resonant laser ionisation of the vapourised tin atoms is achieved in two steps. The first step excites tin atoms from their ground state $5s^2 5p^2\ ^3P_0$ (J=0) to the intermediate level $5p6s\,^1P_1$ (J=1). The atoms are then further excited into an autoionising state above the ionisation potential corresponding to the 5p7f configuration, as shown in Figure 5.2.
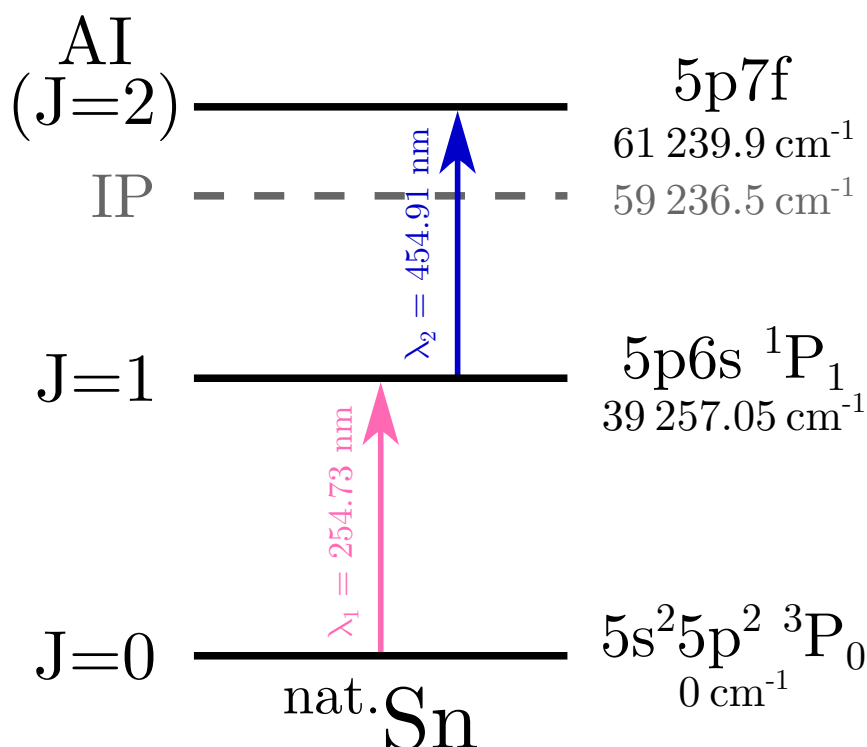


FIGURE 5.2   Two-step laser ionisation scheme for natural tin, adapted from [160].

Some of the lasers used for these tests are Ti:sa resonators pumped by 10-kHz repetition rate Nd:YAG lasers, as described in Section 2.2.1. To pump the Ti:sa cavities is a Lee Laser LDP-200 pump laser is used, providing 10–25 W of 532 nm laser light.

The laser configuration of the two experiments was slightly different. However, since the same ionisation scheme is used, the same wavelength of $\lambda_1 = 254.73$ nm (in vacuum) is required for the first step.

In the first experiment, performed in February 2020, this was achieved by a broadband Ti:sa cavity laser. In the second experiment, an injection-locked Ti:sa cavity with a typical linewidth of 20 MHz in the fundamental. This laser is seeded with a continuous-wave Matisse Ti:sa laser, in a configuration discussed in [194].

The fundamental light generated from this cavity is externally frequency tripled to reach the wavelength required for the first step.

In both experiments, the second step of the ionisation is performed by a frequency-doubled Ti:sa broadband laser, used to produce a $\lambda_2 = 454.91$ nm beam of laser light.

Information of the saturation of the laser power can be obtained by monitoring the count rate of $^{120}$Sn, the most abundant isotope of tin, at the MCP in detector station 2 as a function of laser power. A saturation profile fit (Equation 5.1) can be performed on these data, from which a saturation power, $P_s$, can be extracted:

$$I(P) = I_0 + A\frac{P/P_s}{1 + P/P_s},$$
(5.1)

where $I(P)$ is the count rate in terms of $P$, the laser power; $A$ is a constant and $I_0$ is an offset parameter to account for non-resonant photoionisation.

Scans in laser power for both steps were performed at the beginning of each experiment, with power being measured at the optical table in the FURIOS laboratory. The optical path from the optical table to the IGISOL target chamber is roughly 10 m, which results in an energy loss of approximately 50% for both steps.

A scan of the first step in the February 2020 tests, with a saturation profile fit, is shown in Figure 5.3. The saturation power extracted from this fit is $P_s = 5$ mW. For the second step, the maximum available power of 400 mW was required. A power scan was therefore not performed, as this value was comfortably below saturation.

For the September 2021 tests, power scans of both steps were taken and fitted with a saturation profile; they are shown in Figure 5.4. The obtained saturation powers obtained for the first and second step are 83 mW and 411 mW, respectively. In different experimental conditions, these laser powers would differ. Usually, intensity, rather than power, is used to quantify saturation. However, in these experiments, difficulties measuring the spot size were encountered. In experimental conditions where spot sizes are different, the saturation power would not be the same.

In both experiments, lasers are set to a fraction of their saturation power in order to minimise the effect of power broadening. In the February 2020 experiment, the powers were lowered to ∼1 mW and 300 mW for the first- and second-step lasers, respectively. The lower powers used for the September 2021 experiment were 21 mW and 97 mW, respectively, for the first and second steps. Frequency scans were then attempted for each of the ionisation steps while the dipole magnet settings were set on mass-over-charge ratio 120, to select for $^{120}$Sn$^+$ ions.

In the first experiment, mode hopping of the broadband first step laser hampered data collection, allowing only for the second step to be scanned. This issue was resolved by injection-locking before the second experiment, thus allowing data to be collected for both steps in this experiment. Scans were performed for a set range of frequencies around $c/\lambda_i$ (with $i$ being the resonant ionisation step) for various argon pressures in order to study the effect of the gas cell pressure on the spectral linewidths and centroids. This was performed for each step individually while keeping the other step at the resonant frequency. The data published in [160] only includes the findings from the February 2020 experiment, while this thesis will include results from both experiments.
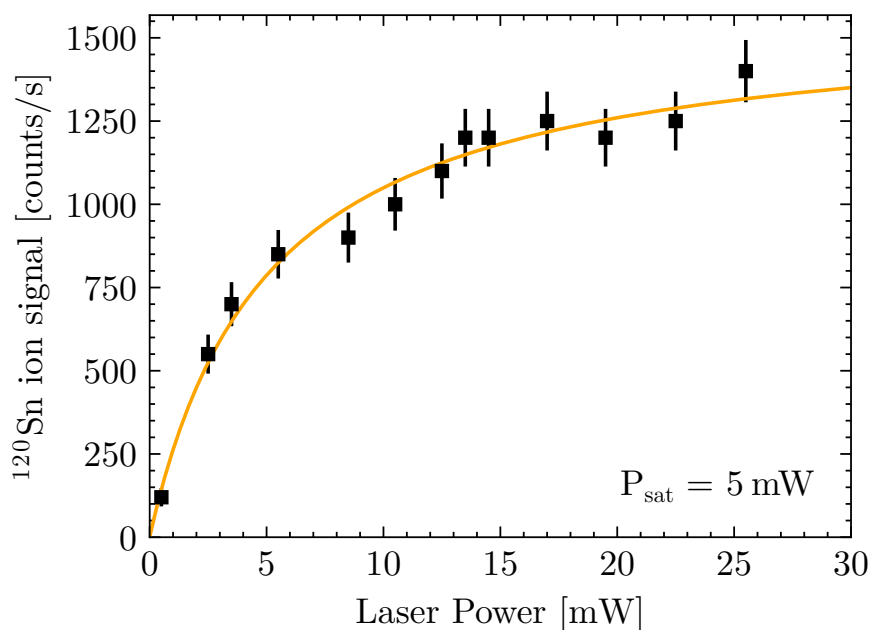


FIGURE 5.3   Saturation scans of the first step laser from the February 2020 laser tests with saturation curve fits.
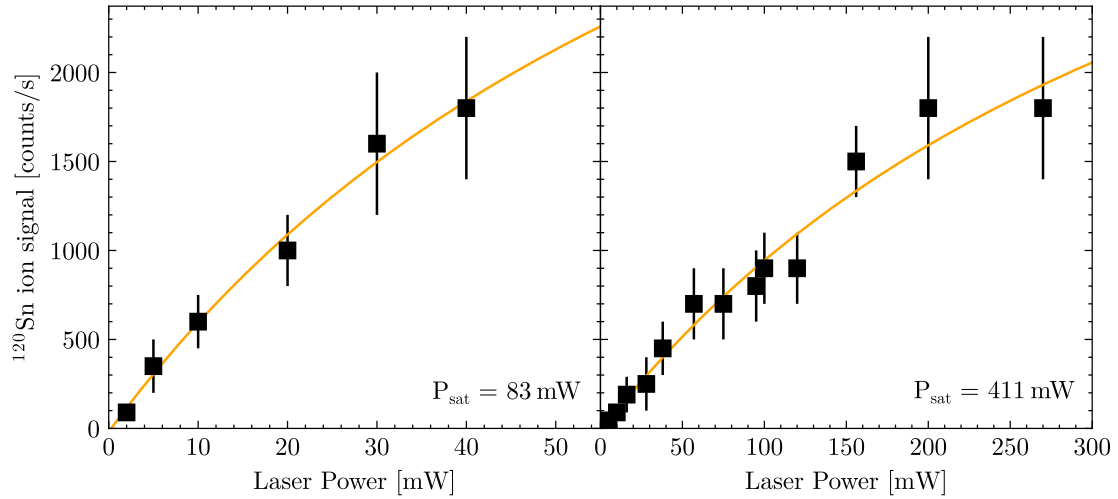
FIGURE 5.4    Saturation scans of the first (left) and second (right) step lasers from the September 2021 laser tests with saturation curve fits.

## 5.2   Analysis

For resonant laser ionisation in a gas environment, several effects contribute to the atomic resonance broadening. On the one hand, the broadening due to the Doppler effect causes a Gaussian broadening of the resonance. This effect arises due to the atoms in the gas having a distribution of velocities when transported by the buffer gas, thus being subjected to a corresponding distribution of frequencies in their frame of reference. On the other hand, collisions between the tin and argon atoms introduce a homogeneous Lorentzian-profile broadening. Additionally, due to the laser geometry used in these experiments, there was a large region of laser overlap throughout the ionisation volume of the gas cell and also the free gas jet produced by the nozzle. This translates into a strong asymmetry in the collected data, resulting from lasers ionising atoms in very diverse gas conditions, especially due to many gas velocities being probed, from sub- to supersonic. This is accentuated in particular in the region close to the gas cell nozzle, where gas densities and velocities change drastically as the gas Mach number changes leading to the gas jet.

To account for all of these various effects, an asymmetric Voigt profile is used to fit the frequency scans. This is a convolution of a Cauchy-Lorentz distribution and a Gaussian distribution, with an additional asymmetry parameter, shown in Equation 5.2:

$$V_a(x; A, \mu, \sigma, \gamma, s) = \left\{ 1 + \mathrm{erf} \left[ \frac{s(x - \mu)}{\sigma \sqrt{2}} \right] \right\} V(x; A, \mu, \sigma, \gamma), \qquad (5.2)$$

where $s$ is a skew parameter, quantifying the asymmetry of the distribution, $A$ is the amplitude of the Voigt profile, $V(x)$, $\mu$ is the centroid of the distribution and $\sigma$ and $\gamma$ are the width parameters of the Gaussian and Lorentzian components, respectively. The symmetric Voigt profile $V(x)$, in turn, is shown in Equation 5.3:

$$
\begin{aligned}
V(x; A, \mu, \sigma, \gamma) &= A \frac{\mathfrak{Re}\{w(z)\}}{\sigma\sqrt{2\pi}}, \\
w(z) &= e^{-z^2}\mathrm{erfc}(-iz), \\
z &= \frac{x - \mu + i\gamma}{\sigma\sqrt{2}},
\end{aligned}
\tag{5.3}
$$

where $\mathfrak{Re}\{z\}$ denotes the real part of the complex number $z$ and erf(z) and erfc(z) are the error function and the complementary error function, respectively, defined in Equation 5.4:

$$
\mathrm{erfc}(z) = 1 - \mathrm{erf}(z) = 1 - \frac{2}{\sqrt{\pi}} \int_0^z e^{-t^2} \mathrm{d}t.
\tag{5.4}
$$

The fitting of $V_a(x)$ to the data was performed with the use of the LMFIT optimisation and data-fitting package in Python [195]. Asymmetric Voigt fits were performed to the raw data from frequency scans, which were collected in non-uniform steps. Selected examples of good and poor fits are shown in Figure 5.5.

Due to the lack of uniformity in the frequency scans and some fitting difficulties, rebinning of the data was carried out. Poor fitting of the data to Voigt profiles is evident in Figure 5.5, especially in the top left fit, where the fit converges with parameters that generate a shape that does not reproduce the peak well. This also happens, to a lesser extent, for all the fits presented in this figure. The most likely explanation for this is the higher density of points away from the peak skewing the fit parameters. Rebinning can help mitigate this effect.

It is also worth noting that some of the examples shown in Figure 5.5 exhibit what could be seen as a second peak structure. This is most notable on the bottom left subfigure, showing the second laser step scan at 120 mbar gas pressure from the September 2021 experiment. A second peak is not expected from the resonant laser ionisation scheme; the effect is attributed to the sudden but momentary change of laser cavity resonator mode. This phenomenon is known as mode hopping.

Mode hopping disturbs the control and data acquisition systems, causing an inaccurate frequency reading. It is impossible to eliminate this effect from the existing data, but the second, smaller peak should not be considered when fitting. New measurements with a more stable setup are required to preclude this effect.

When the data is rebinned, more counts are achieved per bin, therefore achieving a more statistically significant fit. Data was re-binned into different numbers of bins while fitting with the same asymmetric Voigt function. Fit parameters were studied, varying the bin number until fit parameters were not affected by the change in number of bins. A range of bin numbers was obtained for which the fit parameters were identical, ensuring that the binning was not a major factor in the determination of these parameters. A number of bins in the centre of this range was chosen, resulting in an optimal binning of 13 bins for the February 2020 experiment, corresponding to bins of $\sim$21 GHz in width, and 30 bins for the September 2021 data, corresponding to bins of $\sim$1.7 GHz in width. The same selection of examples from Figure 5.5 is shown in Figure 5.6, but with the optimal binning for the data. Asymmetric Voigt fits of these histograms are also shown.

Through mere visual inspection, it can be seen that the fits are a better match with the re-binned data than with the raw experimental points. This is confirmed by the reduced chi-squared ($\chi^2$) statistic, shown on all subfigures in Figures 5.5 and 5.6. For the same data, binning reduces the $\chi^2$ by a factor $\sim$2 or higher. While results from both the raw and re-binned data is presented in this work, the lower $\chi^2$ values for the latter give strength to the idea that these data should be re-binned for a better statistical analysis and fitting.

Two parameters obtained from the asymmetric Voigt fits are of importance in this analysis: the centroid frequency of the fit and its full width at half maximum (FWHM). The centroid frequency is extracted directly as the $\mu$ parameter in Equation 5.2, whereas the FWHM of the fit has to be calculated from the $\gamma$ and $\sigma$ parameters by the use of an approximation, shown in Equation 5.5, which is accurate to 0.02% [196].

$$\text{FWHM} = 1.0692\,\gamma + \sqrt{0.8664\,\gamma^2 + 5.545083\,\sigma^2}. \tag{5.5}$$
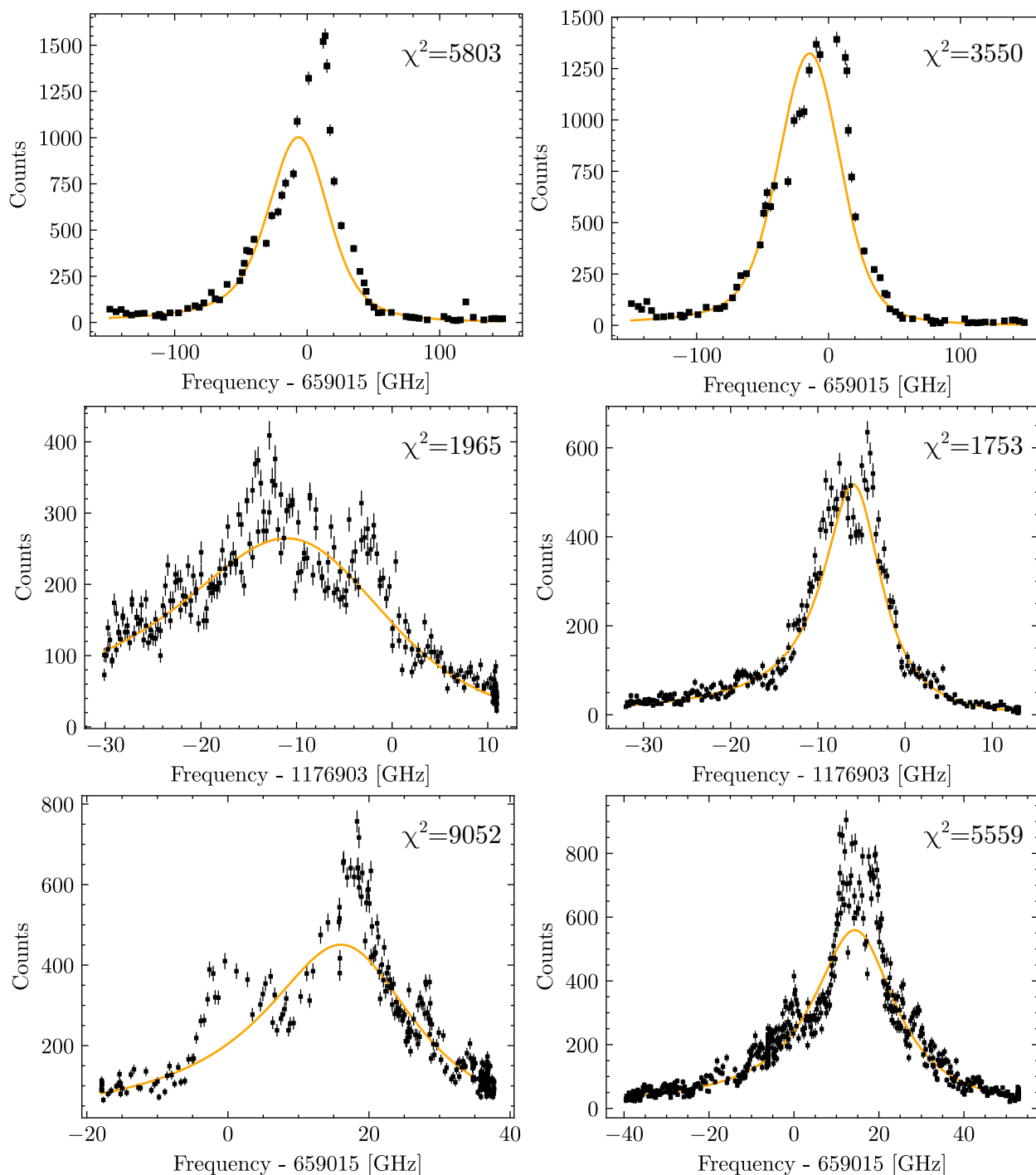
FIGURE 5.5 Examples of Voigt fits (orange) to raw experimental points (black) from the second step in the February 2020 experiment at 97 mbar and 170 mbar (top row left and right, respectively), and the first step at 200 mbar and 50 mbar (middle row left and right, respectively), and second step at 120 mbar and 100 mbar (bottom row left and right, respectively) in the September 2021 experiment. The examples on the left depict poor agreement between fit and data, while those on the right depict better fits, as evidenced by the $\chi^2$ values shown on each plot.
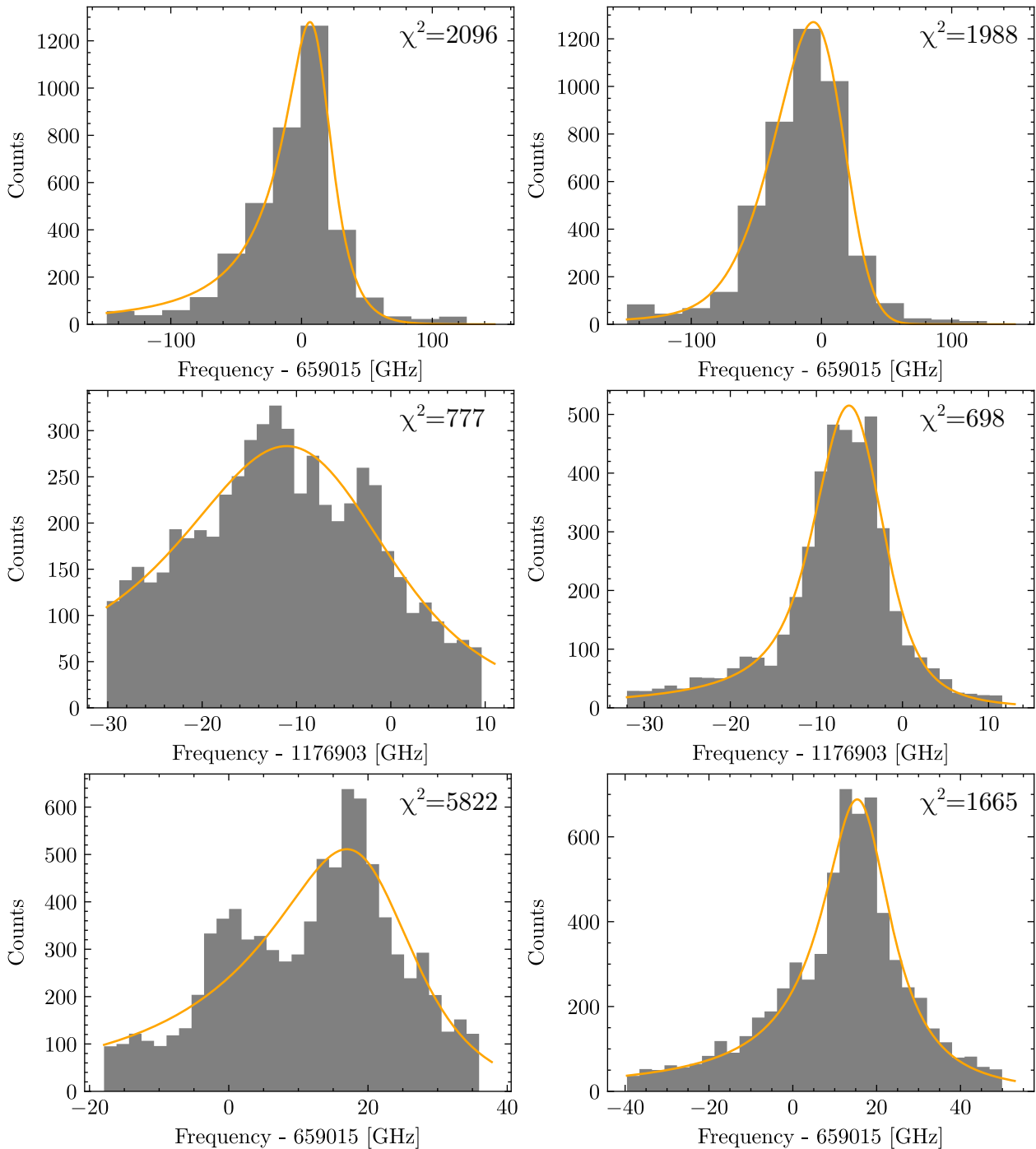
FIGURE 5.6    Examples of Voigt fits (orange) to re-binned data (grey) from the second step in the February 2020 experiment (top row), grouped into 13 bins, and the first step (middle row) and second step (bottom row) in the September 2021 experiment, both grouped into 30 bins. The examples show the same datasets in the same order as those shown in Figure 5.5. $\chi^2$ values for the fits are shown.

Centroid and FWHM values are plotted for all steps and fitted to a first-order polynomial (straight line) function in Figure 5.7. A corresponding parameter can be extracted from the linear fit gradient: frequency shift and broadening, respectively, for centroid and FWHM values. This is performed for both the raw data fits (in black in the figure) as well as the re-binned data fits (in grey) for all laser steps studied in this analysis, extracted values are shown in Table 5.1.

The change in centroid as a function of pressure is interpreted as a frequency shift. A shift of the transition lineshape in frequency space occurs as a product of so-called quenching (inelastic) and phase-perturbing (elastic) collisions, due to the modulation of the transition frequency by the perturbing gas on the level structure of the atom being ionised. Because of this, the shift is characteristic of the atom and buffer gas combination. In particular, the use of helium as a buffer gas gives rise to a positive frequency shift (blueshift), while the shift is negative (redshift) when argon is used. This is a result of the sign of the low-energy electron-scattering length of these gases [197].

The change in FWHM of the fit with pressure is interpreted as a broadening of the atomic resonance, as a consequence of the combination of elastic collisions [197, 198] and effects such as Doppler broadening. The isotope shifts of tin isotopes is of the order of $10^{-2}\,\mathrm{cm}^{-1}$ [199], that is, of the order of $0.3\,\mathrm{GHz}$.

TABLE 5.1   Centroid shift and broadening of the atomic resonance in the resonant laser ionisation of tin obtained from the linear fits shown in Figure 5.7. Parameters are shown for both the fits performed for the raw and the re-binned data.

| Experiment | Step | Data | Shift [MHz/mbar] | Broadening [MHz/mbar] |
|---|---|---|---|---|
| Feb 2020 | 2 | raw | -190(18) | 35(85) |
|  |  | re-binned | -103(67) | 950(140) |
| Feb 2020 | 2 | raw | -190(18) | 35(85) |
|  |  | re-binned | -103(67) | 950(140) |
|  |  |  | [MHz/mbar] | [MHz/mbar] |
| Feb 2020 | 2 | raw | -190(18) | 35(85) |
|  |  | re-binned | -103(67) | 950(140) |
| Sep 2021 | 1 | raw | -22(3) | 129(5) |
|  |  | re-binned | -45(17) | 119(16) |
|  | 2 | raw | -44(4) | 115(7) |
|  |  | re-binned | -29(1) | 117(16) |
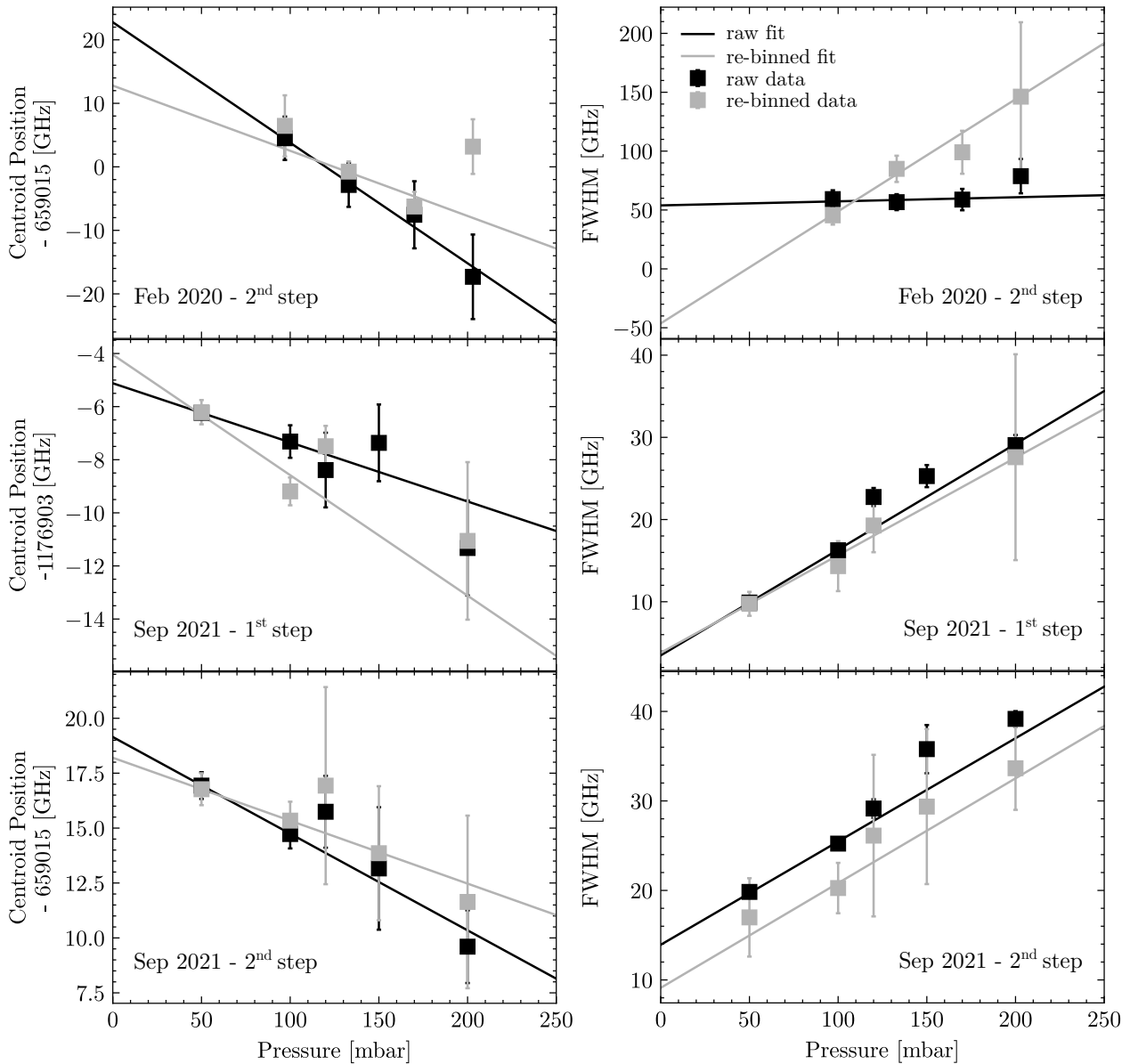
FIGURE 5.7 Linear fits of the centroid positions (left) and FWHM (right) in terms of pressure for the different laser steps in the experiments. Black squares and lines show the raw collected data and grey squares and lines show re-binned data. The top row plots show data from the second step laser in the February 2020 experiment. The middle and bottom row show data from the September 2021 experiment, from the first and second laser steps, respectively.

With the broadenings obtained in this work, in the best case scenario, the line-shape broadening for an argon pressure of 500 mbar would be in the order of 20 GHz. It would be impossible, therefore, to resolve the isotope shift or to study the hyperfine structure of tin isotopes via this technique. In-gas-jet laser spectroscopy is crucial for this, as the conditions in the jet reduce the line broadening drastically, improving the resolution of peaks by a factor 15 [136].

In the experiments presented in this thesis, it is not possible to assign the shift and broadening of the atomic resonance to any particular effect or set of effects. The laser powers used for these experiments were relatively low. This translates into a very strong focus being required for efficient laser ionisation, whose position is very challenging to control. In the case in which the laser focus is close to the gas cell exit nozzle, where gas density and velocity are rapidly changing, the collisional and Doppler broadening conditions change drastically within the ionisation region. The values obtained from these fits are thus specific to the conditions in these experiments. If well-defined gas conditions were being probed, a Voigt line profile would be expected. The deviation of the data from this shape is also reflected in the large reduced $\chi^2$ values obtained for the fits to both the raw and re-binned data.

The asymmetric Voigt fit to the re-binned data can be considered of higher quality due to improved $\chi^2$ values and the use of bins with a higher number of counts. Therefore, the parameters obtained via linear fits of the re-binned data are more credible overall than those obtained from the raw data for each resonance laser ionisation scheme step scan. However, additional measurements are required with a stable laser setup and the appropriate crossed-beam configuration to obtain higher quality data.

## 5.3 Related Works

Laser ionisation of tin was performed at the LISOL facility in Belgium as part of an experimental campaign aimed at studying the feasibility of laser spectroscopy using the IGLIS technique at $S^3$ [143]. Two two-step ionisation schemes were used for these experiments, one of which is identical to the one used in the experiments reported in this work (see Figure 5.2).

Both laser steps were directed into the gas cell in a collinear configuration, parallel to the gas flow direction. However, the gas cell used for this particular work at LISOL is not horned-shaped; it possesses an ionisation chamber of a constant width, designed for this laser configuration, in which the gas behaves in a uniform manner in terms of velocity and pressure [200]. The coefficients obtained in these experiments are therefore directly correlated with the pressure shift and

broadening, in contrast to the ones obtained with the MARA-LEB gas cell and reported earlier in this chapter. The MARA-LEB gas cell possesses a region where a cross-beam configuration can be used to probe atoms of the same velocity profile, but geometrical limitations in the position of laser windows on the IGISOL target chamber constrained its use for the experiments presented in this thesis.

Laser scans were performed as part of this experimental campaign, and fits of the obtained line profiles were presented. The coefficients obtained for pressure shift and broadening for the first step were $\gamma_{sh}$ = -4.0(3) MHz/mbar and $\gamma_{br}$ = 32(4) MHz/mbar, respectively. For the second step, $\gamma_{sh}$ = -150(10) MHz/mbar is reported for the shift coefficient, which is described as surprisingly large. While not strictly comparable, the second step shift coefficient reported for these experiments and the one presented in Table 5.1 for the February 2020 tests are compatible. This is possibly because the laser and gas conditions in the MARA-LEB gas cell for this part of the tests resembled that of the LISOL gas cell fortuitously.

The LISOL experimental campaign, in a similar fashion to what is reported in this thesis, clearly indicates the difficulty of studying the hyperfine structure of tin when performing RIS in the gas cell. The use of in-gas-jet laser ionisation is therefore the only choice with the ionisation schemes presented here.

Similar experiments have been performed for the commissioning of the $S^3$-LEB gas cell. In one of these, resonant ionisation of erbium was performed [62]. In that experiment, both in-gas-cell and in-gas-jet laser ionisation are carried out with a two-step resonance laser ionisation scheme. Pressure broadening and shift coefficients are presented for a frequency scan of the first step. In spite of this and the fact that erbium was used in the $S^3$-LEB gas cell commissioning, compared to the MARA-LEB gas cell experiments which used tin, a comparison of the results from both is possible. The overall trends are similar for both sets of experiments. A clear shift of the centroids is observed towards smaller frequencies as a function of pressure. Peaks in both experiments broaden as pressure in the gas cell increases. For both of these parameters, the results of the September 2021 MARA-LEB gas cell tests are about an order of magnitude greater than those obtained with the $S^3$-LEB gas cell. This difference could be produced by the increased area of laser overlap in the collinear configuration, contrasting to the crossed-beam configuration in the $S^3$-LEB gas cell.

It would be necessary to repeat these experiments in the new MARA-LEB gas cell chamber, which possesses the appropriate laser windows to allow for the crossed-beam configuration for in-gas-cell and in-gas-jet laser ionisation, before any conclusion can be drawn. Such experiment will be planned in the near future, during the testing and construction phase of the MARA-LEB facility.

# 6 ON-LINE EXPERIMENTS USING THE MARA SEPARATOR

As part of the development phase of the MARA-LEB facility, two experiments were carried out using the MARA separator. These experiments aimed to provide information to be used in the design of MARA-LEB components and to assess the feasibility of potential experimental campaigns.

The first experiment, with experiment code M17, was designed to study the production of exotic $^{94}$Ag and $^{96}$Ag isotopes at MARA. For this, a $^{40}$Ca target of thickness 0.8 mg/cm$^2$ was used, onto which a beam of $^{58}$Ni at 270 MeV or $^{60}$Ni at 256 MeV could be impinged. The reactions of interest were $^{40}$Ca($^{58}$Ni, p3n)$^{94}$Ag and $^{40}$Ca($^{60}$Ni, p3n)$^{96}$Ag. For MARA-LEB instrumentation purposes, the reaction $^{40}$Ca($^{60}$Ni, 2p2n)$^{96}$Pd also became important during the experiment.

The second experiment, JM20, was performed as part of a collaboration between GSI (Germany) and JYFL (Finland) aiming to study the dynamics of non-fusion reactions [95] in medium-heavy to heavy nuclei. Two targets were used with the same 350 MeV $^{65}$Cu beam. The first target, $^{209}$Bi, was used to produce nuclei heavier than bismuth, up to the lightest actinides. The second target, $^{238}$U, produced nuclei in the mid to heavy actinides, with $Z > 92$.

The results of these experiments are presented in this chapter and have been published in [46].

## 6.1 Experimental Setup

In an experiment at MARA, a high-energy beam impinges on a thin solid target, which generates nuclear reactions. Products of these reactions are formed in highly-excited states and rapidly decay. The radiation emitted in these decays can be detected by the use of detectors surrounding the target position.

MARA separates reaction products, or recoils, by the use of magnetic and electric fields. The ion-optical aspects of the MARA separator have been discussed in Section 2.1. This combination of fields allows for recoils to be separated by their mass-over-charge ratios ($m/q$).

Separated recoils are grouped into clusters of equal $m/q$. It is common for ions with similar masses and with the same charge to be focused physically close together. These clusters of the same charge but including several masses are referred to as charge states, see Figure 6.1 (top) for an example of a Multi-Wire Proportional Chamber (MWPC) charge state distribution from the $^{40}$Ca+$^{60}$Ni reaction in experiment M17. Within a charge state, it is possible to identify the mass clusters, shown for one of the charge states in Figure 6.1 (bottom).

Unlike other separators, for example, S$^3$, MARA cannot operate in a converging mode. That is, recoils will always be separated into charge state clusters. A converging mode, which would require additional quadrupole elements after the dipole magnet, would focus all separated recoils onto a single focal point, allowing for practically all recoils to be transmitted into the gas cell.

Early performance calculations of S$^3$ suggested that the use of a converging mode results in a 25% increase in momentum acceptance and a 100% increase in horizontal angular acceptance [201]. Due to the unfeasibility of installing the required quadrupole elements, similar calculations have not been performed for MARA. However, it can be roughly estimated from the results presented in this chapter that a twofold improvement in transmission into the MARA-LEB gas cell could be achieved were a converging mode possible at MARA.

### 6.1.1 Target Position

In both experiments, the JUROGAM-3 germanium detector array [52] surrounded the target position, where the nuclear reactions occurred, aiming to detect prompt $\gamma$ radiation. JUROGAM-3 is composed of 15 tapered Phase1-type detectors and 24 Clover detectors, arranged in 4 rings, at 157.6°, 133.6°, 104.5° and 75.5° with respect to the beam axis. For experiment M17, the full 39-detector array was available for use. Experiment JM20, on the other hand, only had the 15 Phase1-type detectors in the first two rings. The analysis of these experiments presented
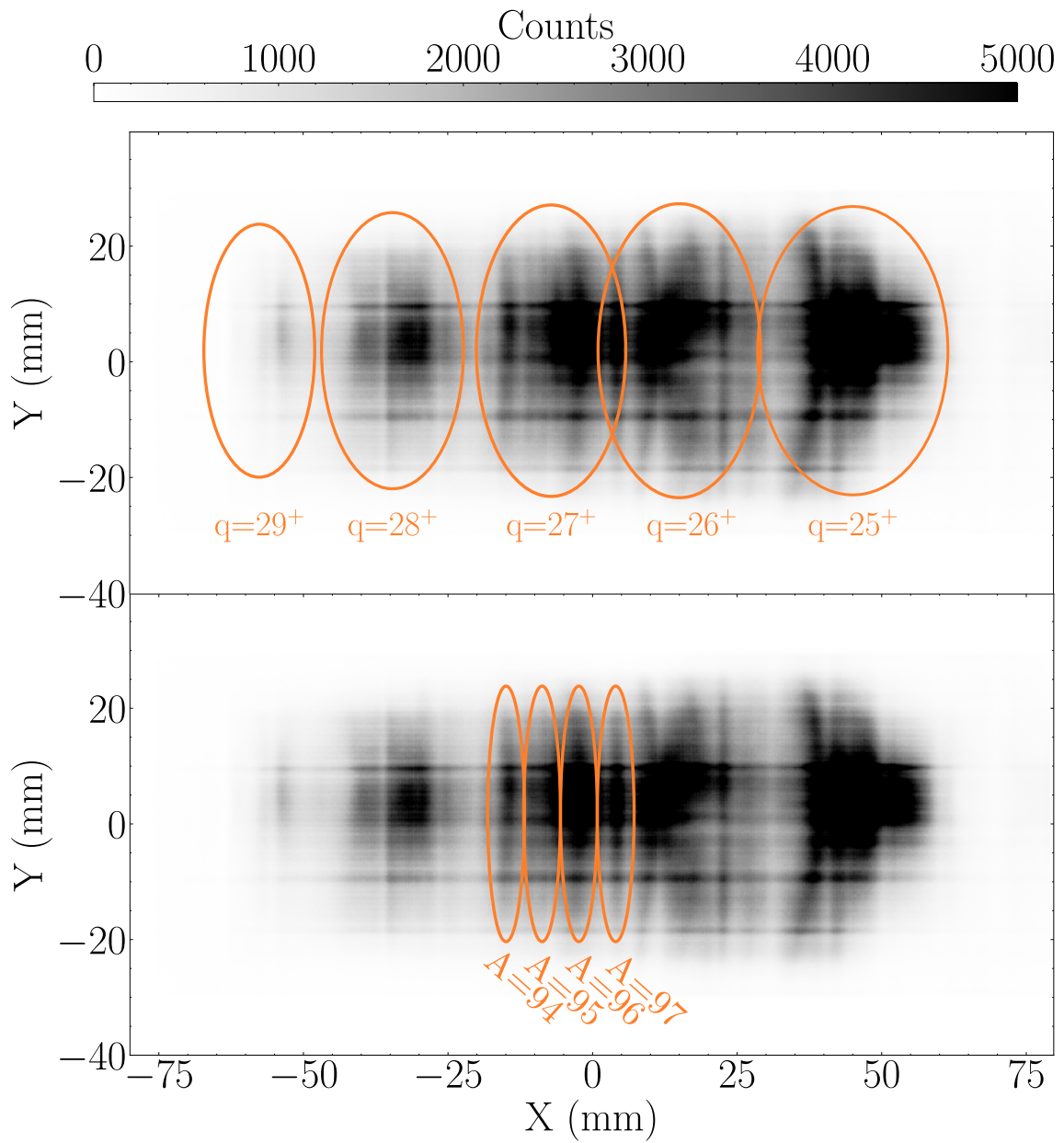
FIGURE 6.1 Recoil image at the MWPC with charge states (top) and mass clusters for charge state $27^+$ (bottom) highlighted. Data taken from the $^{40}Ca+^{60}Ni$ reaction in experiment M17.

in this thesis does not make use of prompt γ rays, but these detectors are always used when available.

Experiment M17 made use of the Jyväskylä-York Tube (JYTube) detector, the successor of the University of York Tube (UoYTube) [202]. This scintillator array can be used to detect charged particles and determine the reaction channel in which a correlated recoil was produced, with a single-proton observation efficiency of 70%. This is useful to discard events that are not produced in the desired reaction channel. JYTube can be placed directly around the target, surrounding it almost completely, with openings only perpendicular to the beam axis. This coverage translates to a veto efficiency of 91% for two-proton channels and 97% for three-proton channels [51]. In M17, the use of JYTube to veto all reactions but those of interest was crucial. This is due to the small cross-sections of the recoils of interest when compared to the overwhelming amount of contaminants.

For experiment JM20, a CD-shaped double-sided silicon strip detector (DSSD) was used at the target position. This detector is annular in shape, as opposed to the rectangular configuration used at the focal plane of MARA. The CD-shaped DSSD used in this experiment has inner and outer radii of 25.918 mm and 70.090 mm, respectively. It is segmented radially into 16 segments on one side and into 45 equal and concentric rings on the other side. This generates a total of 720 pixels, as shown in Figure 6.2.
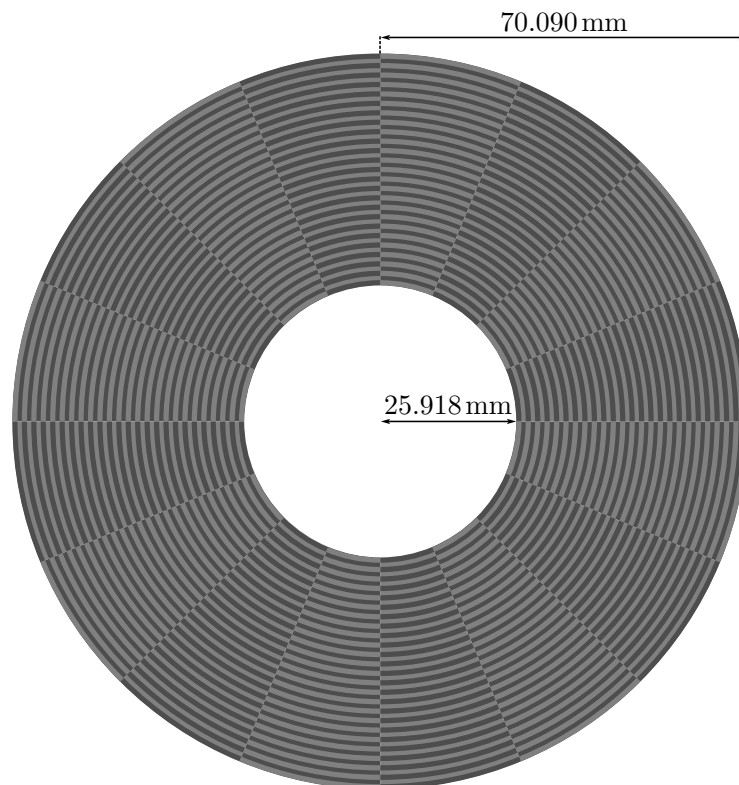


FIGURE 6.2    Dimensions and segmentation of the CD-shaped DSSD detector.

### 6.1.2 Focal Plane

In both experiments carried out as part of the development of MARA-LEB, the focal plane detector configuration was identical. The focus of the MARA ion-optical lenses in both experiments was set onto the transmission detector, an MWPC, as is common in MARA experiments. The MWPC is followed by a DSSD implantation detector, for additional identification and for decay spectroscopy.

#### 6.1.2.1 Multi-Wire Proportional Counter

The position-sensitive MWPC used at JYFL-ACCLAB is a 160 mm $\times$ 60 mm gas-filled detector. It consists of 3 planes of gold-plated tungsten wires of 20 µm in diameter, separated by 1 mm. The $x$-plane has horizontal-running wires, while the $y$-plane has vertically oriented ones. A cathode plane is placed after the $x$- and $y$-planes, all with a separation of 3 mm from each other. The cathode plane is set at -470 V.

The MWPC wires collect the charge induced by the passage of the recoils through the gas, giving timing and position information of the recoil trajectory. Typically, isobutane at 2-3 mbar is used as the gas in the detector. It is contained in the MWPC by 240 µg/cm$^2$-thick mylar foils.

#### 6.1.2.2 Double-Sided Silicon Strip Detector

A DSSD is mounted 40 cm downstream of the MWPC. This serves as the implantation site for recoils. Both the energy of an implantation event and any subsequent decay via a charged particle emission can be detected by the DSSD.

The DSSD used at MARA is the BB20 [203], a 128 mm $\times$ 48 mm detector in the horizontal and vertical directions, respectively. This detector is composed of 192 vertically-oriented strips and 72 horizontally-oriented strips, totalling 13 824 pixels, each of 0.45 mm$^2$ in area.

Events in the DSSD without a matching MWPC event can be classed as decays if the pixel where they occur or a neighbouring one have registered an implantation event within a certain time window. The time-of-flight (ToF) of ions is calculated as the difference between detection at the MWPC and at the DSSD. This information, in addition to the energy of the implanted recoils, serves as a way of identifying fusion recoils and discerning them from scattered beam.

### 6.1.2.3 Focal Plane Ancillary Detectors

In addition to the aforementioned detectors, the MARA focal plane setup usually includes a punch-through detector and a small array of germanium detectors.

A punch-through detector is an additional silicon detector that is placed downstream from the DSSD. This detector serves to exclude (veto) events in which recoils or emitted particles that are too energetic and are not stopped by the DSSD travel ("punch") through the implantation detector. These particles deposit part of their energy in the punch-through detector, which provides the veto signal. Because these energetic particles do not deposit their full energy into the DSSD, they are not identifiable and need to be discarded from the analysis.

The array of germanium detectors around the focal plane of MARA is composed of 3 Mirion Broad Energy Germanium Detectors, BEGe 6530 [204], placed behind, on top and to one side of the DSSD. A Clover detector, similar to those in JUROGAM-3, is placed on the other side of the DSSD. The efficiency of this array peaks at 150 keV at around 20-25% [51].

## 6.2 Gas Cell Acceptance Analysis

The data from the experiments described in this chapter provided information for the design of the MARA-LEB gas cell entrance window. In particular, the radius of the window was under scrutiny due to its effect in the volume and shape of the gas cell. This, in turn, has implications on the buffer gas turbulence within the cell.

The entrance of the gas cell is an aperture in one of the cell walls. Due to the wall's thickness, there are different positions in which the entrance window can be installed. These positions range from the window being flush to the inner surface of the gas cell, to being level with the cell's outer surface. However, having the window closer to the inner wall surface requires a holder that would take up some of the available aperture space, as illustrated in Figure 6.3.

Window Holder

$r_{min}=24\,mm$

$r_{max}=36\,mm$
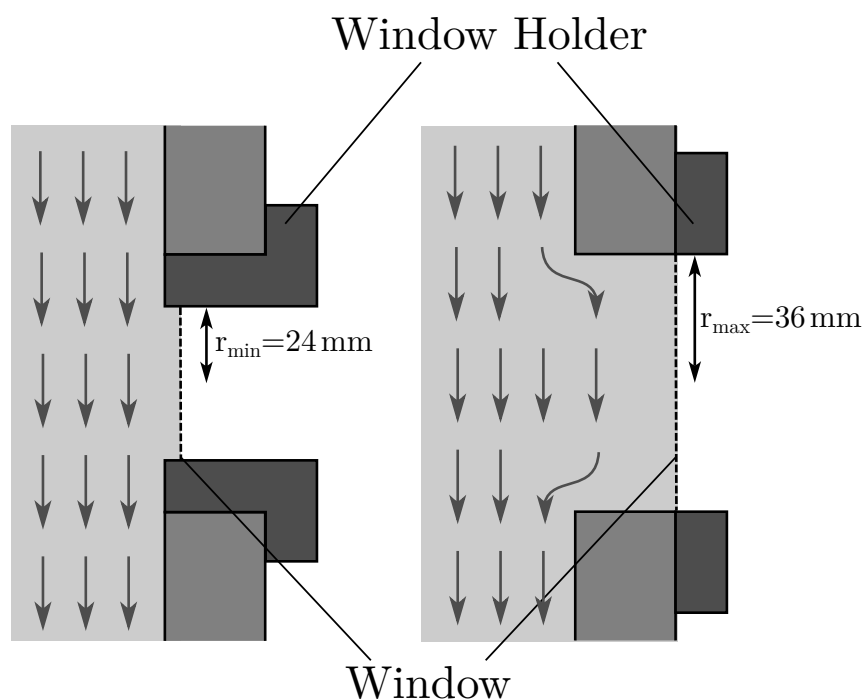
Window

FIGURE 6.3    Illustration of the options for MARA-LEB window position and geometry, showing the smallest and largest possible window radii on the left and right, respectively. Gas flow lines are shown to illustrate the possible effects of the change in geometry, but are not a realistic depiction. Parts are not to scale.

While a larger window would allow more recoils to be accepted into the gas cell, not having the gas cell window flush to the inner surface generates turbulences in the otherwise laminar gas flow within the cell. The presence of turbulences could lead to recoil losses due to collisions with the walls and a slower extraction from the cell, which is relevant in short-lived isotopes.

A larger gas cell, in which a larger window and a smoother gas flow could co-exist would both maximise the recoil acceptance and minimise the gas turbulences. However, the increased volume would result in a longer path to the exit nozzle for recoils, in turn increasing the extraction times and limiting the capabilities of MARA-LEB to study isotopes with shorter half-lives.

The effect of turbulences was studied using COMSOL gas flow simulations, using 300 mbar argon at 300 K as the buffer gas. Only losses due to diffusion were taken into account in these simulations. Recoil evacuation time and efficiency were analysed with COMSOL comparing the gas cell geometries with the window flush with the inner and outer surfaces of the gas cell wall. These showed that the differences between geometries were not very pronounced. The extraction efficiency and evacuation times were affected only slightly. Having the gas cell window flush to the outer wall surface led to less smooth distributions of these magnitudes. Given the little impact that window placement has on gas flow, recoil acceptance into the gas cell can be studied in terms of window size.

The extreme window sizes, with the smallest radius at 24 mm and the largest at 36 mm, are shown in Figure 6.3, where the difference in geometry in the gas cell can be appreciated.

The gas cell entrance is located at the MARA focal plane (where the implantation detector is located in Figure 2.1). The focal point of the MARA ion-optical system is normally on the MWPC, however, for MARA-LEB experiments this can be adjusted so recoils can be focused onto the gas cell entrance window. After the focal point, recoils disperse. If the focus is kept on the MWPC position, therefore, some recoils would not impinge on the gas cell entrance window and would be lost. Changing the focus to the gas cell position hence improves the transmission efficiency into the gas cell.

To gauge the effect of window size on recoil acceptance, data from experiments M17 and JM20 were analysed. The spatial distribution of recoils on the MWPC for the different reactions was explored while varying the position and size of the MARA-LEB gas cell entrance window. The aforementioned extreme window sizes, as shown in Figure 6.3, are overlaid onto a recoil distribution map of the MWPC in Figure 6.4. This recoil image is taken from experiment M17, where MARA magnetic rigidity and electric field settings were tuned to direct recoils with $q = 26.5$ e and $m = 96$ u to the centre of the MWPC. The use of a half charge state allows the two most intense charge-state clusters to be accepted into the gas cell. These two charge states contain over half (56.5%) of the recoils that arrive at the MWPC. An estimated efficiency of 30% from the target position to the DSSD can be assumed [131]. This takes into account the charge-state acceptance, as well as cross-section distributions. Of all ions of interest produced at the target position, therefore, around 17% are contained within the two most populated charge-state clusters.

The recoils were additionally required to be in coincidence with a 1415.3 keV $\gamma$ ray detected at the focal plane germanium detectors, corresponding to the transition from the lowest-energy excited state ($I^P = 2^+$) to the ground state ($I^P = 0^+$) of $^{96}$Pd in a cascade fed by an $8^+$ isomer with a half-life of 2.1 µs. This ensures that the observed recoils are all $^{96}$Pd and not contaminants. $^{96}$Pd was chosen instead of $^{96}$Ag due to the former being produced several orders of magnitude more intensely than the latter. Recoil distribution is only affected by $m/q$, so a certain recoil image can be generalised for all of its isobars.

Acceptance into the gas cell was studied with this recoil image for window radii up to 40 mm. The number of recoils within the window is shown in Figure 6.5 as a percentage of the total counts detected at the MWPC. Dotted lines in this figure represent the extreme window sizes and the finally selected radius.

The change within the possible sizes is not very pronounced, as the acceptance curve plateaus for the range of feasible radii.

Using the same recoil image, the centre of the windows was shifted to the centre of the cluster with $q = 27$ e. This simulates a change of MARA settings to centre on this state. The smallest and biggest possible windows are overlaid onto this image in Figure 6.6. It can be observed that while the smaller window only accepts one cluster into the gas cell, the bigger window is able to fit the neighbouring clusters almost completely. This manifests as a major increase in acceptance, as can be seen in Figure 6.7, which shows the acceptance curve for this configuration in terms of window radius.

The very large change in acceptance within the range of window radii made it clear that window size must be maximised. Considering gas flow effects, a compromise between window size and depth was reached, finally setting the entrance window radius at 32 mm. With this window radius, the two most intense clusters lie fully within the gas cell entrance when focusing on charge state 26.5 e. When focusing on charge state 27 e, the most intense cluster is fully accepted and most (71%) of the counts in the adjacent clusters enter the gas cell. Both of these scenarios are represented in Figure 6.8, with a projection along the dispersive (horizontal) axis and acceptance values are presented in Table 6.1.
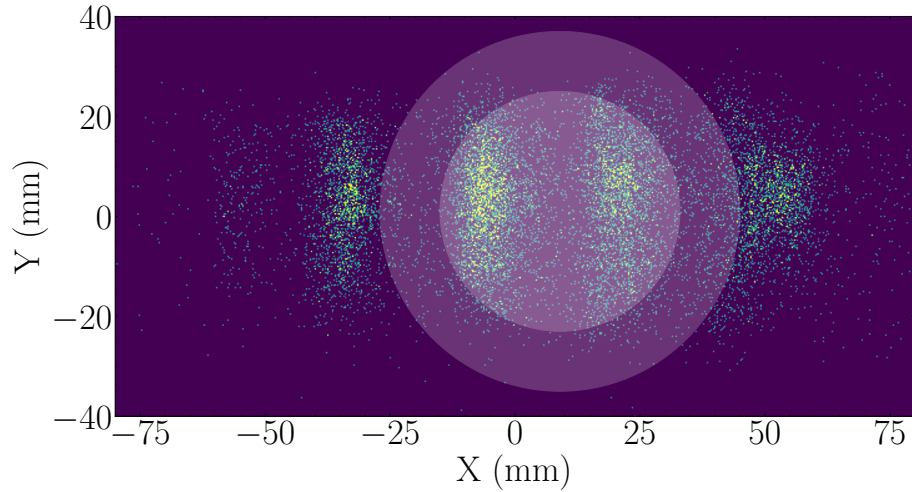
FIGURE 6.4    $^{96}$Pd recoil image at the MWPC with MARA set for charge state 26.5. Windows with the minimum and maximum possible radii have been overlaid to illustrate the difference in recoil acceptance.
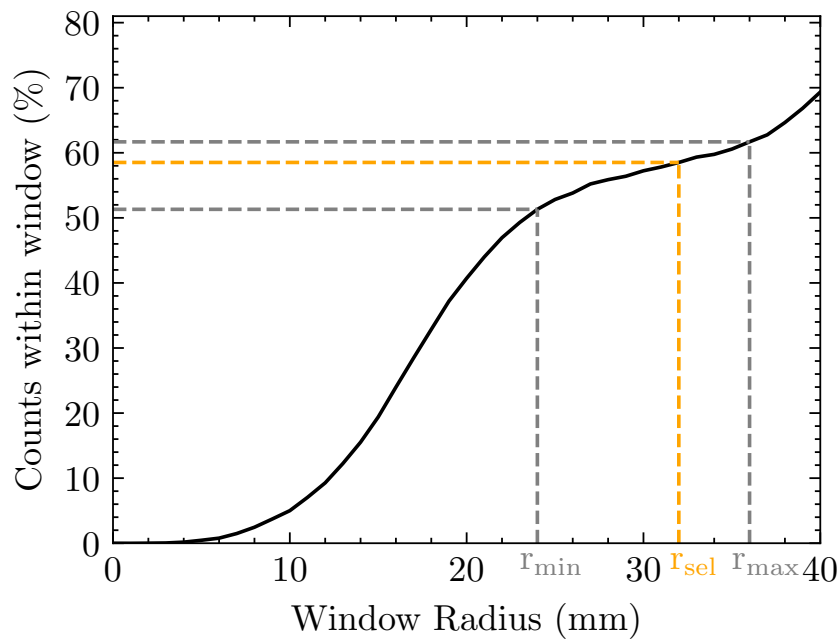


FIGURE 6.5    Number of recoils that lie within a window of a certain radius as a percentage of all $^{96}$Pd recoils that arrive at the MWPC. MARA settings for charge state 26.5. The dotted lines show the minimum and maximum window radii, $r_{min}$ and $r_{max}$, and the selected radius, $r_{sel}$, in grey and orange, respectively.
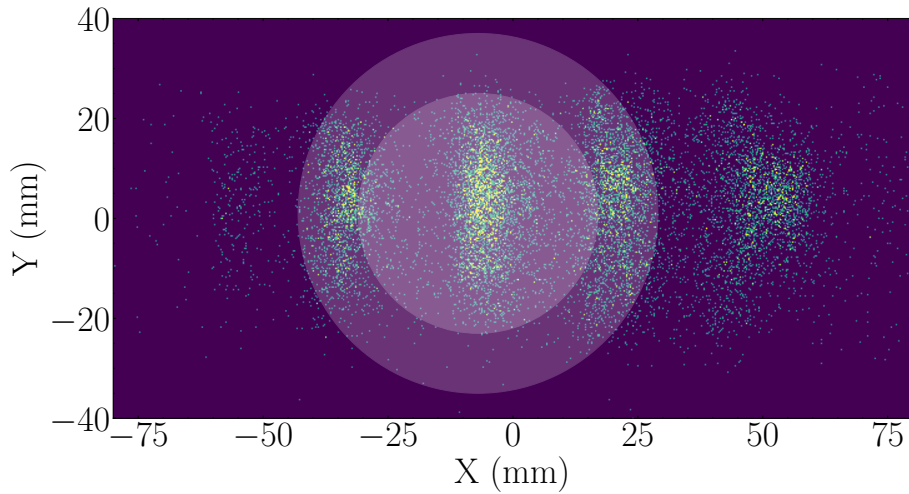
FIGURE 6.6   $^{96}$Pd recoil image at the MWPC with MARA set for charge state 27. Windows with the minimum and maximum possible radii have been overlaid to illustrate the difference in recoil acceptance.
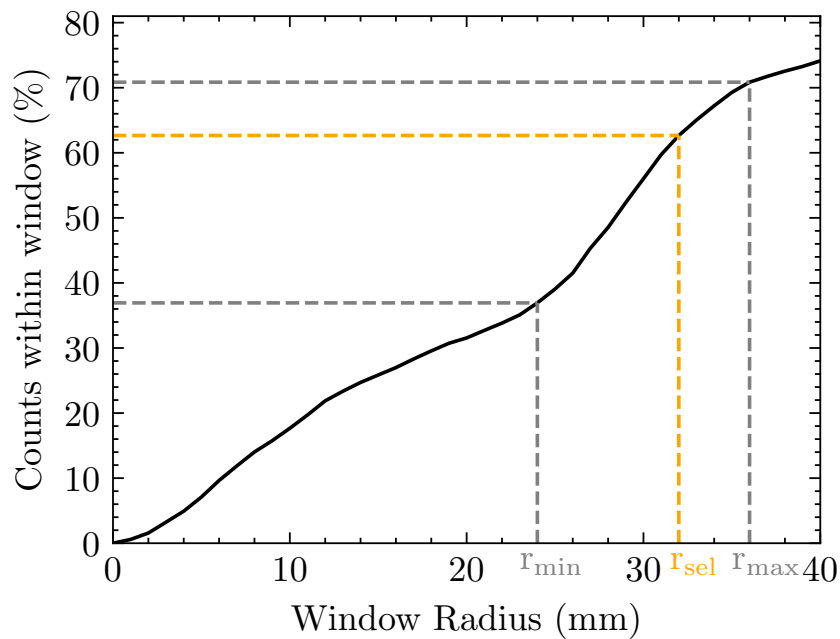


FIGURE 6.7   Number of recoils that lie within a window of a certain radius as a percentage of all $^{96}$Pd recoils that arrive at the MWPC. MARA settings for charge state 27. The dotted lines show the minimum and maximum window radii, $r_{min}$ and $r_{max}$, and the selected radius, $r_{sel}$, in grey and orange, respectively.

The same analysis was repeated for the reactions in experiment JM20. $^{213}$Rn and $^{226}$Th were the two most abundant products of the reaction when using the bismuth and uranium targets, respectively, and thus were used to perform the same window acceptance analysis. Figure 6.9 shows the recoil images in the MWPC for $^{213}$Rn (left) and $^{226}$Th (right) and their projections along the horizontal axis. In this case, pure recoil images are obtained by α-decay tagging. $^{213}$Rn was identified using its 8089 keV α decay, with a lifetime of 19.5 µs. The 6234 keV, 30.5 minute α decay of $^{226}$Th was used to identify this recoil.

Acceptance data was recorded for all three nuclei, with data for $^{96}$Pd being analysed for the two aforementioned charge state configurations. Due to their much lower production cross sections, the distribution of $^{213}$Rn and $^{226}$Th recoils is sparser than the lighter $^{96}$Pd. This results in only one intense charge state cluster per MWPC image. It is therefore not necessary to adjust the position of the recoils, as the maximum acceptance will occur when the most intense cluster is focused onto the window centre. Table 6.1 shows the acceptance for these selected cases into the gas cell with a window of radius 32 mm.

TABLE 6.1   Acceptance of recoils into the gas cell with a 32 mm radius window as a percentage of those that arrive at the MWPC, for different cases and centred charge state cluster.

| Recoil | Central Charge State [e] | Acceptance [%] |
|---|---|---|
| $^{96}$Pd | 26.5 | 58.5 |
|  | 27 | 62.7 |
| $^{213}$Rn | 31 | 70.6 |
| $^{226}$Th | 38 | 75.0 |

The increase in acceptance when centering on charge state 27 e in $^{96}$Pd is 7.2% relative to the acceptance when centering on charge state 26.5 e.

Charge states in lighter ions are closer together when transmitted to the focal plane. For lighter nuclei, centering the most intense charge state with respect to the entrance window will allow for a higher proportion of the ions in the adjacent charge states to be accepted into the gas cell. In the case where the midpoint between the two most intense charge states is centred onto the gas cell window, all $^{96}$Pd ions in those charge states are accepted. Therefore, the lower separation of charge states in lighter nuclei does not affect acceptance, as the entirety of both charge states is already included within the window. This suggests that the acceptance increase when selecting for 3 charge states will be more pronounced for lighter ions.
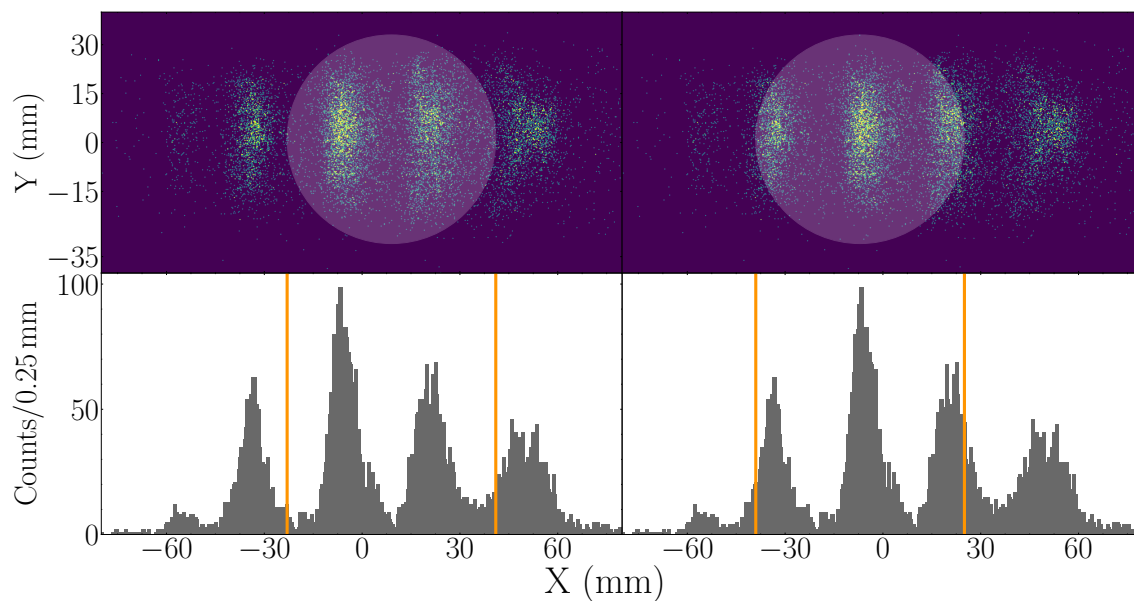
FIGURE 6.8    MWPC image for $^{96}$Pd (top) and its dispersive plane projection (bottom), with a 32 mm radius gas cell window overlaid. The window is centred on charge states 26.5 e (left) and 27 e (right).
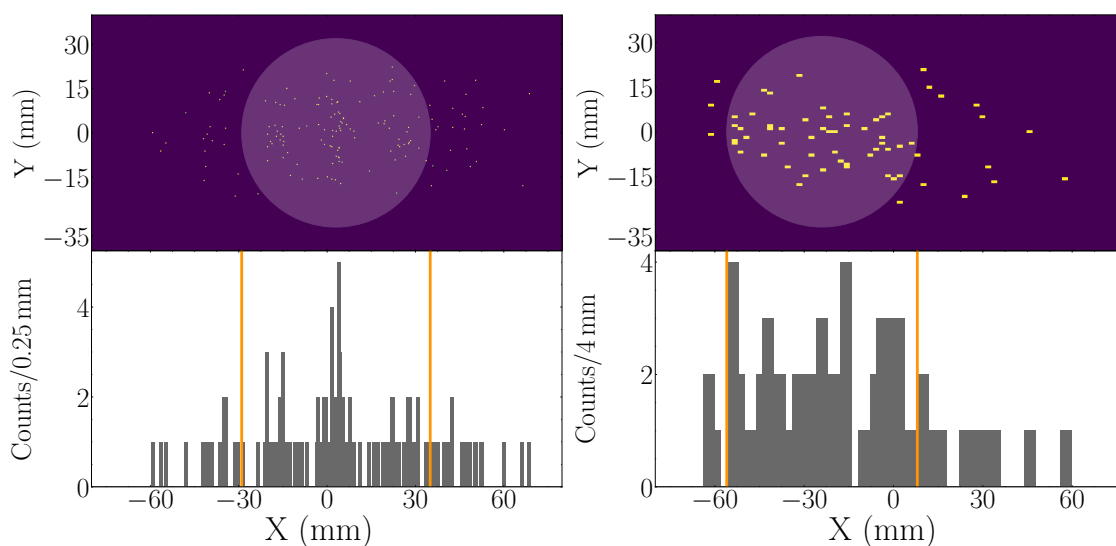


FIGURE 6.9    MWPC image for $^{213}$Rn (top left) and $^{226}$Th (top right) and their dispersive plane projections (bottom), with a 32 mm radius gas cell window overlaid. The window is centred on the most intense charge state in each case, and the binning has been made coarser for $^{226}$Th for ease of visualisation.

## 6.3  Reaction Yields

While it was not the original intent, experiment JM20 served as a proof of concept for the investigation of actinide isotopes at MARA-LEB. For reference for future experimental campaigns, cross-sections were calculated for products of the $^{65}$Cu+$^{209}$Bi and $^{65}$Cu+$^{238}$U reactions at different recoil emission energies. These data serve both as an assessment of the count rates that could be expected in MARA-LEB experiments and to determine the best ion-optical parameters for each of the species produced in JM20.

Reaction products in this experiment are primarily α emitters. Their identification was therefore carried out using their characteristic α decays. The α decays are only considered if they occur in the same pixel as an implantation event in the DSSD at the MARA focal plane within a certain time window. As shown in Figure 6.10, some recoils can be identified from their energies alone. This is because the measured energy matches only one α emission in the region of possible products. The orange line in the same figure is an example of a peak whose energy matches more than one α decay.

In addition to energy, the time difference between the recoil implantation and the decay events can be used, as the half-life will also be characteristic of each α emitter. The combination of decay energy and timing can uniquely identify the α emitter, as shown in Figure 6.11. Additionally, subsequent correlated decays can be used to determine decay chains.
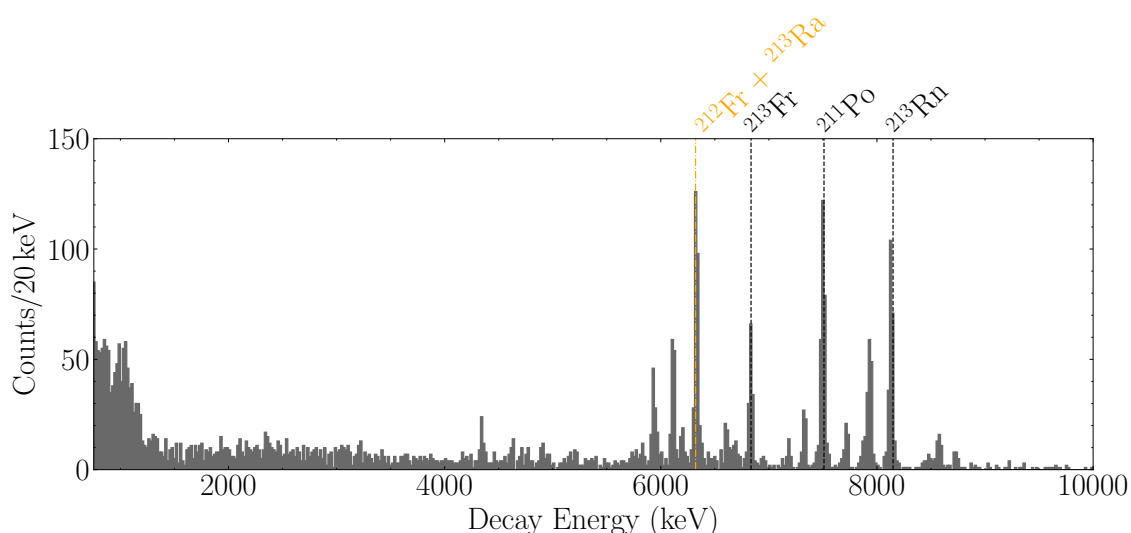


FIGURE 6.10   Example of an α-decay spectrum, labelled with several unambiguously identified peaks in black dashed lines. The orange dot-dashed line shows a peak whose energy matches multiple α decays. This data is taken from a run with the $^{209}$Bi target with MARA settings selecting for recoil exit energy of 150 MeV.
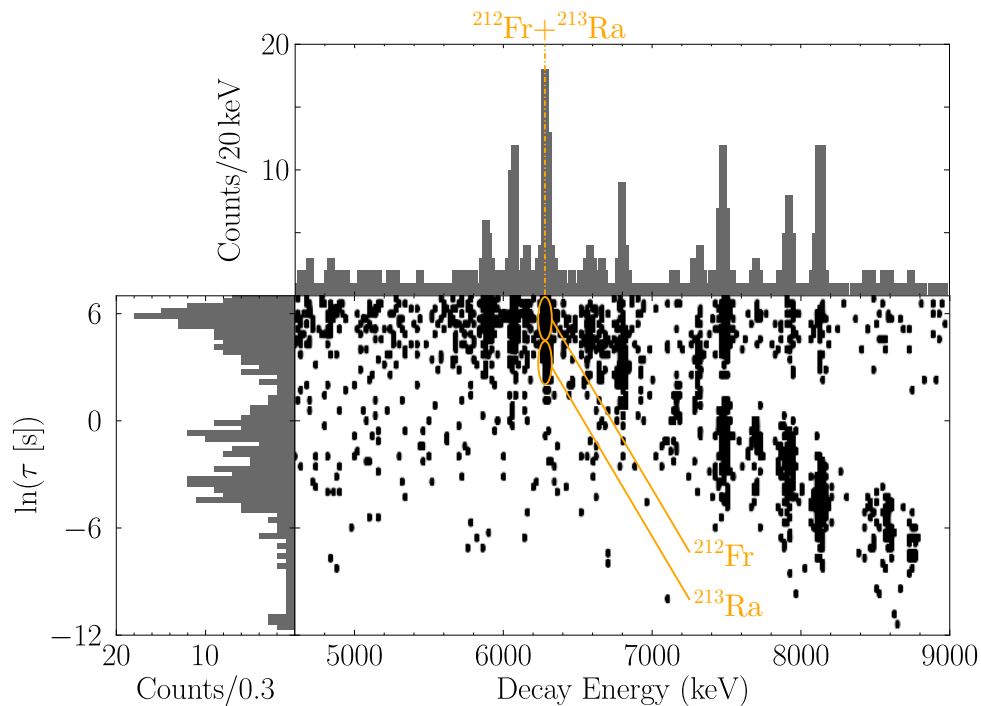
FIGURE 6.11    Example of a decay energy vs timing two-dimensional histogram.  The projections on both axes are also shown.  The well-defined clusters in the two-dimensional histogram are a clear indication of α decays.  The components in the ambiguous peak highlighted in Figure 6.10 can be resolved thanks to their different timing.  This data is taken from a run with the $^{209}$Bi target with MARA settings selecting for recoil exit energy of 150 MeV. Note the energy range when comparing to Figure 6.10.

By identifying all α-decaying species implanted onto the DSSD in every experimental run, it is possible to calculate the yield of these reaction products in terms of the experimental conditions. From the calculated yields, production cross sections can be obtained.

The cross section for the production of a certain recoil can be calculated using Equation 6.1:

$$\sigma[\mu b] = \frac{A_T[g/mol] \cdot R_T[s^{-1}]}{3.882 \cdot I_{beam}[pnA] \cdot \theta[mg/cm^2]},\tag{6.1}$$

where $A_t$ is the atomic mass number of the target, $R_T$ is the rate of recoil production at the target position, $I_{beam}$ is the intensity of the primary beam in particle-nanoamperes and $\theta$ is the surface density (sometimes imprecisely referred to as "thickness") of the target. The 3.882 conversion factor is introduced to allow for the use of units typically used in experiments.

To calculate the production rate at the target position, $R_T$, from the number of recoils detected at the DSSD several factors must be considered. Firstly, the detection efficiency of an $\alpha$ emission from an implanted recoil at the DSSD can be taken to be 50%, $\varepsilon_{\text{DSSD}} = 0.5$. This is purely geometrical, as the emission of $\alpha$ particles by the implanted recoils is isotropic, but only about half of the solid angle surrounding the nucleus will be covered by the DSSD. Calculations using the average recoil energy and mass give a rough implantation of about 15-20 $\mu$m into the DSSD. Considering the range of 6-9 MeV $\alpha$ particles in Si, roughly 60% of the alphas deposit most of their energy within the detector, the used efficiency of 50% reflects the approximate proportion of particles that deposit all of their energy within the DSSD.

Secondly, the recoil transmission efficiency, $\varepsilon_{trans}$, is the fraction of produced recoils at the target position that arrive at the DSSD. This can be taken to be 50% too, given the experimental conditions and the acceptance of the MARA separator from the target chamber [131]. This estimation is slightly higher than typically used for fusion-evaporation reactions, as the emission geometry is different for the non-fusion reactions that take place in this experiment, namely multi-nucleon transfer (MNT). In particular, the emission cone in the forward angle is narrower for an MNT reaction than for a fusion-evaporation reaction, however, while the latter reaction type results in a uniform cone, MNT emission cones have a hollow section, which affects transmission into the separator. Because of this, a 50% transmission efficiency factor is a good approximation, but to actually determine a precise value is experimentally very challenging.

By defining $R_{\text{T}}/I_{\text{beam}} = Y_{\text{T}} = Y/(\varepsilon_{\text{DSSD}}\varepsilon_{trans})$, where $Y_{\text{T}}$ and $Y$ are the yield per second and per particle-nanoampere at the target and the DSSD, respectively, Equation 6.1 becomes:

$$\sigma[\mu\text{b}] = \frac{A_{\text{T}}[\text{g/mol}] \cdot Y[\text{s}^{-1}(\text{pnA})^{-1}]}{3.882 \cdot \varepsilon_{\text{DSSD}} \cdot \varepsilon_{trans} \cdot \theta[\text{mg/cm}^2]} = \frac{A_{\text{T}}[\text{g/mol}] \cdot Y[\text{s}^{-1}(\text{pnA})^{-1}]}{1.03 \cdot \theta[\text{mg/cm}^2]}. \quad (6.2)$$

Yields at the DSSD, $Y$, for the reaction products with the bismuth and uranium targets are shown in Figures 6.12 and 6.13, respectively, for different recoil exit energies. That is, for different selected kinetic energies when produced at the target position. This is possible thanks to the combination of magnetic and electric fields utilised by the MARA separator.

The yields are obtained from the number of events per experimental run divided by the length of the run and the primary beam intensity during the run. The uncertainties reported for these are derived from the counting uncertainty, calculated as the square root of the number of counted events; the uncertainty of the length of an experimental run, 1 minute in the case of these experiments; and the uncertainty in beam intensity, at 1 enA or 0.07 pnA.
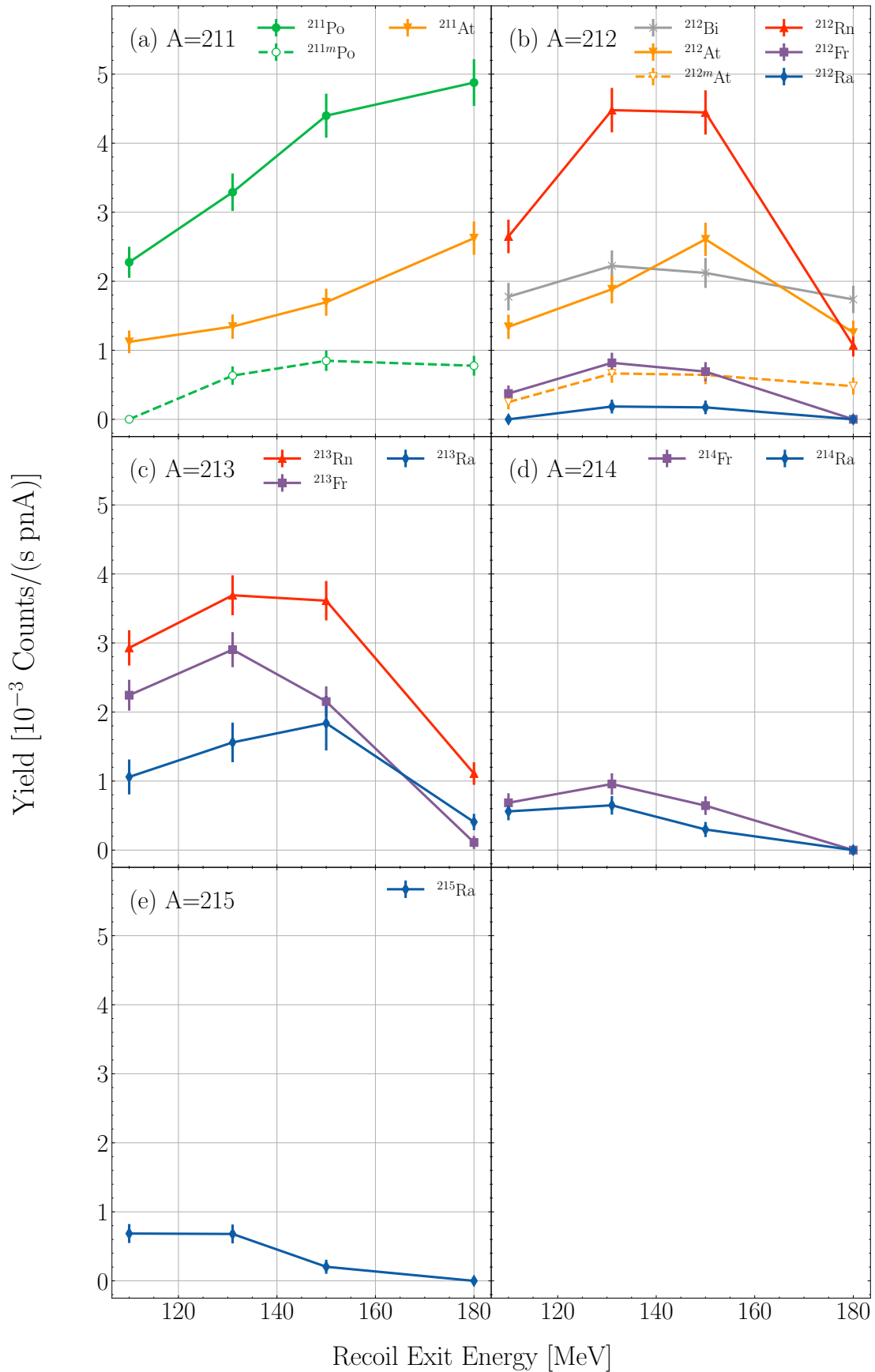
FIGURE 6.12 Yields of the $^{65}$Cu + $^{209}$Bi reaction products for different selected recoil exit energies. Each subfigure corresponds to a recoil mass, ranging from 211 u to 215 u.
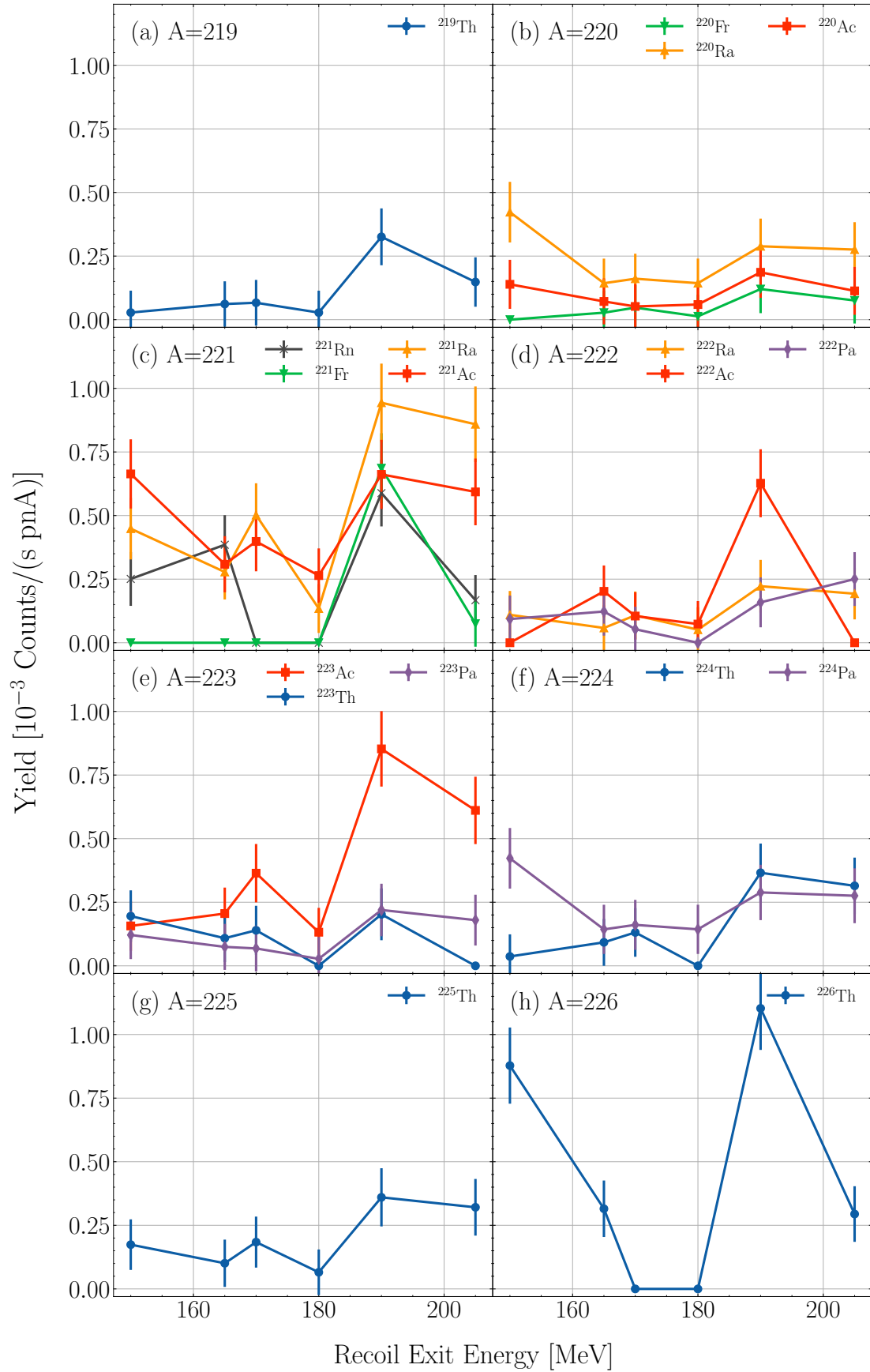
**FIGURE 6.13** Yields of the $^{65}$Cu + $^{238}$U reaction products for different selected recoil exit energies. Each subfigure corresponds to a recoil mass, ranging from 219 u to 226 u.

TABLE 6.2    Cross sections ($\sigma$) for all identified reaction products with the $^{209}$Bi (left) and $^{238}$U (right) targets.

| | $^{209}$Bi Target | | | | $^{238}$U Target | | |
|---|---|---|---|---|---|---|---|
| Recoil | $\sigma[\mu b]$ | Recoil | $\sigma[\mu b]$ | Recoil | $\sigma[\mu b]$ | Recoil | $\sigma[\mu b]$ |
| $^{211}$Po | 2.9 (2) | $^{213}$Rn | 2.2 (1) | $^{219}$Th | 0.7(2) | $^{222}$Ac | 1.4(2) |
| $^{211m}$Po | 0.51(7) | $^{213}$Fr | 1.8 (1) | $^{220}$Fr | 0.3(1) | $^{222}$Pa | 0.3(1) |
| $^{211}$At | 1.6 (1) | $^{213}$Ra | 1.1 (1) | $^{220}$Ra | 1.0(2) | $^{223}$Ac | 1.9(3) |
| $^{212}$Bi | 1.3 (1) | $^{214}$Fr | 0.58(8) | $^{220}$Ac | 0.4(1) | $^{223}$Th | 0.4(1) |
| $^{212}$At | 1.6 (1) | $^{214}$Ra | 0.39(6) | $^{221}$Rn | 1.3(2) | $^{223}$Pa | 0.5(1) |
| $^{212m}$At | 0.4 (6) | $^{215}$Ra | 0.41(6) | $^{221}$Fr | 1.5(2) | $^{224}$Th | 0.8(2) |
| $^{212}$Rn | 2.7 (2) | | | $^{221}$Ra | 2.0(3) | $^{224}$Pa | 1.0(2) |
| $^{212}$Fr | 0.49(7) | | | $^{221}$Ac | 1.6(3) | $^{225}$Th | 0.8(2) |
| $^{212}$Ra | 0.11(3) | | | $^{222}$Ra | 0.5(1) | $^{226}$Th | 2.4(3) |

Table 6.2 shows the cross sections of all identified recoils in experiment JM20 calculated using Equation 6.1. To validate these findings, the obtained cross sections were compared to a previous experiment (code JR36) performed at JYFL-ACCLAB using the RITU separator [205].

As part of that former experiment, a 331 MeV $^{65}$Cu beam was impinged on a $^{209}$Bi target. This is identical to one of the reactions presented in this chapter, at only 5% lower beam energy, therefore, the obtained cross sections should be rather similar. A comparison between production cross sections from experiment JR36 and this work is shown in Figure 6.14. The nuclei for which comparison was possible between [205] and this work are presented to the left of the dotted line. To the right of the dotted line, selected products of the reaction with the $^{238}$U target are also shown for comparison.

Cross sections calculated from the data in this work are in good agreement with those presented in [205]. The disagreements between these two experiments can be explained by two major experimental differences.

Firstly, experiment JR36 was performed using the RITU separator, while JM20 used MARA. The most important difference between these regarding the calculation of cross sections is the aperture connecting the separators to their target chambers. RITU has a rectangular aperture, with a horizontal acceptance of $\pm25$ mrad and a vertical acceptance of $\pm85$ mrad [48]. The aperture in the MARA separator is much less asymmetrical, with $\pm45$ mrad and $\pm55$ mrad in the horizontal and vertical directions, respectively [131]. While not dramatic in overall solid angle coverage, the difference in geometry of these two apertures can affect measured yields because of the dependence of cross sections with angle.

Secondly, the slight difference in beam energy between the two experiments can explain the differences in measured production cross section. Due to every nucleus having a different dependence between production cross section and energy, the effect of a small change in beam energy can be drastically different for the different reaction products. This can explain the good agreement in some of the cases when discrepancies in other cases are present.

The cross sections obtained for actinide nuclei using the MARA separator are promising for future experimental campaigns at the MARA-LEB facility. Laser spectroscopy has been proven possible with production cross sections as low as 0.5 µb and beam intensities in the order of hundreds of particle-nanoamperes [206]. Similar beam intensities are planed for use at MARA-LEB, suggesting that laser spectroscopy of actinides can be achievable given the production rates, assuming sufficient efficiencies for the stopping, thermalisation, neutralisation and laser ionisation of recoils in the gas cell. These parameters will need to be carefully investigated in the future.
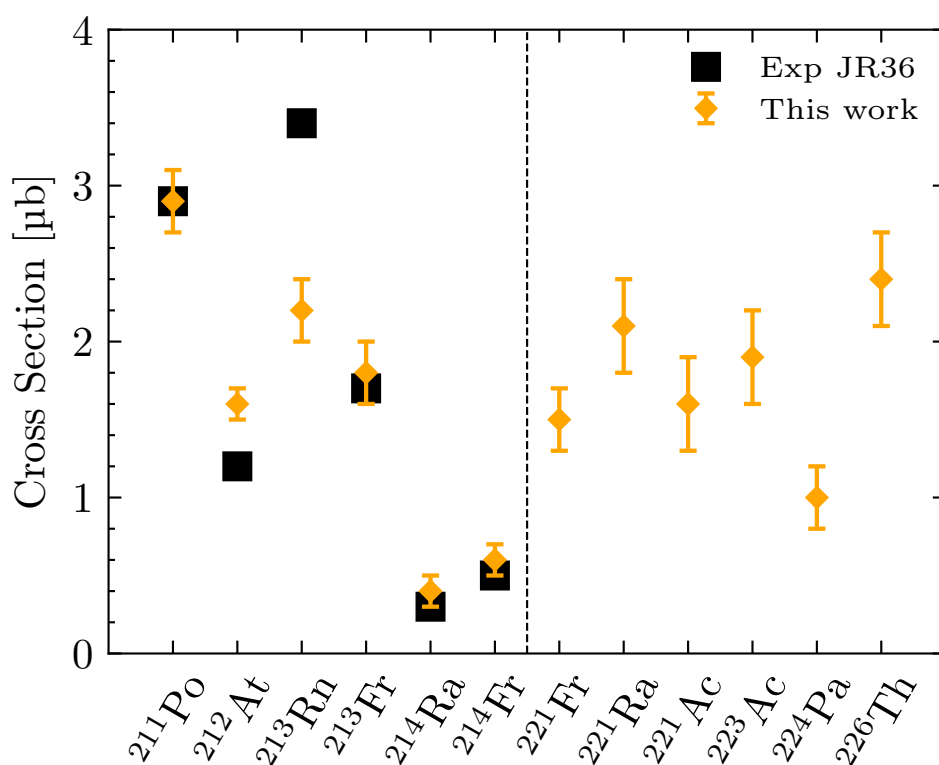


FIGURE 6.14 Production cross sections from experiment JR36 [205] (black squares) compared to selected cross sections from experiment JM20 (this work, orange rhombi). Products from the $^{65}$Cu+$^{209}$Bi are shown to the left of the dotted line, products of $^{65}$Cu+$^{238}$U to the right.

# Part IV

# Conclusion

# 7   OVERVIEW AND OUTLOOK

Throughout this thesis, the design of the MARA-LEB facility is outlined, including the experimental interests the facility was envisioned for and additional possibilities that have arisen since its inception.

The nuclear regions of interest for MARA-LEB have been described, with proton-rich nuclei in the vicinity of the $N = Z$ line being the primary case for experimental endeavours at the facility due to their relevance in astrophysical processes, such as stellar nucleosynthesis. The precise measurement of the mass, excitation levels or charge radii of these nuclei can unlock valuable information which can contribute to improve the models that describe these processes. Among these, the nuclei with masses close to $A = 80$, $A = 94$ and $A = 100$ are of interest, with conjugate nuclei $^{80}$Zr, $^{94}$Ag and $^{100}$Sn at the cores of said regions.

The lanthanide elements close to the proton drip line, which exhibit extreme ground-state deformation in different shapes, have also been presented as a region of interest for the MARA-LEB facility, in particular via decay spectroscopy. Laser spectroscopy of actinide elements, which has gained attention within the nuclear physics community in recent years thanks to novel techniques, has also been highlighted as the potential focus of future MARA-LEB campaigns. This is additionally supported in this thesis with the experimental measurement of actinide production yields at MARA.

The experimental capabilities of the facility are presented, with in-gas-cell and in-gas-jet resonant laser spectroscopy, high-precision mass measurements and decay spectroscopy as the central techniques in the MARA-LEB repertoire. The combination of all three techniques to perform laser-assisted, mass-separated decay spectroscopy of exotic nuclei is a possibility at MARA-LEB.

The components of MARA-LEB have been described and detailed within this work. A study of recoil and contaminant transmission through the MARA separator is carried out for a typical fusion-evaporation reaction used to produce exotic nuclei in the $N \sim Z$ region of interest, showing the need for further beam purification that the MARA-LEB facility provides. An overview of the individual systems that comprise the facility is given, with an increased focus on the laser system, with titanium-sapphire resonator cavities in different configurations as the principal sources of laser light; the mass measurement system, consisting of a cooler-buncher and a multi-reflection time-of-flight mass spectrometer, both based on designs in development at IGISOL; and the vacuum system, including details on the differential pumping system that gradually reduces the high pressures that are input into the chambers to the high vacuum required for the optimal operation of other components.

The design of the MARA-LEB gas cell, a core component of the facility, has been outlined. A description of the sub-volumes that comprise the gas cell and their roles regarding the gas flow within has been presented. A discussion on the gas purity and the MARA-LEB gas purification system is presented, with a comparison between argon and helium, the two buffer gases to be used in MARA-LEB experiments, outlining the suitability to experimental conditions of each of the noble gases. Simulations performed with COMSOL to illustrate the different gas velocity regimes are shown and compared to test results, where the transport efficiency and evacuation times of the gas cell were measured with the use of an $\alpha$-recoil source. An extraction and transport efficiency of 12.7(1.3)% was achieved in 300 mbar of helium at the IGISOL facility. Extraction times of 100 ms and 294 ms were measured for $^{219}$Rn$^+$ ions at pressures of 200 mbar of helium and 100 mbar of argon, respectively. The ratio of these evacuation times was reasonably close to the rough approximation expected from a simple ratio of speeds of sound in each of the gases.

A study was performed to obtain the best window composition to stop recoils at the centre of the gas cell while minimising losses from ions being stopped within the window. This was realised via the use of TRIM simulations to characterise the interaction between products of selected reactions of interest and different possible window materials and thicknesses, for each of the buffer gases to be used at MARA-LEB.

A detailed description of the MARA-LEB ion transport system is given. This system consists of the primary transport system, comprising two RFQ ion guides; the acceleration optics, in which the ions are accelerated to 30 keV; and the ion transfer line, in which ions are further mass separated via the use of electric quadrupole multiplets, a magnetic dipole and an electrostatic deflector. Transmission efficiencies and beam emittance for the different buffer gases have been calculated using SIMION, with a study of ion loss locations that led to the redesign of a part of the system. Maximum transport efficiencies of 99.2% and 93% are ob-

tained with helium and argon, respectively, for $^{94}$Ag$^+$ ions. Optimal working voltage amplitudes are reported for the RFQ system.

PIOL simulations of the ion transfer line, carried out utilising the outputs of the primary transport system simulations, are presented. With these, optimal working voltages for the electric quadrupole muliplets are found. The shape of the ion beam through the system is presented, and a total transmission through the entire ion transport system is found at 94.5% for the $^{94}$Ag$^+$ ions.

As part of the commissioning of the MARA-LEB gas cell, experiments were carried out at the IGISOL facility in which in-gas-cell resonance laser ionisation of stable tin isotopes was performed using argon as a buffer gas. A two-step resonance laser ionisation scheme was used, for which two laser beams were introduced into the ionisation volume of the gas cell in a collinear configuration. Frequency scans of both steps being carried out for different argon pressures in the gas cell and the effect of pressure on the spectral lineshape of the atomic resonance is presented.

The laser configuration proved problematic due to the collinear configuration coupled with a strong focus close to the gas cell exit hole. This resulted in the probing of rapidly changing gas velocities and densities, affecting the magnitude of the broadening mechanisms and thus the atomic resonance lineshape. Frequency broadening and shift parameters are nonetheless presented and their validity discussed in the chapter. The need for in-gas-jet laser ionisation is demonstrated when comparing the results of these experiments with hyperfine structure parameters for tin isotopes. These experiments are also compared to relevant works at other laboratories, such as LISOL in Belgium, where resonance ionisation of tin is performed, and GANIL, where the S$^3$-LEB gas cell, with a very similar design to the MARA-LEB gas cell, is used to achieve resonant laser ionisation of erbium.

Finally, the experimental setup and results of two experiments performed with the MARA separator are presented. The first experiment, aiming to produce and study $^{94}$Ag and $^{96}$Ag served to obtain information on the position of mass $A = 96$ nuclei at the focal plane of MARA. The study of transmission of $^{96}$Pd recoils into the gas cell as a function of the gas cell widow radius was performed and is presented. Acceptances into the gas cell of 58.5% and 62.7% were obtained for the cases in which 2 and 3 charge states, respectively, are focused onto a gas cell entrance window of radius 32 mm.

The second experiment, studying non-fusion reaction dynamics, provided additional information on gas cell acceptance, in this case for heavier reaction products. The acceptances for the most intense charge states of $^{213}$Rn and $^{226}$Th with a 32 mm entrance window were obtained at 70.6% and 75.0%, respectively. This second experiment was also used to estimate the production yields at MARA of

multiple heavy non-fusion reaction products in the region of $^{209}$Bi and in the light actinide region. Cross-sections compatible with laser spectroscopy were found and are reported in this thesis, namely 2.9(2) µb for $^{211}$Po and 2.7(2) µb for $^{212}$Rn in the region close to stable bismuth, and 2.1(3) µb for $^{221}$Ra and 2.4(3) µb for $^{226}$Th in the actinide region.

## 7.1  Current and Future Work

Currently, the MARA-LEB facility is built in a temporary horizontal configuration, shown in Figure 7.1, in which it can be commissioned off-line before being set up in its vertical and final configuration and attached to the MARA separator. Its components are being installed and tested in this horizontal configuration, with offline experiments utilising the entire beamline expected to take place in the coming year.
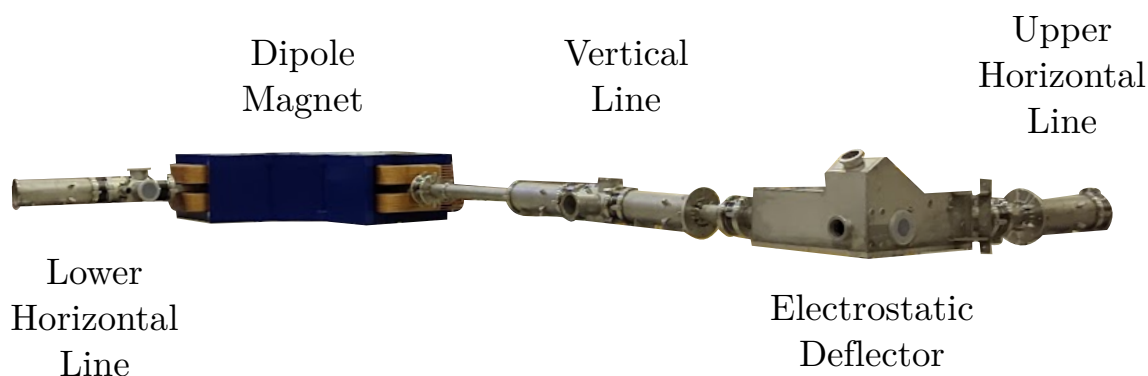


FIGURE 7.1   Horizontal layout of the MARA-LEB facility for commissioning, downstream from the main vacuum vessel. The lower horizontal line is connected to the main vacuum vessel, but was not at the time this photograph was taken.

As the facility is assembled, tested and commissioned, different experimental techniques will become available at MARA-LEB. The first online experimental campaigns will use decay spectroscopy as the main experimental technique. A project funded by the Academy of Finland has been recently approved for the development and construction of a bespoke decay station for MARA-LEB, which will improve the decay spectroscopy capabilities of the facility once it is online. Laser spectroscopy will be available early on too, as the MARA-LEB titanium-sapphire laser cavities have been constructed and used for tests and experiments in the IGISOL facility. Finally, the latest phases of the facility will see the inclusion of the mass measurement system for precision mass measurement experimental campaigns.

# REFERENCES

[1] E. Rutherford, Retardation of the α particle from radium in passing through matter, The London, Edinburgh, and Dublin Philosophical Magazine and Journal of Science 12 (1906) 134. doi:/10.1080/14786440609463525.

[2] J. Uusitalo, J. Sarén, J. Partanen, J. Hilton, Mass Analyzing Recoil Apparatus, MARA, Acta Physica Polonica B 50 (2019) 319. doi:/10.5506/APhysPolB.50.319.

[3] S. Heinz, Multinucleon transfer reactions – a pathway to new heavy and superheavy nuclei?, Journal of Physics Conference Series (Online) 1014 (2018). doi:/10.1088/1742-6596/1014/1/012005.

[4] V. Zagrebaev, W. Greiner, Production of New Heavy Isotopes in Low-Energy Multinucleon Transfer Reactions, Physical Review Letters 101 (2008) 122701. doi:/10.1103/PhysRevLett.101.122701.

[5] L. Corradi, G. Pollarolo, S. Szilner, Multinucleon transfer processes in heavy-ion reactions, Journal of Physics G: Nuclear and Particle Physics 36 (2009) 113101. doi:/10.1088/0954-3899/36/11/113101.

[6] H. Schatz, L. Bildsten, J. Görres, T. Rauscher, F.-K. Thielemann, M. Wiescher, Nucleosynthesis at the proton drip line—a challenge for nuclear physics, AIP Conference Proceedings 425 (1998) 559. doi:/10.1063/1.55175.

[7] T. Faestermann, M. Gorska, H. Grawe, The Structure of Sn-100 and Neighbouring Nuclei, Progress in Particle and Nuclear Physics 69 (2013) 85. doi:/10.1016/j.ppnp.2012.10.002.

[8] P. Gysbers, G. Hagen, J. D. Holt, G. R. Jansen, T. D. Morris, P. Navrátil, T. Papenbrock, S. Quaglioni, A. Schwenk, S. R. Stroberg, K. A. Wendt, Discrepancy Between Experimental and Theoretical $\beta$-decay Rates Resolved from First Principles, Nature Physics 15 (2019) 428. doi:/10.1038/s41567-019-0450-7.

[9] W. Nazarewicz, J. Dudek, R. Bengtsson, T. Bengtsson, I. Ragnarsson, Microscopic study of the high-spin behaviour in selected $a \approx 80$ nuclei, Nuclear Physics A 435 (1985) 397. doi:/10.1016/0375-9474(85)90471-3.

[10] T. R. Rodríguez, J. L. Egido, Multiple shape coexistence in the nucleus $^{80}$Zr, Physics Letters B 705 (2011) 255. doi:/10.1016/j.physletb.2011.10.003.

[11] P. Campbell, I. Moore, M. Pearson, Laser spectroscopy for nuclear structure physics, Progress in Particle and Nuclear Physics 86 (2016) 127. doi:https://doi.org/10.1016/j.ppnp.2015.09.003.

[12] Y. Liu, E. Romero-Romero, D. Garand, J. Lantis, K. Minamisono, D. Stracener, Three-step resonance ionization of zirconium with Ti:Sapphire lasers, Spectrochimica Acta Part B: Atomic Spectroscopy 158 (2019) 105640. doi:https://doi.org/10.1016/j.sab.2019.105640.

[13] P. Van Isacker, D. D. Warner, D. S. Brenner, Test of Wigner's Spin-Isospin Symmetry from Double Binding Energy Differences, Physics Review Letters 74 (1995) 4607. doi:/10.1103/PhysRevLett.74.4607.

[14] R. K. Wallace, S. E. Woosley, Explosive Hydrogen Burning, Astrophysics Journal Suppl. Ser. 45 (1981) 398. doi:/10.1086/190717.

[15] H. Schatz, The importance of nuclear masses in the astrophysical rp-process, International Journal of Mass Spectrometry 251 (2006) 293. doi:/10.1016/j.ijms.2006.02.014.

[16] H. Schatz, A. Aprahamian, J. Gorres, M. Wiescher, T. Rauscher, J. F. Rembges, F. K. Thielemann, B. Pfeiffer, P. Moller, K. L. Kratz, H. Herndl, B. A. Brown, H. Rebel, rp-process nucleosynthesis at extreme temperature and density conditions, Physics Reports 294 (1998) 167. doi:/10.1016/S0370-1573(97)00048-3.

[17] M. Reponen, R. P. de Groote, L. Al Ayoubi, O. Beliuskina, M. L. Bissell, P. Campbell, L. Cañete, B. Cheal, K. Chrysalidis, C. Delafosse, A. de Roubin, C. S. Devlin, T. Eronen, R. F. Garcia Ruiz, S. Geldhof, W. Gins, M. Hukkanen, P. Imgram, A. Kankainen, M. Kortelainen, Á. Koszorús, S. Kujanpää, R. Mathieson, D. A. Nesterenko, I. Pohjalainen, M. Vilén, A. Zadvornaya, I. D. Moore, Evidence of a sudden increase in the nuclear size of proton-rich silver-96, Nature Communications 12 (2021) 4596. doi:/10.1038/s41467-021-24888-x.

[18] I. Mukha, E. Roeckl, L. Batist, A. Blazhev, J. Döring, H. Grawe, L. Grigorenko, M. Huyse, Z. Janas, R. Kirchner, M. La Commara, C. Mazzocchi, S. L. Tabor, P. Van Duppen, Proton-proton correlations observed in two-proton radioactivity of 94Ag, Nature 439 (7074) (2006) 298—302. doi:10.1038/nature04453.

[19] O. L. Pechenaya, C. J. Chiara, D. G. Sarantites, W. Reviol, R. J. Charity, M. P. Carpenter, R. V. F. Janssens, T. Lauritsen, C. J. Lister, D. Seweryniak, S. Zhu, L.-L. Andersson, E. K. Johansson, D. Rudolph, Level structure of $^{92}$Rh: Implications for the two-proton decay of $^{94}$Ag$^{m}$, Physical Review C 76 (2007) 011304. doi:10.1103/PhysRevC.76.011304.

[20] J. Cerny, D. M. Moltz, D. W. Lee, K. Peräjärvi, B. R. Barquest, L. E. Grossman, W. Jeong, C. C. Jewett, Reinvestigation of the Direct Two-Proton Decay of the Long-Lived Isomer $^{94}$Ag$^{m}$ [0.4 s, 6.7 MeV, (21+)], Physical Review Letters 103 (2009) 152502. doi:10.1103/PhysRevLett.103.152502.

[21] A. Kankainen, V.-V. Elomaa, L. Batist, S. Eliseev, T. Eronen, U. Hager, J. Hakala, A. Jokinen, I. D. Moore, Y. N. Novikov, H. Penttilä, A. Popov, S. Rahaman, S. Rinta-Antila, J. Rissanen, A. Saastamoinen, D. M. Seliverstov, T. Sonoda, G. Vorobjev, C. Weber, J. Äystö, Mass measurements and implications for the energy of the high-spin isomer in $^{94}$Ag, Physical Review Letters 101 (2008) 142503. doi:/10.1103/PhysRevLett.101.142503.

[22] M. Górska, Trends in the Structure of Nuclei near 100Sn, Physics 4 (2022) 364. doi:10.3390/physics4010024.

[23] J. Eberz, U. Dinger, G. Huber, H. Lochmann, R. Menges, G. Ulm, R. Kirchner, O. Klepper, T. U. Kühl, D. Marx, Nuclear spins, moments and charge radii of $^{108-111}$Sn, Zeitschrift für Physik A Atomic Nuclei 326 (1987) 121. doi:/10.1007/BF01283586.

[24] M. Lindroos, Review of ISOL-type Radioactive Beam Facilities, in: 9th European Particle Accelerator Conference (EPAC 2004), 2004.

[25] C. B. Hinke, M. Böhmer, P. Boutachkov, T. Faestermann, H. Geissel, J. Gerl, R. Gernhäuser, M. Górska, A. Gottardo, H. Grawe, J. L. Grębosz, R. Krücken, N. Kurz, Z. Liu, L. Maier, F. Nowacki, S. Pietri, Z. Podolyák, K. Sieja, K. Steiger, K. Straub, H. Weick, H.-J. Wollersheim, P. J. Woods, N. Al-Dahan, N. Alkhomashi, A. Ataç, A. Blazhev, N. F. Braun, I. T. Čeliković, T. Davinson, I. Dillmann, C. Domingo-Pardo, P. C. Doornenbal, G. de France, G. F. Farrelly, F. Farinon, N. Goel, T. C. Habermann, R. Hoischen, R. Janik, M. Karny, A. Kaşkaş, I. M. Kojouharov, T. Kröll, Y. Litvinov, S. Myalski, F. Nebel, S. Nishimura, C. Nociforo, J. Nyberg, A. R. Parikh, A. Procházka, P. H. Regan, C. Rigollet, H. Schaffner, C. Scheidenberger, S. Schwertel, P.-A. Söderström, S. J. Steer, A. Stolz, P. Strmeň, Superallowed gamow–teller decay of the doubly magic nucleus 100sn, Nature 486 (2012) 341. doi:/10.1038/nature11116.

[26] D. Lubos, J. Park, T. Faestermann, R. Gernhäuser, R. Krücken, M. Lewitowicz, S. Nishimura, H. Sakurai, D. S. Ahn, H. Baba, B. Blank, A. Blazhev, P. Boutachkov, F. Browne, I. Čeliković, G. de France, P. Doornenbal, Y. Fang, N. Fukuda, J. Giovinazzo, N. Goel, M. Górska, S. Ilieva, N. Inabe, T. Isobe, A. Jungclaus, D. Kameda, Y. K. Kim, I. Kojouharov, T. Kubo, N. Kurz, Y. K. Kwon, G. Lorusso, K. Moschner, D. Murai, I. Nishizuka, Z. Patel, M. M. Rajabali, S. Rice, H. Schaffner, Y. Shimizu, L. Sinclair, P.-A. Söderström, K. Steiger, T. Sumikama, H. Suzuki, H. Takeda, Z. Wang, N. Warr, H. Watanabe, J. Wu, Z. Xu, Improved value for the gamow-teller strength of the $^{100}$Sn beta decay, Physical Review Letters 122 (2019) 222502. doi:/10.1103/PhysRevLett.122.222502.

[27] A. Mollaebrahimi, C. Hornung, T. Dickel, D. Amanbayev, G. Kripko-Koncz, W. R. Plaß, S. Ayet San Andrés, S. Beck, A. Blazhev, J. Bergmann, H. Geissel, M. Górska, H. Grawe, F. Greiner, E. Haettner, N. Kalantar-Nayestanaki,

I. Miskun, F. Nowacki, C. Scheidenberger, S. Bagchi, D. L. Balabanski, Z. Brencic, O. Charviakova, P. Constantin, M. Dehghan, J. Ebert, L. Gröf, O. Hall, M. N. Harakeh, S. Kaur, A. Kankainen, R. Knöbel, D. A. Kostyleva, N. Kurkova, N. Kuzminchuk, I. Mardor, D. Nichita, J.-H. Otto, Z. Patyk, S. Pietri, S. Purushothaman, M. P. Reiter, A.-K. Rink, H. Roesch, A. Spătaru, G. Stanic, A. State, Y. K. Tanaka, M. Vencelj, H. Weick, J. S. Winfield, M. I. Yavor, J. Zhao, Studying Gamow-Teller transitions and the assignment of isomeric and ground states at N=50, Physics Letters B 839 (2023) 137833. doi:/10.1016/j.physletb.2023.137833.

[28] M. Mougeot, D. Atanasov, J. Karthein, R. N. Wolf, P. Ascher, K. Blaum, K. Chrysalidis, G. Hagen, J. D. Holt, W. J. Huang, G. R. Jansen, I. Kulikov, Y. A. Litvinov, D. Lunney, V. Manea, T. Miyagi, T. Papenbrock, L. Schweikhard, A. Schwenk, T. Steinsberger, S. R. Stroberg, Z. H. Sun, A. Welker, F. Wienholtz, S. G. Wilkins, K. Zuber, Mass measurements of $^{99-101}$In challenge ab initio nuclear theory of the nuclide $^{100}$Sn, Nature Physics 17 (2021) 1099. doi:/10.1038/s41567-021-01326-9.

[29] J. Skalski, Octupolly deformed nuclei near 112Ba, Physics Letters B 238 (1990) 6. doi:/10.1016/0370-2693(90)92090-6.

[30] E. S. Paul, H. R. Andrews, T. E. Drake, J. DeGraaf, V. P. Janzen, S. Pilotte, D. C. Radford, D. Ward, Evidence for octupole correlations at high spins in neutron-deficient $^{110}$Te, Phys. Rev. C 50 (1994) R534. doi:/10.1103/PhysRevC.50.R534.

[31] K. Auranen, D. Seweryniak, M. Albers, A. D. Ayangeakaa, S. Bottoni, M. P. Carpenter, C. J. Chiara, P. Copp, H. M. David, D. T. Doherty, J. Harker, C. R. Hoffman, R. V. F. Janssens, T. L. Khoo, S. A. Kuvin, T. Lauritsen, G. Lotay, A. M. Rogers, J. Sethi, C. Scholey, R. Talwar, W. B. Walters, P. J. Woods, S. Zhu, Superallowed $\alpha$ decay to doubly magic $^{100}$Sn, Physical Review Letters 121 (2018) 182501. doi:/10.1103/PhysRevLett.121.182501.

[32] C. Fröhlich, G. Martínez-Pinedo, M. Liebendörfer, F.-K. Thielemann, E. Bravo, W. R. Hix, K. Langanke, N. T. Zinner, Neutrino-Induced Nucleosynthesis of A>64 Nuclei: The νp process, Physical Review Letters 96 (2006) 142502. doi:/10.1103/PhysRevLett.96.142502.

[33] H. Schatz, W.-J. Ong, Dependence of x-ray burst models on nuclear masses, The Astrophysical Journal 844 (2017) 139. doi:/10.3847/1538-4357/aa7de9.

[34] P. Arumugam, L. Ferreira, E. Maglione, Proton emission, gamma deformation, and the spin of the isomeric state of 141Ho, Physics Letters B 680 (2009) 443. doi:/10.1016/j.physletb.2009.09.038.

[35] M. J. Taylor, D. M. Cullen, M. G. Procter, A. J. Smith, A. McFarlane, V. Twist, G. A. Alharshan, L. S. Ferreira, E. Maglione, K. Auranen, T. Grahn, P. T. Greenlees, K. Hauschild, A. Herzan, U. Jakobsson, R. Julin, S. Juutinen,

S. Ketelhut, J. Konki, M. Leino, A. Lopez-Martens, J. Pakarinen, J. Partanen, P. Peura, P. Rahkila, S. Rinta-Antila, P. Ruotsalainen, M. Sandzelius, J. Sarén, C. Scholey, J. Sorri, S. Stolze, J. Uusitalo, M. Doncel, Oblately deformed isomeric proton-emitting state in [151]Lu, Physcal Review C 91 (2015) 044322. doi:/10.1103/PhysRevC.91.044322.

[36] S. Modi, M. Patial, P. Arumugam, L. S. Ferreira, E. Maglione, Decay of [147]Tm and the role of triaxiality studied with a nonadiabatic quasiparticle approach, Physical Review C 96 (2017) 064308. doi:/10.1103/PhysRevC.96.064308.

[37] R. D. Page, Proton emission - new results and future prospects, EPJ Web of Conferences 123 (2016) 01007. doi:10.1051/epjconf/201612301007.

[38] A. Sonzogni, Proton Radioactivity in $Z > 50$ Nuclides, Nuclear Data Sheets 95 (2002) 1. doi:/10.1006/ndsh.2002.0001.

[39] M. Procter, D. Cullen, M. Taylor, G. Alharshan, L. Ferreira, E. Maglione, K. Auranen, T. Grahn, P. Greenlees, U. Jakobsson, R. Julin, A. Herzáň, J. Konki, M. Leino, J. Pakarinen, J. Partanen, P. Peura, P. Rahkila, P. Ruotsalainen, M. Sandzelius, J. Sarén, S. Stolze, C. Scholey, J. Sorri, J. Uusitalo, T. Braunroth, E. Ellinger, A. Dewald, D. Joss, C. McPeake, B. Saygi, Proton emission from an oblate nucleus 151Lu, Physics Letters B 725 (2013) 79. doi:/10.1016/j.physletb.2013.06.045.

[40] K. Auranen, A. D. Briscoe, L. S. Ferreira, T. Grahn, P. T. Greenlees, A. Herzáň, A. Illana, D. T. Joss, H. Joukainen, R. Julin, H. Jutila, M. Leino, J. Louko, M. Luoma, E. Maglione, J. Ojala, R. D. Page, J. Pakarinen, P. Rahkila, J. Romero, P. Ruotsalainen, M. Sandzelius, J. Sarén, A. Tolosa-Delgado, J. Uusitalo, G. Zimba, Nanosecond-Scale Proton Emission from Strongly Oblate-Deformed [149]Lu, Physical Review Letters 128 (2022) 112501. doi:/10.1103/PhysRevLett.128.112501.

[41] M. L. Marsh, F. D. White, S. S. Galley, T. E. Albrecht-Schmitt, Chapter 299 - Comparison of the Electronic Properties of $f^7$, $f^8$, and $f^9$ Lanthanides With Formally Isoelectronic Actinides, in: Including Actinides, Vol. 53 of Handbook on the Physics and Chemistry of Rare Earths, 2018, p. 1. doi:/10.1016/bs.hpcre.2018.01.001.

[42] S. A. Giuliani, Z. Matheson, W. Nazarewicz, E. Olsen, P. Reinhard, J. Sadhukhan, B. Schuetrumpf, N. Schunck, P. Schwerdtfeger, Colloquium: Superheavy elements: Oganesson and beyond, Reviews of Modern Physics 91 (2019).

[43] H. L. Liu, F. R. Xu, Y. Sun, P. M. Walker, R. Wyss, On the stability of high-K isomers in the second well of actinide nuclei, The European Physical Journal A 47 (2011) 135. doi:/10.1140/epja/i2011-11135-y.

[44] K. Nomura, R. Rodríguez-Guzmán, L. M. Robledo, J. E. García-Ramos, Quadrupole-octupole coupling and the onset of octupole deformation in actinides, Physical Review C 103 (2021) 044311. doi:/10.1103/PhysRevC.103.044311.

[45] M. Block, M. Laatiaoui, S. Raeder, Recent progress in laser spectroscopy of the actinides, Progress in Particle and Nuclear Physics 116 (2021) 103834. doi:/10.1016/j.ppnp.2020.103834.

[46] J. Romero, K. Auranen, M. Block, A. D. Briscoe, T. Eronen, W. Gins, T. Grahn, P. T. Greenlees, A. Illana, R. Julin, H. Joukainen, H. Jutila, J. Khuyagbaatar, J. Krier, M. Leino, J. Louko, M. Luoma, I. D. Moore, P. Mosat, J. Ojala, A. Ortiz-Cortes, J. Pakarinen, P. Papadakis, A. M. Plaza, P. Rahkila, A. Raggio, P. Ruotsalainen, J. Sarén, M. Sandzelius, A. Tolosa-Delgado, J. Uusitalo, G. Zimba, Nuclear Reaction Studies and Prospects for the New MARA-LEB Facility, Acta Physica Polonica B Proceedings Supplement 16 (2023) 4–A12. doi:/10.5506/APhysPolBSupp.16.4-A12.

[47] P. Heikkinen, The Jyväskylä K130 Cyclotron Magnet, 12th International Conference on Cyclotrons and Their Applications G2.01 (1991) 464. doi:/10.1142/0990.

[48] J. Sarén, J. Uusitalo, M. Leino, J. Sorri, Absolute transmission and separation properties of the gas-filled recoil separator RITU, Nuclear Instruments and Methods in Physics Research A Section A: Accelerators, Spectrometers, Detectors and Associated Equipment 654 (2011) 508. doi:/10.1016/j.nima.2011.06.068.

[49] M. Leino, J. Äystö, T. Enqvist, P. Heikkinen, A. Jokinen, M. Nurmia, A. Ostrowski, W. Trzaska, J. Uusitalo, K. Eskola, P. Armbruster, V. Ninov, Gas-filled recoil separator for studies of heavy elements, Nuclear Instruments and Methods in Physics Research Section B: Beam Interactions with Materials and Atoms 99 (1995) 653. doi:/10.1016/0168-583X(94)00573-7.

[50] J. Uusitalo, P. Jones, P. Greenlees, P. Rahkila, M. Leino, A. Andreyev, P. Butler, T. Enqvist, K. Eskola, T. Grahn, R.-D. Herzberg, F. Hessberger, R. Julin, S. Juutinen, A. Keenan, H. Kettunen, P. Kuusiniemi, A.-P. Leppänen, P. Nieminen, R. Page, J. Pakarinen, C. Scholey, In-beam spectroscopy using the JYFL gas-filled magnetic recoil separator RITU, Nuclear Instruments and Methods in Physics Research Section B: Beam Interactions with Materials and Atoms 204 (2003) 638. doi:/10.1016/S0168-583X(02)02144-4.

[51] J. Sarén, J. Uusitalo, H. Joukainen, In-flight recoil separators RITU and MARA and the standard detector setups, Nuclear Instruments and Methods in Physics Research Section B: Beam Interactions with Materials and Atoms 541 (2023) 33. doi:/10.1016/j.nimb.2023.04.040.

[52] J. Pakarinen, J. Ojala, P. Ruotsalainen, H. Tann, H. Badran, T. Calverley, J. Hilton, T. Grahn, P. T. Greenlees, M. Hytönen, A. Illana, A. Kauppinen, M. Luoma, P. Papadakis, J. Partanen, K. Porras, M. Puskala, P. Rahkila, K. Ranttila, J. Sarén, M. Sandzelius, S. Szwec, J. Tuunanen, J. Uusitalo, G. Zimba, The JUROGAM-3 Spectrometer, The European Physical Journal A 56 (2020) 149. doi:10.1140/epja/s10050-020-00144-6.

[53] P. Papadakis, R. D. Herzberg, J. Pakarinen, P. T. Greenlees, J. Sorri, P. A. Butler, P. J. Coleman-Smith, D. Cox, J. R. Cresswell, K. Hauschild, P. Jones, R. Julin, I. H. Lazarus, S. C. Letts, E. Parr, P. Peura, V. F. E. Pucknell, P. Rahkila, J. Sampson, M. Sandzelius, D. A. Seddon, J. Simpson, J. Thornhill, D. Wells, The SAGE spectrometer: A tool for combined in-beam $\gamma$-ray and conversion electron spectroscopy, Journal of Physics: Conference Series 312 (2011) 052017. doi:10.1088/1742-6596/312/5/052017.

[54] R. Page, A. Andreyev, D. Appelbe, P. Butler, S. Freeman, P. Greenlees, R.-D. Herzberg, D. Jenkins, G. Jones, P. Jones, D. Joss, R. Julin, H. Kettunen, M. Leino, P. Rahkila, P. Regan, J. Simpson, J. Uusitalo, S. Vincent, R. Wadsworth, The GREAT spectrometer, Nuclear Instruments and Methods in Physics Research Section B: Beam Interactions with Materials and Atoms 204 (2003) 634. doi:/10.1016/S0168-583X(02)02143-2.

[55] H. Joukainen, J. Sarén, P. Ruotsalainen, Position sensitive plastic scintillator for beta particle detection, Nuclear Instruments and Methods in Physics Research Section A: Accelerators, Spectrometers, Detectors and Associated Equipment 1027 (2022) 166253. doi:/10.1016/j.nima.2021.166253.

[56] I. Moore, T. Eronen, D. Gorelov, J. Hakala, A. Jokinen, A. Kankainen, V. Kolhinen, J. Koponen, H. Penttilä, I. Pohjalainen, M. Reponen, J. Rissanen, A. Saastamoinen, S. Rinta-Antila, V. Sonnenschein, J. Äystö, Towards commissioning the new IGISOL-4 facility, Nuclear Instruments and Methods in Physics Research Section B: Beam Interactions with Materials and Atoms 317 (2013) 208. doi:/10.1016/j.nimb.2013.06.036.

[57] T. Eronen, V. S. Kolhinen, V.-V. Elomaa, D. Gorelov, U. Hager, J. Hakala, A. Jokinen, A. Kankainen, P. Karvonen, S. Kopecky, I. D. Moore, H. Penttilä, S. Rahaman, S. Rinta-Antila, J. Rissanen, A. Saastamoinen, J. Szerypo, C. Weber, J. Äystö, JYFLTRAP: a Penning trap for precision mass spectroscopy and isobaric purification, The European Physical Journal A 48 (2012) 46. doi:10.1140/epja/i2012-12046-1.

[58] S. Kujanpää, A. Raggio, R. de Groote, M. Athanasakis-Kaklamanakis, M. Block, A. Candiello, W. Gins, A. Koszorús, I. Moore, M. Reponen, J. Warbinek, RAPTOR: A new collinear laser ionization spectroscopy and laser-radiofrequency double-resonance experiment at the IGISOL facility, Nuclear Instruments and Methods in Physics Research Section B: Beam Interactions with Materials and Atoms 541 (2023) 388. doi:/10.1016/j.nimb.2023.05.014.

[59] D. Ackermann, L. Adoui, G. de Angelis, G. Auger, T. Aumann, F. Azaiez, E. Balanzat, G. Baldacchino, M. Barthe, E. Bauge, P. Bem, M. Bender, K. Bennaceur, J.-F. Berger, B. Blank, J. Blomqvist, Y. Blumenfeld, S. Boucard, S. Bouffard, A. Bracco, R. Calabrese, B. Cederwall, R. Cee, P. Chomaz, G. Colo, M. Colonna, D. Curien, P. Danielewicz, R. Dayras, F. de Oliveira, M. Di Toro, E. Diegele, J. Dobaczewski, T. Ethvignot, U. Fischer, G. de France, M. Freer, U. Garg, W. Gelletly, A. Gillibert, M. Girod, S. Goriely, H. Goutte, J. Grandin, F. Gunsing, P. Heenen, M. Heil, K. Heyde, S. Hilaire, S. Hofmann, P. Indelicato, Z. Janas, A. Jokinen, J. Jose, F. Kaeppeler, E. Khan, J. Knödlseder, A. Krasznahorkay, K. Kratz, E. Lamour, K. Langanke, V. Lapoux, E. Le Bigot, F. Le Blanc, X. Ledoux, M. Leino, S. Lenzi, S. Leoni, M. Lewitowicz, D. Lunney, E. Maglione, A. Maj, P. Mantica, J. Marques, M. Matsuo, V. Méot, W. Mittig, E. Morse, O. Naviliat-Cuncic, W. Nazarewicz, G. Neyens, Y. Novikov, S. Oberstedt, T. Otsuka, F. Parente, S. Péru, N. Pillet, A. Plompen, C. Prigent, R. Reifarth, D. Ridikas, M. Rivet, E. Roeckl, M. Rousseau, P. Roussel-Chomaz, J. Rozet, G. Rudolf, K. Rykaczewski, M. Saint-Laurent, D. Santonocito, J.-P. Santos, P. Sapienza, H. Savajols, M. Schädel, H. Schatz, N. Severijns, J. Sida, F. Sobrio, O. Sorlin, A. Stefanini, C. Stodel, L. Stuttge, I. Testard, C. Theisen, J. Thomas, J. Thomas, I. Thompson, M. Toulemonde, P. van Isacker, D. Verney, D. Vernhet, D. Vieira, A. Villari, C. Volpe, D. Vretenar, D. Warner, J. Wieleczko, J. Wörtche, R. Wyss, The Scientific Objectives of the SPIRAL2 project, Research report, GANIL (2006).
URL https://hal.in2p3.fr/in2p3-00101412

[60] F. Déchery, H. Savajols, M. Authier, A. Drouart, J. Nolen, D. Ackermann, A. Amthor, B. Bastin, A. Berryhill, D. Boutin, L. Caceres, M. Coffey, O. Delferrière, O. Dorvaux, B. Gall, K. Hauschild, A. Hue, B. Jacquot, N. Karkour, B. Laune, F. Le Blanc, N. Lecesne, A. Lopez-Martens, F. Lutton, S. Manikonda, R. Meinke, G. Olivier, J. Payet, J. Piot, O. Pochon, V. Prince, M. Souli, G. Stelzer, C. Stodel, M.-H. Stodel, B. Sulignano, E. Traykov, D. Uriot, The Super Separator Spectrometer S3 and the associated detection systems: SIRIUS & LEB-REGLIS3, Nuclear Instruments and Methods in Physics Research Section B: Beam Interactions with Materials and Atoms 376 (2016) 125. doi:/10.1016/j.nimb.2016.02.036.

[61] J. Romans, A. Ajayakumar, M. Authier, F. Boumard, L. Caceres, J.-F. Cam, A. Claessens, S. Damoy, P. Delahaye, P. Desrues, A. Drouart, P. Duchesne, R. Ferrer, X. Fléchard, S. Franchoo, P. Gangnant, R. P. de Groote, S. Kraemer, N. Lecesne, R. Leroy, J. Lory, F. Lutton, V. Manea, Y. Merrer, I. Moore, A. Ortiz-Cortes, B. Osmond, J. Piot, O. Pochon, B.-M. Retailleau, H. Savajols, S. Sels, E. Traykov, J. Uusitalo, C. Vandamme, M. Vandebrouck, P. Van den Bergh, P. Van Duppen, M. Verlinde, E. Verstraelen, K. Wendt, First offline results from the s3 low-energy branch, Atoms 10 (2022) 21. doi:/10.3390/atoms10010021.

[62] A. Ajayakumar, J. Romans, M. Authier, Y. Balasmeh, A. Brizard, F. Boumard, L. Caceres, J.-F. Cam, A. Claessens, S. Damoy, P. Delahaye, P. Desrues, W. Dong, A. Drouart, P. Duchesne, R. Ferrer, X. Fléchard, S. Franchoo, P. Gangnant, S. Geldhof, R. P. de Groote, F. Ivandikov, N. Lecesne, R. Leroy, J. Lory, F. Lutton, V. Manea, Y. Merrer, I. Moore, A. Ortiz-Cortes, B. Osmond, J. Piot, O. Pochon, S. Raeder, A. de Roubin, H. Savajols, D. Studer, E. Traykov, J. Uusitalo, C. Vandamme, P. Van den Bergh, P. Van Duppen, K. Wendt, In-gas-jet laser spectroscopy with S3-LEB, Nuclear Instruments and Methods in Physics Research Section B: Beam Interactions with Materials and Atoms 539 (2023) 102. doi:/10.1016/j.nimb.2023.03.020.

[63] Yu. Kudryavtsev, P. Creemers, R. Ferrer, C. Granados, L. Gaffney, M. Huyse, E. Mogilevskiy, S. Raeder, S. Sels, P. Van den Bergh, P. Van Duppen, A. Zadvornaya, A new in-gas-laser ionization and spectroscopy laboratory for offline studies at KU Leuven, Nuclear Instruments and Methods in Physics Research Section B: Beam Interactions with Materials and Atoms 376 (2016) 345. doi:/10.1016/j.nimb.2016.02.040.

[64] P. Chauveau, P. Delahaye, G. De France, S. El Abir, J. Lory, Y. Merrer, M. Rosenbusch, L. Schweikhard, R. Wolf, PILGRIM, a Multi-Reflection Time-of-Flight Mass Spectrometer for Spiral2-S3 at GANIL, Nuclear Instruments and Methods in Physics Research Section B: Beam Interactions with Materials and Atoms 376 (2016) 211. doi:/10.1016/j.nimb.2016.01.025.

[65] M. Vandebrouck, Spectroscopy Electron Alpha in Silicon bOx couNter – SEASON, Agence Nationale de la Recherche. Accessed June 2023.
URL https://anr.fr/Project-ANR-20-CE31-0005

[66] A. Drouart, A. Amthor, D. Boutin, O. Delferrière, M. Duval, S. Manikonda, J. Nolen, J. Payet, H. Savajols, M.-H. Stodel, D. Uriot, The Super Separator Spectrometer (S3) for SPIRAL2 stable beams, Nuclear Physics A 834 (2010) 747c. doi:/10.1016/j.nuclphysa.2010.01.135.

[67] T. Kubo, D. Kameda, H. Suzuki, N. Fukuda, H. Takeda, Y. Yanagisawa, M. Ohtake, K. Kusaka, K. Yoshida, N. Inabe, T. Ohnishi, A. Yoshida, K. Tanaka, Y. Mizoi, BigRIPS separator and ZeroDegree spectrometer at RIKEN RI Beam Factory, Progress of Theoretical and Experimental Physics 2012 (2012). doi:/10.1093/ptep/pts064.

[68] T. Ohnishi, T. Kubo, K. Kusaka, A. Yoshida, K. Yoshida, M. Ohtake, N. Fukuda, H. Takeda, D. Kameda, K. Tanaka, N. Inabe, Y. Yanagisawa, Y. Gono, H. Watanabe, H. Otsu, H. Baba, T. Ichihara, Y. Yamaguchi, M. Takechi, S. Nishimura, H. Ueno, A. Yoshimi, H. Sakurai, T. Motobayashi, T. Nakao, Y. Mizoi, M. Matsushita, K. Ieki, N. Kobayashi, K. Tanaka, Y. Kawada, N. Tanaka, S. Deguchi, Y. Satou, Y. Kondo, T. Nakamura, K. Yoshinaga, C. Ishii, H. Yoshii, Y. Miyashita, N. Uematsu, Y. Shiraki,

T. Sumikama, J. Chiba, E. Ideguchi, A. Saito, T. Yamaguchi, I. Hachiuma, T. Suzuki, T. Moriguchi, A. Ozawa, T. Ohtsubo, M. A. Famiano, H. Geissel, A. S. Nettleton, O. B. Tarasov, D. P. Bazin, B. M. Sherrill, S. L. Manikonda, J. A. Nolen, Identification of 45 New Neutron-Rich Isotopes Produced by In-Flight Fission of a 238U Beam at 345 MeV/nucleon, Journal of the Physical Society of Japan 79 (2010) 073201. doi:/10.1143/JPSJ.79.073201.

[69] J. Park, R. Krücken, D. Lubos, R. Gernhäuser, M. Lewitowicz, S. Nishimura, D. S. Ahn, H. Baba, B. Blank, A. Blazhev, P. Boutachkov, F. Browne, I. Čeliković, G. de France, P. Doornenbal, T. Faestermann, Y. Fang, N. Fukuda, J. Giovinazzo, N. Goel, M. Górska, H. Grawe, S. Ilieva, N. Inabe, T. Isobe, A. Jungclaus, D. Kameda, G. D. Kim, Y.-K. Kim, I. Kojouharov, T. Kubo, N. Kurz, Y. K. Kwon, G. Lorusso, K. Moschner, D. Murai, I. Nishizuka, Z. Patel, M. M. Rajabali, S. Rice, H. Sakurai, H. Schaffner, Y. Shimizu, L. Sinclair, P.-A. Söderström, K. Steiger, T. Sumikama, H. Suzuki, H. Takeda, Z. Wang, H. Watanabe, J. Wu, Z. Y. Xu, New and comprehensive $\beta$- and $\beta p$-decay spectroscopy results in the vicinity of $^{100}$Sn, Physical Review C 99 (2019) 034313. doi:/10.1103/PhysRevC.99.034313.

[70] J. Park, R. Krücken, A. Blazhev, D. Lubos, R. Gernhäuser, M. Lewitowicz, S. Nishimura, D. S. Ahn, H. Baba, B. Blank, P. Boutachkov, F. Browne, I. Čeliković, G. de France, P. Doornenbal, T. Faestermann, Y. Fang, N. Fukuda, J. Giovinazzo, N. Goel, M. Górska, H. Grawe, S. Ilieva, N. Inabe, T. Isobe, A. Jungclaus, D. Kameda, G. D. Kim, Y.-K. Kim, I. Kojouharov, T. Kubo, N. Kurz, Y. K. Kwon, G. Lorusso, K. Moschner, D. Murai, I. Nishizuka, Z. Patel, M. M. Rajabali, S. Rice, H. Sakurai, H. Schaffner, Y. Shimizu, L. Sinclair, P.-A. Söderström, K. Steiger, T. Sumikama, H. Suzuki, H. Takeda, Z. Wang, H. Watanabe, J. Wu, Z. Y. Xu, Spectroscopy of $^{99}$Cd and $^{101}$In from $\beta$ decays of $^{99}$In and $^{101}$Sn, Physical Review C 102 (2020) 014304. doi:/10.1103/PhysRevC.102.014304.

[71] J. Dilling, R. Krücken, G. Ball, ISAC overview, Hyperfine Interactions 225 (2014) 1. doi:/10.1007/s10751-013-0877-7.

[72] C. E. Svensson, A. B. Garnsworthy, The GRIFFIN spectrometer, Hyperfine Interactions 225 (2014) 127. doi:/10.1007/s10751-013-0889-3.

[73] C. E. Svensson, P. Amaudruz, C. Andreoiu, A. Andreyev, R. A. E. Austin, G. C. Ball, D. Bandyopadhyay, A. J. Boston, R. S. Chakrawarthy, A. A. Chen, R. Churchman, T. E. Drake, P. Finlay, P. E. Garrett, G. F. Grinyer, G. Hackman, B. Hyland, B. Jones, R. Kanungo, R. Maharaj, J. P. Martin, D. Morris, A. C. Morton, C. J. Pearson, A. A. Phillips, J. J. Ressler, R. Roy, F. Sarazin, M. A. Schumaker, H. C. Scraggs, M. B. Smith, N. Starinsky, J. J. Valiente-Dobón, J. C. Waddington, L. M. Watters, TIGRESS: TRIUMF-ISAC gamma-ray escape-suppressed spectrometer, Journal of Physics G: Nuclear and Particle Physics 31 (2005) S1663. doi:/10.1088/0954-3899/31/10/050.

[74] J. Dilling, P. Bricault, M. Smith, H.-J. Kluge, The proposed TITAN facility at ISAC for very precise mass measurements on highly charged short-lived isotopes, Nuclear Instruments and Methods in Physics Research Section B: Beam Interactions with Materials and Atoms 204 (2003) 492. doi:/10.1016/S0168-583X(02)02118-3.

[75] A. Voss, T. Procter, O. Shelbaya, P. Amaudruz, F. Buchinger, J. Crawford, S. Daviel, E. Mané, M. Pearson, W. A. Tamimi, The Collinear Fast Beam laser Spectroscopy ($C_{FBS}$) experiment at TRIUMF, Nuclear Instruments and Methods in Physics Research Section A: Accelerators, Spectrometers, Detectors and Associated Equipment 811 (2016) 57. doi:/10.1016/j.nima.2015.11.145.

[76] A. Voss, M. R. Pearson, F. Buchinger, J. E. Crawford, R. F. Kiefl, C. D. P. Levy, W. A. MacFarlane, E. Mané, G. D. Morris, O. T. J. Shelbaya, Q. Song, D. Wang, High precision measurement of the 11Li and 9Li quadrupole moment ratio using zero-field β-NQR, Journal of Physics G: Nuclear and Particle Physics 41 (2013) 015104. doi:/10.1088/0954-3899/41/1/015104.

[77] E. J. Prime, J. Lassen, T. Achtzehn, D. Albers, P. Bricault, T. Cocolios, M. Dombsky, F. Labrecque, J. P. Lavoie, M. R. Pearson, T. Stubbe, N. Lecesne, C. Geppert, K. D. A. Wendt, TRIUMF resonant ionization laser ion source, Hyperfine Interactions 171 (2006) 127. doi:/10.1007/s10751-006-9493-0.

[78] P. Kunz, C. Andreoiu, P. Bricault, M. Dombsky, J. Lassen, A. Teigelhöfer, H. Heggen, F. Wong, Nuclear and in-source laser spectroscopy with the ISAC yield station, Review of Scientific Instruments 85 (2014) 053305. doi:/10.1063/1.4878718.

[79] E. M. Lykiardopoulou, G. Audi, T. Dickel, W. J. Huang, D. Lunney, W. R. Plaß, M. P. Reiter, J. Dilling, A. A. Kwiatkowski, Exploring the limits of existence of proton-rich nuclei in the $Z = 70 - -82$ region, Physical Review C 107 (2023) 024311. doi:/10.1103/PhysRevC.107.024311.

[80] J. Dilling, R. Krücken, L. Merminga, ARIEL overview, 2014, p. 253. doi:/10.1007/978-94-007-7963-1$_3$0.

[81] G. Münzenberg, P. Armbruster, H. Folger, P. F. Heßberger, S. Hofmann, J. Keller, K. Poppensieker, W. Reisdorf, K.-H. Schmidt, H.-J. Schött, M. E. Leino, R. Hingmann, The identification of element 108, Zeitschrift für Physik A Atoms and Nuclei 317 (1984) 235. doi:/10.1007/BF01421260.

[82] G. Münzenberg, P. Armbruster, F. P. Heßberger, S. Hofmann, K. Poppensieker, W. Reisdorf, J. H. R. Schneider, W. F. W. Schneider, K.-H. Schmidt, C.-C. Sahm, D. Vermeulen, Observation of one correlated α-decay in the reaction $^{58}$Fe on $^{209}$Bi→ $^{267}$109, Zeitschrift für Physik A Atoms and Nuclei 309 (1982) 89. doi:/10.1007/BF01420157.

[83] S. Hofmann, V. Ninov, F. P. Heßberger, P. Armbruster, H. Folger, G. Münzenberg, H. J. Schött, A. G. Popeko, A. V. Yeremin, A. N. Andreyev, S. Saro, R. Janik, M. Leino, Production and decay of $^{269}$110, Zeitschrift für Physik A Hadrons and Nuclei 350 (1995) 277. doi:/10.1007/BF01291181.

[84] S. Hofmann, V. Ninov, F. P. Heßberger, P. Armbruster, H. Folger, G. Münzenberg, H. J. Schött, A. G. Popeko, A. V. Yeremin, A. N. Andreyev, S. Saro, R. Janik, M. Leino, The new element 111, Zeitschrift für Physik A Hadrons and Nuclei 350 (1995) 281. doi:/10.1007/BF01291182.

[85] S. Hofmann, V. Ninov, F. P. Heßberger, P. Armbruster, H. Folger, G. Münzenberg, H. J. Schött, A. G. Popeko, A. V. Yeremin, S. Saro, R. Janik, M. Leino, The new element 112, Zeitschrift für Physik A Hadrons and Nuclei 354 (1996) 229. doi:/10.1007/BF02769517.

[86] G. Münzenberg, W. Faust, S. Hofmann, P. Armbruster, K. Güttner, H. Ewald, The velocity filter ship, a separator of unslowed heavy ion fusion products, Nuclear Instruments and Methods 161 (1979) 65. doi:/10.1016/0029-554X(79)90362-8.

[87] M. Laatiaoui, H. Backe, M. Block, F.-P. Heßberger, P. Kunz, F. Lautenschläger, W. Lauth, M. Sewtz, T. Walther, On laser spectroscopy of the element nobelium (Z = 102), The European Physical Journal D 68 (2014) 71. doi:/10.1140/epjd/e2014-40617-6.

[88] J. Warbinek, B. Anđelić, M. Block, P. Chhetri, A. Claessens, R. Ferrer, F. Giacoppo, O. Kaleja, T. Kieck, E. Kim, M. Laatiaoui, J. Lantis, A. Mistry, D. Münzberg, S. Nothhelfer, S. Raeder, E. Rey-Herme, E. Rickert, J. Romans, E. Romero-Romero, M. Vandebrouck, P. Van Duppen, T. Walther, Advancing Radiation-Detected Resonance Ionization towards Heavier Elements and More Exotic Nuclides, Atoms 10 (2022). doi:/10.3390/atoms10020041.

[89] J. Dilling, D. Ackermann, J. Bernard, F. P. Hessberger, S. Hofmann, W. Hornung, H. J. Kluge, E. Lamour, M. Maier, R. Mann, G. Marx, R. B. Moore, G. Münzenberg, W. Quint, D. Rodriguez, M. Schädel, J. Schönfelder, G. Sikler, C. Toader, L. Vermeeren, C. Weber, G. Bollen, O. Engels, D. Habs, P. Thirolf, H. Backe, A. Dretzke, W. Lauth, W. Ludolphs, M. Sewtz, The SHIPTRAP project: A capture and storage facility at GSI for heavy radionuclides from SHIP, Hyperfine Interactions 127 (2000) 491. doi:/10.1023/A:1012638322226.

[90] S. Schmidt, C. Geppert, Z. Andelkovic, Laser spectroscopy methods for probing highly charged ions at GSI, Hyperfine Interactions 227 (2014) 29. doi:/10.1007/s10751-014-1048-1.

[91] A. Semchenkov, W. Brüchle, E. Jäger, E. Schimpf, M. Schädel, C. Mühle, F. Klos, A. Türler, A. Yakushev, A. Belov, T. Belyakova, M. Kaparkova, V. Kukhtin, E. Lamzin, S. Sytchevsky, The TransActinide Separator and Chemistry Apparatus (TASCA) at GSI – Optimization of ion-optical structures and magnet designs, Nuclear Instruments and Methods in Physics Research Section B: Beam Interactions with Materials and Atoms 266 (2008) 4153. doi:/10.1016/j.nimb.2008.05.132.

[92] L.-L. Andersson, D. Rudolph, P. Golubev, R.-D. Herzberg, R. Hoischen, E. Merchán, D. Ackermann, C. Düllmann, K. Eberhardt, J. Even, J. Gerl, F. Heßberger, E. Jäger, J. Khuyagbaatar, I. Kojouharov, J. Kratz, J. Krier, N. Kurz, W. Prokopowicz, M. Schädel, H. Schaffner, B. Schausten, E. Schimpf, A. Semchenkov, A. Türler, H.-J. Wollersheim, A. Yakushev, P. Thörle-Pospiech, W. Hartmann, A. Hübner, B. Lommel, B. Kindler, J. Steiner, TASISpec—A highly efficient multi-coincidence spectrometer for nuclear structure investigations of the heaviest nuclei, Nuclear Instruments and Methods in Physics Research Section A: Accelerators, Spectrometers, Detectors and Associated Equipment 622 (2010) 164. doi:/10.1016/j.nima.2010.06.243.

[93] A. Bronis, F. P. Heßberger, S. Antalic, B. Andel, D. Ackermann, S. Heinz, S. Hofmann, J. Khuyagbaatar, B. Kindler, I. Kojouharov, P. Kuusiniemi, M. Leino, B. Lommel, R. Mann, K. Nishio, A. G. Popeko, B. Streicher, B. Sulignano, J. Uusitalo, M. Venhart, A. V. Yeremin, Decay studies of new isomeric states in $^{255}$No, Physical Review C 106 (2022) 014602. doi:/10.1103/PhysRevC.106.014602.

[94] D. M. Cox, A. Såmark-Roth, D. Rudolph, L. G. Sarmiento, R. M. Clark, J. L. Egido, P. Golubev, J. Heery, A. Yakushev, S. Åberg, H. M. Albers, M. Albertsson, M. Block, H. Brand, T. Calverley, R. Cantemir, B. G. Carlsson, C. E. Düllmann, J. Eberth, C. Fahlander, U. Forsberg, J. M. Gates, F. Giacoppo, M. Götz, S. Götz, R.-D. Herzberg, Y. Hrabar, E. Jäger, D. Judson, J. Khuyagbaatar, B. Kindler, I. Kojouharov, J. V. Kratz, J. Krier, N. Kurz, L. Lens, J. Ljungberg, B. Lommel, J. Louko, C.-C. Meyer, A. Mistry, C. Mokry, P. Papadakis, E. Parr, J. L. Pore, I. Ragnarsson, J. Runke, M. Schädel, H. Schaffner, B. Schausten, D. A. Shaughnessy, P. Thörle-Pospiech, N. Trautmann, J. Uusitalo, Spectroscopy along flerovium decay chains. II. Fine structure in odd-$A$ $^{289}$Fl, Physical Review C 107 (2023) L021301. doi:/10.1103/PhysRevC.107.L021301.

[95] J. Khuyagbaatar, on behalf of the GSI-JYFL Collaboration, Results of the JM20 experiment, *To be published*.

[96] K. Blasche, D. Böhne, B. Franzke, H. Prange, The SIS Heavy Ion Synchrotron Project, IEEE Transactions on Nuclear Science NS-32 (1985) 2657. doi:/10.1109/TNS.1985.4334010.

[97] H. Geissel, P. Armbruster, K. Behr, A. Brünle, K. Burkard, M. Chen, H. Folger, B. Franczak, H. Keller, O. Klepper, B. Langenbeck, F. Nickel, E. Pfeng, M. Pfützner, E. Roeckl, K. Rykaczewski, I. Schall, D. Schardt, C. Scheidenberger, K.-H. Schmidt, A. Schröter, T. Schwab, K. Sümmerer, M. Weber, G. Münzenberg, T. Brohm, H.-G. Clerc, M. Fauerbach, J.-J. Gaimard, A. Grewe, E. Hanelt, B. Knödler, M. Steiner, B. Voss, J. Weckenmann, C. Ziegler, A. Magel, H. Wollnik, J. Dufour, Y. Fujita, D. Vieira, B. Sherrill, The GSI projectile fragment separator (FRS): a versatile magnetic system for relativistic heavy ions, Nuclear Instruments and Methods in Physics Research Section B: Beam Interactions with Materials and Atoms 70 (1992) 286. doi:/10.1016/0168-583X(92)95944-M.

160

[98] B. Franzke, The heavy ion storage and cooler ring project ESR at GSI, Nuclear Instruments and Methods in Physics Research Section B: Beam Interactions with Materials and Atoms 24-25 (1987) 18. doi:/10.1016/0168-583X(87)90583-0.

[99] R. Schneider, J. Friese, J. Reinhold, K. Zeitelhack, T. Faestermann, R. Gernhäuser, H. Gilg, F. Heine, J. Homolka, P. Kienle, H. Körner, H. Geissel, G. Münzenberg, K. Sümmerer, Identification of 100Sn, Nuclear Physics A 583 (1995) 853. doi:/10.1016/0375-9474(94)00773-G.

[100] M. Bernas, Production and $\beta$-Decay Half-Lives of Very N-Rich Nuclei, 2002, p. 71. doi:/10.1007/0-306-46927-8$_6$.

[101] An international accelerator facility for beams of ions and anti-protons. Conceptual design report (2001).

[102] C. Engelmann, F. Ameil, P. Armbruster, M. Bernas, S. Czajkowski, P. Dessagne, C. Donzaud, H. Geissel, A. Heinz, Z. Janas, C. Kozhuharov, C. Miehé, G. Münzenberg, M. Pfützner, C. Röhl, W. Schwab, C. Stéphan, K. Sümmerer, L. Tassan-Got, B. Voss, Production and identification of heavy Ni isotopes: evidence for the doubly magic nucleus $^{78}_{28}$Ni, Zeitschrift für Physik A: Hadrons and Nuclei 352 (1995) 351. doi:/10.1007/BF01299748.

[103] P. Spiller, G. Franchetti, The FAIR accelerator project at GSI, Nuclear Instruments and Methods in Physics Research Section A: Accelerators, Spectrometers, Detectors and Associated Equipment 561 (2006) 305. doi:/10.1016/j.nima.2006.01.043.

[104] H. Geissel, H. Weick, M. Winkler, G. Münzenberg, V. Chichkine, M. Yavor, T. Aumann, K. Behr, M. Böhmer, A. Brünle, K. Burkard, J. Benlliure, D. Cortina-Gil, L. Chulkov, A. Dael, J.-E. Ducret, H. Emling, B. Franczak, J. Friese, B. Gastineau, J. Gerl, R. Gernhäuser, M. Hellström, B. Jonson, J. Kojouharova, R. Kulessa, B. Kindler, N. Kurz, B. Lommel, W. Mittig, G. Moritz, C. Mühle, J. Nolen, G. Nyman, P. Roussell-Chomaz, C. Scheidenberger, K.-H. Schmidt, G. Schrieder, B. Sherrill, H. Simon, K. Sümmerer, N. Tahir, V. Vysotsky, H. Wollnik, A. Zeller, The Super-FRS project at GSI, Nuclear Instruments and Methods in Physics Research Section B: Beam Interactions with Materials and Atoms 204 (2003) 71. doi:/10.1016/S0168-583X(02)01893-1.

[105] D. Rodríguez, K. Blaum, W. Nörtershäuser, M. Ahammed, A. Algora, G. Audi, J. Äystö, D. Beck, M. Bender, J. Billowes, M. Block, C. Böhm, G. Bollen, M. Brodeur, T. Brunner, B. A. Bushaw, R. B. Cakirli, P. Campbell, D. Cano-Ott, G. Cortés, J. R. Crespo López-Urrutia, P. Das, A. Dax, A. De, P. Delheij, T. Dickel, J. Dilling, K. Eberhardt, S. Eliseev, S. Ettenauer, K. T. Flanagan, R. Ferrer, J.-E. García-Ramos, E. Gartzke, H. Geissel, S. George, C. Geppert, M. B. Gómez-Hornillos, Y. Gusev, D. Habs, P.-H. Heenen, S. Heinz, F. Herfurth, A. Herlert, M. Hobein, G. Huber, M. Huyse, C. Jesch, A. Jokinen, O. Kester, J. Ketelaer, V. Kolhinen, I. Koudriavtsev, M. Kowalska, J. Krämer, S. Kreim, A. Krieger, T. Kühl, A. M. Lallena, A. Lapierre, F. Le Blanc, Y. A. Litvinov, D. Lunney, T. Martínez,

G. Marx, M. Matos, E. Minaya-Ramirez, I. Moore, S. Nagy, S. Naimi, D. Neidherr, D. Nesterenko, G. Neyens, Y. N. Novikov, M. Petrick, W. R. Plaß, A. Popov, W. Quint, A. Ray, P.-G. Reinhard, J. Repp, C. Roux, B. Rubio, R. Sánchez, B. Schabinger, C. Scheidenberger, D. Schneider, R. Schuch, S. Schwarz, L. Schweikhard, M. Seliverstov, A. Solders, M. Suhonen, J. Szerypo, J. L. Taín, P. G. Thirolf, J. Ullrich, P. Van Duppen, A. Vasiliev, G. Vorobjev, C. Weber, K. Wendt, M. Winkler, D. Yordanov, F. Ziegler, MATS and LaSpec: High-precision experiments using ion traps and lasers at FAIR, The European Physical Journal Special Topics 183 (2010) 1. doi:10.1140/epjst/e2010-01231-2.

[106] H.-J. Kluge, T. Beier, K. Blaum, L. Dahl, S. Eliseev, F. Herfurth, B. Hofmann, O. Kester, S. Koszudowski, C. Kozhuharov, G. Maero, W. Nörtershäuser, J. Pfister, W. Quint, U. Ratzinger, A. Schempp, R. Schuch, T. Stöhlker, R. Thompson, M. Vogel, G. Vorobjev, D. Winters, G. Werth, Chapter 7 HITRAP: A Facility at GSI for Highly Charged Ions, in: S. Salomonson, E. Lindroth (Eds.), Current Trends in Atomic Physics, Vol. 53 of Advances in Quantum Chemistry, Academic Press, 2008, p. 83. doi:/10.1016/S0065-3276(07)53007-8.

[107] The FRIB Science Community, FRIB400 - The Scientific Case for the 400 MeV/u Energy Upgrade of FRIB (2023).
URL https://frib.msu.edu/_files/pdfs/frib400_final.pdf

[108] D. Morrissey, B. Sherrill, M. Steiner, A. Stolz, I. Wiedenhoever, Commissioning the A1900 projectile fragment separator, Nuclear Instruments and Methods in Physics Research Section B: Beam Interactions with Materials and Atoms 204 (2003) 90. doi:/10.1016/S0168-583X(02)01895-5.

[109] S. Schwarz, G. Bollen, D. Lawton, P. Lofy, D. Morrissey, J. Ottarson, R. Ringle, P. Schury, T. Sun, V. Varentsov, L. Weissman, The low-energy-beam and ion-trap facility at NSCL/MSU, Nuclear Instruments and Methods in Physics Research Section B: Beam Interactions with Materials and Atoms 204 (2003) 507. doi:/10.1016/S0168-583X(02)02122-5.

[110] A. Hamaker, G. Bollen, M. Eibach, C. Izzo, D. Puentes, M. Redshaw, R. Ringle, R. Sandler, S. Schwarz, I. Yandow, SIPT - An ultrasensitive mass spectrometer for rare isotopes, Hyperfine Interactions 240 (2019) 34. doi:/10.1007/s10751-019-1576-9.

[111] K. Minamisono, P. Mantica, A. Klose, S. Vinnikova, A. Schneider, B. Johnson, B. Barquest, Commissioning of the collinear laser spectroscopy system in the BECOLA facility at NSCL, Nuclear Instruments and Methods in Physics Research Section A: Accelerators, Spectrometers, Detectors and Associated Equipment 709 (2013) 85. doi:/10.1016/j.nima.2013.01.038.

[112] A. Hamaker, E. Leistenschneider, R. Jain, G. Bollen, S. A. Giuliani, K. Lund, W. Nazarewicz, L. Neufcourt, C. R. Nicoloff, D. Puentes, R. Ringle, C. S. Sumithrarachchi, I. T. Yandow, Precision mass measurement of lightweight self-

162

conjugate nucleus 80Zr, Nature Physics 17 (2021) 1408. doi:/10.1038/s41567-021-01395-w.

[113] S. Schwarz, B. Barquest, G. Bollen, R. Ferrer, A. Kwiatkowski, D. Lincoln, D. Morrissey, R. Ringle, J. Savory, High-precision mass measurements of Ge and As isotopes near N = Z, Nuclear Physics A 989 (2019) 201. doi:/10.1016/j.nuclphysa.2019.06.007.

[114] A. A. Valverde, M. Brodeur, G. Bollen, M. Eibach, K. Gulyuz, A. Hamaker, C. Izzo, W.-J. Ong, D. Puentes, M. Redshaw, R. Ringle, R. Sandler, S. Schwarz, C. S. Sumithrarachchi, J. Surbrook, A. C. C. Villari, I. T. Yandow, High-Precision Mass Measurement of $^{56}$Cu and the Redirection of the $rp$-Process Flow, Physical Review Letters 120 (2018) 032701. doi:/10.1103/PhysRevLett.120.032701.

[115] C. Izzo, G. Bollen, M. Brodeur, M. Eibach, K. Gulyuz, J. D. Holt, J. M. Kelly, M. Redshaw, R. Ringle, R. Sandler, S. Schwarz, S. R. Stroberg, C. S. Sumithrarachchi, A. A. Valverde, A. C. C. Villari, Precision mass measurements of neutron-rich Co isotopes beyond $N = 40$, Physical Review C 97 (2018) 014309. doi:/10.1103/PhysRevC.97.014309.

[116] E. Leistenschneider, E. Dunling, G. Bollen, B. A. Brown, J. Dilling, A. Hamaker, J. D. Holt, A. Jacobs, A. A. Kwiatkowski, T. Miyagi, W. S. Porter, D. Puentes, M. Redshaw, M. P. Reiter, R. Ringle, R. Sandler, C. S. Sumithrarachchi, A. A. Valverde, I. T. Yandow, Precision Mass Measurements of Neutron-Rich Scandium Isotopes Refine the Evolution of $N = 32$ and $N = 34$ Shell Closures, Physical Review Letters 126 (2021) 042501. doi:/10.1103/PhysRevLett.126.042501.

[117] F. Sommer, K. König, D. M. Rossi, N. Everett, D. Garand, R. P. de Groote, J. D. Holt, P. Imgram, A. Incorvati, C. Kalman, A. Klose, J. Lantis, Y. Liu, A. J. Miller, K. Minamisono, T. Miyagi, W. Nazarewicz, W. Nörtershäuser, S. V. Pineda, R. Powel, P.-G. Reinhard, L. Renth, E. Romero-Romero, R. Roth, A. Schwenk, C. Sumithrarachchi, A. Teigelhöfer, Charge Radii of $^{55,56}$Ni Reveal a Surprisingly Similar Behavior at $N = 28$ in Ca and Ni Isotopes, Physical Review Letters 129 (2022) 132501. doi:/10.1103/PhysRevLett.129.132501.

[118] M. J. G. Borge, B. Jonson, ISOLDE past, present and future, Journal of Physics G: Nuclear and Particle Physics 44 (2017) 044011. doi:/10.1088/1361-6471/aa5f03.

[119] E. Kugler, D. Fiander, B. Johnson, H. Haas, A. Przewloka, H. Ravn, D. Simon, K. Zimmer, The new cern-isolde on-line mass-separator facility at the ps-booster, Nuclear Instruments and Methods in Physics Research Section B: Beam Interactions with Materials and Atoms 70 (1992) 41. doi:/10.1016/0168-583X(92)95907-9.

[120] Y. Kadi, M. A. Fraser, A. Papageorgiou-Koufidou, HIE-ISOLDE : technical design report for the energy upgrade, CERN Yellow Reports: Monographs (2018). doi:/10.23731/CYRM-2018-001.

[121] M. Alcorta, A. N. Andreyev, P. A. Butler, J. Cederkäll, T. E. Cocolios, F. Flavigny, B. Fulton, H. O. U. Fynbo, L. Gaffney, R. Gernhäuser, D. G. Jenkins, D. Joss, B. P.

Kay, O. S. Kirsebom, S. Klupp, M. Labiche, A. Moro, A. Murphy, D. Mücher, G. O'Neill, K. Nowak, R. Orlandi, R. D. Page, R. Raabe, A. H. Wuosmaa, $d(^{11}\text{Be}, t)$ studied with a new solenoidal spectrometer, Tech. rep., CERN, Geneva (2012). URL https://cds.cern.ch/record/1482709

[122] H. Fynbo, O. S. Kirseboom, O. Tengblad, Isolde decay station for decay studies of interest in astrophysics and exotic nuclei, Journal of Physics G: Nuclear and Particle Physics 44 (2017) 044005. doi:10.1088/1361-6471/aa5e09.

[123] E. Nacher, A. Algora, B. Rubio, Upgrade and scientific programme of LUCRECIA, the Total Absorption Spectrometer at ISOLDE, Tech. rep., CERN, Geneva (2020). URL https://cds.cern.ch/record/2705974

[124] J. Eberth, G. Pascovici, H. Thomas, N. Warr, D. Weisshaar, D. Habs, P. Reiter, P. Thirolf, D. Schwalm, C. Gund, H. Scheit, M. Lauer, P. Van Duppen, S. Franchoo, M. Huyse, R. Lieder, W. Gast, J. Gerl, K. Lieb, MINIBALL A Ge detector array for radioactive ion beam facilities, Progress in Particle and Nuclear Physics 46 (2001) 389. doi:/10.1016/S0146-6410(01)00145-4.

[125] R. Neugart, S. L. Kaufman, W. Klempt, G. Moruzzi, E.-W. Otten, B. Schinzler, High-resolution spectroscopy in fast atomic beams, in: Laser Spectroscopy III, 1977, p. 446.

[126] K. Flanagan, CRIS: A New Sensitive Device for Laser Spectroscopy of Exotic Nuclei, Nuclear Physics News 23 (2013) 24. doi:/10.1080/10619127.2013.793094.

[127] V. Lagaki, H. Heylen, I. Belosevic, P. Fischer, C. Kanitz, S. Lechner, F. Maier, W. Nörtershäuser, P. Plattner, M. Rosenbusch, S. Sels, L. Schweikhard, M. Vilen, F. Wienholtz, R. Wolf, S. Malbrunot-Ettenauer, An accuracy benchmark of the MIRACLS apparatus: Conventional, single-passage collinear laser spectroscopy inside a MR-ToF device, Nuclear Instruments and Methods in Physics Research Section A: Accelerators, Spectrometers, Detectors and Associated Equipment 1014 (2021) 165663. doi:/10.1016/j.nima.2021.165663.

[128] H. Schnatz, G. Bollen, P. Dabkiewicz, P. Egelhof, F. Kern, H. Kalinowsky, L. Schweikhard, H. Stolzenberg, H.-J. Kluge, In-flight capture of ions into a penning trap, Nuclear Instruments and Methods in Physics Research Section A: Accelerators, Spectrometers, Detectors and Associated Equipment 251 (1986) 17. doi:/10.1016/0168-9002(86)91145-9.

[129] L. Nies, D. Atanasov, M. Athanasakis-Kaklamanakis, M. Au, K. Blaum, J. Dobaczewski, B. S. Hu, J. D. Holt, J. Karthein, I. Kulikov, Y. A. Litvinov, D. Lunney, V. Manea, T. Miyagi, M. Mougeot, L. Schweikhard, A. Schwenk, K. Sieja, F. Wienholtz, Isomeric Excitation Energy for $^{99}\text{In}^m$ from Mass Spectrometry Reveals Constant Trend Next to Doubly Magic $^{100}\text{Sn}$, Physical Review Letters 131 (2023) 022502. doi:/10.1103/PhysRevLett.131.022502.

[130] D. T. Yordanov, L. V. Rodríguez, D. L. Balabanski, J. Bieroń, M. L. Bissell, K. Blaum, B. Cheal, J. Ekman, G. Gaigalas, R. F. Garcia Ruiz, G. Georgiev, W. Gins,

M. R. Godefroid, C. Gorges, Z. Harman, H. Heylen, P. Jönsson, A. Kanellakopoulos, S. Kaufmann, C. H. Keitel, V. Lagaki, S. Lechner, B. Maaß, S. Malbrunot-Ettenauer, W. Nazarewicz, R. Neugart, G. Neyens, W. Nörtershäuser, N. S. Oreshkina, A. Papoulia, P. Pyykkö, P.-G. Reinhard, S. Sailer, R. Sánchez, S. Schiffmann, S. Schmidt, L. Wehner, C. Wraith, L. Xie, Z. Xu, X. Yang, Structural trends in atomic nuclei from laser spectroscopy of tin, Communications Physics 3 (2020) 107. doi:/10.1038/s42005-020-0348-9.

[131] J. Sarén, The ion-optical design of the MARA recoil separator and absolute transmission measurements of the RITU gas-filled recoil separator, PhD thesis, University of Jyväskylä (2011).

[132] H. Ikezoe, T. Ikuta, S. Mitsuoka, S. Hamada, Y. Nagame, I. Nishinaka, Y. Tsukada, Y. Oura, T. Ohtsuki, The feature of the jaeri recoil mass separator, Nuclear Instruments and Methods in Physics Research Section B: Beam Interactions with Materials and Atoms 126 (1997) 340, international Conference on Electromagnetic Isotope Separators and Techniques Related to Their Applications. doi:/10.1016/S0168-583X(96)01005-1.

[133] C. Davids, B. Back, K. Bindra, D. Henderson, W. Kutschera, T. Lauritsen, Y. Nagame, P. Sugathan, A. Ramayya, W. Walters, Startup of the Fragment Mass Analyzer at ATLAS, Nuclear Instruments and Methods in Physics Research Section B: Beam Interactions with Materials and Atoms 70 (1992) 358. doi:/10.1016/0168-583X(92)95951-M.

[134] B. Davids, C. N. Davids, Emma: A recoil mass spectrometer for isac-ii at triumf, Nuclear Instruments and Methods in Physics Research Section A: Accelerators, Spectrometers, Detectors and Associated Equipment 544 (2005) 565. doi:/10.1016/j.nima.2005.01.297.

[135] C. J. Lister, M. Campbell, A. A. Chishti, W. Gelletly, L. Goettig, R. Moscrop, B. J. Varley, A. N. James, T. Morrison, H. G. Price, J. Simpson, K. Connel, O. Skeppstedt, Gamma radiation from the N=Z nucleus $^{80}_{40}$Zr$_{40}$, Physical Review Letters 59 (1987) 1270. doi:/10.1103/PhysRevLett.59.1270.

[136] R. Ferrer, A. Barzakh, B. Bastin, R. Beerwerth, M. Block, P. Creemers, H. Grawe, R. de Groote, P. Delahaye, X. Fléchard, S. Franchoo, S. Fritzsche, L. P. Gaffney, L. Ghys, W. Gins, C. Granados, R. Heinke, L. Hijazi, M. Huyse, T. Kron, Yu. Kudryavtsev, M. Laatiaoui, N. Lecesne, M. Loiselet, F. Lutton, I. D. Moore, Y. Martínez, E. Mogilevskiy, P. Naubereit, J. Piot, S. Raeder, S. Rothe, H. Savajols, S. Sels, V. Sonnenschein, J.-C. Thomas, E. Traykov, C. Van Beveren, P. Van den Bergh, P. Van Duppen, K. Wendt, A. Zadvornaya, Towards high-resolution laser ionization spectroscopy of the heaviest elements in supersonic gas jet expansion, Nature Communications 8 (2017) 14520. doi:/10.1038/ncomms14520.

[137] M. Laatiaoui, W. Lauth, H. Backe, M. Block, D. Ackermann, B. Cheal, P. Chhetri, C. E. Düllmann, P. van Duppen, J. Even, R. Ferrer, F. Giacoppo, S. Götz, F. P. Heßberger, M. Huyse, O. Kaleja, J. Khuyagbaatar, P. Kunz, F. Lautenschläger,

A. K. Mistry, S. Raeder, E. M. Ramirez, T. Walther, C. Wraith, A. Yakushev, Atom-at-a-time laser resonance ionization spectroscopy of nobelium, Nature 538 (2016) 495. doi:/10.1038/nature19345.

[138] G. Samuel Hurst, V. S. Letokhov, Resonance Ionization Spectroscopy, Physics Today 47 (1994) 38. doi:/10.1063/1.881420.

[139] A new highly efficient method of atomic spectroscopy for nuclides far from stability, Nuclear Instruments and Methods in Physics Research Section B: Beam Interactions with Materials and Atoms 69 (1992) 517. doi:/10.1016/0168-583X(92)95309-F.

[140] V. Fedosseev, D. Fedorov, R. Horn, G. Huber, U. Köster, J. Lassen, V. Mishin, M. Seliverstov, L. Weissman, K. Wendt, Atomic spectroscopy studies of short-lived isotopes and nuclear isomer separation with the isolde rilis, Nuclear Instruments and Methods in Physics Research Section B: Beam Interactions with Materials and Atoms 204 (2003) 353. doi:/10.1016/S0168-583X(02)01959-6.

[141] L. Vermeeren, N. Bijnens, M. Huyse, Yu. A. Kudryavtsev, P. Van Duppen, J. Wauters, Z. N. Qamhieh, P. Thoen, E. Vandeweert, R. E. Silverans, An on-line laser ion source based on resonance photoionization in a gas cell, Physical Review Letters 73 (1994) 1935. doi:/10.1103/PhysRevLett.73.1935.

[142] Yu. Kudryavtsev, R. Ferrer, M. Huyse, P. Van den Bergh, P. Van Duppen, The in-gas-jet laser ion source: Resonance ionization spectroscopy of radioactive atoms in supersonic gas jets, Nuclear Instruments and Methods in Physics Research Section B: Beam Interactions with Materials and Atoms 297 (2013) 7. doi:/10.1016/j.nimb.2012.12.008.

[143] R. Ferrer, B. Bastin, D. Boilley, P. Creemers, P. Delahaye, E. Liénard, X. Fléchard, S. Franchoo, L. Ghys, M. Huyse, Yu. Kudryavtsev, N. Lecesne, H. Lu, F. Lutton, E. Mogilevskiy, D. Pauwels, J. Piot, D. Radulov, L. Rens, H. Savajols, J. Thomas, E. Traykov, C. Van Beveren, P. Van den Bergh, P. Van Duppen, In gas laser ionization and spectroscopy experiments at the Superconducting Separator Spectrometer ($S^3$): Conceptual studies and preliminary design, Nuclear Instruments and Methods in Physics Research Section B: Beam Interactions with Materials and Atoms 317 (2013) 570. doi:/10.1016/j.nimb.2013.07.028.

[144] M. Reponen, I. Moore, I. Pohjalainen, V. Sonnenschein, A. Jokinen, The FURIOS laser ion source at IGISOL-4, Nuclear Instruments and Methods in Physics Research Section B: Beam Interactions with Materials and Atoms 317 (2013) 422. doi:/10.1016/j.nimb.2013.05.061.

[145] Mesa$^{TM}$ Diode pumped Nd:YAG laser., Accessed: October 2023.
URL https://amplitude-laser.com/wp-content/uploads/2019/01/Mesa_ref-f.pdf

[146] M. Reponen, V. Sonnenschein, T. Sonoda, H. Tomita, M. Oohashi, D. Matsui, M. Wada, Towards in-jet resonance ionization spectroscopy: An injection-locked

Titanium:Sapphire laser system for the PALIS-facility, Nuclear Instruments and Methods in Physics Research Section A: Accelerators, Spectrometers, Detectors and Associated Equipment 908 (2018) 236. doi:/10.1016/j.nima.2018.08.073.

[147] H. Wollnik, M. Przewloka, Time-of-flight mass spectrometers with multiply reflected ion trajectories, International Journal of Mass Spectrometry and Ion Processes 96 (1990) 267. doi:/10.1016/0168-1176(90)85127-N.

[148] R. Wolf, D. Beck, K. Blaum, C. Böhm, C. Borgmann, M. Breitenfeldt, F. Herfurth, A. Herlert, M. Kowalska, S. Kreim, D. Lunney, S. Naimi, D. Neidherr, M. Rosenbusch, L. Schweikhard, J. Stanja, F. Wienholtz, K. Zuber, On-line separation of short-lived nuclei by a multi-reflection time-of-flight device, Nuclear Instruments and Methods in Physics Research Section A: Accelerators, Spectrometers, Detectors and Associated Equipment 686 (2012) 82. doi:/10.1016/j.nima.2012.05.067.

[149] R. Wolf, F. Wienholtz, D. Atanasov, D. Beck, K. Blaum, C. Borgmann, F. Herfurth, M. Kowalska, S. Kreim, Y. A. Litvinov, D. Lunney, V. Manea, D. Neidherr, M. Rosenbusch, L. Schweikhard, J. Stanja, K. Zuber, ISOLTRAP's multi-reflection time-of-flight mass separator/spectrometer, International Journal of Mass Spectrometry (2013) 123doi:/10.1016/j.ijms.2013.03.020.

[150] M. Rosenbusch, M. Wada, S. Chen, A. Takamine, S. Iimura, D. Hou, W. Xian, S. Yan, P. Schury, Y. Hirayama, Y. Ito, H. Ishiyama, S. Kimura, T. Kojima, J. Lee, J. Liu, S. Michimasa, H. Miyatake, J. Moon, M. Mukai, S. Naimi, S. Nishimura, T. Niwase, T. Sonoda, Y. Watanabe, H. Wollnik, The new MRTOF mass spectrograph following the ZeroDegree spectrometer at RIKEN's RIBF facility, Nuclear Instruments and Methods in Physics Research Section A: Accelerators, Spectrometers, Detectors and Associated Equipment 1047 (2023) 167824. doi:/10.1016/j.nima.2022.167824.

[151] A. Nieminen, J. Huikari, A. Jokinen, J. Äystö, P. Campbell, E. Cochrane, Beam cooler for low-energy radioactive ions, Nuclear Instruments and Methods in Physics Research Section A: Accelerators, Spectrometers, Detectors and Associated Equipment 469 (2001) 244. doi:/10.1016/S0168-9002(00)00750-6.

[152] V. Virtanen, Offline commissioning of the multi-reflection time-of-flight mass separator at JYFLTRAP, Master thesis, University of Jyväskylä (2019).

[153] V. Virtanen, *To be published*, PhD thesis, University of Jyväskylä.

[154] E. Mané, J. Billowes, K. Blaum, P. Campbell, B. Cheal, P. Delahaye, K. T. Flanagan, D. H. Forest, H. Franberg, C. Geppert, T. Giles, A. Jokinen, M. Kowalska, R. Neugart, G. Neyens, W. Nörtershäuser, I. Podadera, G. Tungate, P. Vingerhoets, D. T. Yordanov, An ion cooler-buncher for high-sensitivity collinear laser spectroscopy at ISOLDE, The European Physical Journal A 42 (2009) 503.

[155] B. S. Cooper, H. A.Perrett, C. M. Ricketts, C. Read, G. Edwards, K. T. Flanagan, J. Billowes, C. L. Binnersley, M. L. Bissell, T. E. Cocolios, R. P. de Groote, G. J.

Farooq-Smith, R. F. G. Ruiz, W. Gins, A. Koszorus, G. Neyens, F. P-Gustafsson, H. H. Stroke, A. R. Vernon, K. D. A. Wendt, S. G. Wilkins, X. F. Yang, A compact RFQ cooler buncher for CRIS experiments, Hyperfine Interactions 240 (2019) 52. doi:/10.1007/s10751-019-1586-7.

[156] J. Ruotsalainen, Design of FAIR low-energy cooler-buncher with simulations, Master thesis, University of Jyväskylä (2021).

[157] Edwards Vacuum, Accessed: May 2023.
URL https://www.edwardsvacuum.com/

[158] A. Roth, Vacuum Technology. Third, Updated and Enlarged Edition, ISBN 9780444598745 (1990).

[159] Comsol Multiphysics, Accessed: May 2023.
URL https://www.comsol.com

[160] A. Zadvornaya, J. Romero, T. Eronen, W. Gins, A. Kankainen, I. Moore, P. Papadakis, I. Pohjalainen, M. Reponen, S. Rinta-Antila, J. Sarén, D. Simonovski, J. Uusitalo, Offline Commissioning of a New Gas Cell for the MARA Low-Energy Branch, Nuclear Instruments and Methods in Physics Research Section B: Beam Interactions with Materials and Atoms 539 (2023) 33. doi:/10.1016/j.nimb.2023.03.016.

[161] I. Moore, New concepts for the ion guide technique, Nuclear Instruments and Methods in Physics Research Section B: Beam Interactions with Materials and Atoms 266 (2008) 4434. doi:/10.1016/j.nimb.2008.05.054.

[162] T. Kessler, I. Moore, Yu. Kudryavtsev, K. Peräjärvi, A. Popov, P. Ronkanen, T. Sonoda, B. Tordoff, K. Wendt, J. Äystö, Nuclear Instruments and Methods in Physics Research Section B: Beam Interactions with Materials and Atoms 266 (2008) 681. doi:/10.1016/j.nimb.2007.11.076.

[163] I. Pohjalainen, I. D. Moore, T. Eronen, A. Jokinen, H. Penttilä, S. Rinta-Antila, Gas purification studies at IGISOL-4, Hyperfine Interactions 227 (2014) 169. doi:/10.1007/s10751-013-1006-3.

[164] SAES Getters, MonoTorr PS4 Series, Accessed: October 2023.
URL https://www.puregasproducts.com/pdf/L130-014_-_487.pdf

[165] R. J. van Sonsbeek, R. Cooper, R. N. Bhave, Pulse radiolysis studies of ion–electron recombination in helium. Pressure and temperature effects, The Journal of Chemical Physics 97 (1992) 1800. doi:/10.1063/1.463167.

[166] R. Cooper, R. J. van Sonsbeek, R. N. Bhave, Pulse radiolysis studies of ion-electron recombination in gaseous argon, The Journal of Chemical Physics 98 (1993) 383. doi:/10.1063/1.464631.

[167] M. Facina, B. Bruyneel, S. Dean, J. Gentens, M. Huyse, Yu. Kudryavtsev, P. Van den Bergh, P. Van Duppen, A gas cell for thermalizing, storing and transporting radioactive ions and atoms. Part II: On-line studies with a laser ion source, Nuclear Instruments and Methods in Physics Research Section B: Beam Interactions with Materials and Atoms 226 (2004) 401. doi:/10.1016/j.nimb.2004.06.031.

[168] A. Zadvornaya, P. Creemers, K. Dockx, R. Ferrer, L. P. Gaffney, W. Gins, C. Granados, M. Huyse, Yu. Kudryavtsev, M. Laatiaoui, E. Mogilevskiy, S. Raeder, S. Sels, P. Van den Bergh, P. Van Duppen, M. Verlinde, E. Verstraelen, M. Nabuurs, D. Reynaerts, P. Papadakis, Characterization of Supersonic Gas Jets for High-Resolution Laser Ionization Spectroscopy of Heavy Elements, Physical Review X 8 (2018) 041008. doi:/10.1103/PhysRevX.8.041008.

[169] M. Reponen, I. Moore, I. Pohjalainen, T. Kessler, P. Karvonen, J. Kurpeta, B. Marsh, S. Piszczek, V. Sonnenschein, J. Äystö, Gas jet studies towards an optimization of the IGISOL LIST method, Nuclear Instruments and Methods in Physics Research Section A: Accelerators, Spectrometers, Detectors and Associated Equipment 635 (2011) 24. doi:/10.1016/j.nima.2011.01.125.

[170] J. F. Ziegler, SRIM - The Stopping and Range of Ions in Matter, Accessed: July 2023.
URL https://www.srim.org

[171] E. F. Izard, Production of polyethylene terephthalate, United States Patent no. 2534028 (1950).

[172] Hamilton Precision Metals, Havar® · UNS R30004 , Accessed: July 2023.
URL https://www.hpmetals.com/products/materials/nickel-strip-foil/havar

[173] P. Papadakis, J. Liimatainen, J. Sarén, I. Moore, T. Eronen, J. Partanen, I. Pohjalainen, S. Rinta-Antila, J. Tuunanen, J. Uusitalo, The MARA-LEB ion transport system, Nuclear Instruments and Methods in Physics Research Section B: Beam Interactions with Materials and Atoms 463 (2020) 286. doi:/10.1016/j.nimb.2019.05.007.

[174] Adaptas S.I.S., SIMION 8.1, Accessed: July 2021.
URL https://www.simion.com/info/

[175] J. Liimatainen, Simulation and Design of the Ion Guide System for MARA Low-Energy Branch, Master's Thesis, University of Jyväskylä (2021).
URL http://urn.fi/URN:NBN:fi:jyu-202112176006

[176] W. Gins, T. Kalvas, J. Sarén, PIOL 0.1b Documentation, Accessed: October 2023.
URL http://users.jyu.fi/~tvkalvas/piol/index.html

[177] S. Sels, R. Ferrer, K. Dockx, C. Granados Buitrago, M. Huyse, Yu. Kudryavtsev, S. Kraemer, S. Raeder, P. Van Den Bergh, P. Van Duppen, M. Verlinde, E. Verstraelen, A. Zadvornaya, Design and commissioning of an ion guide system for In-Gas

Laser Ionization and Spectroscopy experiments, Nuclear Instruments and Methods in Physics Research Section B: Beam Interactions with Materials and Atoms 463 (2020) 148. doi:/10.1016/j.nimb.2019.06.005.

[178] R.E. March, An Introduction to Quadrupole Ion Trap Mass Spectrometry, Journal of Mass Spectrometry 32 (1997) 351. doi:/10.1002/(SICI)1096-9888(199704)32:4<351::AID-JMS512>3.0.CO;2-Y.

[179] É. Mathieu, Mémoire sur le mouvement vibratoire d'une membrane de forme elliptique, Journal de Mathématiques Pures et Appliquées 13 (1868) 137.
URL http://eudml.org/doc/234720

[180] D.A. Manura, Collision Model HS1, Accessed: July 2021.
URL https://simion.com/info/collision_model_hs1.html

[181] A. Laugier, J. Garai, Derivation of the Ideal Gas Law, Journal of Chemical Education 84 (2007) 1832. doi:/10.1021/ed084p1832.

[182] Bureau international des poids et mesures, International System of Units (SI), 9th Edition, 2019.
URL https://www.bipm.org/documents/20126/41483022/SI-Brochure-9-EN.pdf/2d2b50bf-f2b4-9661-f402-5f9d66e4b507

[183] G. D. Peckham, I. J. McNaught, Applications of Maxwell-Boltzmann Distribution Diagrams, Journal of Chemical Education 69 (1992) 554. doi:/10.1021/ed069p554.

[184] L. Ding, M. Sudakov, S. Kumashiro, A Simulation Study of the Digital Ion Trap Mass Spectrometer, International Journal of Mass Spectrometry 221 (2002) 117. doi:/10.1016/S1387-3806(02)00921-1.

[185] A. D. Appelhans, D. A. Dahl, SIMION Ion Optics Simulations at Atmospheric Pressure, Int. J. Mass Spectrom. 244 (2005) 1. doi:/10.1016/j.ijms.2005.03.010.

[186] A. D. Appelhans, D. A. Dahl, Measurement of external ion injection and trapping efficiency in the ion trap mass spectrometer and comparison with a predictive model, International Journal of Mass Spectrometry 216 (2002) 269. doi:/10.1016/S1387-3806(02)00627-9.

[187] A. Bondi, Van der Waals Volumes and Radii, Journal of Physical Chemistry 68 (1964) 441. doi:/10.1021/j100785a001.

[188] P. Papadakis, I. Moore, I. Pohjalainen, J. Sarén, J. Uusitalo, Development of a low-energy radioactive ion beam facility for the MARA separator, Hyperfine Interactions 237 (2016) 152. doi:/10.1007/s10751-016-1364-8.

[189] H. Wollnik, B. Hartmann, M. Berz, Principles of GIOS and COSY, AIP Conference Proceedings 177 (1988) 74. doi:/10.1063/1.37817.

[190] P. Virtanen, R. Gommers, T. E. Oliphant, M. Haberland, T. Reddy, D. Courna-peau, E. Burovski, P. Peterson, W. Weckesser, J. Bright, S. J. van der Walt, M. Brett, J. Wilson, K. J. Millman, N. Mayorov, A. R. J. Nelson, E. Jones, R. Kern, E. Larson, C. J. Carey, İ. Polat, Y. Feng, E. W. Moore, J. VanderPlas, D. Laxalde, J. Perktold, R. Cimrman, I. Henriksen, E. A. Quintero, C. R. Harris, A. M. Archibald, A. H. Ribeiro, F. Pedregosa, P. van Mulbregt, SciPy 1.0 Contributors, SciPy 1.0: Funda-mental Algorithms for Scientific Computing in Python, Nature Methods 17 (2020) 261. doi:/10.1038/s41592-019-0686-2.

[191] G. Dumont, H. Pattyn, M. Huyse, G. Lhersonneau, J. Verplancke, J. Vanklinken, J. Deraedt, D. L. Sastry, LISOL, the Leuven Isotope Separator On-Line at the "CYCLONE"-Cyclotron, Nuclear Instruments and Methods 153 (1978) 81.

[192] N. Lecesne, R. Alvès-Condé, E. Coterreau, F. De Oliveira, M. Dubois, J. L. Flambard, H. Franberg, T. Gottwald, P. Jardin, J. Lassen, F. Le Blanc, R. Leroy, C. Mattolat, A. Olivier, J. Y. Pacquet, A. Pichard, S. Rothe, M. G. Saint-Laurent, K. Wendt, GISELE: A resonant ionization laser ion source for the production of radioactive ions at GANIL, Review of Scientific Instruments 81 (2010) 02A910. doi:/10.1063/1.3279301.

[193] P. Karvonen, I. Moore, T. Sonoda, T. Kessler, H. Penttilä, K. Peräjärvi, P. Ronka-nen, J. Äystö, A sextupole ion beam guide to improve the efficiency and beam quality at IGISOL, Nuclear Instruments and Methods in Physics Re-search Section B: Beam Interactions with Materials and Atoms 266 (2008) 4794. doi:/10.1016/j.nimb.2008.07.022.

[194] V. Sonnenschein, I. D. Moore, S. Raeder, M. Reponen, H. Tomita, K. Wendt, Char-acterization of a pulsed injection-locked Ti:sapphire laser and its application to high resolution resonance ionization spectroscopy of copper, Laser Physics 27 (2017) 085701. doi:/10.1088/1555-6611/aa7834.

[195] M. Newville, T. Stensitzki, D. B. Allen, A. Ingargiola, LMFIT: Non-Linear Least-Square Minimization and Curve-Fitting for Python (2014). doi:/10.5281/zenodo.11813.

[196] J. F. Kielkopf, New approximation to the Voigt function with applications to spectral-line profile analysis, Journal of the Optical Society of America 63 (1973) 987. doi:/10.1364/JOSA.63.000987.

[197] K.-D. Heber, P. J. West, E. Matthias, Pressure shift and broadening of Sr I Rydberg states in noble gases, Physical Review A 37 (1988) 1438.

[198] W. Demtröder, Laser Spectroscopy. Vol. 1: Basic Principles, ISBN 9783540734185 (2008). doi:/10.1007/978-3-540-73418-5.

[199] A. T. Goble, J. D. Silver, D. N. Stacey, Isotope shifts in the atomic spectrum of tin: 112Sn, 114Sn and 115Sn, Journal of Physics B: Atomic and Molecular Physics 7 (1974) 26. doi:/10.1088/0022-3700/7/1/010.

[200] Yu. Kudryavtsev, T. Cocolios, J. Gentens, M. Huyse, O. Ivanov, D. Pauwels, T. Sonoda, P. V. den Bergh, P. V. Duppen, Dual chamber laser ion source at LISOL, Nuclear Instruments and Methods in Physics Research Section B: Beam Interactions with Materials and Atoms 267 (2009) 2908. doi:/10.1016/j.nimb.2009.06.013.

[201] A. Drouart, J. Nolen, H. Savajols, the S3 collaboration, The Super Separator Spectrometer (S$^3$) for the SPIRAL2 facility, Journal of Physics: Conference Series 1643 (2020) 012032. doi:/10.1088/1742-6596/1643/1/012032.

[202] J. Corkhill, Development of UoYTube Detector for Ionising Radiation, Master thesis, University of York (2016).

[203] Micron Semiconductor Ltd, BB20, Accessed August 2023.
URL http://www.micronsemiconductor.co.uk/product/bb20/

[204] Mirion Technologies, BEGe, Accessed August 2023.
URL https://www.mirion.com/products/technologies/spectroscopy-scientific-analysis/gamma-spectroscopy/detectors/hpge-detectors-accessories/bege-broad-energy-germanium-detectors

[205] U. Jakobsson, Neutronirikkaiden keveiden ydinten tutkiminen käyttäen RITU-separaattoria (Investigation of neutron-rich light nuclei using the RITU separator), Master thesis (in Finnish only), University of Jyväskylä. (2006).

[206] S. Raeder, D. Ackermann, H. Backe, R. Beerwerth, J. C. Berengut, M. Block, A. Borschevsky, B. Cheal, P. Chhetri, C. E. Düllmann, V. A. Dzuba, E. Eliav, J. Even, R. Ferrer, V. V. Flambaum, S. Fritzsche, F. Giacoppo, S. Götz, F. P. Heßberger, M. Huyse, U. Kaldor, O. Kaleja, J. Khuyagbaatar, P. Kunz, M. Laatiaoui, F. Lautenschläger, W. Lauth, A. K. Mistry, E. Minaya Ramirez, W. Nazarewicz, S. G. Porsev, M. S. Safronova, U. I. Safronova, B. Schuetrumpf, P. Van Duppen, T. Walther, C. Wraith, A. Yakushev, Probing sizes and shapes of nobelium isotopes by laser spectroscopy, Physical Review Letters 120 (2018) 232503. doi:/10.1103/PhysRevLett.120.232503.

# ORIGINAL PAPERS

# PI

## NUCLEAR REACTION STUDIES AND PROSPECTS FOR THE NEW MARA-LEB FACILITY

by

Romero, J., Auranen, K., Block, M., Briscoe, A. D., Eronen, T., Gins, W., Grahn, T., Greenlees, P. T., Illana, A., Julin, R., Joukainen, H., Jutila, H., Khuyagbaatar, J., Krier, J., Leino, M., Louko, J., Luoma, M., Moore, I. D., Mosat, P., Ojala, J., Ortiz-Cortes, A., Pakarinen, J., Papadakis, P., Plaza, A. M., Rahkila, P., Raggio, A., Ruotsalainen, P., Saren, J., Sandzelius, M., Tolosa-Delgado, A., Uusitalo, J., and Zimba, G. 2023

# NUCLEAR REACTION STUDIES AND PROSPECTS FOR THE NEW MARA-LEB FACILITY*

J. Romero[a,b], K. Auranen[a], M. Block[c,d,e], A.D. Briscoe[a]
T. Eronen[a], W. Gins[a], T. Grahn[a], P.T. Greenlees[a], A. Illana[a]
R. Julin[a], H. Joukainen[a], H. Jutila[a], J. Khuyagbaatar[c,d]
J. Krier[c], M. Leino[a], J. Louko[a], M. Luoma[a], I.D. Moore[a]
P. Mosat[c], J. Ojala[a,b], A. Ortiz-Cortés[a,f], J. Pakarinen[a]
P. Papadakis[g], A.M. Plaza[a,b], P. Rahkila[a], A. Raggio[a]
P. Ruotsalainen[a], J. Sarén[a], M. Sandzelius[a]
A. Tolosa-Delgado[a], J. Uusitalo[a], G. Zimba[a]

[a]Accelerator Laboratory, Department of Physics, University of Jyväskylä
40014 Jyväskylä, Finland
[b]Department of Physics, Oliver Lodge Laboratory, University of Liverpool
Liverpool, L69 7ZE, UK
[c]GSI Helmholtzzentrum für Schwerionenforschung, Darmstadt, 64291, Germany
[d]Helmholtz Institute Mainz, 55099 Mainz, Germany
[e]Department of Chemistry, University of Mainz, 55099 Mainz, Germany
[f]Grand Accélérateur National d'Ions Lourds (GANIL), CEA/DSM-CNRS/IN2P3
14000 Caen, France
[g]STFC Daresbury Laboratory, Warrington, WA4 4AD, UK

A Low Energy Branch for the MARA separator, MARA-LEB, is under construction at the University of Jyväskylä, Finland. It will be used to purify and study exotic beams initially via nuclear decay and laser spectroscopy. Two experiments have been performed using the MARA separator to determine the acceptance of the gas cell and to assess the feasibility of future experiments at the new facility. Products of different reaction mechanisms have been produced and their transmission from the focal plane of MARA into the LEB gas cell has been estimated. In one experiment, medium-mass nuclei have been produced in fusion–evaporation reactions. In a second experiment, with the primary goal of studying the non-fusion reaction dynamics, heavy target-like fragments from multi-nucleon transfer reactions have been produced. Production cross sections have been measured and are presented in this work.

---

* Presented by J. Romero at the Zakopane Conference on Nuclear Physics, *Extremes of the Nuclear Landscape*, Zakopane, Poland, 28 August–4 September, 2022.

## 1. Introduction

The Low Energy Branch (LEB) [1] for the Mass Analysing Recoil Apparatus (MARA) [2] is a facility under construction in the Accelerator Laboratory of the University of Jyväskylä. MARA-LEB is designed to investigate exotic nuclei far from stability, taking advantage of MARA's high mass selectivity [2]. In the early conceptual design phase of the facility, the proton-rich $N \sim Z$ regions around $^{80}$Zr, $^{94}$Ag, and $^{100}$Sn were highlighted due to their scientific interest. Their proximity to the $N = 50$ and $Z = 50$ magic numbers, the $N = Z$ line, and the proton dripline makes this region a fertile ground for the testing of nuclear models and their predictions [3, 4]. The rapid proton capture (rp) [5] and the neutrino-induced nucleosynthesis ($\nu$p) [6] processes traverse this region, thus accurately measuring the nuclear properties of these isotopes becomes crucial in the development and verification of astrophysical nucleosynthesis models.

The actinide elements ($89 \leq Z \leq 103$) have emerged as a new region of interest for MARA-LEB. These nuclei have grown in scientific significance in recent years, especially due to the technical and methodological developments of laser spectroscopy that have allowed access to ground-state nuclear structure properties of exotic species in this region [7]. Access to this region of nuclei can be achieved via fusion–evaporation (FE) reactions. Other reaction channels, such as multi-nucleon transfer (MNT), provide alternative access routes to the region. However, the reaction dynamics of these alternative paths are not yet fully understood and intensive experimental study is ongoing [8, 9]. The use of MNT reactions in combination with the MARA-LEB facility is foreseen as a promising future opportunity for experiments, opening up the possibility of laser spectroscopy of actinides.

## 2. The MARA-LEB facility

The MARA-LEB facility combines several ion manipulation techniques to purify low-energy radioactive beams produced and initially separated by MARA [1]. Reaction products, known as recoils, are focused by MARA into a small-volume gas cell, containing a laminar flow of a noble buffer gas (typically helium or argon). Recoils are stopped, thermalised, and neutralised in argon gas before being laser ionised via multi-step resonant laser ionisation. For experiments not involving laser ionisation, helium can be used for reduced extraction times, in a manner similar to operations at the IGISOL facility.

Multi-step laser ionisation of neutralised recoils allows for the selection of specific elements, while others remain neutral. Non-neutralised recoils are collected by electrodes before exiting the gas cell. Ionised recoils are extracted and accelerated to 30 kV by the use of radio-frequency quadrupole

guides and ion-optical elements [10]. The ions are further mass and energy separated by the use of a dipole magnet and an electrostatic deflector operated at 90°, which also directs the ions towards experimental stations.

## 3. Experiments at MARA

The combination of ion-optical elements at MARA allows for recoils to be separated by their mass-over-charge ($m/q$) ratios, in addition to being focused onto a position-sensitive detector [2], usually a Multi-Wire Proportional Chamber (MWPC). The products of nuclear reactions are mass- and energy-selected and focused onto the focal plane detector system. They are detected by the MWPC in well-defined $m/q$ clusters, known as charge states. The MARA ion-optical settings can be adjusted to centre a particular charge state or the midpoint between two consecutive charge states (referred to as focusing on a half-charge state) onto the middle of the MWPC. In both of these cases, adjacent charge state clusters can also be detected in the MWPC with the distance between them depending on the selected mass and energy of the recoils.

The MARA-LEB gas cell will be positioned at the focal plane of MARA, thus the design of its entrance window is dependent on the spatial distribution of recoils at the focal plane.

An experiment, designed to estimate the production of $^{94,96}$Ag, was performed at the MARA facility using the $^{40}$Ca($^{58,60}$Ni, $p3n$)$^{94,96}$Ag fusion–evaporation reactions. The production of both silver isotopes of interest in this more limited, exploratory type of experiment proved insufficient for them to be clearly identified over other contaminants with higher production cross sections, further justifying the need for additional beam purification with MARA-LEB for studies in this region. Instrumental data, however, could be extracted from the experiment. Namely, by selecting a contaminant of mass number $A = 96$, the spatial distribution of recoils of this mass could be examined in order to make decisions on the design of the gas-cell window. $^{96}$Pd was abundantly produced via $^{40}$Ca($^{58}$Ni, $2p$)$^{96}$Pd. By identifying it via $\gamma$-ray tagging and excluding all other recoils, an image of palladium ions at the focal plane could be produced. By analysing these images with different MARA focus settings, the influence of window size on gas-cell acceptance could be quantified.

Acceptance into the gas cell was analysed in terms of the radius of the windows while scanning across the position of the charge states on the window. The cases of two- and three-charge states being accepted into the gas cell were studied and are exemplified on the left and right, respectively, of Fig. 1. At a radius of 32 mm, centring the window on a half-charge state, the entirety of the clusters with charges 26 and 27 enter the gas
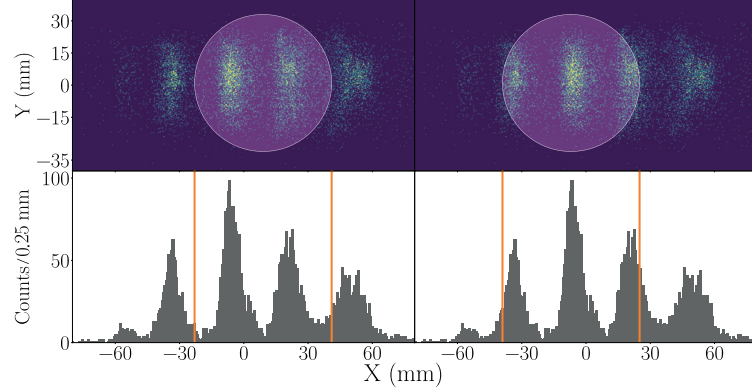
Fig. 1. 32 mm-radius gas-cell window superimposed onto the recoil image at the MARA focal plane (top) and its dispersive plane projection (bottom) for $^{96}$Pd recoils. On the left, the window is centred between charge states 26 and 27, accepting two entire charge states. On the right, the window is centred onto charge state 27, accepting it entirely and most of the adjacent charge states.

cell (Fig. 1, left). This constitutes an acceptance of 58% of the $^{96}$Pd recoils arriving at the MWPC. For a window of the same size, but centred on the most intense charge state, 63% of the recoils detected in the MWPC enter the gas cell, as an entire cluster and most of the immediate adjacent ones are accepted (Fig. 1, right).
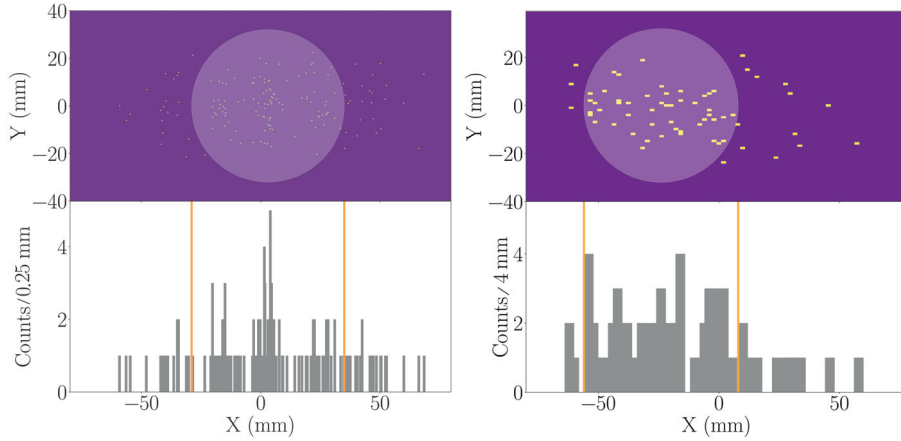


Fig. 2. 32 mm-radius gas-cell window superimposed onto the recoil image at the MARA focal plane (top) and its dispersive plane projection (bottom), centred on the most populated charge state. $^{213}$Rn is shown on the left. $^{226}$Th is shown on the right, with a coarser binning that allows for data to be more easily visualised.

Recently, experiments have been performed at MARA by the GSI-JYFL Collaboration aiming to study the dynamics of non-fusion reactions. The experimental data from these experiments are currently under evaluation [11].

In connection with MARA-LEB, the energy and position of certain reaction products were investigated. Figure 2 illustrates the position of $^{213}$Rn and $^{226}$Th, produced via the $^{65}$Cu+$^{209}$Bi and $^{65}$Cu+$^{238}$U reactions, respectively. Considering a gas-cell window with a radius of 32 mm, the acceptance into the gas cell as a percentage of the total number of recoils of the same species arriving at the MWPC is given in Table 1 for all reactions. These reactions were also used to estimate production yields for heavier isotopes which are now of interest for MARA-LEB. Table 2 shows the preliminary cross-section values for selected products of these reactions within the 10 msr acceptance of the MARA separator.

Table 1. Acceptance ($\alpha$) of different recoils into the gas cell as a percentage of those that arrive at the MWPC, for different cases and number of charge states ($n_{\mathrm{chst}}$) accepted into the window.

| Case | $n_{\mathrm{chst}}$ | $\alpha$ [%] |
|---|---|---|
| $^{96}$Pd | 2 | 58.5 |
| $^{96}$Pd | 3 | 62.7 |
| $^{213}$Rn | 3 | 70.6 |
| $^{226}$Th | 3 | 75.0 |

Table 2. Preliminary cross-section values ($\sigma$) for selected products within the MARA separator accepted solid angle.

| Isotope | Target | $\sigma$ [$\mu$b] |
|---|---|---|
| $^{211}$Po | $^{209}$Bi | 2.9(2) |
| $^{212}$Rn | $^{209}$Bi | 2.7(2) |
| $^{213}$Rn | $^{209}$Bi | 2.2(2) |
| $^{213}$Fr | $^{209}$Bi | 1.8(2) |
| $^{221}$Ac | $^{238}$U | 1.6(3) |
| $^{221}$Ra | $^{238}$U | 2.1(3) |
| $^{223}$Ac | $^{238}$U | 1.9(3) |
| $^{226}$Th | $^{238}$U | 2.4(3) |

## 4. Conclusions

In addition to supporting the design of the MARA-LEB gas-cell window, the experiments described in this work have served as a proof of concept for experiments at the new facility. In particular, the production of recoils from FE and MNT reactions is a promising first step for new experimental possibilities for MARA-LEB.

Cross sections as low as 0.5 $\mu$b have proven to be sufficient for laser spectroscopy with primary beam intensities in the order of hundreds of particle nA [12]. Primary beam intensities of that order and similar target thicknesses can be expected in MARA-LEB experiments, thus laser spectroscopy of actinides and other heavy isotopes may well be feasible at the new facility, depending on the different efficiencies that will need to be determined once the facility is operational.

## REFERENCES

[1] P. Papadakis *et al.*, *Hyperfine Interact.* **237**, 152 (2016).

[2] J. Uusitalo, J. Sarén, J. Partanen, J. Hilton, *Acta Phys. Pol. B* **50**, 319 (2019).

[3] T. Faestermann, M. Górska, H. Grawe, *Prog. Part. Nucl. Phys.* **69**, 85 (2013).

[4] P. Gysbers *et al.*, *Nat. Phys.* **15**, 428 (2019).

[5] R.K. Wallace, S.E. Woosley, *Astrophys. J. Suppl. Ser.* **45**, 389 (1981).

[6] C. Fröhlich *et al.*, *Phys. Rev. Lett.* **96**, 142502 (2006).

[7] M. Block, M. Laatiaoui, S. Raeder, *Prog. Part. Nucl. Phys.* **116**, 103834 (2021).

[8] S. Heinz, H.M. Devaraja, *Eur. Phys. J. A* **58**, 114 (2022).

[9] A. Di Nitto *et al.*, *Phys. Lett. B* **784**, 199 (2018).

[10] P. Papadakis *et al.*, *Nucl. Instrum. Methods Phys. Res. B* **463**, 286 (2020).

[11] J. Khuyagbaatar *et al.*, to be published.

[12] S. Raeder *et al.*, *Phys. Rev. Lett.* **120**, 232503 (2018).

# PII

# OFFLINE COMMISSIONING OF A NEW GAS CELL
# FOR THE MARA LOW-ENERGY BRANCH

by

Zadvornaya, A., Romero, J., Eronen, T., Gins, W., Kankainen, A., Moore, I.
D., Papadakis, P., Pohjalainen, I., Reponen, M., Rinta-Antila, S., Sarén, J.,
Simonovski, D., & Uusitalo, J. 2023
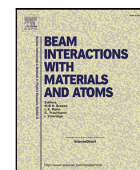
# Offline commissioning of a new gas cell for the MARA Low-Energy Branch ☆

A. Zadvornaya [a],[*], J. Romero [a],[c], T. Eronen [a], W. Gins [a], A. Kankainen [a], I.D. Moore [a],
P. Papadakis [b], I. Pohjalainen [a], M. Reponen [a], S. Rinta-Antila [a], J. Sarén [a], D. Simonovski [d],[e],
J. Uusitalo [a]

[a] *Accelerator Laboratory, Department of Physics, University of Jyväskylä, P.O. Box 35, 40014 Jyväskylä, Finland*
[b] *Nuclear Physics Group, STFC Daresbury Laboratory, Keckwick Lane, Warrington, Cheshire, WA4 4AD, United Kingdom*
[c] *Oliver Lodge Laboratory, University of Liverpool, Liverpool, L69 7ZE, United Kingdom*
[d] *Saint Petersburg State University, 7/9 Universitetskaya Emb., 199034, Saint Petersburg, Russian Federation*
[e] *Konstantinov Petersburg Nuclear Physics Institute (PNPI), National Research Center Kurchatov Institute, Gatchina, Leningradskaya Oblast, Russian Federation*

## ARTICLE INFO

## ABSTRACT

Results of offline commissioning tests for a new dedicated gas cell for the Mass Analysing Recoil Apparatus (MARA) Low-Energy Branch are reported. Evacuation time, ion survival and transport efficiency in helium buffer gas were characterized with a radioactive $^{223}$Ra $\alpha$-recoil source. Suppression of the ion signal, originating from non-neutralized species in the gas cell, was explored with $^{219}$Rn ions, the daughter recoil of $^{223}$Ra, as a function of voltage applied to one of the ion-collector electrodes. Two-step laser resonance ionization of stable tin isotopes produced inside the gas cell from a heated bronze filament was demonstrated, and broadening of the atomic resonances in argon buffer gas was studied. These tests indicate the suitability of the new gas cell for future in-gas laser spectroscopy studies of exotic nuclei at the Accelerator Laboratory of the University of Jyväskylä.

## 1. Introduction

The MARA Low-Energy Branch (MARA-LEB) is a new low-energy radioactive ion beam facility under development at the Accelerator Laboratory of the University of Jyväskylä (JYFL-ACCLAB) for the study of exotic nuclei using high-resolution laser spectroscopy, mass measurements and nuclear decay spectroscopy [1]. MARA-LEB aims to provide a detailed understanding of exotic nuclear-structure phenomena by exploring several regions of the nuclear chart, including nuclei with $N \sim Z$ between Zr ($Z = 40$) and Sn ($Z = 50$), nuclei just above $^{100}$Sn, as well as heavier, rare-earth proton dripline nuclei favored for extreme ground-state prolate deformation. Nuclei close to the $N = Z$ line provide a fertile landscape to explore nuclear phenomena including the effects of enhanced proton–neutron interactions and related pairing effects, long-lived isomeric states, exotic nuclear decays and the evolution of nuclear shapes and sizes. Additionally, the astrophysical rapid proton capture (rp) process [2] and the $\nu p$ process [3] traverse through this region. The isotopic selectivity of MARA-LEB, in combination with a planned high-efficiency decay station, will offer opportunities for nuclear decay spectroscopy of rare-earth nuclei ($57 \leq Z \leq 71$), in particular the study of proton decay fine structure and nuclear shapes. More

recently, multi-nucleon transfer reaction studies at the MARA vacuum-mode recoil separator have been performed, and reaction products of light actinide isotopes have been identified and their production cross sections measured [4]. Depending on the available primary beam intensities and experimental efficiencies, optical spectroscopy of actinide isotopes may be feasible at the new facility.

The first phase of MARA-LEB is under construction, with all major parts of the setup being manufactured [1,5]. Stable primary beams from the K130 heavy-ion cyclotron are delivered to MARA with intensities of at least 200 pnA, impinging on thin foil targets mounted on a rotating wheel at the target position of the separator. Recoiling ions with a variety of mass-to-charge ratios are separated with a combination of static electric and magnetic fields. Depending on the reaction symmetry, two to six charge states corresponding to the mass of interest are transported to the focal plane detection system [6]. MARA has a mass resolving power of roughly 250, and uses sets of movable mechanical slits to improve this value at a cost of acceptance. For the operation of MARA-LEB, a gas cell will be located at the focal plane. From the original charge-state distribution, one to three charge states can be accepted through the gas-cell window. In this manner, mass-selected recoil ions of interest, e.g., $^{94}$Ag or $^{102}$Sn with an energy of about 200 MeV
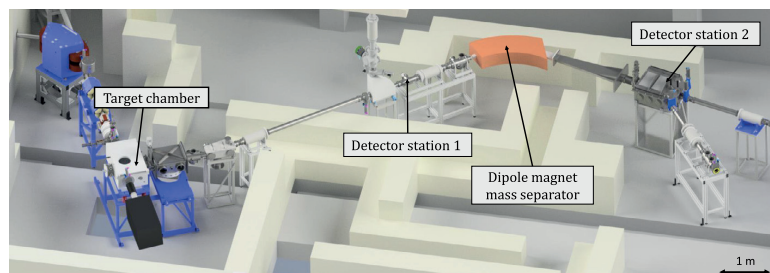
---

**Fig. 1.** A simplified three-dimensional overview of the parts of the IGISOL facility relevant to this work. The gas cell, not visible in this overview, was housed in the target chamber. The dipole magnet for mass separation and detector stations 1 (silicon detector) and 2 (silicon and MCP detectors) are denoted.

and yields of a few ions/s, will be stopped and thermalized in either argon or helium. In the case of argon, ions will be neutralized, allowing for subsequent selective resonance laser ionization and spectroscopy of elements of interest either via in-gas cell or in-gas jet configurations, similar to the approach described in [7]. Helium on the other hand is less conducive to neutralization, and thus ions have a higher survival probability. Nevertheless, shorter evacuation times can be achieved in helium, giving access to the study of nuclei with shorter half-lives that do not require laser re-ionization. After extraction from either helium or argon gas, ions will be re-accelerated to 30 keV towards the low-energy branch for downstream experiments.

A prototype gas cell has been designed at the In-Gas Laser Ionization and Spectroscopy (IGLIS) laboratory of KU Leuven (Belgium) for future use at the online Rare Element in Gas Laser Ion source and Spectroscopy (REGLIS[3]) facility at S[3] GANIL (France) [8]. COMSOL Multiphysics software [9] was used to optimize the gas-cell geometry in order to minimize the diffusion losses and the transport time of ions extracted through the gas cell [8]. Studies have shown that to overcome the effect of collisional- and temperature-broadening mechanisms to the atomic line spectral resolution, resonance ionization spectroscopy must be performed in the low-density and low-temperature medium of a supersonic gas flow rather than in the subsonic flow inside the gas cell [10]. Formation of uniform and spatially extended gas jets is essential for high efficiency and high resolution of the in-gas jet method, and can be achieved with carefully designed and manufactured de Laval nozzles of high Mach numbers, $M$ [11].

In this work, we present an overview and results from commissioning tests of a new gas cell for MARA-LEB, the design of which is similar to the gas cell planned for the S[3] facility, GANIL. These tests were performed at the Ion Guide Isotope Separator On-Line (IGISOL) facility [12] which is briefly described in Section 2. A radioactive $^{223}$Ra $\alpha$-recoil source [13] was installed inside the gas cell. The evacuation time, ion survival and transport efficiency were characterized using the daughter $^{219}$Rn recoil ions stopped in helium buffer gas, discussed in Section 3. These tests were followed by in-gas cell laser ionization of stable tin isotopes, this time in an argon buffer-gas environment (Section 4). The latter work is in anticipation of one part of the planned science program of the MARA-LEB facility, aiming to study the ground-state electromagnetic moments and mean-squared charge radii for neutron-deficient tin isotopes. Such information is not yet available for isotopes with neutron number $N < 58$ [14]. We note that in-gas laser ionization of stable tin isotopes has earlier been demonstrated at the LISOL facility as part of the preparatory experiments towards REGLIS[3] at S[3] GANIL [7]. Our conclusions are presented in Section 5.

## 2. Experimental method

### 2.1. IGISOL facility

Commissioning tests with the MARA-LEB gas cell were carried out at the IGISOL facility at the University of Jyväskylä. Fig. 1 highlights

the relevant parts of the facility used in this work. The MARA-LEB gas cell was installed in the target chamber of the facility. Isotopes of interest were produced and stopped in the gas cell filled with high-purity helium or argon gas and transported by the gas flow towards the free jet nozzle and into a sextupole ion guide (SPIG) [15]. The recombination rate coefficient of argon ions in neutral argon gas is an order of magnitude larger than that for helium [16,17]. For this reason, argon is favored as the buffer gas of choice when performing selective resonant laser re-ionization under online conditions as the larger re-combination rate leads to a higher probability of neutralization [18]. It is important to note, only high-purity gases were used in the following tests. Purification of helium was achieved with liquid nitrogen-cooled cold traps, while for argon, a getter purifier was used (Saes MonoTor PS4-MT15) as described in detail in Ref. [19]. Subsequently, after guidance through the SPIG, the ions were accelerated to 30 keV and transported towards a magnetic dipole mass separator having a mass resolving power $M/\Delta M$ of about 500.

Two detector stations were used in the commissioning tests, as shown in Fig. 1. Detector station 1, located before the mass separator, consists of a silicon detector and was used to determine ion survival and transport efficiency by measuring the number of implanted ions identified via their radioactive (alpha) decays. Detector station 2 is located in the focal plane area of the separator, within the so-called electrostatic switchyard, and consists of a silicon detector and a mi-crochannel plate (MCP) detector. The MCP detector is used when mass scans are performed, and to determine the evacuation time of mass-separated ions extracted from the gas cell as it allows for time-resolved ion counting. Similar to Detector station 1, the silicon detector after the mass separator can be used to determine the ion survival and transport efficiency of radioactive ions, but cannot be used for stable beams.

A two-step resonant laser ionization scheme for tin was realized using solid-state lasers from the Fast Universal Resonant laser IOn Source (FURIOS) laboratory [20]. The Titanium:sapphire (Ti:Sa) laser resonators, pumped by 10-kHz repetition rate Nd:YAG lasers, are either in-house built or sourced from Johannes Gutenberg University Mainz. The FURIOS laboratory, located directly above the target chamber on the second floor of the facility, houses two pump lasers, model Lee Laser LDP-200, with a nominal output power of about 100 W at 532 nm with 100 ns temporal pulse width. Each Ti:Sa laser is pumped with 10–25 W, split from the main pump beam using half-wave plates and polarizing beam splitter cubes. The Ti:Sa lasers are either in $Z$-shaped or bowtie cavity configurations, with the latter providing narrowband operation via injection-locking techniques [21]. In this work, only the broadband $Z$-shaped resonators are used. The lasers are equipped with intra-cavity second harmonic generation capability and have access to external harmonic generation setups enabling a wavelength tunability from about 210–500 nm and 690–1000 nm.
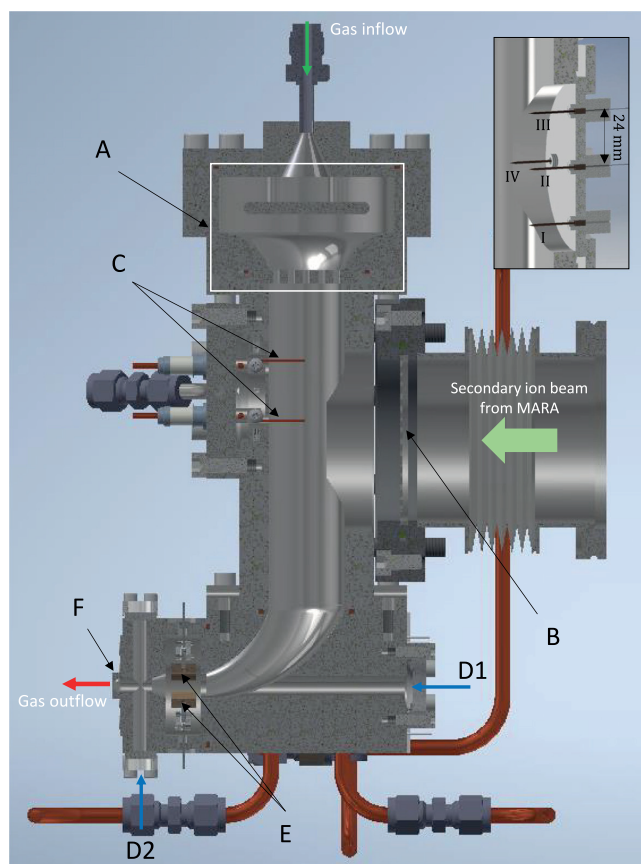
**Fig. 2.** Cutaway view of the MARA-LEB gas cell. Gas inflow and outflow are indicated with green and red arrows, respectively. The mass-selected secondary ion beam from the MARA separator is denoted with a light green arrow. A — pre-chamber for gas-flow conditioning (houses obstacle and honeycomb flanges), B — entrance window (foil window), C — filament feedthroughs, D1 and D2 — laser viewports for collinear and transverse resonant laser ionization configurations, respectively, E — ion-collector electrodes, F — free jet/de Laval nozzle. The entrance window can be replaced by a flange to which a $^{223}$Ra $\alpha$-recoil source can be mounted in different positions as shown in the inset on the upper right.

### 2.2. MARA-LEB gas cell

The geometry of the MARA-LEB gas cell is based on the design to be used for the REGLIS[3] facility, S[3] GANIL [8]. A cutaway view of the gas cell is shown in Fig. 2. A number of modifications have been implemented, including an increase in the diameter of the entrance window through which the recoil products from the MARA separator must pass, and the location of the flange housing two filament feedthroughs, which has been moved from the central axis of the separator. Three individual operational modes are feasible:

- Online mode: the ions from the MARA separator will enter the gas cell through a thin foil window, typically havar or mylar with a thickness up to ~10 μm and an open diameter of 64 mm. The window is supported by a honeycomb frame. Recoils are thermalized and stopped in a high-purity gas.
- Offline mode with α-recoil source: the foil window can be replaced by a flange to which a $^{223}$Ra $\alpha$-recoil source is mounted, as shown in the inset in Fig. 2.
- Offline mode with filaments containing stable (or long-lived) isotopes of interest: two filaments can be mounted on a flange, offset and opposite to the entrance window. Through resistive heating, a continuous source of atoms is produced (in this work, a bronze filament is used to produce stable tin isotopes).

In this work, the MARA-LEB gas cell was operated only in the aforementioned offline modes. Ion-collector electrodes (ICs) installed before the free jet nozzle of the gas cell are used to collect non-neutralized ions transported from the stopping region, thereby increasing the selectivity when in-gas cell/in-gas jet laser ionization is used under online conditions. Stopping and laser ionization volumes are physically separated in order to reduce the effects of recombination of photo-ions. This allows for more efficient low-resolution in-gas cell resonance ionization spectroscopy (RIS). In-gas laser ionization can be implemented in collinear, transverse or crossed-beam geometries with respect to the atom flow via laser viewports D1 and D2 (see Fig. 2). Finally, isotopes of interest and the buffer gas atoms leave the gas cell via a free jet or de Laval nozzle, the latter employed to form collimated high Mach number gas jets. In this work, a free jet nozzle with a diameter of 1.65 mm was used.

### 3. Offline tests with a $^{223}$Ra $\alpha$-recoil source

Combined efficiency of ion survival and transport, as well as evacuation time from the gas cell are important parameters characterizing gas-cell performance. These parameters have been studied in this work with a radioactive $^{223}$Ra $\alpha$-recoil source, installed inside the gas cell operated using helium buffer gas. Fig. 3 shows the gas cell mounted inside the target chamber of the IGISOL facility. Prior to the tests, $^{223}$Ra ions ($T_{1/2}$ = 11.4 d) were accumulated on the tip of a needle
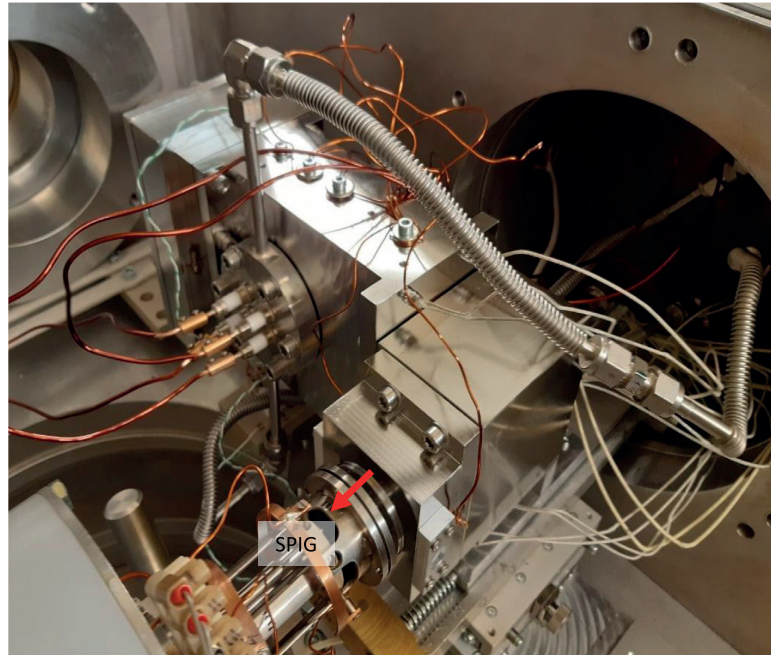
**Fig. 3.** MARA-LEB gas cell installed in the target chamber of the IGISOL facility during the commissioning tests. The free jet nozzle cannot be seen due to its close distance, ∼2 mm, to the SPIG electrode (labeled in the photograph). Gas outflow is indicated with a red arrow.

(the "needle source") installed in an $\alpha$-recoil generator, with $^{227}$Ac ($T_{1/2}$ = 21.8 y) used as the primary source. An accumulated activity of $(4.0\pm0.4)$ kBq of $^{223}$Ra was measured in a separate vacuum chamber before installing the needle into the gas cell. During the following tests, performed over several consecutive days, the source was installed in four positions as shown in the inset in Fig. 2. For each position, $\alpha$-recoil spectra of $^{219}$Rn ions, the daughter product of $^{223}$Ra with a half-life of 3.96 s, were recorded at Detector station 1 for different values of pressure $P_0$ inside the gas cell. An example spectrum is shown in Fig. 4 for the source in position I and helium pressure $P_0$ of 300 mbar. During these measurements, only 50% of the $^{219}$Rn ions were released into the buffer gas due to the source geometry at a rate of about 1300 ions/s. The measured counting rate at Detector station 1 for this source position was 160 counts/s. Analysis of the accumulated spectra was performed in a manner similar to that described in [22], and the efficiency of ion survival and transport to the detector station was extracted. We note that helium was chosen as the buffer gas due to the smaller recombination rate coefficient compared to that of argon. We could therefore anticipate higher counting rates of the detected recoil ions. Indeed, such comparisons have been studied at the IGISOL facility in the past and support this choice of gas for ion survival.

To determine the evacuation time for different starting coordinates inside the gas cell, voltage pulses were applied to the needle. The source was connected to a power supply, the output voltage of which could be programmed by using TTL logic. During a recording cycle, lasting 0.67 s for helium and 1.34 s for argon, the voltage at the needle was maintained at −30 V, except for short periods of 50 ms or 150 ms (for helium and argon, respectively) when the voltage was set to 0 V, thus allowing the release of $^{219}$Rn ions into the gas flow. Time profiles of singly-charged ions extracted from the gas cell were subsequently recorded using a multi-channel scaler (MCS) for time-resolved counting of the ion signal from the MCP detector at Detector station 2, located in the electrostatic switchyard as shown in Fig. 1. A timing card was used to provide the trigger for the MCS to start recording and to change the
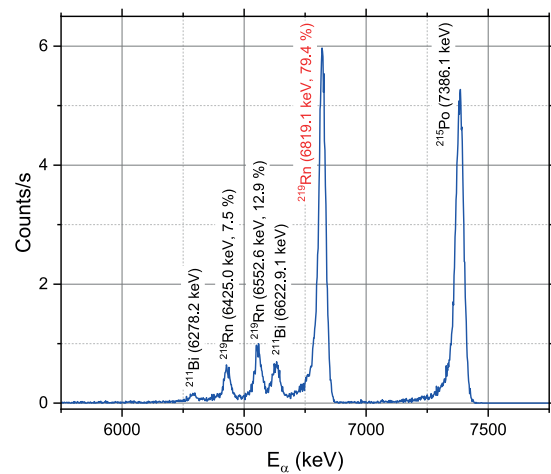


**Fig. 4.** Example of an $\alpha$-decay spectrum of $^{219}$Rn measured at Detector station 1 for the needle source in position I and a helium pressure $P_0$ of 300 mbar. The $^{219}$Rn peak used for extracting the efficiency is denoted in red. The peaks are labeled according to the alpha decay from the respective isotope, energy of the alpha particle and, for $^{219}$Rn, the branching ratio.

voltage at the needle source. To improve the signal-to-noise ratio, time profiles were accumulated over a number of recording cycles.

### 3.1. Ion survival and transport efficiency

The ion survival and transport efficiency was measured for all positions of the needle source as a function of helium gas pressure $P_0$ up
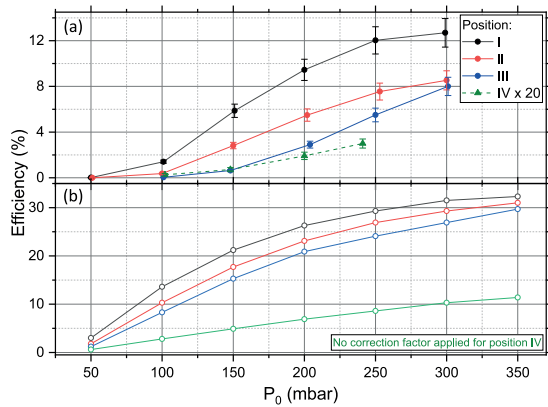
**Fig. 5.** Efficiency for the needle source in positions I, II, III and IV at different values of helium pressure $P_0$. (a) Ion survival and transport efficiency measured at Detector station 1. The results for position IV are multiplied by a factor of 20. (b) Numerical calculations of the efficiency of ion survival against diffusion losses.

to 300 mbar, limited by the pressure in the surrounding IGISOL target chamber. We note that this limitation will be mitigated at MARA-LEB due to the anticipated use of a nozzle with a smaller diameter of 1 mm and, therefore, smaller flow rate, for which the pumping capacity for MARA-LEB has been tailored accordingly. Moving the needle source to a new position required venting of the target chamber, thus potentially exposing the gas cell to the ambient air. This could detrimentally affect the efficiency via potential losses of charged recoils to molecular adducts. For this reason, after measuring at every needle position the gas cell was baked overnight using cartridge heaters ($T \approx 100°C$) and subsequently cooled to room temperature with a small flow of helium ($P_0 \approx 50$ mbar). The efficiency is shown in Fig. 5(a). As the measurements were performed using Detector station 1 there is no separation of different mass-to-charge (m/q) values, nor identification of potential molecular ions. However, Detector station 2 was also used to verify that no higher charged states or heavier molecular ions were present in the extracted beam. A maximum efficiency of $(12.7 \pm 1.3)$ % was measured for the source in position I for a pressure $P_0$ of 300 mbar. We note that this efficiency includes the transport efficiency from the exit of the gas cell to the detector station, in addition to the extraction through the helium gas. The tip of the needle was unfortunately scratched on the gas-cell surface while moving it from position II to position III, resulting in a loss of activity compared with what would be expected from the half-life alone (this was confirmed after the gas-cell measurements). The results shown in Fig. 5(a) for positions III and IV have therefore been corrected for this reduction factor of 2.9. Moreover, the results for position IV in Fig. 5(a) are multiplied by a factor of 20, for better readability of the measured data.

Numerical calculations were performed using the Computational Fluid Dynamics (CFD) module of COMSOL Multiphysics software [9]. The velocity of the gas flow inside the gas cell depends on the cross-sectional area of the gas outflow and therefore the diameter of the available free jet nozzle was accurately measured to be $(1.65 \pm 0.07)$ mm. The output of the numerical calculations for the velocity of the helium gas flow and its streamlines is shown in Fig. 6. The calculations only include the diffusion losses of the simulated atoms to the inner walls of the gas cell. The losses are defined by the outflow diameter, the geometry of the gas cell, and the diffusion coefficient of the simulated atoms in the buffer gas. Due to the absence of a diffusion coefficient for radon in the literature, the coefficient for mercury ($A \sim 200$) in helium at normal conditions (273.15 K and 1013 mbar) was used as a Ref. [23], $D_{ref} = 5.32 \times 10^{-5}$ m$^2$/s, and scaled to the value of the helium

pressure $P_0$. No significant influence on the calculated diffusion losses is expected. Results of the numerical calculations for the transport efficiency in the gas are shown in Fig. 5(b).

The notable difference between the absolute values of the measured and numerically calculated efficiency is anticipated. One factor that may contribute is that ion losses in the gas cell are determined not only by diffusion, but also by the presence of impurities in the buffer gas. Potential losses due to molecular formation were not considered in the simulation, but are expected to be present in the gas, albeit at significantly reduced amounts after the gas-cell baking. Impurities are also involved in other ion-loss mechanisms e.g., neutralization of ions via three-body recombination involving a free electron, dissociative recombination and charge-exchange reactions [24]. It has been shown that an ion survival and transport efficiency of up to 30 % can be reached for $^{219}$Rn ions in gas cells operating with cryogenic helium at temperatures below 90 K [25,26]. This is due to the ultra-pure conditions attained by freezing out the impurities. Moreover, the efficiency depends on the chemical nature of the elements and therefore will be different for $^{219}$Rn ions in, for example, helium and argon gas. A second factor is the transport efficiency from the gas cell to the silicon detector that depends on the tuning of the SPIG and mass separator. The simulations only include the transport through the gas cell.

Despite the discrepancy in the absolute values, it is encouraging to see that the general trend of the efficiency growth as a function of helium pressure is reproduced rather well, in particular for needle source positions I and II, for which the simulations and measurements show a similar saturation above 250 mbar. In addition, the relative efficiencies between the source locations are in agreement with experiment, i.e. the highest efficiency is obtained for position I and the lowest for position IV. The simulated efficiency of the latter position is most discrepant with the experimental values, perhaps indicating both an underestimated loss due to diffusion towards the walls of the gas cell, or other loss mechanisms not accounted for in the simulation and amplified in regions of slower gas flow close to position IV.

### 3.2. Evacuation time

Evacuation time profiles of $^{219}$Rn$^+$, $^{20}$Ne$^+$ and $^{40}$Ar$^+$ ions extracted from the gas cell were recorded and analyzed for all positions of the needle source with the MCP detector at Detector station 2. In these measurements, argon and in-house recycled helium buffer gases were used. The helium included neon as an impurity, not present in the commercially bought argon [19]. Measurements were performed with a pressure $P_0$ of about 200 and 100 mbar in the cases of helium and argon gas, respectively, with the results shown in Fig. 7. Time profiles were fitted using the built-in Extreme Peak function from OriginPro software [27], which allowed the extraction of the peak centroid $t_{max}$ and its full width at half maximum $\Delta t$, highlighted in Fig. 7, as well as the corresponding error bars. The fitting results, shown in Fig. 8, were then compared with a more sophisticated function analytically derived for the evacuation time by solving the diffusion–convection equations [28] and were found to be in good agreement within error bars, justifying therefore the use of a simpler function. The error bars of the peak centroids, as well of the widths in helium, are smaller than the data points shown in Fig. 8.

A higher signal-to-noise ratio was achieved for the $^{20}$Ne$^+$ time profiles accumulated over a fewer number of recording cycles compared to $^{219}$Rn$^+$. The extracted peak centroids of $^{219}$Rn$^+$ and $^{20}$Ne$^+$ ions are in agreement for the needle source in positions I and II and have a difference of less than 10 % for the needle source in position III. The evacuation time profile of $^{219}$Rn$^+$ for the needle source in position IV was not recorded due to insufficient statistics. Moreover, peak centroids of $^{219}$Rn$^+$ and $^{40}$Ar$^+$ ions are in agreement for the measurements performed with argon buffer gas. This leads to the conclusion that ionization of buffer gas and its impurities ($^{20}$Ne$^+$, in case of helium buffer gas) takes place within a couple of mm around the needle tip by
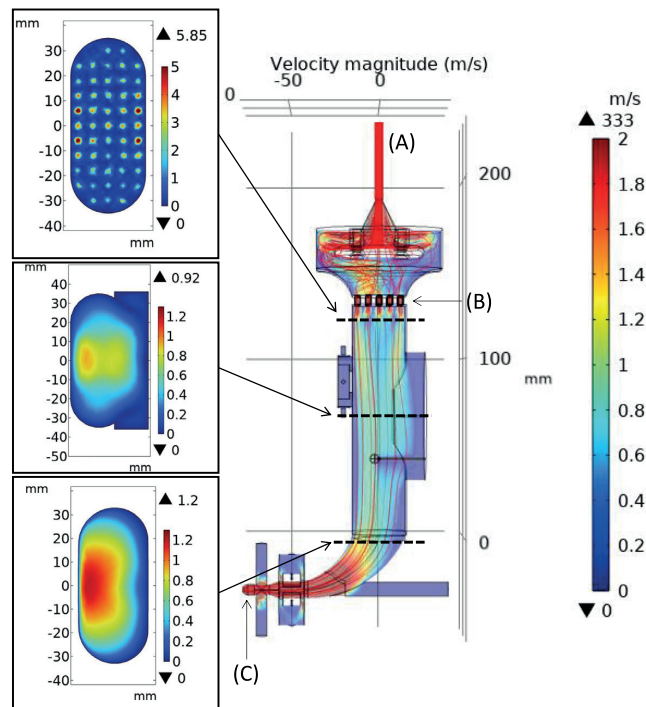
**Fig. 6.** Output of the numerical calculations of the velocity and flow streamlines inside the MARA-LEB gas cell. The color bar indicates the velocity magnitude with the upper limit set to 2 m/s to allow visualization of a slower gas flow in the central part of the gas cell. The gas inlet (A) is denoted. The effect of the honeycomb structure (B) used to achieve a uniform flow condition is clearly visible. The ions exit the gas cell at position (C). Velocity profile maps from different cross-sections of the gas cell are shown at the corresponding locations.

the $^{219}$Rn$^+$ ions, released in the decay of $^{223}$Ra with an energy of about 104 keV. On the other hand, the alpha particles released with an energy of 5.7 MeV, deposit only about 30 keV per 1 cm traveled in 200 mbar helium buffer gas. Therefore, for the cases when the extracted ion signal of $^{219}$Rn$^+$ is too small, evacuation time profiles of ions of buffer gas and/or of its impurities can be used to estimate the evacuation time. Full widths at half-maximum of lighter $^{20}$Ne$^+$ and $^{40}$Ar$^+$ ions are larger compared to those of $^{219}$Rn$^+$, which can be explained by a larger diffusion coefficient.

The needle source positions I, II and III are separated by 24 mm, as indicated in the inset in Fig. 2. The corresponding peak centroids for $^{20}$Ne$^+$ ions are delayed by approximately 27 ms for each subsequent position, allowing the velocity of the helium gas to be estimated as 0.9 m/s in that section of the gas cell, in good agreement with numerical calculations of the velocity shown in Fig. 6. Moreover, peak centroids of $^{20}$Ne$^+$ coincide for the source in positions II and IV, thus illustrating that the gas velocity is rather constant in the coordinate perpendicular to the flow direction, as the distance between these two positions is also 24 mm.

The ratio of the measured peak centroids of $^{219}$Rn$^+$ ions for the needle source in position I for argon and helium buffer gas was calculated to be 2.94 ± 0.02. This value is reasonably close to the estimate of 3.16, calculated from $\sqrt{A_{Ar}/A_{He}}$, where $A_{Ar}$ and $A_{He}$ are standard atomic weights of argon and helium gas, respectively. This straightforward estimate is based on the fact that the speed of sound $a \sim \sqrt{1/A}$ and, therefore, does not take into account subtle details such as viscous effects that slightly reduce the effective nozzle diameter, the different dynamic viscosity of helium and argon, and minor differences in flow structure e.g., velocity streamlines, between the two gases.

Evacuation time profiles of $^{219}$Rn$^+$ ions for the needle source in helium and argon buffer gas were calculated in the CFD module. Results

for the calculated centroids agree well with the experimental data for all positions of the source (see Fig. 8). However, the calculated full widths at half maximum are considerably larger than the measured values for helium buffer gas. This may be caused by erroneous assessment of diffusion in lighter gases and requires more detailed investigation.

### 3.3. Ion-collector tests

The performance of the ion-collector (IC) electrodes was tested with the $^{223}$Ra $\alpha$-recoil source installed in position I. Measurements were obtained with helium gas at a pressure $P_0$ of 166 mbar. Mass-separated $^{219}$Rn$^+$ ions were detected as a function of ion-collector voltage at Detector station 2 with the MCP detector, the results are shown in Fig. 9. A suppression to less than 2% of the initial amount was achieved with a voltage of 5 V continuously applied to one of the ICs, while the other was grounded. In order to verify a pulsed operation of the ICs, time profiles of mass-separated $^{219}$Rn$^+$ and $^{20}$Ne$^+$ ions were accumulated with a −20 V amplitude pulse applied to one electrode for 100 ms (see the inset in Fig. 9).

### 4. In-gas cell laser ionization of tin

In-gas cell laser ionization of stable tin isotopes was performed within argon gas at a pressure $P_0$ of 100 mbar. The isotopes were produced by resistively heating bronze filaments (91 % copper and 9 % tin, by mass) installed in the gas cell, as shown in Fig. 2. Atomic vapor, produced in this way, was transported by a high-purity argon flow towards the free jet nozzle. Two-step broadband (∼ few GHz) laser ionization was used to selectively ionize tin in a collinear geometry, in which both laser beams were transported to the interaction region
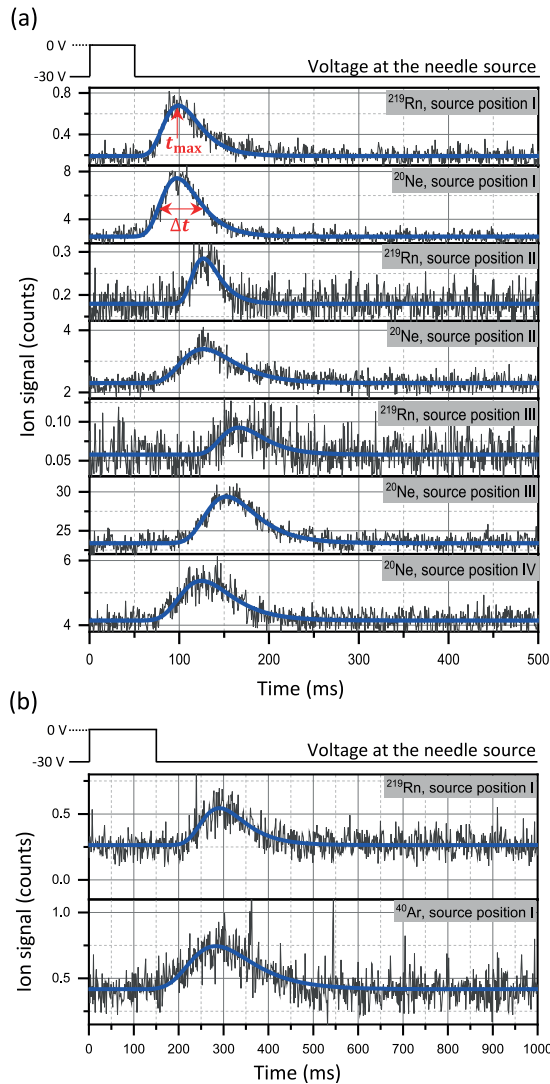
## (a)



## (b)



**Fig. 7.** Evacuation time profiles of the mass-separated $^{219}$Rn$^+$, $^{20}$Ne$^+$ and $^{40}$Ar$^+$ ions. Time profiles of $^{20}$Ne$^+$ were accumulated within 400 to 700 recording cycles (higher statistics required for the needle source positions with smaller ion counting rates, such as position IV), while for $^{219}$Rn$^+$ about 4 times longer accumulation was used. Blue solid lines show fitting of measured data (black line) using the Extreme Peak function discussed in the text. (a) Voltage pulsed with a release time of 50 ms applied to the needle source in the gas cell filled with helium buffer gas ($P_0 = 200$ mbar). The counting rate of $^{20}$Ne$^+$ ions was about an order of magnitude larger than that of $^{219}$Rn$^+$. (b) Voltage pulsed with a release time of 150 ms applied to the needle source, using argon as buffer gas ($P_0 = 100$ mbar). The counting rate of $^{40}$Ar$^+$ was measured to be approximately the same as that of $^{219}$Rn$^+$.

through viewport D1 (see Fig. 2). The geometry was chosen primarily due to the ease of optical access via a window on the target chamber. A more versatile optical access that allows for transverse and crossed-beams geometry, as well as for in-gas jet laser ionization will be available on the target chamber of the MARA-LEB facility.

The laser ionization scheme used in these tests is shown in Fig. 10(a), taken from Ref. [29]. The Sn atoms were promoted from the ground state $5s^2 5p^2\ ^3P_0$ ($J = 0$) to the intermediate level $5p6s\ ^1P_1$

($J = 1$), using frequency-tripled laser light at 254.73 nm (wavelength in vacuum). This transition was easily saturated with the available average laser power of 70 mW measured at the optical table in the FURIOS laboratory. The excited atoms were then ionized via an autoionizing state above the ionization potential, a state that corresponds to the $5p7f$ configuration, using frequency-doubled laser light at 454.9 nm. By monitoring the count rate of the most abundant isotope, $^{120}$Sn, at the MCP of Detector station 2 as a function of the laser power, saturation data can be obtained (see Fig. 10(b)). From a saturation profile fit to the data, a saturation power $P_s$ of 4 mW for the first step was determined. We note that all laser power measurements were made on the optical table, roughly 10 m from the target chamber. Approximately 50% of energy losses are expected for the transport of UV light to the target chamber. The second step transition was not saturated with the available average power of about 400 mW.

By independently blocking the first- and second-step lasers, we verified that the ion signal primarily comes from two-step ionization. The count rate at the MCP dropped to the noise level when the first-step laser was blocked. Blocking only the second-step laser led to the signal decreasing to less than 10 % from its initial value, indicating only a small contribution from any non-resonant ionization processes. Without needing to tune the laser frequency, the mass separator can be used to obtain a mass scan of the laser-ionized tin. As can be seen in Fig. 11, the experimental data is in reasonable agreement with the expected natural isotopic abundances for all isotopes apart from an unexplained underabundance seen at $^{120}$Sn. Suppression of laser-ionized $^{120}$Sn to around 40 % of its initial value was achieved with 5 V applied to one of the ICs. Further suppression to less than 20 % was achieved with the voltage higher than 20 V. When 5 V were applied to both ICs, the ion signal dropped only to around 60 % due to a cancellation effect of the voltages on the ion beam.

Frequency scans were attempted for both transitions in order to study the effect of the gas pressure on the spectral linewidths and centroids. Unfortunately, the first-step transition was hampered by mode hopping of the broadband laser, making it impossible to do a smooth scan over the desired frequency range. In the future this limitation will be addressed by implementing an injection-locked Ti:Sa laser resonator. Scanning of the second-step transition was however achieved at argon pressure $P_0$ values ranging from 97 mbar to 203 mbar, with the mass separator tuned to $^{120}$Sn. The laser power was reduced to ~1 mW and 300 mW for the first and second steps, respectively, to reduce the effect of power broadening. The results of the frequency scans are shown in Fig. 12. It can be seen that the spectral line broadens as the pressure increases. Notably there is a strong asymmetry in the data. We surmise that the asymmetry arises due to the geometry of the laser ionization. The laser beams pass through viewport D1 (Fig. 2) and are gradually focused towards the free jet nozzle. Ionization is therefore occurring in a collinear geometry both within the gas cell as well as in the volume around the free jet nozzle. The irradiated gas volume contains a convolution of different collisional and Doppler regions. For example, in the nozzle region, the Mach number, velocity and density of gas flow change rapidly over distances as short as a millimeter. This therefore complicates any analysis of the spectral profiles with parametric models to extract pressure broadening and shift coefficients from the data. A non-parametric method of extracting the width of the peaks was used, by determining the range of experimental values that are located above the half maximum of the peak. From this data, an observed broadening of the atomic resonances was found to be on the order of 240 MHz/mbar. In future work, a crossed-beam geometry with a well-defined region of laser-beam overlap is preferable in order to minimize complexities due to convoluting regions of different gas flow.

## 5. Conclusions

The gas cell designed for the MARA-LEB facility has been characterized at the Accelerator Laboratory of the University of Jyväskylä using
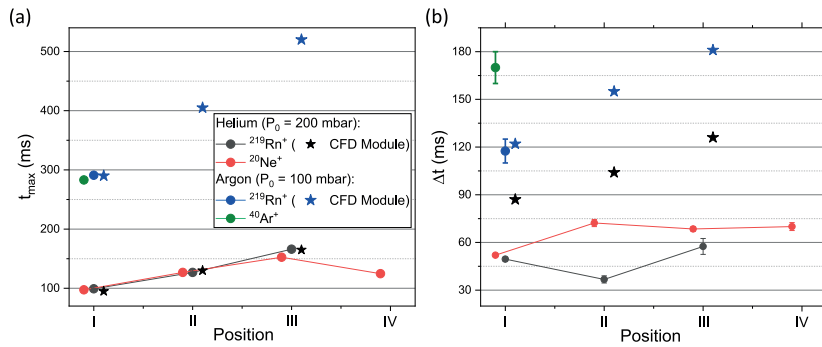
**Fig. 8.** (a) Peak centroids, $t_{max}$, and (b) full widths at half maximum, $\Delta t$, extracted from $^{219}$Rn$^+$, $^{20}$Ne$^+$ and $^{40}$Ar$^+$ evacuation time profiles, shown in Fig. 7. Overlapping data points are offset around their X-coordinates for clarity.
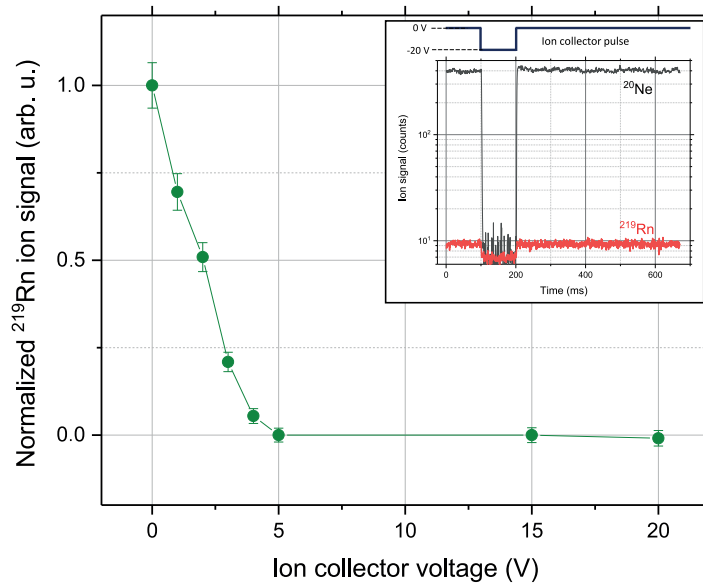


**Fig. 9.** Normalized signal of $^{219}$Rn$^+$ ions measured at the MCP detector (Detector station 2) with different voltages applied to one of the ICs. The inset shows time profiles of the mass-separated $^{219}$Rn$^+$ and $^{20}$Ne$^+$ ions accumulated in 850 and 130 recording cycles, respectively, each lasting for 0.67 s, with voltage pulses applied to the ion collector (100 ms long and −20 V amplitude). $P_0 = 166$ mbar in all measurements.
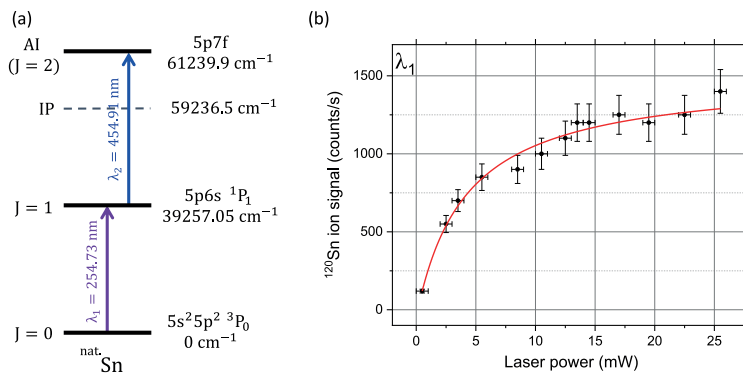


**Fig. 10.** (a) Two-step laser resonance ionization scheme for tin. (b) Saturation curve for the first-step transition. The laser power (P) was measured in the FURIOS laboratory. The data was fitted (red curve) with a conventional saturation function of the form $I(P) = I_0 + A \frac{P/P_s}{(1+P/P_s)}$, where $I_0$ is an offset parameter to account for non-resonant photoionization.
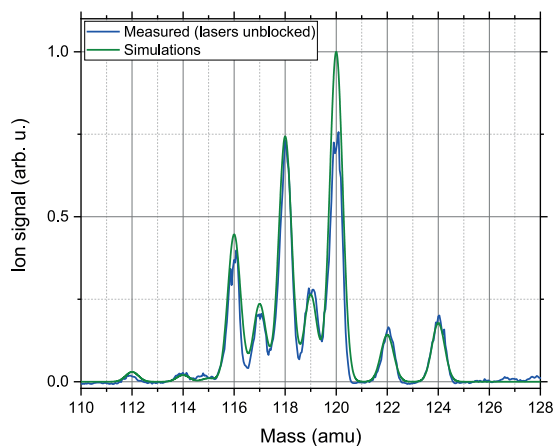
**Fig. 11.** A scan of the dipole sector magnet of the IGISOL mass separator, showing the resulting laser-ionized stable isotopes of tin (blue line). The green line is a simulated mass scan with the expected isotopic abundances. The experimental data is normalized to the simulated $^{118}$Sn peak.
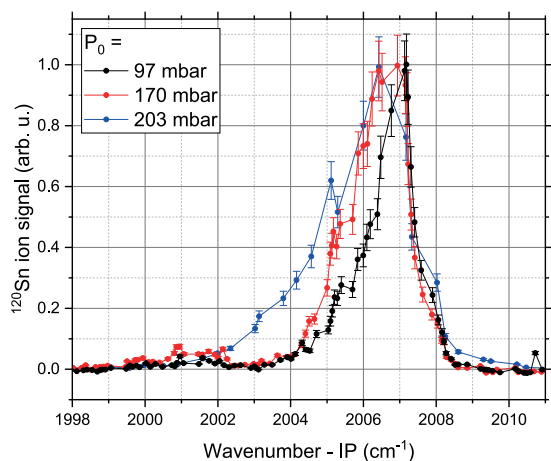


**Fig. 12.** Normalized ion count rate as a function of the wavenumber of the second-step transition using mass-separated $^{120}$Sn, performed at different values of argon pressure $P_0$. The two-step laser resonance ionization scheme shown in Fig. 10 was used. The horizontal axis indicates the wavenumber (cm$^{-1}$) with respect to the value of the ionization potential (IP), 59236.5 cm$^{-1}$.

a $^{223}$Ra $\alpha$-recoil source as well as resonantly-ionized tin isotopes from a heated filament. The ion survival and transport efficiency have been measured at Detector position 1 as a function of recoil source position as well as buffer gas pressure, with a maximum value of $\sim$12.7% obtained for the source located closest to the outflow when helium gas is used. For the same source position and gas type, a corresponding evacuation time of $\sim$100 ms has been measured. An ion survival and transport efficiency of $\sim$8.5% and an evacuation time of $\sim$127 ms were measured for the source positioned in the location at the middle of the entrance window. It has been shown that ionization of the buffer gas and its impurities takes place in the immediate vicinity of the needle tip by the released $^{219}$Rn recoils. Numerical calculations of the time profiles of the extracted ions when the recoil source is operated in a pulsed-release mode showed good agreement with the measured data. Suppression of the ion signal of $^{219}$Rn was successfully achieved

with 5 V applied to one of the ion-collector electrodes, verifying their potential use for improving the selectivity of the in-gas laser resonant ionization process in future experiments.

In-gas-cell laser resonance ionization of stable tin isotopes has been performed and broadening of the atomic resonances with increase of the gas cell pressure was observed for the second step transition. The chosen collinear laser-atom geometry, although successfully used for laser ionization, indicates a strong sensitivity to different regions of gas flow (both Doppler and collisional effects are convoluting), prohibiting extraction of pressure broadening and shift coefficients. This supports a crossed-beams geometry with a well-defined, localized laser ionization volume within the gas cell, to explore the effect of pressure changes on the spectral lineshape. The broadening seen highlights the expected challenges in resolving isotope shifts and hyperfine structure of exotic radioactive tin isotopes in the future, necessitating the requirement of performing resonant laser ionization in the low density and low temperature media of high Mach number gas jets formed downstream from the de Laval nozzles, rather than within the subsonic gas flow regime inside the gas cell.

**CRediT authorship contribution statement**

**A. Zadvornaya:** Investigation, Formal analysis, Supervision, Writing – original draft. **J. Romero:** Investigation, Formal analysis. **T. Eronen:** Investigation. **W. Gins:** Investigation, Formal analysis. **A. Kankainen:** Writing – review & editing. **I.D. Moore:** Supervision, Writing – review & editing. **P. Papadakis:** Project administration, Investigation, Writing – review & editing. **I. Pohjalainen:** Investigation. **M. Reponen:** Investigation. **S. Rinta-Antila:** Investigation. **J. Sarén:** Writing – review & editing. **D. Simonovski:** Investigation, Formal analysis, Validation. **J. Uusitalo:** Writing – review & editing.

**Declaration of competing interest**

The authors declare that they have no known competing financial interests or personal relationships that could have appeared to influence the work reported in this paper.

**Data availability**

Data will be made available on request

**Acknowledgments**

**References**

[1] P. Papadakis, I. Moore, I. Pohjalainen, J. Sarén, J. Uusitalo, Development of a low-energy radioactive ion beam facility for the MARA separator, Hyperfine Interact. 237 (2016) 152, http://dx.doi.org/10.1007/s10751-016-1364-8.

[2] H. Schatz, A. Aprahamian, J. Görres, M. Wiescher, T. Rauscher, J. Rembges, F.-T. Thielemann, B. Pfeiffer, P. Möller, K.-L. Kratz, H. Herndl, B. Brown, H. Rebel, rp-process nucleosynthesis at extreme temperature and density conditions, Phys. Rep. 294 (4) (1998) 167–263, http://dx.doi.org/10.1016/S0370-1573(97)00048-3.

[3] C. Fröhlich, G. Martínez-Pinedo, M. Liebendörfer, F.-K. Thielemann, E. Bravo, W.R. Hix, K. Langanke, N.T. Zinner, Neutrino-induced nucleosynthesis of $A > 64$ nuclei: The $\nu p$ process, Phys. Rev. Lett. 96 (2006) 142502, http://dx.doi.org/10.1103/PhysRevLett.96.142502.

[4] J. Romero, K. Auranen, M. Block, A.D. Briscoe, T. Eronen, W. Gins, T. Grahn, P.T. Greenlees, A. Illana, R. Julin, H. Joukainen, H. Jutila, J. Khuyagbaatar, J. Krier, M. Leino, J. Louko, M. Luoma, I.D. Moore, P. Mosat, J. Ojala, A. Ortiz-Cortes, J. Pakarinen, P. Papadakis, A.M. Plaza, P. Rahkila, A. Raggio, P. Ruotsalainen, J. Saren, M. Sandzelius, A. Tolosa-Delgado, J. Uusitalo, G. Zimba, Nuclear reaction studies and prospects for the new MARA-LEB facility, Acta Phys. Pol. B Proc. Suppl. 16 (2023) (in press).

[5] P. Papadakis, J. Liimatainen, J. Sarén, I. Moore, T. Eronen, J. Partanen, I. Pohjalainen, S. Rinta-Antila, J. Tuunanen, J. Uusitalo, The MARA-LEB ion transport system, Nucl. Instrum. Methods B 463 (2020) 286–289, http://dx.doi.org/10.1016/j.nimb.2019.05.007.

[6] J. Uusitalo, J. Sarén, J. Partanen, J. Hilton, Mass analyzing recoil apparatus, MARA, Acta Phys. Polon. B 50 (2019) 319, http://dx.doi.org/10.5506/APhysPolB.50.319.

[7] R. Ferrer, et al., In gas laser ionization and spectroscopy experiments at the superconducting separator spectrometer ($S^3$): Conceptual studies and preliminary design, Nucl. Instrum. Methods B 317 (2013) 570–581, http://dx.doi.org/10.1016/j.nimb.2013.07.028.

[8] Y. Kudryavtsev, P. Creemers, R. Ferrer, C. Granados, L. Gaffney, M. Huyse, E. Mogilevskiy, S. Raeder, S. Sels, P. Van den Bergh, P. Van Duppen, A. Zadvornaya, A new in-gas-laser ionization and spectroscopy laboratory for off-line studies at KU Leuven, Nucl. Instrum. Methods B 376 (2016) 345–352, http://dx.doi.org/10.1016/j.nimb.2016.02.040, Proceedings of the XVIIth International Conference on Electromagnetic Isotope Separators and Related Topics (EMIS2015), Grand Rapids, MI, U.S.A., 11-15 May 2015.

[9] COMSOL Multiphysics, https://www.comsol.com/.

[10] Y. Kudryavtsev, R. Ferrer, M. Huyse, P. Van den Bergh, P. Van Duppen, The in-gas-jet laser ion source: Resonance ionization spectroscopy of radioactive atoms in supersonic gas jets, Nucl. Instrum. Methods B 297 (2013) 7–22, http://dx.doi.org/10.1016/j.nimb.2012.12.008.

[11] A. Zadvornaya, et al., Characterization of supersonic gas jets for high-resolution laser ionization spectroscopy of heavy elements, Phys. Rev. X 8 (2018) 041008, http://dx.doi.org/10.1103/PhysRevX.8.041008.

[12] J. Äystö, A. Jokinen, T. Eronen, A. Kankainen, I. Moore, H. Penttilä (Eds.), Three Decades of Research Using IGISOL Technique at the University of Jyväskylä, Springer, International, 2014.

[13] J. Huikari, P. Dendooven, A. Jokinen, A. Nieminen, H. Penttilä, K. Peräjärvi, A. Popov, S. Rinta-Antila, J. Äystö, Production of neutron deficient rare isotope beams at IGISOL: on-line and off-line studies, Nucl. Instrum. Methods B 222 (3) (2004) 632–652, http://dx.doi.org/10.1016/j.nimb.2004.04.164.

[14] J. Eberz, U. Dinger, G. Huber, H. Lochmann, R. Menges, G. Ulm, R. Kirchner, O. Klepper, T. Kühl, D. Marx, Nuclear spins, moments and charge radii of $^{108-111}$Sn, Z. Phys. A 326 (1987) 121–129, http://dx.doi.org/10.1007/BF01283586.

[15] P. Karvonen, I.D. Moore, T. Sonoda, T. Kessler, H. Penttilä, K. Peräjärvi, P. Ronkanen, J. Äystö, A sextupole ion beam guide to improve the efficiency and beam quality at IGISOL, Nucl. Instrum. Methods B 266 (21) (2008) 4794–4807, http://dx.doi.org/10.1016/j.nimb.2008.07.022.

[16] R.J. van Sonsbeek, Ronald Cooper, R.N. Bhave, Pulse radiolysis studies of ion–electron recombination in helium. Pressure and temperature effects, J. Chem. Phys. 97 (1992) http://dx.doi.org/10.1063/1.463167, 1800–.

[17] Ronald Cooper, R.J. van Sonsbeek, R.N. Bhave, Pulse radiolysis studies of ion-electron recombination in gaseous argon, J. Chem. Phys. 98 (1993) http://dx.doi.org/10.1063/1.464631, 383–.

[18] M. Facina, B. Bruyneel, S. Dean, J. Gentens, M. Huyse, Y. Kudryavtsev, P. Van den Bergh, P. Van Duppen, A gas cell for thermalizing, storing and transporting radioactive ions and atoms. Part II: On-line studies with a laser ion source, Nucl. Instrum. Methods B 226 (3) (2004) 401–418, http://dx.doi.org/10.1016/j.nimb.2004.06.031.

[19] I. Pohjalainen, I.D. Moore, T. Eronen, A. Jokinen, H. Penttilä, S. Rinta-Antila, Gas purification studies at IGISOL-4, Hyperfine Interact. 227 (2014) 169–180, http://dx.doi.org/10.1007/s10751-013-1006-3.

[20] M. Reponen, I.D. Moore, I. Pohjalainen, V. Sonnenschein, A. Jokinen, The FURIOS laser ion source at IGISOL-4, Nucl. Instrum. Methods B 317 (2013) 422–425, http://dx.doi.org/10.1016/j.nimb.2013.05.061, XVIth International Conference on ElectroMagnetic Isotope Separators and Techniques Related to their Applications, December 2–7, 2012 at Matsue, Japan.

[21] V. Sonnenschein, I.D. Moore, S. Raeder, M. Reponen, H. Tomita, K. Wendt, Characterization of a pulsed injection-locked Ti:sapphire laser and its application to high resolution resonance ionization spectroscopy of copper, Laser Phys. 27 (8) (2017) 085701, http://dx.doi.org/10.1088/1555-6611/aa7834.

[22] M. Reponen, Resonance Laser Ionization Developments for IGISOL-4 (Ph.D. thesis), 2012.

[23] P.J. Gardner, P. Pang, S.R. Preston, Binary gaseous diffusion coefficients of mercury and of zinc in hydrogen, helium, argon, nitrogen, and carbon dioxide, J. Chem. Eng. Data 36 (0021–9568) (1991) http://dx.doi.org/10.1021/je00003a003.

[24] Y. Kudryavtsev, B. Bruyneel, M. Huyse, J. Gentens, P. Van den Bergh, P. Van Duppen, L. Vermeeren, A gas cell for thermalizing, storing and transporting radioactive ions and atoms. Part I: Off-line studies with a laser ion source, Nucl. Instrum. Methods B 179 (3) (2001) 412–435, http://dx.doi.org/10.1016/S0168-583X(01)00575-4.

[25] P. Dendooven, S. Purushothaman, K. Gloos, On a cryogenic noble gas ion catcher, Nucl. Instrum. Methods A 558 (2) (2006) 580–583, http://dx.doi.org/10.1016/j.nima.2005.12.201.

[26] W. Plaß, T. Dickel, S. Purushothaman, P. Dendooven, H. Geissel, J. Ebert, E. Haettner, C. Jesch, M. Ranjan, M. Reiter, H. Weick, F. Amjad, S. Ayet, M. Diwisch, A. Estrade, F. Farinon, F. Greiner, N. Kalantar-Nayestanaki, R. Knöbel, J. Kurcewicz, J. Lang, I. Moore, I. Mukha, C. Nociforo, M. Petrick, M. Pfützner, S. Pietri, A. Prochazka, A.-K. Rink, S. Rinta-Antila, D. Schäfer, C. Scheidenberger, M. Takechi, Y. Tanaka, J. Winfield, M. Yavor, The FRS Ion Catcher – A facility for high-precision experiments with stopped projectile and fission fragments, Nucl. Instrum. Methods B 317 (2013) 457–462, http://dx.doi.org/10.1016/j.nimb.2013.07.063.

[27] OriginPro, Version 2017, OriginLab Corporation, Northampton, MA, USA, https://www.originlab.com/.

[28] D. Simonovski, Offline Tests with the Fission Ion Guide and MARA-LEB Gas Cell at the IGISOL-4 Facility, Tech. Rep., University of Jyväskylä.

[29] A. Nadeem, S.A. Bhatti, N. Ahmad, M.A. Baig, Two-step laser excitation of $5p_{3/2}n$p, $n$f $J = 1$ and 2 autoionizing Rydberg levels of tin, J. Phys. B: At. Mol. Opt. Phys. 33 (18) (2000) 3729, http://dx.doi.org/10.1088/0953-4075/33/18/321.